

UC San Diego

UC San Diego Electronic Theses and Dissertations

Title

Avian Feathers: An Examination of Lightweight Resilience and Bioinspired Designs

Permalink

<https://escholarship.org/uc/item/9s34g3f8>

Author

Sullivan, Tarah

Publication Date

2017

Peer reviewed|Thesis/dissertation

UNIVERSITY OF CALIFORNIA, SAN DIEGO

Avian Feathers: An Examination of Lightweight Resilience and Bioinspired Designs

A dissertation submitted in partial satisfaction of the requirements
for the degree of Doctor of Philosophy

in

Materials Science and Engineering

by

Tarah Naoe Sullivan

Committee in charge:

Professor Marc A. Meyers, Chair
Professor Shengqiang Cai
Professor Vlado A. Lubarda
Professor Joanna McKittrick
Professor Jan B. Talbot
Professor Michael T. Tolley

2017

Copyright

Tarah Naoe Sullivan, 2017

All rights reserved.

The Dissertation of Tarah Naoe Sullivan is approved, and it is acceptable in quality and form for publication on microfilm and electronically:

Chair

University of California, San Diego

2017

DEDICATION

This work is dedicated to my family.

EPIGRAPH

In all things of nature there is something of the marvelous.

Aristotle

TABLE OF CONTENTS

SIGNATURE PAGE	iii
DEDICATION	iv
EPIGRAPH	v
TABLE OF CONTENTS	vi
LIST OF FIGURES	x
LIST OF TABLES.....	xvii
ACKNOWLEDGEMENTS	xviii
VITA	xxi
ABSTRACT OF THE DISSERTATION	xxiii
1. Introduction and Objectives.....	1
1.1. Bioinspiration and Materials Science	1
1.2. Research Focus and Motivation.....	2
1.3. Research Objectives.....	5
2. Background.....	6
2.1. Evolution of Birds and Feathers	6
2.2. Bird Wing Background.....	8
2.3. Wing Loading in Flight.....	11
2.3.1. Bending and Torsion.....	12
2.4. Wing Design Concepts: Wing Bones and Feathers	14
2.4.1. Thin, Dense Exterior.....	15
2.4.2. Reinforcing Internal Structures.....	21
2.5. Efficiently Tailored Designs Based on Specific Conditions.....	23
2.5.1. The Effect of Flight Style and Diving on Wing Bones.....	25
2.5.2. The Effect of Flight Style and Diving on Flight Feathers	27
2.6. Differences Between Wings of Birds and Pterosaurs and Bats	28
2.7. Feather Background.....	30
2.7.1. The Importance of Feathers for Flight	30
2.7.2. Feather Types and Structure	31
2.7.3. Feather Composition.....	34
2.7.4. Mechanical Properties of the Flight Feather.....	36
2.8. Natural Adhesives.....	37
2.9. Shape Memory Polymers.....	40
2.10. Conclusions.....	42
2.11. Acknowledgements.....	43

3.	Scaling Relationships of Bird Wings and Feathers for Efficient Flight	44
3.1.	Introduction.....	44
3.2.	Materials and Methods.....	49
3.2.1.	Avian Bone Specimens	49
3.2.2.	Avian Bone Characterization	49
3.2.3.	Feather Specimens	50
3.2.4.	Feather Characterization	50
3.2.5.	Data from Literature	50
3.3.	Results and Discussion	51
3.3.1.	Allometric Scaling of Avian Wing Bone Due to Materials Limit	51
3.3.2.	Allometric Scaling of Wing Bone to Accommodate Flight Style	53
3.3.3.	Scaling Trends Observed in the Avian Feather	59
3.4.	Conclusions.....	64
3.5.	Acknowledgements.....	65
4.	Resilience of Feather Barbs	67
4.1.	Introduction.....	67
4.2.	Materials and Methods.....	71
4.2.1.	Test Specimens	71
4.2.2.	Mechanical Tests	71
4.2.3.	Scanning Electron Microscopy.....	72
4.2.4.	Computer Aided-Design Measurements.....	73
4.2.5.	Finite Element Modeling	73
4.2.6.	Statistical Analysis.....	74
4.3.	Theory and Calculations	74
4.3.1.	Elastic Modulus of the Barb's Foam-filled Center	74
4.3.2.	Simplified Block Model of Single Barb Deflection	75
4.3.3.	Analytical Model of Single Barb Deflection	79
4.3.4.	Finite Element Model of a Single Barb in Flexure	80
4.4.	Results and Discussion	80
4.4.1.	Materials Characterization	80
4.4.2.	Cyclic Testing of Single Barbs	83
4.4.3.	Linear Deflection of Single Barbs	86
4.4.4.	Comparison between the Experimental Results and Models.....	87
4.4.5.	Deflection of Multiple Barbs	90
4.4.6.	Strengthening Mechanisms of the Feather Vane	91
4.5.	Conclusions.....	92
4.6.	Acknowledgements.....	92
5.	Feather Barbules	94
5.1.	Introduction.....	94
5.2.	Materials and Methods.....	99
5.2.1.	Feather Samples	99
5.2.2.	Feather Vane Adhesion.....	99
5.2.3.	Barbule Flexure Tests	100
5.2.4.	Wind Tunnel Test Specimens and Setup	102
5.2.5.	Wind Tunnel: Barbule Adhesion and Air Capture	103

5.2.6.	Wind Tunnel: Directional Permeability of the Vane	103
5.2.7.	Barbule Characterization	104
5.2.8.	Statistical Analysis.....	104
5.3.	Results and Discussion	104
5.3.1.	Adhesion Within the Feather Vane.....	104
5.3.2.	Barbule Flexure.....	116
5.3.3.	Barbule Adhesion and the Feather’s Ability to Capture Air.....	117
5.3.4.	Directional Permeability of the Feather Vane	120
5.4.	Conclusions.....	123
5.5.	Acknowledgements.....	124
6.	Hydration Induced Shape and Strength Recovery of the Feather.....	125
6.1.	Introduction.....	125
6.2.	Materials and Methods.....	129
6.2.1.	Test Specimens	129
6.2.2.	Flexure Tests on the Feather Shaft.....	129
6.2.3.	Cyclical Flexure Tests on the Feather Shaft	130
6.2.4.	Water Retention and Swelling Experiments	130
6.2.5.	Tensile Tests on Cortex	131
6.2.6.	Transmission Electron Microscopy	131
6.3.	Results and Discussion	132
6.3.1.	Shape and Strength Recovery of the Feather	132
6.3.2.	Mechanism for Shape Memory Recovery	140
6.4.	Conclusions.....	145
6.5.	Acknowledgements.....	146
7.	Bioinspired Designs of the Avian Feather.....	147
7.1.	Introduction and Background: Bird Wing Bioinspiration and Analogous Designs.....	148
7.1.1.	Avian Wing Shape Design.....	148
7.1.2.	Avian Wing Bone Design	149
7.1.3.	Feather Design	151
7.2.	Materials and Methods.....	152
7.2.1.	Fabrication of Barbule Inspired Structures by Additive Manufacturing 152	
7.2.2.	Fabrication of Bioinspired Feather Laminate	152
7.2.3.	Adhesion Tests of Flexible Bioinspired Hooks and Grooves.....	153
7.3.	Results and Discussion: Barbule Inspired Structures	153
7.3.1.	Barbule Structure Simplification	154
7.3.2.	Flexible Barbule Design	155
7.3.3.	Barbule Inspired Designs With Membrane Flaps.....	158
7.3.4.	Barbule-Inspired Designs to Allow for Tailored Air Permeability	160
7.3.1.	Summary of Bioinspired Barbules.....	165
7.4.	Designs Inspired by the Feather Shaft	168
7.4.1.	Bioinspired Medullary Foam Design.....	168
7.4.2.	Bioinspired Feather Laminate Design	168
7.4.3.	Shape Memory Recovery Inspired Design Concept.....	169

7.4.4.	Shape Change Inspired Design	170
7.5.	Conclusions.....	170
7.6.	Acknowledgements.....	171
8.	Summary and Future Outlook.....	172
8.1.	Summary	172
8.2.	Future Outlook	174
9.	Appendix.....	175
9.1.	Foam Calculations	175
9.2.	Determining the Location of the Neutral Axis	176
9.3.	Deriving the Inverse Curvature of M_y	178
9.4.	Acknowledgments.....	178
10.	References.....	179

LIST OF FIGURES

Figure 1.1 A famous example of bioinspiration: (a.) Scanning electron micrograph of the mechanical hook-and-loop adhesive Velcro [2], and (b.) the burdock plant burr, from which Velcro was inspired [3].	1
Figure 1.2 Ancient cave painting of a bird landing from “Cueva de la Soledad”. Red arrows point to the alula. Image modified from [6].	2
Figure 1.3 A page from Leonardo da Vinci’s “Codex on the Flight of Birds” [7].	3
Figure 1.4 (a) The kingfisher bird dives into water without creating a splash due to its beak shape[9]. (b) The Shinkansen nose cone design was inspired by the kingfisher beak [10].	4
Figure 2.1: The evolution of flight is strongly correlated to the development of the modern feather, as highlighted by the red circles and boxes. Image taken from [13].	6
Figure 2.2 The predecessor to the modern feather in dinosaurs was thought to be used in thermoregulation or sexual selection. Reconstructions of the dinosaur Epidexipteryx hui (a) and Gigantoraptor erlianensis (b) demonstrate what these structures may have looked like. Images are taken [21], [22] respectively.	7
Figure 2.3 The evolution of feathers from single filaments to highly hierarchical structures. Most modern birds have stage four or five feathers [20].	7
Figure 2.4 The proposed evolution of the bird wing and flight in birds. (i) bipedal and terrestrial dinosaur, (ii) development of anisodactyl foot structure, (iii) dinosaur leaps on lower branches, (iv) tail reduction, (v, vi) development of feathers, (vii, viii) formation of fully developed feathers (Figure from [23], drawn by O. Orekhova-Sokolova).	8
Figure 2.5: Precursors to modern feathers were much less developed as shown in (c) by the plumage of a non-avian dinosaur from ~99 million years ago preserved in Burmese amber (image from L. Xing et al. (2016) [28]).	10
Figure 2.6 Wing Loading in Flight	14
Figure 2.7 Micro computerized tomography scans of the wing bones of the: (a) Wandering albatross (<i>Diomedea exulans</i>), which has the largest wingspan of any living bird[47], (b) Turkey Vulture (<i>Cathartes aura</i>)[47], and (c) California Condor (<i>Gymnogyps californianus</i>).	17
Figure 2.8 The hierarchical structure of bone (a): Tropocollagen molecules and mineral crystals organize to form fiber bundles. These form lamellae that surround an osteon, which form cancellous and cortical bone. [47]	19
Figure 2.9 Micro computerized tomography (μ -CT) generated images of an Andean Condor (<i>Vultur gryphus</i>) primary feather.	21
Figure 2.10 Internal reinforcements in the avian bone and feather.	23
Figure 2.11 Variation of wing types: (a) High-aspect ratio, (b) High-speed, (c) Elliptical, (d) High-lift. Images taken from [34].	24

Figure 2.12 The mid-humerus of the Cape Vulture (*Gyps coprotheres*) (a) has high torsion resistance, while the mid-humerus of the California Gull (*Larus Californicus*) (b) has low torsional resistance. 26

Figure 2.13 Cross sections of the wing feathers of the: (a) Ostrich (*Struthio camelus*), a flightless bird and (b) the American White Pelican (*Pelecanus erythrorhynchos*) a flying bird, where scale bars are 1mm..... 28

Figure 2.14 Wing retraction in the (a.) bird, (b.) bat, and (c.) pterosaur [24,72]..... 29

Figure 2.15 Lilenthal conducted experiments to determine what effects the feathers had on flight. In this example, the bird was still able to fly high and fast [73]. 30

Figure 2.16 The mutilated wings of the house sparrow from Brown and Cogley’s experiments: (a.) With only the outermost six primaries remaining, (b.) With 8 mm cut off of the ends of the primaries, (c.) With 16 mm cut off, (d.) With 24 mm cut off [74]. 31

Figure 2.17 Birds have a variety of feathers for different functions. Image taken from [76]...... 32

Figure 2.18 The flight feather is composed of the feather shaft (rachis and calamus) and the feather vane (barbs and barbules). Barbs are foam-filled asymmetrical beams that branch from the rachis and barbules are minute hooked beams and grooves that branch from barbs to interlock with each other.. 33

Figure 2.19 The hierarchical structure of the feather shaft cortex (a): β -keratin filaments form macrofibrils and these bundle to form fibers. The orientation of the fibers varies throughout the feather shaft. 35

Figure 2.20 Types of adhesive mechanisms found in nature along with the physical effects involved in achieving adhesion [95]. 38

Figure 2.21 Functions of attachment [95]: Attachment to substrate (ex. eggs of butterfly, spider silk, ivy root, mussel thread; Locomotion (ex. fly leg hairs to adhere to glass, spider claws, grasshopper adhesive pad); Parasitism (ex. lice leg clamp, mouthpart of mite, aquatic mite); 39

Figure 2.22 Existing and potential bioinspired biological attachment devices. A, wet adhesion; B, hooks; C, lock; D, suction cup; E, friction; F, spacer; G, clamp; H, dry adhesion [95]...... 40

Figure 2.23 Shape memory polyamide returns to its original state after thermal annealing [101]...... 41

Figure 2.24 The various types of stable polymer networks and reversible switching transitions in shape memory polymers [102]...... 42

Figure 3.1 The human brain scales with positive allometry while the human heart scales isometrically [128–130]. 45

Figure 3.2 A replot of Tennekes’ “Great Flight Diagram”. 48

Figure 3.3 Examples of humerus bones measured (top to bottom): Turkey vulture (*cathartes aura*), red-tailed hawk (*buteo jamaicensis*), Barn owl (*tyto alba*), American coot

(fulica americana). The respective weights of these birds are 15.5 N, 10.9 N, 2.8 N and 4.35 N..... 49

Figure 3.4 The humerus is considered to be a hollow cylinder with length L_H , diameter $2c$ and thickness t . The sum of the distributed force, $w(L_H)$, and the point load (F_2), which represents loading on the distal part of the wing, is equal to the weight of the bird (W) divided by 2..... 52

Figure 3.5 Experimental data demonstrates that the humerus length L_H scales allometrically with the weight W of the bird. The upper curve designates allometry from Equation 3.8. Isometric scaling would require $L_H \propto W^{0.33}$ (lower curve)..... 53

Figure 3.6 The cruising speed is plotted against wing area on a log - log scale for a variety of birds. The weight of the bird is indicated by the color coding. Diagonal grey lines represent calculated values of lift, which are nearly equal to the weight of the bird. Data plotted are from [139–141]..... 55

Figure 3.7 The cruising speed and wing area are plotted against one another. The percent wingspan composed of humerus (humerus length/half of wingspan) is plotted with color. Data plotted are from [139–141]..... 56

Figure 3.8 Birds (1) and (2) have the same mass and humerus length. Bird 1 however, has a much smaller wing area and therefore has higher wing loading. To compensate for this, a larger percent of bird 1’s wingspan is composed of humerus bone. 57

Figure 3.9 The percent of the wingspan L_H/L composed of the humerus plotted against wing loading W/A on a log-log scale. The cruising velocity is color mapped..... 58

Figure 3.10 The total feather shaft length scales with bird mass following the trend $y=2.3x^{0.34}$ with an R^2 value of 0.95 (where measurement uncertainty is $\pm 0.05\text{cm}$). This trend is very close to the trend expected through isometric scaling with bird mass. Images taken from [47]. 60

Figure 3.11 The width of the feather shaft at its midpoint scales with bird mass exponentially following the trend $y=0.19x^{0.35}$ with an R^2 value of 0.95 (measurement uncertainty is $\pm 0.02\text{ mm}$)[47]. 61

Figure 3.12 The barb length of the trailing and leading feather vane follow $y=4.29x^{0.27}$ ($R^2=0.91$), and $y=2.58x^{0.25}$ ($R^2=0.83$) respectively (standard deviations range from 0.02-0.2mm)[47]. 61

Figure 3.13 Surprisingly, the spacing between trailing hooked barbules does not follow this trend and ranges between 8-16 micrometers across all bird masses[47]. 62

Figure 3.14 An example of the barbule spacing dimension is shown in (a). A bioinspired model created by additive manufacturing (b) was used to show the behavior of the barbule membrane flaps..... 64

Figure 4.1 Barb and barbule structure: barbs are asymmetrically shaped and foam filled. On the distal side of the barb barbules have hooklets and on the proximal side barbules are grooved. Barbules from neighboring barbs interlock with each other. Redrawn[77] after Lucas and Stettenheim (1972) [145]. 68

Figure 4.2 Barbs and barbules from various bird species: in nearly all flying birds, barbs and barbules have a similar shape, as demonstrated in this comparison between the razor-billed curassow (*Mitu tuberosum*), house sparrow (*Passer domesticus*), and California seagull (*Larus californicus*)[77]. 70

Figure 4.3 Experimental configuration: cantilever flexure tests on single barbs and four zipped barbs [77]. 72

Figure 4.4 Simplified barb used in theoretical calculations: (a) the definitions of dimensions used, where $h_2=h_4=h_5$ (b) sketch of the orientation of the applied force. 76

Figure 4.5 (a) Barb cross sectional shape and size: the barb becomes smaller and more symmetrical towards the tip. Characterizing the foam of the barb: The cell size distribution of the foam shows that at (b) 5% and especially (c) 30% from the rachis the cell size is more diverse than at (d) 90% of the barb length from the rachis. 81

Figure 4.6 The (a) x-, (b) y- and (c) xy- area moments of inertia of the barb's cortex and foam were found to follow an exponential decay trend. The foam and cortex were combined as explained in section 4.3.3. 83

Figure 4.7 The deflection of a barb: a typical experimental plot of displacement and force as a function of time. Black indicates loading and blue indicates unloading. The barb first (a) deflects in the y-direction, then (b) twists, resulting in a decrease in stiffness with respect to the y-axis. 84

Figure 4.8 The repeatability of flexure tests: the maximum force and effective barb length are plotted against the percent damage between the first and second cycles. With shorter barbs there are higher resistive forces and stresses, therefore the percent damage increases. 85

Figure 4.9 Experimental slope of force versus deflection: the slope of the linear portion of the first cycle of experimental trials versus the effective length of each sample. The slope of a barb with a constant cross section throughout its length is shown for comparison... 86

Figure 4.10 Comparison between the analytical and experimental force/deflection for the linear region of single barbs. Analytical calculations are based on the method described in section 4.3.3. 87

Figure 4.11 Finite element model of the deflected barb with the von Mises stress (MPa) plotted. Higher stresses appear on the dorsal and ventral sides of the end held in place and at the foam-cortex interface of the end contacting the wedge. This stress plotted corresponds to a prescribed displacement of 0.045mm. 88

Figure 4.12 Comparison of the force versus deflection of an experimental run, a representative simplified block model, analytical model based on analysis presented in section 4.3.3, and finite element model described in section 4.3.4. 89

Figure 4.13 Yielding point of four-zipped barbs and single barbs: an example of the first cycle of flexure tests for (a) four-zipped barbs and (b) single barbs. 90

Figure 4.14 The interlocking structure of the barbules: micrographs of the House sparrow (*Passer domesticus*) show (a) the hooklet sliding into the grooved proximal barbule, (b) overlapping barbules within a feather. 91

Figure 5.1 (a) Flight feathers are composed of a main shaft (rachis and calamus), barbs that branch from the rachis and barbules that stem from barbs. 95

Figure 5.2 Hooked Barbule SEM images of the American white pelican (*Pelecanus erythrorhynchos*) demonstrate their abundance on each distal barbule. 96

Figure 5.3 (a) Bat’s wings are composed of continuous skin flaps (patagium) while the complex feathers of birds allow for localized failure. (b) One of the advantages of the feather vane is that it can be separated and reattached; images of the feather vane taken at various moments during unzipping and re-zipping. 98

Figure 5.4 Schematics of various experiments: (a) experimental setup of feather vane tension tests; the darker lines within the feather represent barbs and lighter lines barbules. (b) Bioinspired interlocking barbules, with arrows showing directions of displacement in tension tests. 100

Figure 5.5 (a) The AFM cantilever contacts the barbule at angle θ to the normal; the dotted black line is the corrected force component. (b) The barbule structure is simplified into three sections (purple, green and blue). (c) The dimensions of the simplified barbule were found by averaging corresponding dimensions measured in SEM images. 102

Figure 5.6 In-plane tension tests of the pelican feather vane: (a) An example plot of the measured force vs. displacement reveals that on the macro-scale pelican feathers exhibit brittle-like failure when unzipped. (b) Before failure, barbules maintain attachment as barbs rotate proximally at angle θ throughout the test. 106

Figure 5.7 Schematic of the lengths and angles of the hooked barbule (L_h, β) and grooved barbule (L_g, α) from in-plane adhesion experiments: (a) A rectangular section of the feather vane is sliced. 107

Figure 5.8 (a) The simplified hooklet is shown with an applied load P at the end of segment 2. (b) Both the long and short segments (1 and 2) of the hooklet are expected to undergo large deflections with the application of load P . An accurate solution to this problem would likely require the use of finite elements. 108

Figure 5.9 (a) Schematic of the idealized microhook used in calculations, where dimensions are listed in Table 5.2. (b) Because segment 1 is assumed to be rigid, segment 2 is configured as a cantilever beam that undergoes large deflections. Terms are defined in section 5.3.1. 112

Figure 5.10 (a) Schematic of the idealized microhook used in calculations. (b) The definition of θ_1 and θ_2 are obtained when both segments 1 and 2 undergo large deflections. 114

Figure 5.11 (a) Critical snapshots of the barbule during in situ SEM flexure experiments: (left) at the initial position immediately before contact, (right) at the maximum load, just before separation. (b) Force versus percent of the vane unzipped for the guineafowl feather. 119

Figure 5.12 (a) An arrow points to an example of a barbule membrane. (b) A simplified, 3D-printed model of the feather vane, and (c) the hypothesized reaction of membrane flaps as air is blown dorsally (top) and ventrally (bottom), where circles represent the location of airflow. 120

Figure 5.13 (a) Experimental results plotting f , a quantitative measurement of the effect of barbule membranes on air capture, vs. airspeed for the three species tested. 122

Figure 6.1 The hierarchical structure of the feather: The flight feather of the Cape Vulture (*Gyps coprotheres*) is divided into the (a) rachis and (b) calamus. 127

Figure 6.2 Four Point Bending: Flexure tests were conducted on feather samples embedded in aluminum tubing. Steel rollers contacted the inner and outer parts of the top and bottom of the aluminum tubing..... 130

Figure 6.3 Recovery of the feather shaft in water: (a) A strip of the feather shaft cortex is severely deformed and recovers in water. (b) A rachis section with the vane removed is bent and recovers in water, red arrows highlight the location of the deformation. All scale bars are 1mm..... 133

Figure 6.4 Strength recovery of the feather shaft through hydration: Flexural test data of a calamus sample with no hydration step (a) and with a hydration step between test trials (b)..... 134

Figure 6.5 (a) Optical microscope images of calamus samples tested until failure (left a,b) and recovered with no hydration step (a, right) and with a hydration step (b, right). Scale bars are 0.5 mm..... 135

Figure 6.6 Recovery of the feather shaft: Feather shafts were sliced open along the dotted line shown in (a) to view the y-z cross section. Samples shown in (c,d) were tested to failure in bending, while sample (b) was not tested..... 138

Figure 6.7. The proposed mechanism for shape and strength recovery of the feather shaft. The cycle begins in the “initial configuration” showing the composite structure of β -keratin filaments in an amorphous matrix. The fibers undergo “deformation in bending” and buckle in compression..... 141

Figure 6.8 Schematic representation of different mechanical responses of fiber and matrix in the feather shaft. (a) Cross-section showing crystalline fibers and amorphous matrix; (b) overall response of feather in dry and hydrated conditions; (c) matrix and fiber responses. 142

Figure 6.9 Experiments were conducted to determine if the feather swells upon hydration: (a) the length, circumference and area of cross sections (as shown in c) of the rachis and calamus were compared before and after hydration. 144

Figure 7.1 The study of nature allows for the creation of refined bioinspired designs which ultimately allows for a better understanding of the natural system through bioexploration [172]. This is shown here for the sea urchin..... 147

Figure 7.2 Many analogous solutions have been developed through evolution and engineering: (a) The Andean condor’s feathers curl upward at its wing tips for more efficient flight. (b) A similar curvature is observed in the flexible wings of a Boeing 787. 149

Figure 7.3 Engineering has led to similar designs as those found in the avian feather and bone: (a) Nickel metallic foam inspired by the struts in avian bone (taken from X. Jin et

al. (2014) [176]), (b) a computer aided design model of diagonal struts in a multifunctional cellular material (taken from A.G. Evans et al. (2001) [177])...... 150

Figure 7.4 (a) A cross section of a primary feather from the American White Pelican (*Cathartes aura*) demonstrates the reinforcing ridges on the dorsal side of the feather [47]. The hierarchical synthetic composite (b) is inspired by the degrees of hierarchy in the feather (taken from V. Drakonakis et al. (2014) [190])...... 151

Figure 7.5 The interlocking structure of the barbules: micrographs of the House sparrow (*Passer domesticus*) show (a) the hooklet sliding into the grooved proximal barbule, (b) overlapping barbules within a feather. 155

Figure 7.6 The second attempt at a barbule bioinspired model, using a flexible filament material for the barbule hooks and grooves. 156

Figure 7.7 The third attempt at creating a bioinspired barbule model. Barbules were thinner and composed of a flexible filament material. 156

Figure 7.8 Adhesion of bioinspired hook and groove structures [155]: (a) Hooks A-E were created through 3D printing. (b) The maximum force vs. displacement for tension tests of the hook and groove structures reveal that hook A has the maximum force of adhesion. 157

Figure 7.9 The directional permeability in the feather vane is due to membrane flaps that extend from barbules to act as one way valves covering the space between barbules. Scanning electron micrographs show these flaps (a,b). 159

Figure 7.10 (a,b) Features of the feather vane were simplified and 3D printed into a bioinspired model of the entire feather. 160

Figure 7.11 (a) Barbules are bounded on both ends with a flexible material, (b) when these ends are pulled apart, feather become more permeable as space between each barb's barbules opens. 161

Figure 7.12 Grooved structures that slide along one another were created to allow for a design that has tailored permeability based on the distance edges are pulled apart from one another. 162

Figure 7.13 The square tubing model: (a) Squares slide through a tube and are stopped at the end. This allows the material to have tailored permeability. (b) As the material is scaled down smaller, it becomes more flexible as shown in (c). 163

Figure 7.14 (a,b)The square tubing model was altered to stretch in two dimensions, allowing for increased flexibility in the material (c) which is reflected in images of the maximum radius of curvature of closed and opened samples (d). 164

Figure 7.15 Tridimensional structure using the grooved design in which each element has six pegs aligned with three orthogonal axes. 165

Figure 7.16 Timeline of the evolution of bioinspired barbule designs: from the feather to tridimensional structures. 166

Figure 7.17 A foam structure inspired by the fibrous closed-cell structure of the feather's medullary foam would have novel properties. 168

Figure 7.18 Four types of cylindrical feather shaft-inspired samples were created. 169
Figure 7.19 Shape Memory Bioinspired Composite Structure. 170

LIST OF TABLES

Table 4.1 Definitions of variables used in Equations 4.2-4.18.....	77
Table 5.1 Cantilever Stiffness Summary	102
Table 5.2 Values used to determine the force necessary for a deflection of θb of 45°. Values are used in Equations 5.7-5.23.....	111
Table 9.1 Values for Foam Calculations.....	175
Table 9.2 Simplified barb dimensions. Units are in micrometers unless otherwise labeled.	177

ACKNOWLEDGEMENTS

I would like to thank my advisor Marc Meyers for his invaluable guidance and support throughout my PhD. I appreciate his encouragement of my creative pursuits and ideas, and the freedom that he granted me to study my research interests. I would also like to thank my committee members Shengqiang Cai, Vlado Lubarda, Joanna McKittrick, Jan Talbot and Michael Tolley for their suggestions, helpful discussion and support. I also thank Hyonny Kim, who provided helpful suggestions as a part of my senate exam committee.

I thank the San Diego Natural History Museum (Phil Unitt, curator of birds and mammals, the San Diego Zoo (April Gorow, Research Coordinator), the Los Angeles Zoo (Mike Maxcy, Curator of Birds and Dr. Cathleen Cox, Director of Research), and La Bellota Ranch (Raul Aginar) for providing samples for my research. I acknowledge Eduard Arzt, Horacio Espinosa, Pablo Zavattieri and David Kisailus for research collaborations throughout my studies. I thank Mason Mackey for assistance with transmission electron microscopy and Steve Roberts for help with the wind tunnel. I also acknowledge my master's advisor Andrea Tao, and would like to thank Robin Christ and Emilie Dressaire, teachers who have helped me to this point and beyond.

I am grateful to my fellow lab members and friends, especially Bin Wang and Vincent Sherman who helped me to gain my bearings in the lab and showed me how to use a variety of instruments. I would also like to thank the various undergraduate students who have worked with me as well as my colleagues Steven Naleway, Andrei Pissarenko and Frances Su for helpful discussions over the course of my research.

Finally, I would like to thank my family for their love and support. I thank my grandparents Roy and Hilda Takeyama and Mary Sullivan and my brother Matthew Sullivan for their kind encouragement. I would especially like to thank my parents Patrick and Jan Sullivan for always having faith in me and providing wise and thoughtful guidance. I thank my fiancée and best friend Matthew Suiter for his unwavering support of my endeavors. I could not have completed this without all of you.

The research presented in this dissertation was partially supported by the following awards and grants: Air Force Office of Scientific Research MURI grant (AFOSR-FA9550-15-1-0009), the UC San Diego Materials Science Program Fellowship, and the Achievement Rewards for College Scientist (ARCS) Scholarship.

Chapters 2, 3 and 7 in part, are published as a review article in *Materials Today*, authored by T. N. Sullivan, B. Wang, H.D. Espinosa, and M.A. Meyers. The dissertation author was the primary investigator and author on this publication.

Chapter 3 in part, is being prepared for submission by T.N. Sullivan, M.A. Meyers and E. Arzt. The dissertation author is the primary investigator and author on this publication.

Chapter 4, in full and 7 in part is published in *Acta Biomaterialia* and is authored by T.N. Sullivan, A. Pissarenko, S.A. Herrera, D. Kisailus, V.A. Lubarda and M.A. Meyers. The dissertation author was the primary investigator and author on this publication.

Chapter 5, in full and 7 in part is published in *Advanced Functional Materials*, authored by T.N. Sullivan, M. Chon, R. Ramachandramoorthy, M.R. Roenbeck, T.-T.

Hung, H.D. Espinosa, and M.A. Meyers. The dissertation author was the primary investigator and author on this publication.

Chapter 6 in full, and 7 in part will be revised and submitted for publication to *Advanced Materials*, authored by T.N. Sullivan, Y. Zhang, Z. Liu, P. Zavattieri and M.A. Meyers. The dissertation author is the primary investigator and author on this manuscript.

Chapter 7 in part is being prepared for submission for publication, authored by T.N. Sullivan, T.-T. Hung and M.A. Meyers. The dissertation author is the primary investigator and author on this manuscript.

VITA

- 2017 Ph.D. Materials Science and Engineering
University of California, San Diego, La Jolla, CA
Advisor: Marc André Meyers
- 2014 M.S. NanoEngineering
University of California, San Diego, La Jolla, CA
Advisor: Andrea Rae Tao
- 2013 B.S. Mechanical Engineering
Trinity College, Hartford, CT
Advisor: Emilie Dressaire

PUBLICATIONS

Sullivan, Tarah N., Yunlan Zhang, Zida Liu, Pablo D. Zavattieri and Marc A. Meyers. "Hydration induced shape and strength recovery of the feather". *In preparation*.

Sullivan, Tarah N., Tzu-Tying Hung and Marc A. Meyers. "Bioinspired designs of the feather vane". *In preparation*.

Sullivan, Tarah N., Marc A. Meyers and Eduard Arzt. "Scaling relationships of bird wings and feathers". *In preparation*.

Sullivan, Tarah N., Michael Chon, Rajaprakash Ramachandramoorthy, Michael R. Roenbeck, Tzu-Tying Hung, Horacio D. Espinosa, and Marc A. Meyers. "Reversible Attachment with Tailored Permeability: The Feather Vane and Bioinspired Designs." *Advanced Functional Materials* 27 (2017).

Sullivan, Tarah N., Bin Wang, Horacio D. Espinosa, and Marc A. Meyers. "Extreme lightweight structures: avian feathers and bones." *Materials Today* 20 (2017): 337-391.

Sullivan, Tarah N., Andrei Pissarenko, Steven A. Herrera, David Kisailus, Vlado A. Lubarda, and Marc A. Meyers. "A lightweight, biological structure with tailored stiffness: The feather vane." *Acta biomaterialia* 41 (2016): 27-39.

Wang, Bin, Tarah N. Sullivan. "A review of terrestrial, aerial and aquatic keratins: the structure and mechanical properties of pangolin scales, feather shafts and baleen plates." *Journal of the Mechanical Behavior of Biomedical Materials* 76 (2017): 4-20.

Wang, Bin, Tarah N. Sullivan, Audrey J. Hogan, Qiguang He, Alireza Zaheri, Shengqiang Cai, Horacio D. Espinosa and Marc A. Meyers. "Lessons from the Ocean: Whale Baleen Fracture and Impact Resistance." *In preparation*.

ABSTRACT OF THE DISSERTATION

Avian Feathers: An Examination of Lightweight Resilience and Bioinspired Designs

by

Tarah Naoe Sullivan

Doctor of Philosophy in Materials Science and Engineering

University of California, San Diego, 2017

Professor Marc André Meyers, Chair

In bird flight, the majority of the wing surface consists of highly refined and hierarchically organized β -keratinous feathers. Thus, flight feathers contain ingenious combinations of components that optimize lift, stiffness, aerodynamics, and damage resistance. Their design involves two main parts: a central shaft which prescribes stiffness and lateral vanes that allow for the capture of air. Within the feather vane, barbs branch from the shaft and barbules branch from barbs, forming a flat surface and ensuring lift. Microhooks at the end of barbules hold barbs tightly together, providing a close-knit, unified structure and enabling repair of the vane through the reattachment of un-hooked junctions.

In this dissertation, unique aspects of feather architecture are explored to uncover principles translatable to the design of modern aerospace materials and structures.

Specifically, understudied aspects of the feather's lightweight yet resilient properties are investigated. This research has revealed several novel characteristics of the feather. Allometric scaling relationships are developed linking the geometry of a bird's wing components to its flight characteristics and total mass. Barbule spacing within the feather vane is found to be 8-16 μm for birds ranging from 0.02-11 kg. Additionally, it is discovered that strength is recovered with the shape recovery property of feathers, and a mechanism for this phenomenon is proposed. Barbule adhesion within the vane is found to prevent barbs from twisting in flexure, maintaining the vane's stiffness, and the extent to which unzipping these connections affects the feather's ability to capture air is related to barb shape. Directional permeability of the feather vane is experimentally confirmed and related to the intricate microstructure of barbules. Lastly, the exceptional architecture of the feather motivated the design of novel bioinspired structures with tailored and unique properties. The avian feather serves as an excellent springboard for designs that can be adapted to enhance synthetic materials and structures.

1. Introduction and Objectives

1.1. Bioinspiration and Materials Science

Through the process of Darwinian evolution, natural materials and structures have advanced over billions of years of adaptation to ensure survival. These biological materials and organisms self-assemble under mild conditions, are often multifunctional and composed of relatively weak constituents, yet have exceptional mechanical properties[1]. Due to these and many other remarkable features, materials scientists and engineers have much to learn and adapt from nature, and find this space in the field of bioinspired materials. At the intersection of Biology, Engineering and Design, this field provides fertile ground for the creative development of solutions. Recently, the field of bioinspired materials has undergone pronounced growth, possibly due to new experimental techniques that allow for the detailed characterization of natural materials and novel manufacturing methods.

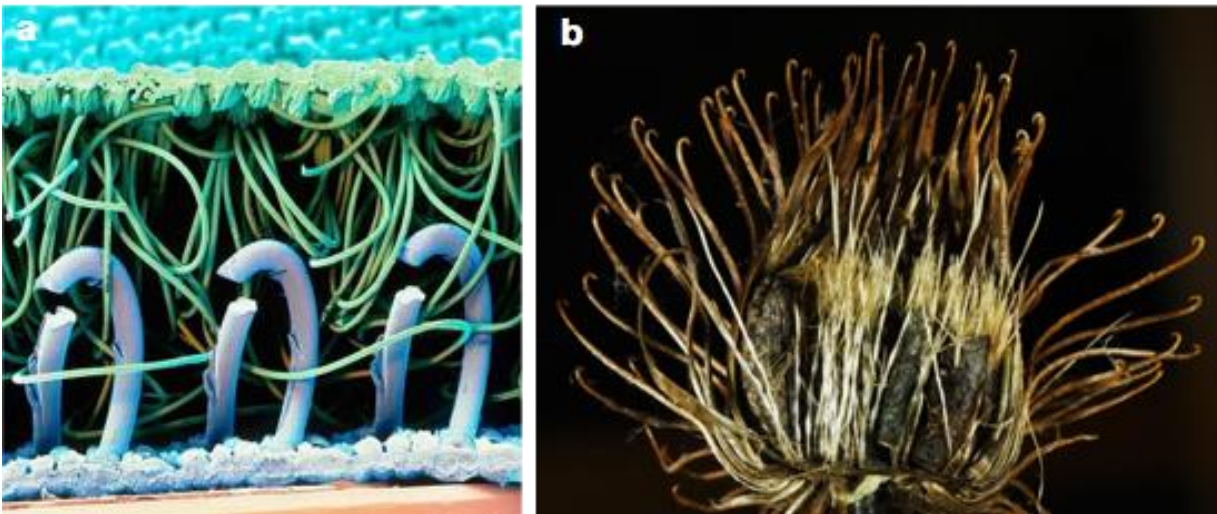


Figure 1.1 A famous example of bioinspiration: (a.) Scanning electron micrograph of the mechanical hook-and-loop adhesive Velcro [2], and (b.) the burdock plant burr, from which Velcro was inspired [3].

One of the most famous bioinspired materials is the hook-and-loop fastener Velcro® (**Figure 1.1**), which was invented by George de Mestral in 1941 after noticing how hooked burdock burrs stuck to his dog’s fur [4]. Other examples of bioinspired materials include structural composites that mimic the design of abalone nacre, light-harvesting photonic materials that imitate photosynthesis, and self-cleaning surfaces inspired by the lotus leaf [5]. In this dissertation, avian feathers are explored as a source of bioinspiration for lightweight, resilient materials.

1.2. Research Focus and Motivation

Since the ancient times mankind has been inspired by birds. Cave paintings in Baja California, Mexico estimated at 11,000 years old depict a bird landing with remarkable accuracy (**Figure 1.2**); Ornithologist J. Videler notes the alula and spread feet observed and copied by the artist [6].

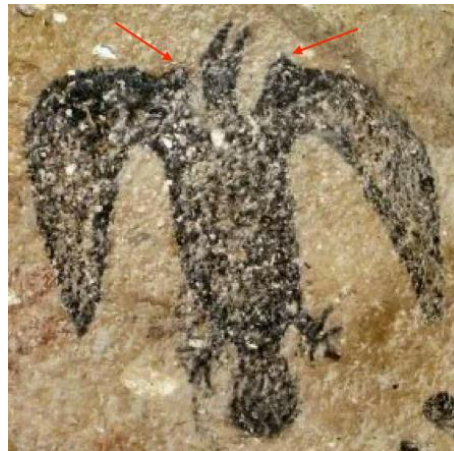


Figure 1.2 Ancient cave painting of a bird landing from “*Cueva de la Soledad*”. Red arrows point to the alula. Image modified from [6].

Leonardo da Vinci attempted to take on the goal of human flight, as documented in his “*Sul volo delgi Uccelli*” which is translated as “*Codex on the Flight of Birds*”, where he analyzed birds and proposed ideas on flight. A page from this text is shown in **Figure 1.3** with sketches of birds in flight.



Figure 1.3 A page from Leonardo da Vinci's "Codex on the Flight of Birds" [7].

More recently, the Shinkansen (Japanese bullet train) nose cone design was inspired by the kingfisher bird's beak shape. The kingfisher beak has evolved to be so streamlined that it allows for the bird to dive into water without creating a splash. The inspired nose cone allows the train to travel more quietly and efficiently[8]. **Figure 1.4** demonstrates the kingfisher diving into the water and the bioinspired train nose cone.



Figure 1.4 (a) The kingfisher bird dives into water without creating a splash due to its beak shape[9]. (b) The Shinkansen nose cone design was inspired by the kingfisher beak [10].

Despite the long history of human interest in bird flight, current aircraft wings differ largely from bird wings in structure and function. First, the bird wing can be extended outward and folded to the body of the animal while airplane wings cannot. Second, the bird wing flaps as well as glides, providing both lift and thrust forces[6], where airplanes require separate systems for these functions. Lastly, most birds are able to land in an extremely small area, such as a tree branch where nearly all airplanes require a large runway to land. These differences demonstrate that there is still much to learn from the flight of birds.

There are numerous evolutionary adaptations that allow the bird to be especially fit for flight. These include a lightweight skeleton, toothless beak, “bastard wing” (or alula) and efficient wing stroke. While these features are important to a bird’s ability to fly, the bird feather has been overlooked and its complex structure oversimplified--until recently. Feathers have many nano- and micro- structured components that are central to a bird’s ability to fly, and allow them to be lightweight, flexible, strong, and exhibit a spring-like behavior[11]. In birds capable of flight, contour feathers contribute 40 to 51% of the bird’s total wingspan [12] and must sustain lift forces without breaking. Since all feathers are composed of β -keratin, the difference in their function

(ranging from insulation to sustaining lift) is not correlated to their composition, but to their morphology and structure. Thus, their design contains ingenious combinations of components that optimize lift, stiffness, aerodynamics, and resilience.

1.3. Research Objectives

The objective of this dissertation is to reveal the mechanisms behind the lightweight and resilient characteristics of the flight feather and create bioinspired designs based on discoveries. We hypothesize that feather resilience is due to the feather's unique hierarchical structure and material properties that arose as a result of many iterations of design optimization through evolution. To investigate our hypothesis, hierarchical components of the flight feather are thoroughly characterized, resulting in simplified bioinspired designs based on findings.

2. Background

2.1. Evolution of Birds and Feathers

Through tens of millions of years of evolution [13] birds have developed to contend with the challenges of flight, a highly complex mode of locomotion that man only came to grasp about one hundred years ago. The bird's design includes a toothless keratinous beak [14] filled with cancellous bone [15], wing stroke efficiency [16], fusion of parts of the skeleton [17], and strong yet lightweight feathers and bones.

The complex design of the modern feather evolved during the Late Jurassic period along with the advancement of aerial locomotion (Figure 2.1) [13]. This unusual integument derived from less sophisticated filaments used for sexual selection and (or) thermoregulation in dinosaurs [18,19] (**Figure 2.2**). The stages of feather evolution have been identified through the amber fossilization of feathers: single hair-like filaments developed gradually into the highly sophisticated structures we see today (Figure 2.3)[20].

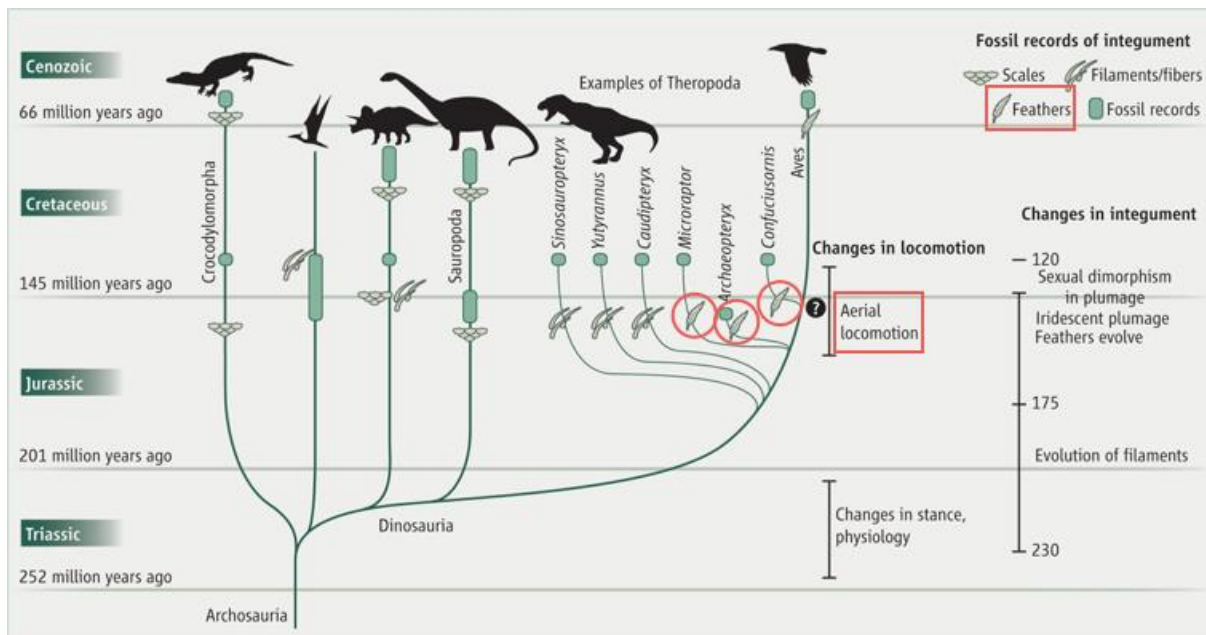


Figure 2.1: The evolution of flight is strongly correlated to the development of the modern feather, as highlighted by the red circles and boxes. Image taken from [13].

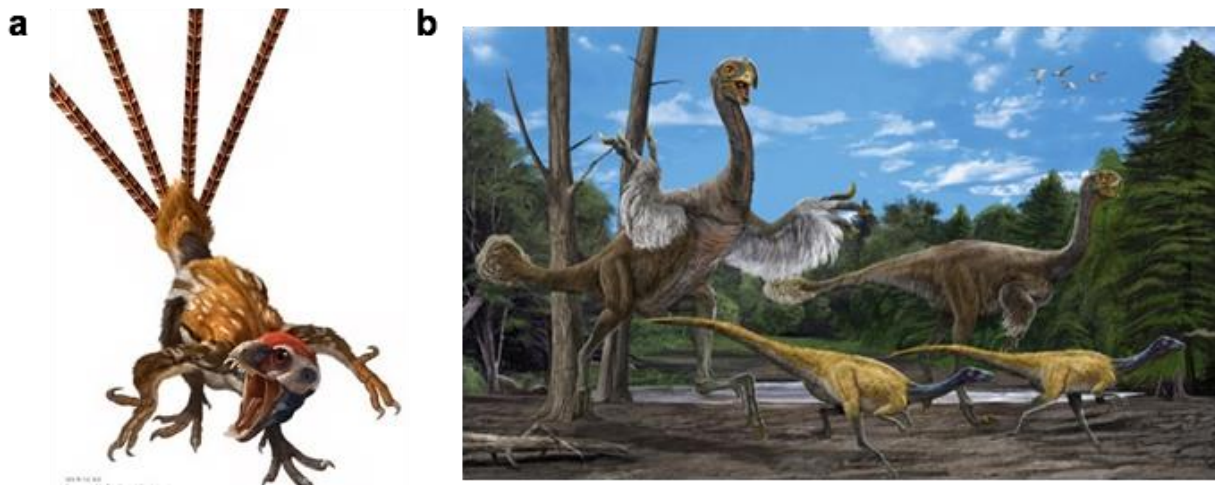


Figure 2.2 The predecessor to the modern feather in dinosaurs was thought to be used in thermoregulation or sexual selection. Reconstructions of the dinosaur *Epidexipteryx hui* (a) and *Gigantoraptor erlianensis* (b) demonstrate what these structures may have looked like. Images are taken [21], [22] respectively.

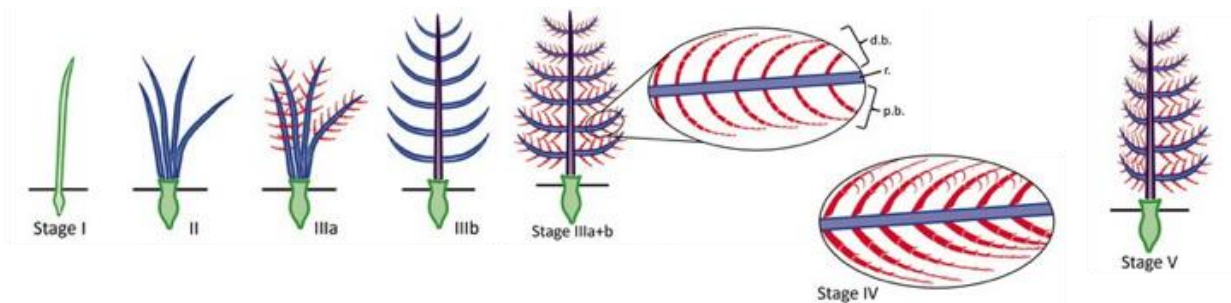


Figure 2.3 The evolution of feathers from single filaments to highly hierarchical structures. Most modern birds have stage four or five feathers [20].

Bird flight is believed to have evolved by dinosaurs jumping to catch their prey, providing an evolutionary advantage with wings that captured air [23]. This jumping led to gliding, and eventually flapping flight. **Figure 2.4** shows the proposed stages of wing development from bipedal dinosaur to flying bird.

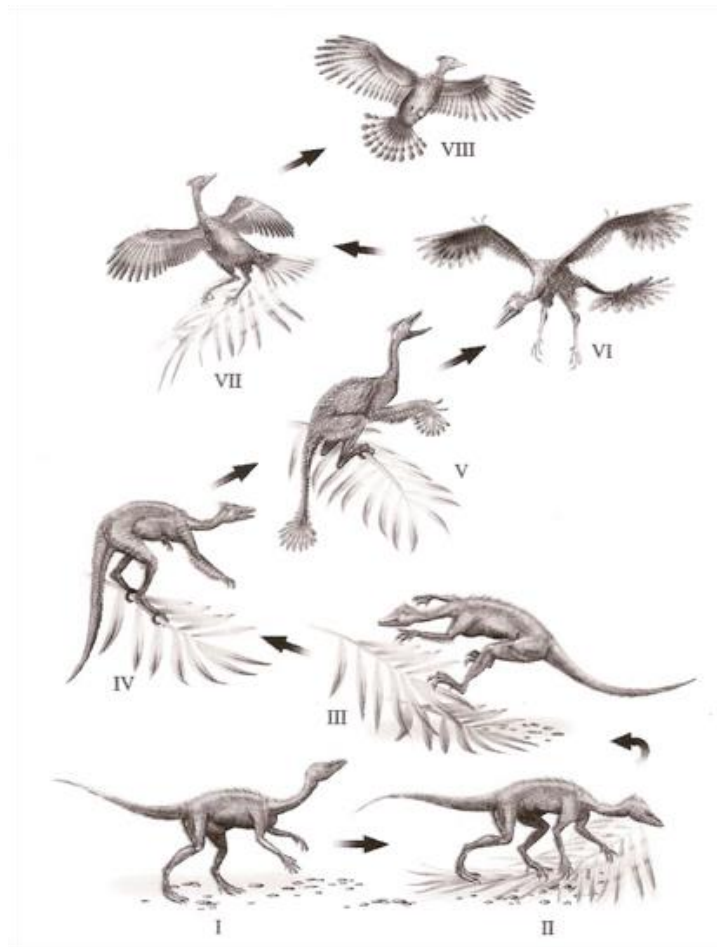


Figure 2.4 The proposed evolution of the bird wing and flight in birds. (i) bipedal and terrestrial dinosaur, (ii) development of anisodactyl foot structure, (iii) dinosaur leaps on lower branches, (iv) tail reduction, (v, vi) development of feathers, (vii, viii) formation of fully developed feathers (Figure from [23], drawn by O. Orekhova-Sokolova).

2.2. Bird Wing Background

Arguably the most crucial evolutionary feat to allow for bird flight, the wing is a system in which the skeleton and feathers act together to allow for a high lift-to-weight ratio. The wing skeleton is particularly lightweight; unlike terrestrial vertebrates' marrow-filled bones, most bird wings are composed of hollow bones, similar to the bones of bats and pterosaurs[24]. These hollow (pneumatic) bones connect to the pulmonary system and allow air circulation which

increases skeletal buoyancy [25–27]. The remiges, or flight feathers on the wings of birds, consist of a main shaft (rachis and calamus) and an interlocking feather vane composed of barbs that branch from the rachis and barbules that branch from barbs (**Figure 2.18**). Neighboring barbules adhere to one another via hook-and-groove structures to form a cohesive feather vane. This complex design of the modern feather evolved in the Late Jurassic period with the advancement of flight [13]. An example of a precursor to the modern feather, thought to have belonged to a non-avian dinosaur ~99 million years ago, was recently discovered preserved in Burmese amber (**Figure 2.5**) [28]. It lacks several features of the modern feather including the interlocking barbule connections and a fully developed rachis. The modern vane is an ingenious structure that is not sealed, but contains channels between barbules through which air can flow [29,30].

Birds have been very successful in populating Earth, with nearly 10,000 recognized species constituting an extremely diverse class of animals [6]. While all birds have certain coinciding bone and feather features, to better understand their efficiency it is critical to note the aspects that differ between them due to distinct environmental constraints. First, birds range enormously in size from hummingbirds that are about 2 g with a wingspan of 8 cm, to the 11 kg Andean condor with wingspan greater than 3 m [6,31]. Besides sheer differences in size, birds differ in flight style. Some birds achieve flight through flapping their wings and soaring (i.e. vultures, eagles); others through flapping and gliding (i.e. seagulls, pelicans) [32,33]. Additionally, certain birds mainly flap their wings (i.e. ravens, ducks, pigeons, crows), a few birds hover (i.e. hummingbirds), and lastly some are flightless (i.e. ostriches, peacocks) [34]. Moreover, some birds dive and swim (i.e. ducks, auks), while others do not. Each of these types of birds have slightly different environmental constraints on their physiology, which result in specific variations to their bone and feather structure.

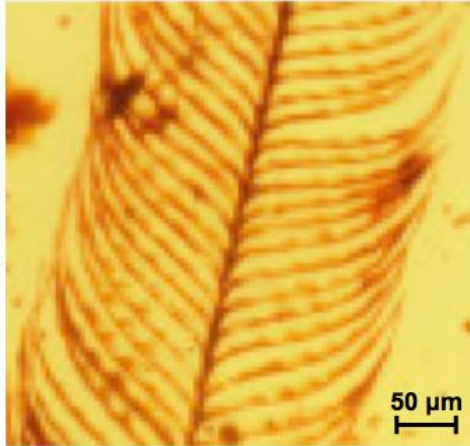


Figure 2.5: Precursors to modern feathers were much less developed as shown in (c) by the plumage of a non-avian dinosaur from ~99 million years ago preserved in Burmese amber (image from L. Xing et al. (2016) [28]).

In most birds the skeleton extends only half-way from the shoulder to the wing tip and therefore the majority of the area of the wing is supported by flight feathers [35]. Wing flight feathers include primaries that branch from the hand skeleton and secondaries that attach to the edge of the ulna. Flight feathers are anchored by a reinforced follicle which transfers the bending and torsional moments from the base of the feather to the skeleton [24]. Primaries do not have any freedom of movement relative to the bones to which they are rigidly attached. Secondaries, on the other hand, are able to hinge up and down relative to the ulna through flexible attachment. When the elbow and wrist joints are fully extended, primaries spread out and secondaries are pulled downward by the tightening of the postpatagial tendon, which results in an increase in camber of the wing [24]. In flapping flight, the elbow and wrist joints are flexed, resulting in a reduced wingspan and loosening of the tendon, providing a less cambered wing shape. Through this system, individual feathers allow for wing adaptability, while transferring the bulk of loading to the more robust skeleton of the bird. Together, the wing skeleton and feathers form an organic airfoil capable of handling the intense loads of flight. Here we review the structure, mechanics, and composition of the avian feather and bone to understand how they maintain integrity with a

minimum weight penalty. While the material composition of the feather and avian bone is the same across species, they have different design adaptations for specific environments. The commonalities in the design principles of the avian bone and feather are discussed to gain insight into the application of these concepts to engineered structures and materials.

2.3. Wing Loading in Flight

Since the main focus of this dissertation is to investigate the extreme lightweight structures of bird wings, and not the aerodynamics of flight, loading is simplified to static forces. In flight a lift force acts upwards, resulting in a bending moment about the wing's connection to the body (**Figure 2.6**). Each wing is loaded with a force= $kmg/2$, where mg is the weight of the bird, and k is a parameter that represents the load multiplication factor. For steady loading and for gliding, $k=1$; for flapping, landing and take off, $k>1$.

The wing can be considered as a series of thin airfoils for which the aerodynamic center of lift occurs at 25% of the chord length from the leading edge of the airfoil [36]. These points of lift are represented by the solid dots in **Figure 2.6b**. If the force of each point of lift is represented as F_i , these can be related to the force on the entire wing by:

$$\sum_{i=1}^n F_i = \frac{kmg}{2} \quad (2.1).$$

While the entire wing skeletal systems of pterosaurs and bats are modified to form structures that resist bending and torsion, only the inner wing skeleton of the bird has this function as flight feathers maintain this distally [24,37]. Because the ulna is roughly perpendicular to the humerus in flight and cannot rotate up and down relative to it, bending moments applied to the outer wing become torsional moments when loads are transferred to humerus [24] (**Figure 2.6b**). Additionally, since most of the area of the wing is behind the radius and ulna, there is a torsional moment applied to the humerus from the secondary flight feathers. In **Figure 2.6b** the bending

and torsion axes are drawn for the humerus. The location of the points of lift are each represented as O_i , where the torsion moment arm is $\overline{AO_i}$ and the bending moment arm is $\overline{BO_i}$. Torsional (T) and bending (B) loads on the humerus for the entire wing can therefore be represented as:

$$T = \sum_{i=1}^n F_i \overline{AO_i} \quad ; \quad B = \sum_{i=1}^n F_i \overline{BO_i} \quad (2.2; 2.3).$$

For the ulna, the same procedure can be repeated.

2.3.1. Bending and Torsion

Basic Mechanics equations connect the applied forces to internal stresses in bones and feathers, and those in turn dictate the architecture and design of the structure. Bones and feathers are subjected to maximum bending stresses that are defined by [38]:

$$\sigma = \frac{Mc}{I} \quad (2.4).$$

Where $M=Fd$, in which F is the magnitude of the applied force and d is the moment arm; c is the distance from the neutral axis to the object's surface, and I is the area moment of inertia.

Likewise in torsion, the maximum shear stress is expressed as [38]:

$$\tau = \frac{Tc}{J} \quad (2.5).$$

Where T is torque, c is the radius of the section, and J is the polar moment of inertia.

The maximum values of I and J , for a specific weight per unit length, minimize the normal and shear stresses of bones and feathers. The feather and bone can be modeled as a hollow cylinder, a section that provides a balance between bending and torsion resistance. For a hollow cylinder [39]:

$$I = \frac{\pi(R_o^4 - R_i^4)}{4} \quad (2.6);$$

$$J = \frac{\pi(R_o^4 - R_i^4)}{2} \quad (2.7).$$

Where R_o denotes the outer radius, and R_i is the inner radius. While thick walls allow for a higher value of both I and J they result in a heavy structure. Thin walls, however, eventually lead to buckling, an undesirable result. To overcome this nature provides two ingenious solutions: internal struts that oppose ovalization and retard buckling in bending; and internal foam resulting in the strengthening of the walls. The former occurs in avian bone, and the latter in the feather. These are shown in **Figure 2.6c**.

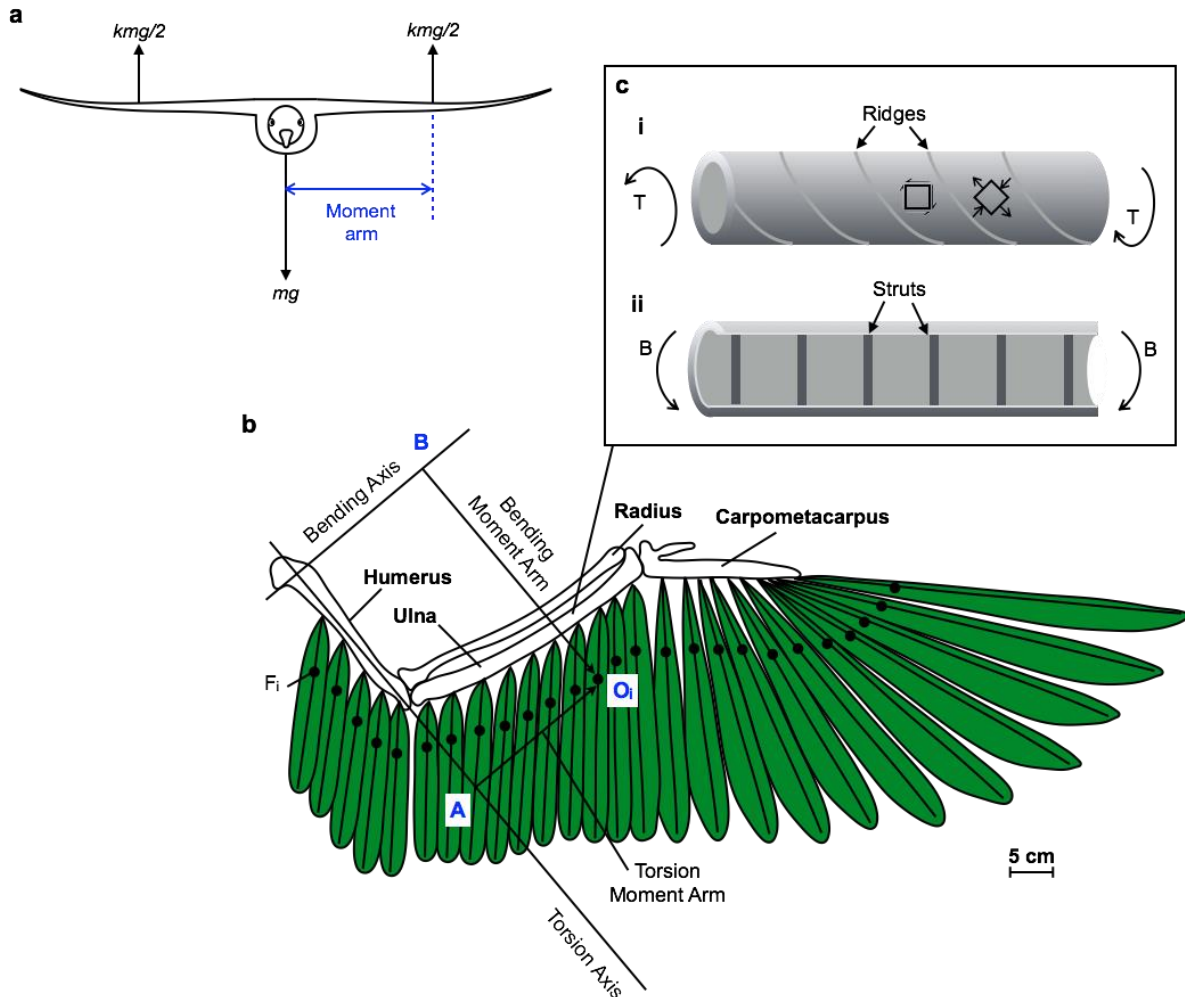


Figure 2.6 Wing Loading in Flight. (a) The upward in-flight lift forces result in a bending moment about the wings connection to the body. When the bird is gliding $k=1$, however in take off, landing or flapping, $k > 1$. (b) The skeletal system and flight feathers of the bird wing. The wing skeleton is a modified quadruped arm skeleton with a humerus (attached to the main flight muscles), ulna, radius and carpometacarpus (a fusion of the wrist and knuckles). The solid dots mark the centers of lift for each feather. The force of each of these points is represented as F_i and the location as O_i . Bending moments occur in the radio-ulna and are transmitted through the elbow joint as a torsional moment. The torsion and bending axes are drawn for the humerus, where B represents the bending axis and A the torsional axis. Adapted from C. Pennycuick (1967) [35]. (c, i) Schematic diagram of how the ridges in avian bone may form as a result of torsional forces (T). These ridges are aligned with the direction of maximum tensile force indicating that ridges increase resistance to tensile failure (taken from E. Novitskaya et al. (2016) [40]). (c, ii) Simplified diagram of internal struts strengthening the bending stiffness of avian bone.

2.4. Wing Design Concepts: Wing Bones and Feathers

Flight is not the exclusive domain of birds; mammals (bats), insects, and some fish have independently developed this ability by the process of convergent evolution. Birds, however,

greatly outperform other flying animals in efficiency and duration; for example the common swift (*Apus apus*) has recently been reported to regularly fly for periods of 10 months during migration. Birds owe this extraordinary capability to their wings, which are composed of extreme lightweight biological materials. They achieve this crucial function through their efficient design spanning multiple length scales. Both feathers and bones have unusual combinations of structural features organized hierarchically from nano- to macroscale and enable a balance between lightweight and bending/torsional stiffness and strength.

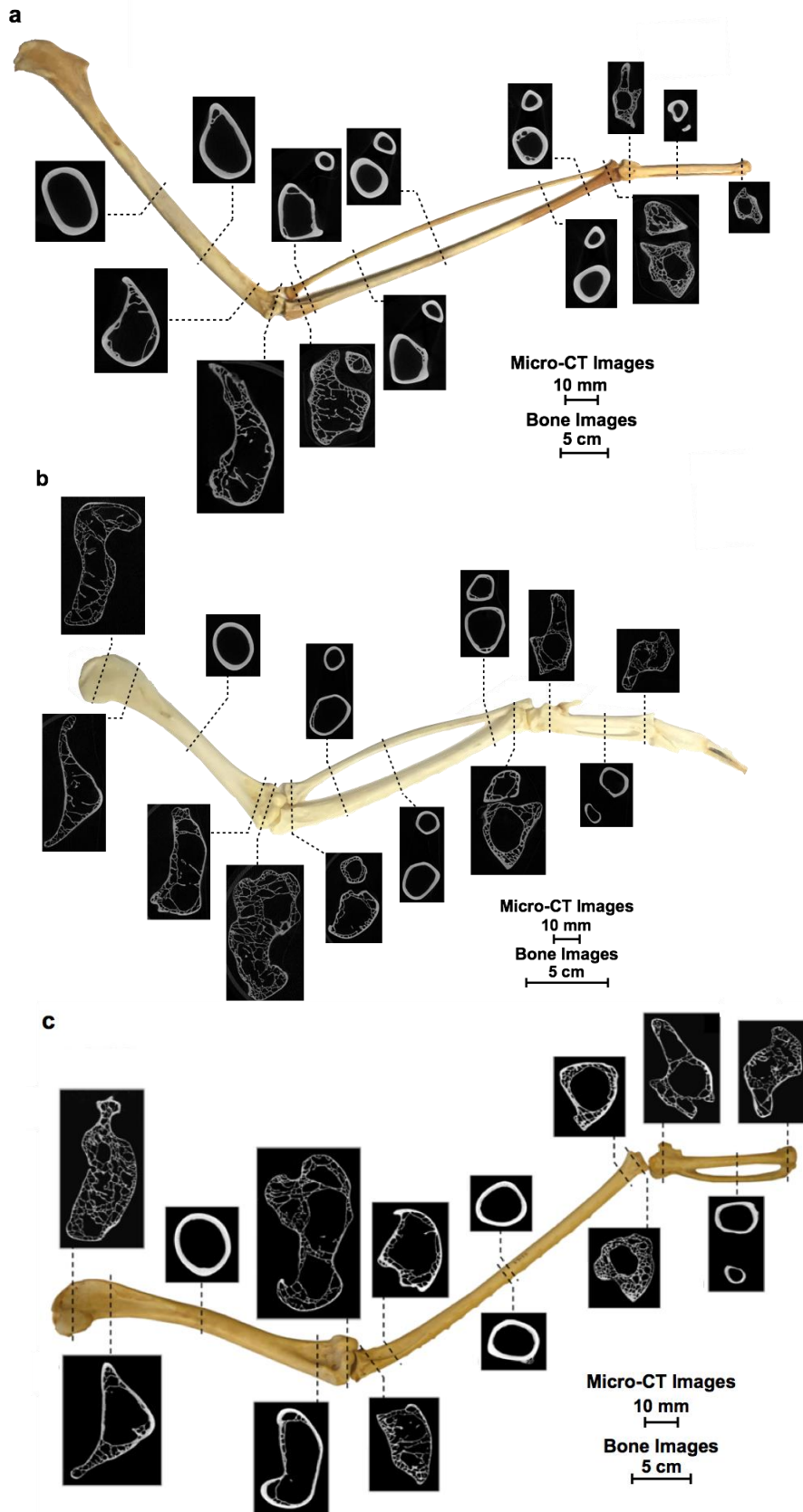
2.4.1. Thin, Dense Exterior

Since both the wing bones and feathers of birds are subject to bending and torsion, it is expected that they have several overlapping structural features. One of these characteristics is a thin, dense exterior with a hollow or less compact interior. This design allows for lightweight resistance to these external loadings. In bending, the stiffness is given by the product of the area moment of inertia and the material's Young's modulus. Therefore material positioned further from the neutral axis is more effective in resisting bending because it undergoes more extension and compression than material close to the neutral axis [41]. In torsion, thin-walled closed cross-sections offer a high torsional stiffness, which is given by the product of the area enclosed by the thin wall and the material's shear modulus. Hence for combined loading, a thin-walled closed cross-section offers optimal performance in both bending and torsion. The other variable contributing to structural stiffness is the material modulus, which increases with density [42,43]. Therefore, structures with a dense exterior wall are expected in both avian bones and feathers. Moreover, modulation of density and wall thickness are expected to depend on wing location because of spatial variations in bending and torsional moments.

As previously stated, many birds have some hollow (pneumatic) bones; across 24 species 70% of bird humeri and 30% of femori were found to be pneumatic [44]. **Figure 2.7** shows micro

computerized-tomography cross sections of the wing bones of the (a) Wandering Albatross (*Diomedea exulans*), (b) Turkey Vulture (*Cathartes aura*), and (c) California Condor (*Gymnogyps californianus*). These wing bones exhibit similar features between the three species: a hollow, circular mid-cross section with struts, ridges and webbing occurring toward the ends of each bone. Pneumatic bones are thinner walled [45] and more dense [42] than marrow-filled bones and have a flexural modulus of 6.9-7.7 GPa [44]. In comparison with various animals, birds have the most dense bone ($\sim 2.15 \text{ g/cm}^3$), which increase their stiffness and strength, followed closely by the bat ($\sim 2.0 \text{ g/cm}^3$), another flying vertebrate, with rodents trailing behind ($\sim 1.85 \text{ g/cm}^3$) [42]. This is the density of the solid bone, which is composed of hydroxyapatite ($\rho = 3.14 \text{ g/cm}^3$), collagen ($\rho = 1.35 \text{ g/cm}^3$), and water ($\rho = 1 \text{ g/cm}^3$) [46].

Figure 2.7 Micro computerized tomography scans of the wing bones of the: (a) Wandering albatross (*Diomedea exulans*), which has the largest wingspan of any living bird[47], (b) Turkey Vulture (*Cathartes aura*)[47], and (c) California Condor (*Gymnogyps californianus*). The bones of all three species have hollow, circular mid-cross sections and reinforcing structures toward the ends of each bone. Figure 2.7c from E. Novitskaya et al. (2017) [40].



Bone is composed of several levels of hierarchical organization (**Figure 2.8**): (1) the sub-nanostructure (below a few hundred nanometers): tropocollagen molecules, mineral crystals, non-collagenous proteins; (2) the nanostructure (hundreds of nanometers-1 μm): collagen fiber bundles, collagen fibrils; (3) the sub-microstructure (1-10 μm): lamellae of cortical bone that surround osteon; (4) the microstructure (10-500 μm): Haversian systems, osteons; (5) the macrostructure: cancellous (spongy interior) and cortical bone (dense “outer shell” of bone) [48–54]. This level of organization allows for the material properties of bone to vary throughout the structure. In the avian humerus, for example, hardness was found to vary along the length, being the greatest in the center of the bone [55]. This may be due to adaptive remodeling of bone in response to the stresses of flight, or because the bone’s mid-shaft is older and more mineralized than its ends [55].

Another instance of an advantage of bone’s composite microstructure is in the orientation of lamellae within it. Laminar tissue, where layers form with different angles to the longitudinal axis, aids when tensile stresses deviate from the long bone axis. Oblique fibers provide more resistance to torsional loads than longitudinal or transversely oriented fibers [56]. Therefore, to maximize torsion resistance, the humerus and ulna have a higher degree of laminarity and higher incidences of oblique collagen fibers than the radius and carpometacarpus [56].

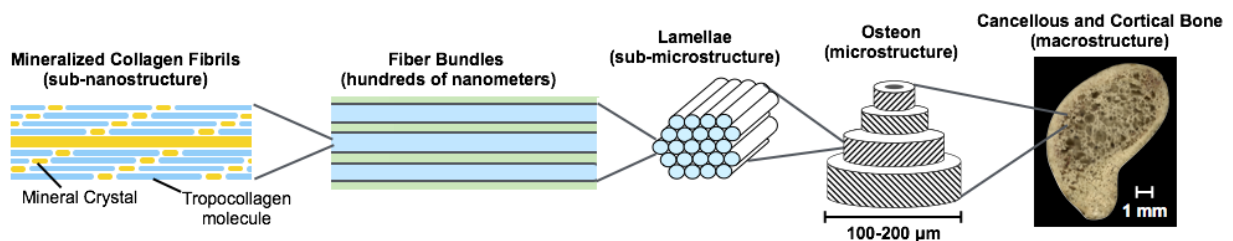


Figure 2.8 The hierarchical structure of bone (a): Tropocollagen molecules and mineral crystals organize to form fiber bundles. These form lamellae that surround an osteon, which form cancellous and cortical bone. [47]

The feather shaft has a thin, compact exterior (cortex) with a hollow, circular base (calamus), which anchors the feather under the skin, and a foam-filled rectangular rachis (**Figure 2.9a,b**). Although both components consist entirely of β -keratin (which is covered in detail in section 2.7.3), the rachis' medullary foam density ranges from 0.037-0.08 g/cm³, while the cortex density ranges from 0.66-0.81 g/cm³ [57,58]. The cortex material is over 100 times stiffer than the medullary foam, which has an elastic modulus of 2.5-6.5 GPa [57–61], whereas the foam's modulus is 0.01-0.03 GPa [57,58]. Due to this large difference, the geometry of the cortex dominates the flexural stiffness of the shaft [57,59,62]. To prevent local buckling and enhance overall strength, bones and feathers have internal reinforcing structures. Adding complexity to the hierarchy, both bones and feathers are comprised of fibers which are directionally aligned in such a manner to maximize resistance to bending and torsion. In the bone, the collagen fibers form lamellae which are interspersed with hydroxyapatite crystals that are structured at the nanoscale. In feathers, the β -keratin fibers are aligned in different orientations to enhance the stability. These topics will be discussed later in this overview.

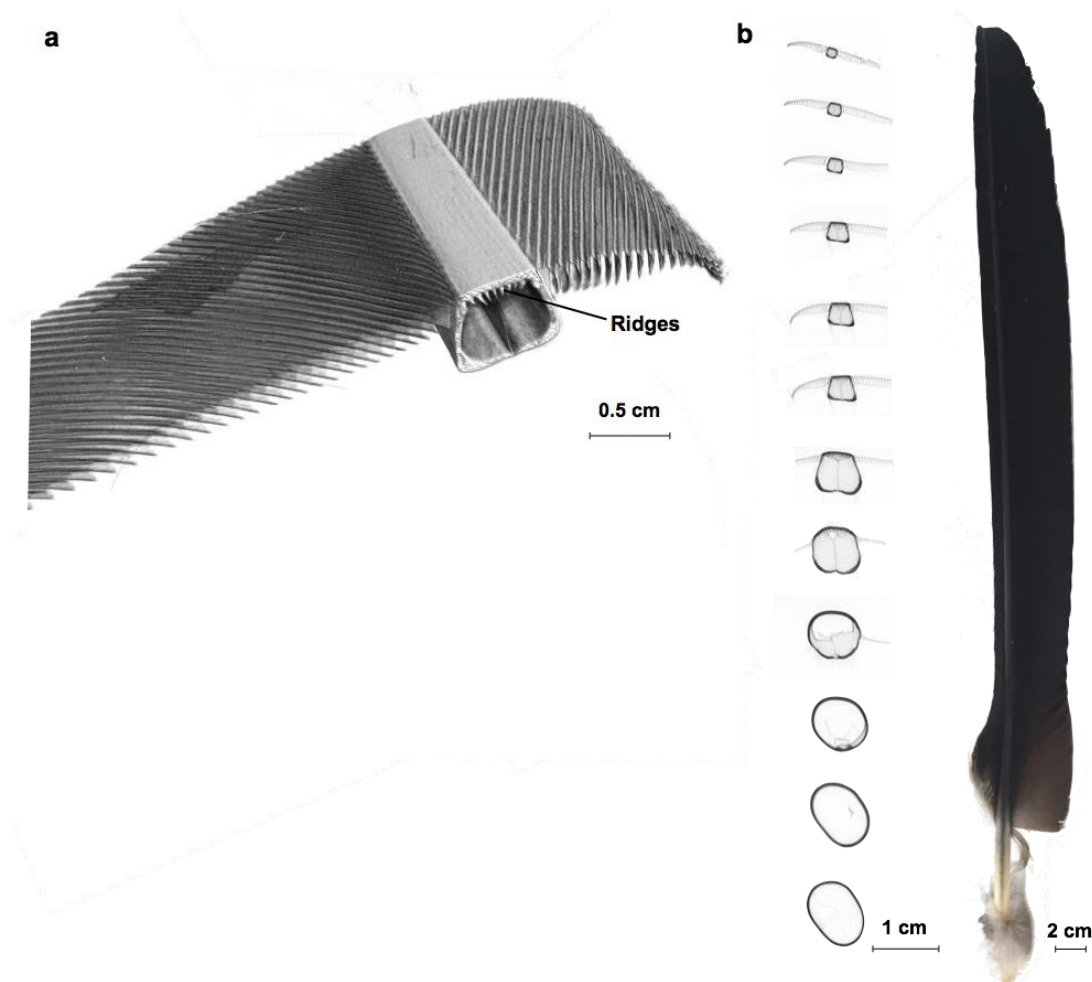


Figure 2.9 Micro computerized tomography (μ -CT) generated images of an Andean Condor (*Vultur gryphus*) primary feather: (a) shows the feather vane and details of the ridges in the rachis[47] while (b) demonstrates the shape change along the length of the feather shaft from circular to rectangular (part of image is from B. Wang et al. (2016) [63]).

2.4.2. Reinforcing Internal Structures

Both the avian bone and feather have internal reinforcing structures that strengthen their design. Due to the high metabolic cost and increased weight of creating more bone or cortex material, it is speculated that these reinforcing structures develop within the wing bone and feather in response to specific stresses of flight.

Ridges are protrusions of bone or cortex that lie flat against the interior walls of the bone or feather (**Figure 2.10a,c**). In avian bone they generally develop at -45° to the horizontal axis of the bone, to increase the resistance of the structure to the large tensile stresses that develop in these directions in torsion [38]. Ridges along this angle are most effective because in torsion axial stresses occur at -45° to the longitudinal axis [40] (**Figure 2.6c**).

In many flight feathers multiple cortex ridges run internally along the length of the rachis' dorsal surface, slowly becoming fewer and less sharply defined distally [59,62]. These small ridges stiffen feathers in dorso-ventral flexure, but do not strongly influence lateral movements [59]. Cortex ridges occur on the dorsal surface because the feather experiences the largest stress in compression during the bird's down stroke, occurring on the dorsal side of the feather shaft [64,65].

Struts are isolated rods that stretch across the interior of pneumatic bone (**Figure 2.10b**). They are mainly found on the ventral side of wing bones of flying birds, appearing to be at locations that have a higher risk of local buckling due to combined bending and torsion loading [24,25,33,40](**Figure 2.6c**).

Taking a different approach to resist local buckling, the feather does not have struts, but the majority of it (the rachis) is foam-filled (**Figure 2.10d**). This fibrous internal medullary foam is considered closed-celled and provides 96% of the transverse compressive rigidity [58]. However, closer examination reveals that the cell walls are indeed porous and consist of fibers. The foam also absorbs the bulk of energy, providing a rachis with a strength higher than the sum of each of its components [58]. Similar to how the bird has evolved to have these unique internal reinforcement features, types of birds have adapted to their specific environment with more specialized structures.

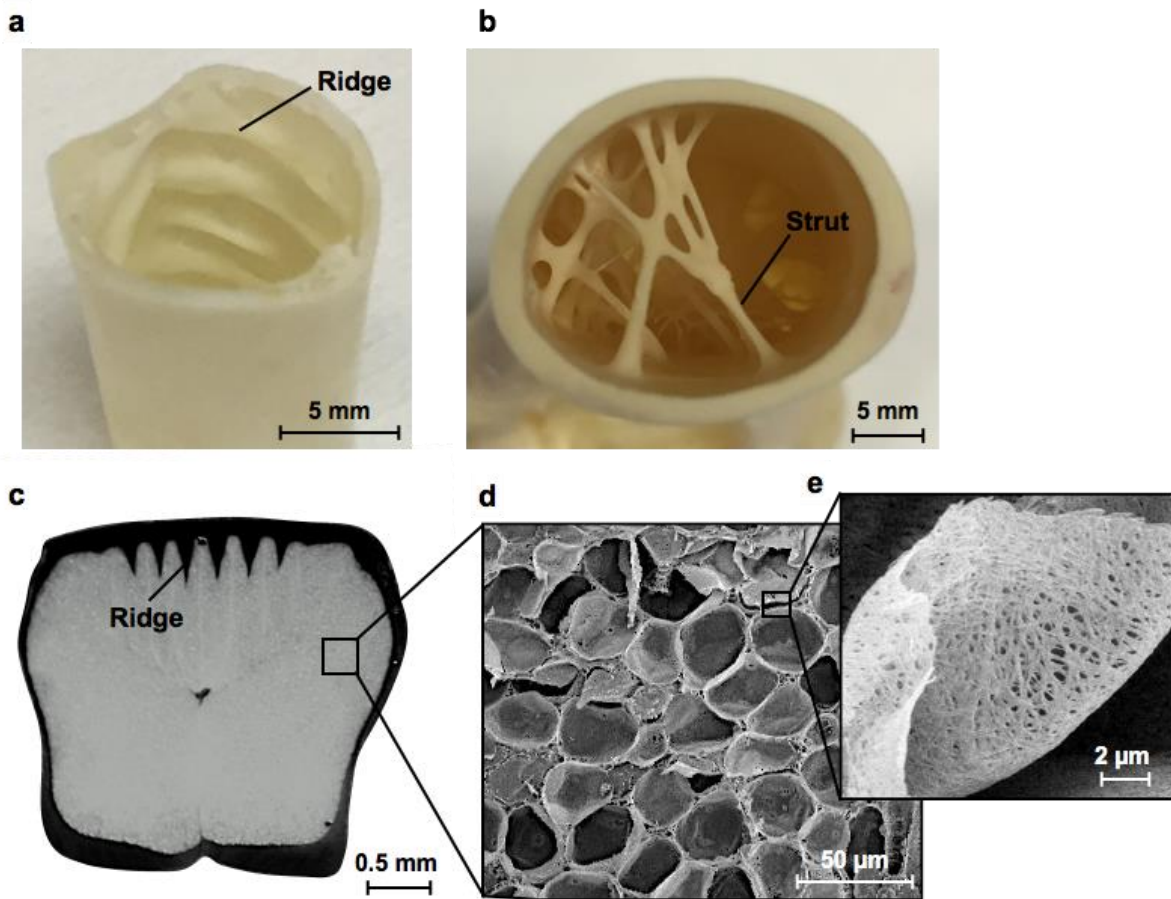


Figure 2.10 Internal reinforcements in the avian bone and feather: (a) ridges in the ulna of the Turkey Vulture (*Cathartes aura*), (b) struts toward the distal end of a Cape Vulture (*Gyps coprotheres*) humerus bone, (c) ridges in the American White Pelican (*Pelecanus erythrorhynchos*) feather, (d) medullary foam of the feather; (e) foam wall exhibiting porosity, thus forming a “foam-in-a-foam”. Image taken from [47].

2.5. Efficiently Tailored Designs Based on Specific Conditions

The wings of birds have a wide variety of shapes that have been adapted for their flight style and lifestyle[66]. In terms of the ratio between length and width, defined as aspect ratio, specialized types of flight styles include [34]:

- 1) Marine soarers: Birds that fly for long periods of time over the ocean and have extremely high aspect-ratio wings and average to low wing loading (ex. albatross, *Procellariiformes*)
- 2) Divers and swimmers: Medium to high aspect-ratio wings and high wing loading (ex. ducks and swans)
- 3) Aerial hunters: High aspect-ratio wings and low wing loading, allowing for maneuverability and rapid flight (ex. swallows and martins, *Passeriformes*)
- 4) Soarers/courasers: Low aspect-ratio and low wing loading (ex. hawks and eagles, *Falconiformes*)
- 5) Short-burst fliers: Low aspect ratio and high wing loading, fly infrequently and only for short distances (ex. turkeys, pheasants, *Galliformes*)
- 6) Hoverers: Able to fly in one position without wind, high aspect-ratio and high wing loading allowing for fast agile flight (hummingbirds, *Apodiformes*).

These differences in flight styles are reflected in the shape of the wing. **Figure 2.11** shows some of the variations of wing styles [34].

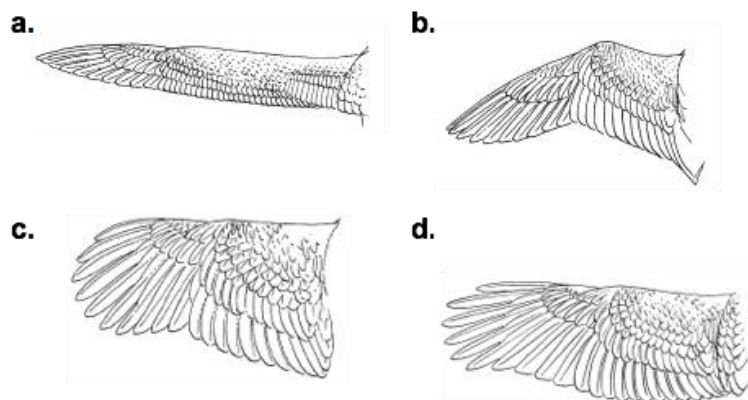


Figure 2.11 Variation of wing types: (a) High-aspect ratio, (b) High-speed, (c) Elliptical, (d) High-lift. Images taken from [34].

2.5.1. The Effect of Flight Style and Diving on Wing Bones

As stated previously most birds have some pneumatic bones, the exceptions generally being birds that share the characteristic of diving [44,56]. It is thought that to maintain strength in impact and prevent excess buoyancy their bones are marrow-filled. Besides a lack of pneumatization, some diving birds dispossess certain macro- and microstructural torsional-resistant characteristics [56]. Torsion-resistant features found in the humerus of most birds include thin bone walls, a circular cross section, oblique collagen fibers, and laminar tissue arrangement [56]. The humeri of the aforementioned diving birds are oval-shaped and thick-walled; examples of variation in bone cross section are shown in **Figure 2.12 a,b**. Furthermore, these birds have little lamellar tissue and mostly longitudinal collagen fibers, indicating that axial compression and tension are significant elements of bone loading for these cases [56]. As witnessed with diving birds, the optimum value of internal to external diameter varies based on the main function of the bone [45].

Since bones are in a constant state of growing and re-growing (remodeling) the reinforcing structures of struts and ridges form in an as-needed basis [67]. Struts and ridges, for example, were found in soaring and gliding birds, but not in flightless birds [24]. Additionally, the humerus of soaring and gliding birds is slightly more dense than the ulna to provide better support for the bird body and redistribute stresses [33].

The wing curvature, or distance between the center of the bone to the axis passing through the midpoints of the ends of the bone, determines the flight style of the bird [68]. **Figure 2.12c-f** shows the wing skeletons of several birds. With increased curvature between the radius and ulna, there is larger space for musculature in the forewing. Birds with a larger curvature between the radius and ulna are therefore more coordinated in unsteady flight [69]. As shown in **Figure 2.12e**,

the Laysan albatross is an example of a bird with minimal musculature within the forelimb. Because of this, it has uncoordinated takeoffs and landings; however it can dynamically soar for long periods of time due to its large wingspan.

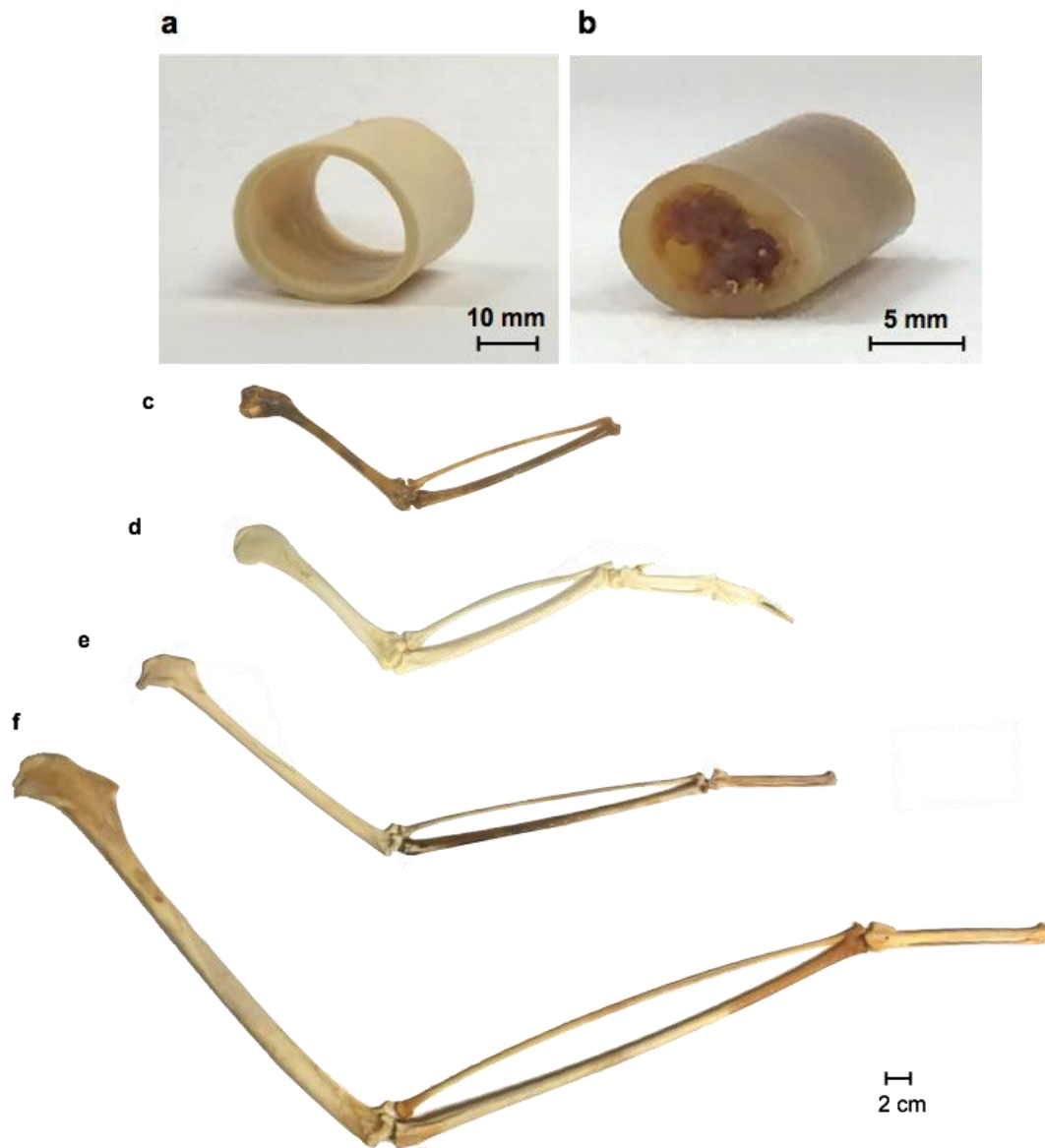


Figure 2.12 The mid-humerus of the Cape Vulture (*Gyps coprotheres*) (a) has high torsion resistance, while the mid-humerus of the California Gull (*Larus Californicus*) (b) has low torsional resistance. Wing bones of the (c) California gull (*Larus Californicus*), (d) Turkey Vulture (*Cathartes aura*), (e) Laysan albatross (*Phoebastria immutabilis*), (f) Wandering albatross (*Diomedea exulans*) have differing degrees of curvature between the radius and ulna. Figure from [47].

2.5.2. The Effect of Flight Style and Diving on Flight Feathers

The general shape of the flight feather shaft transitions from round to rectangular at about 20% along the cross-sectional length of the feather shaft. The transition enables the tailoring of flexural and torsional stiffness subject to the constraint in wing thickness variations from the proximal to distal ends. Interestingly, this is strikingly different from the feathers of flightless birds (i.e. ostrich and peacock) which do not develop a strong rectangular shape throughout their entire length (**Figure 2.13 a,b**) [58,63,70]. The square shape of the flight feathers of flying birds is particularly efficient, since square tubes possess, for the same cross-sectional area and thickness, a higher stiffness per unit area than circular ones, and additionally resist ovalization during flexure [63]. This absence of ovalization enhances the flexural stiffness of the rectangular tube because the area moment of inertia does not decrease in flexure (as it does in ovalization). However, the rectangular shape makes the compressed dorsal region susceptible to local buckling, explaining the presence of internal ridges and the foam filling to compensate for this effect. These are shown in **Figure 2.10c** and are also present in **Figure 2.13**.

The rachises of birds exhibit various structural differences between species. In a comprehensive study comparing aspects of the barn owl and pigeon rachis it was found that the barn owl rachis has a higher area moment of inertia, yet fewer structurally rich features (such as dorsal ridges) when compared with the pigeon [71]. These two birds are of comparable body mass, though they differ in wing size and flight style. **Figure 2.13c** further demonstrates that structural ridges are present in the feathers of certain birds, and absent from others. While structural features of the avian bone and feather are tailored to the flight or lifestyle of the bird, their material composition is the same across all species.

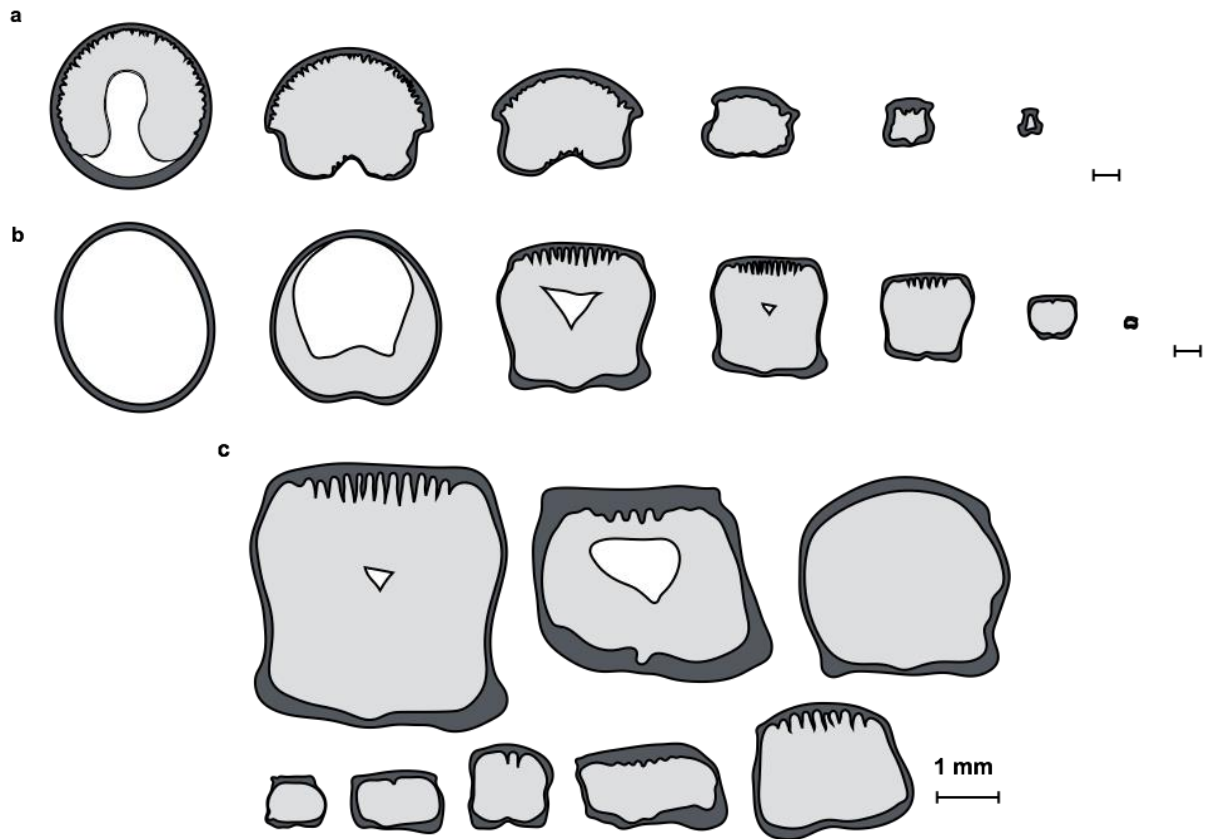


Figure 2.13 Cross sections of the wing feathers of the: (a) Ostrich (*Struthio camelus*), a flightless bird and (b) the American White Pelican (*Pelecanus erythrorhynchos*) a flying bird, where scale bars are 1mm. Primary feather cross sections at the mid point of the feather shaft for the (c): (top row, left to right) American White Pelican (*Pelecanus erythrorhynchos*), Andean Condor (*Vultur gryphus*), Razor-Billed Curassow (*Mitu tuberosum*); (bottom row, left to right) Malayan Long-Tailed Parakeet (*Psittacula longicauda*), Marbled Teal (*Marmatonetta angustirostris*), Bartlett's Bleeding Heart Dove (*Gallicolumba crinigera*), Spectacled Eider (*Somateria fischeri*), Crested Guineafowl (*Guttera pucherani*). Figure 9a adapted from B. Wang et al. (2016) [63]. Figure taken from [47].

2.6. Differences Between Wings of Birds and Pterosaurs and Bats

The independent evolution of flight in birds and bats has resulted in two significantly different wing designs. Bats, as well as the extinct pterosaurs, evolved to have a wing surface area composed of *patagium* or a double layer of skin with no bending stiffness that is stretched out by a skeletal frame [24]. The only type of stress the membrane can resist is tension.

In addition, the skeletal system of birds and bats differs greatly. Using information from the wake of the animals flying in a wind tunnel Muijres et al. found that during the upstroke, the bird wing is made inactive while the bat wing generates significant flight forces [16]. Similarly, Pennycuik found that when wind velocity was increased in a wind tunnel, a pigeon could reduce its wing span by a factor of 0.38, while a bat could only reduce its wings by a factor of 0.82 [72] (**Figure 2.14**). If a pterosaurs' wings worked as Pennycuik postulates they would be able to reduce their wing span by a factor of 0.64 in flight [24]. Both of these studies point to the retractable bird wing and therefore better aerodynamic efficiency in flight as the reason for superior flight performance in birds over bats.

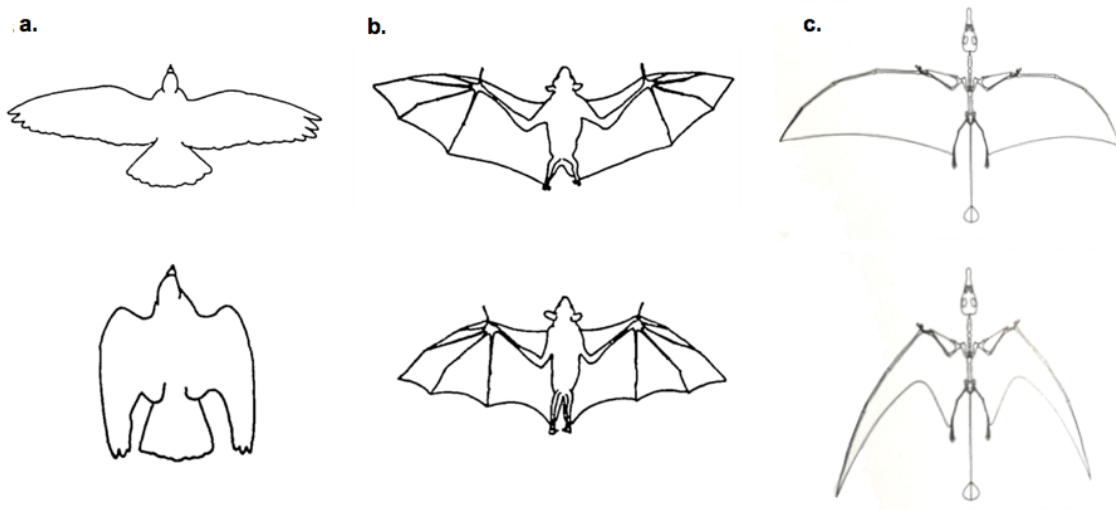


Figure 2.14 Wing retraction in the (a.) bird, (b.) bat, and (c.) pterosaur [24,72].

2.7. Feather Background

In bird flight, the majority of the wing surface consists of highly refined and hierarchically organized feathers. They are composed of barbs that stem from the feather shaft and barbules that branch from barbs, forming a rigid feather vane.

2.7.1. The Importance of Feathers for Flight

To understand the importance of the flight feathers to a bird's ability to fly, several experiments were undertaken to determine the degree of feather necessity for flight. In 1889 Lilienthal tied feathers in live pigeons together to determine how their flight performance would change with alterations [73]. The most extreme experiment in which the pigeon was still able to fly high and fast is shown in **Figure 2.15**.

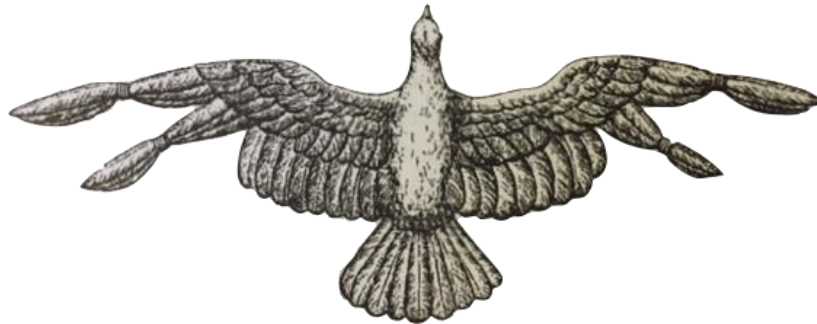


Figure 2.15 Lilienthal conducted experiments to determine what effects the feathers had on flight. In this example, the bird was still able to fly high and fast [73].

In experiments on house sparrows, Brown and Cogley removed all flight feathers except for the outermost six primaries and found that this did not have an effect on the bird's flight in a windless corridor (**Figure 2.16**). An additional 8 and 16 mm were cut from the tip of the remaining primaries without a significant decrease in flight ability. However, when 24 mm were cut off from the tips of the remaining primaries, birds could only fly 10% of the original distance [74]. These

experiments reveal that the outermost primaries are an extremely important part of generating lift and thrust in flapping flight.

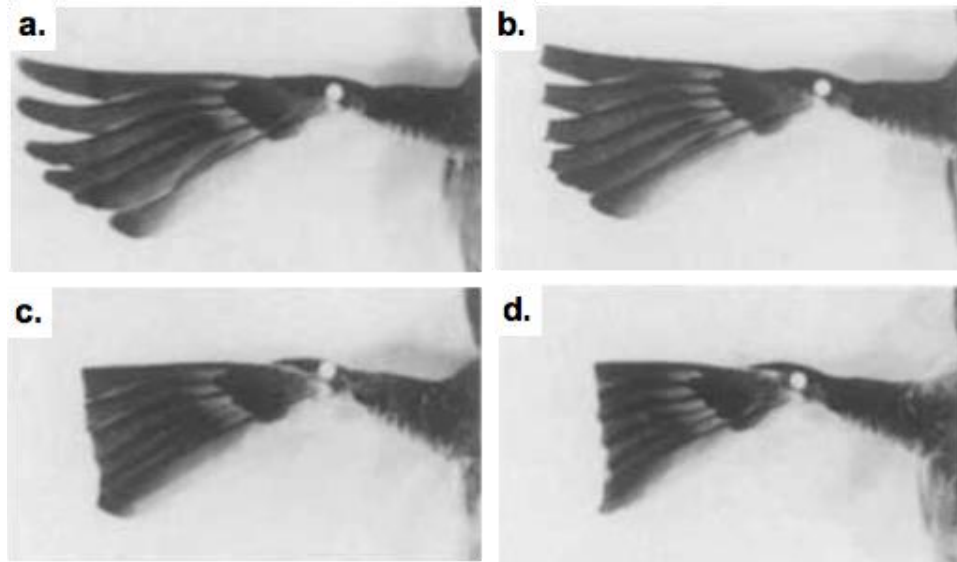


Figure 2.16 The mutilated wings of the house sparrow from Brown and Cogley's experiments: (a.) With only the outermost six primaries remaining, (b.) With 8 mm cut off of the ends of the primaries, (c.) With 16 mm cut off, (d.) With 24 mm cut off [74].

2.7.2. Feather Types and Structure

Contemporary bird feathers are extremely specialized and diverse, ranging from bristles (analogous to whiskers in mammals) to downy feathers [75] (**Figure 2.17**). While filoplumes and bristles are used for sensing, downy feathers are used for insulation, semiplumes for warmth and floating (in water birds), while retrices (tail feathers) and contour feathers are used in flight [25]. The focus of this research is on the flight feathers since these are the feathers subjected to aerodynamic loading.

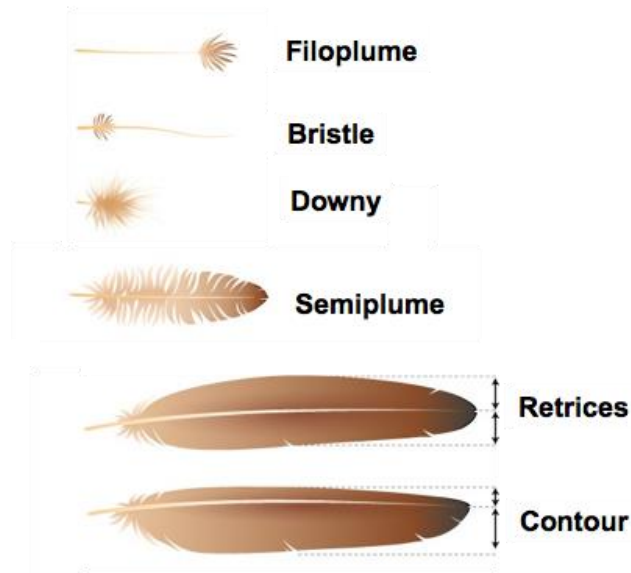


Figure 2.17 Birds have a variety of feathers for different functions. Image taken from [76].

The flight feather consists of a main shaft and a feather vane composed sequentially of barbs that branch from the rachis with barbules that branch from barbs (Figure 2.18). Barbules branching from the distal side of each barb are hooked, while on the distal side they branch as grooved structures. This allows neighboring barbules to interlock with one another, forming a cohesive feather vane.

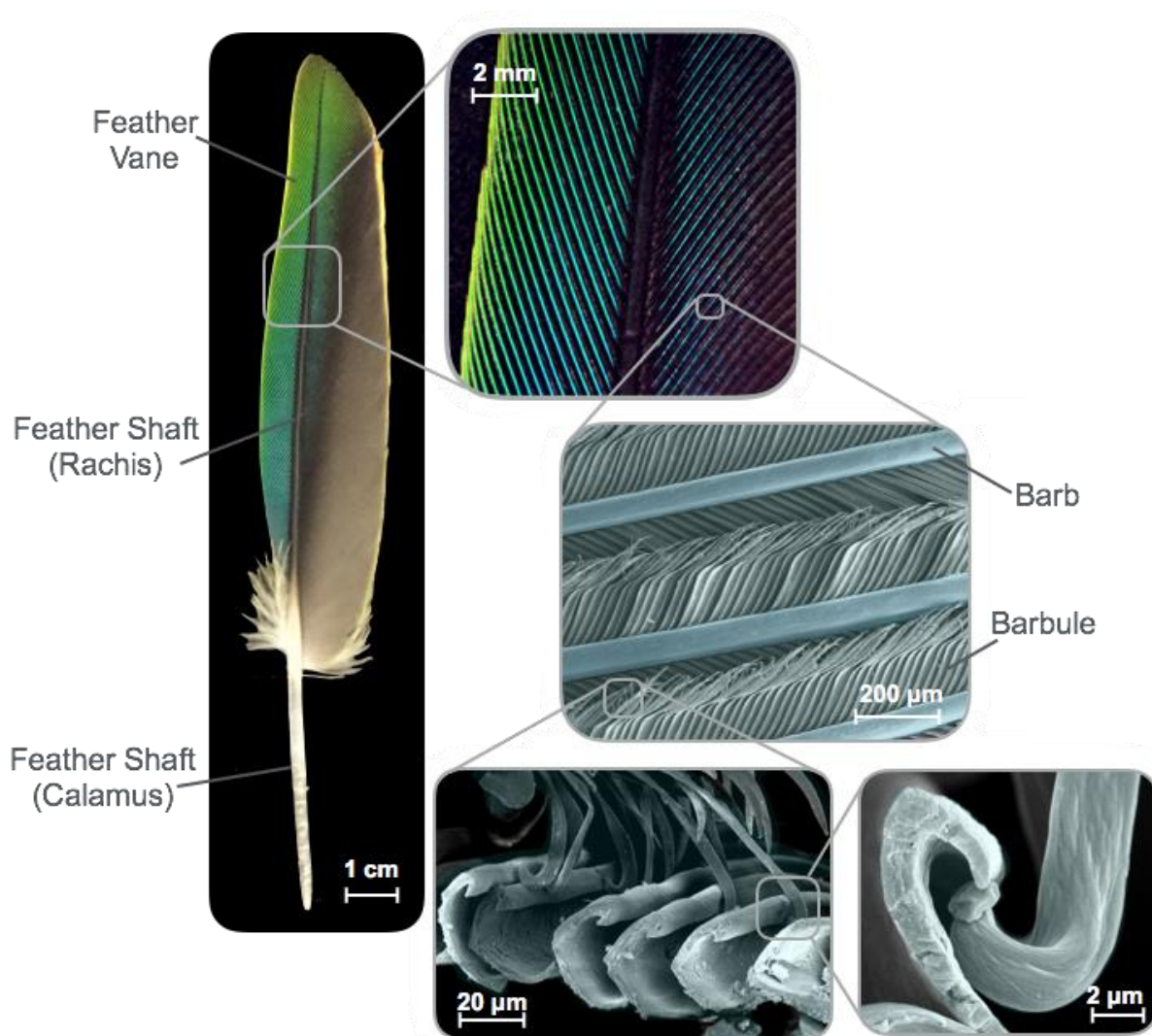


Figure 2.18 The flight feather is composed of the feather shaft (rachis and calamus) and the feather vane (barbs and barbules). Barbs are foam-filled asymmetrical beams that branch from the rachis and barbules are minute hooked beams and grooves that branch from barbs to interlock with each other. Figure from [47]. The two bottom SEM images are taken from T.N. Sullivan et al. (2016) [77].

The feathers shaft resists deformation due to forces acting on the feather vane and transmits this to the skeleton. The wings of flying birds are a tight fan-like structure, where each flight feather slides over its neighbor on the distal side and under its neighbor on the proximal side[24]. As shown in **Figure 2.9**, the feather shaft is tapered, being smaller in cross section at the tip

because: 1) there is a smaller amount of feather vane at the tip of the feather so there is a smaller amount of force to transfer, 2) there is a shorter bending moment arm at the tip [35].

2.7.3. Feather Composition

Although the feather is composed solely of β -keratin, it can be considered a composite at the micro- and nano- scales. This allows for material properties to vary throughout their respective lengths to conform to necessary loading requirements. β -keratin is considered a “dead tissue” and is formed by keratinous cells [78]. The cortex material of the feather can be considered a fiber-reinforced composite with many layers of organization: (1) the sub-nanostructure (~3 nm in diameter): crystalline β -keratin filaments embedded in amorphous matrix proteins; (2) the nanostructure (~200 nm in diameter): filaments bundle to form macrofibrils which are encompassed by amorphous inter-macrofibrillar material; (3) the sub-microstructure (3-5 μ m in diameter): macrofibrils organize into fibers; (4) the microstructure (hundreds of microns): fibers form ordered lamellae within the feather shaft cortex (**Figure 2.19a**) [63,78–84]. Discovery of the shaft’s ordered fibers and macrofibrils by Lingham-Soliar et al. [79] sparked a renewed interest in the feather shaft cortex. It has since been shown that the arrangement of the fibrous keratin composite differs between species, possibly based on the flight style of the bird [85–87].

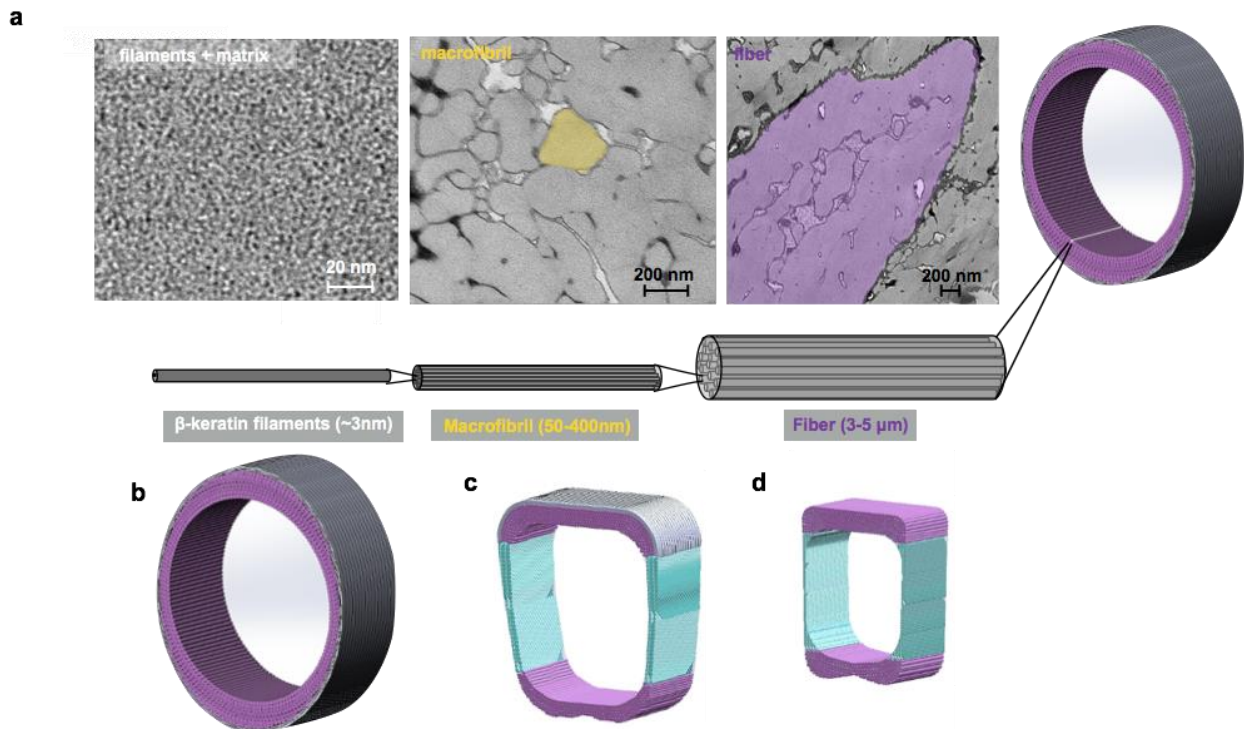


Figure 2.19 The hierarchical structure of the feather shaft cortex (a): β -keratin filaments form macrofibrils and these bundle to form fibers. The orientation of the fibers varies throughout the feather shaft: fibers in the calamus (c) run longitudinally (purple) and circumferentially (grey), within middle and distal rachis (d, e) fibers alternate at angles $\pm 45^\circ$ (green) in the lateral walls. Images (b-d) from B. Wang et al. (2016) [63].

Laminate structures such as those found in the feather are common in nature; they are usually found in structures that necessitate strength and toughness such as the dactyl club of the stomatopod (*Malacostraca*) or the scales of the arapaima fish (*Actinopterygii*) [88]. Busson et al. found that there were three lamina layers in the peacock feather using x-ray microdiffraction [86]. Later, Lingham-Soliar et al. reported two lamina layers in the chicken [11]. Following this it was found by Laurent et al. that laminar properties vary between birds with different flight styles [87]. Wang et al. and Laurent et al. used nanoindentation to determine the Elastic modulus of different layers of each laminae and confirmed distinct differences in moduli as laminae transitioned. While

Laurent et al. used ultra high resolution CT-scanning to determine the direction of the fibers, Wang et al. used a freeze-fracturing method to determine the fiber direction within the feather shaft [87][89]. Because Wang et al.'s findings are most comprehensive, we use these as a basis.

Wang et al. [63] found the California Gull (*Larus californicus*) feather to have a thin outer layer composed of circumferentially wrapped fibers and a thick inner layer of longitudinal fibers within the calamus and the dorsal side of the proximal rachis (**Figure 2.19b**) [63]. This fiber arrangement is commonly used in the design of synthetic composites, and restrains the axial fibers from separating by preventing axial splitting in flexure. Further along the feather, on the dorsal and ventral sides of the distal rachis, there is an increase in longitudinal fibers and decrease of outer circumferential fibers (**Figure 2.19c**) [63]. Since the elastic modulus is determined by the local fibrous structure, the higher proportion of longitudinally aligned fibers can be correlated to the increase in axial modulus along the length of the feather [63,90]. This increase in elastic modulus along the length of the feather shaft (proximal to distal) has been credited as compensating for the decrease in area moment of inertia along the shaft [57,71,91,92].

Another notable feature of the composite design of the feather shaft is the crossed-fiber structure of the lateral walls of the rachis [63,93]. These fibers are oriented at $\pm 45^\circ$ in this region where bending and torsion result in primarily shear stresses (**Figure 2.19c,d**). Hence, the fibers align along the axial stresses, occurring at $\pm 45^\circ$ to the shaft axis to improve torsional stiffness with minimum impact on bending stiffness [93]. At the same time, lateral deflection can occur without buckling and this stiffness is considerably decreased. Thus, the microstructural composite design of the feather is used to create an efficient material that allows the feather to be strong yet lightweight.

2.7.4. Mechanical Properties of the Flight Feather

Using nanoindentation, Bachmann et al. found that there was no significant variation in Elastic modulus between the primary feathers of barn owls (*Tyto alba pratincola*) and pigeons (*Columba livia*) [71]. From two point bending tests, Bachmann et al. found that barn owl had a higher bending stiffness as well as a higher area moment of inertia, thereby attributing the flexural stiffness to be predominantly influenced by the geometry of the feather rather than by its material properties. This is similar to the result found by other researchers [57,62,92]. Although the Elastic modulus was not found to vary significantly between species, it was found to vary along the feather shaft [71,92] as well as on each side of the feather shaft, as measured by tension tests [94].

Corning and Biewener conducted *in-vivo* strain measurements on pigeons in flight to determine the safety factor for feathers. They compared this to four point bending tests done on sections of the rachis and predicted that failure due to flexure was most likely to occur by the wrinkling of the cortex [64].

2.8. Natural Adhesives

Since the feather vane relies on a unique type of natural adhesive system to maintain its cohesiveness, other types of adhesive mechanisms in nature will be briefly reviewed. In plants and animals there is a large diversity of attachment types that have evolved to fit the specific functions of the species. These biological attachment systems have been classified by Gorb [95] based three types of principles: 1) the physical mechanism that allows the system to operate, 2) the biological function of attachment, 3) duration of contact. Gorb states that there are eight recognized fundamental attachment mechanisms: (i) hooks, (ii) lock or snap, (iii) clamp, (iv) spacer or expansion anchor, (v) suction, (vi) dry adhesion, (vii) wet adhesion (glue, capillary) and (viii) friction (**Figure 2.20**).

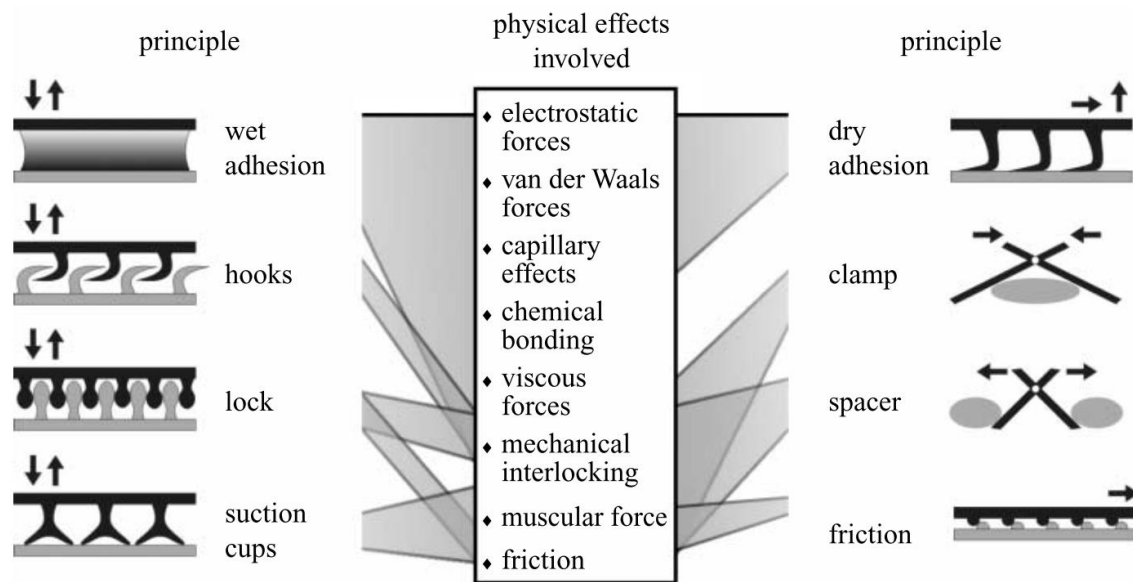


Figure 2.20 Types of adhesive mechanisms found in nature along with the physical effects involved in achieving adhesion [95].

According to Gorb, functions of attachment range from: (i) maintenance of position (such as on a substrate), (ii) locomotion requiring a large number of attachment-detachment cycles, (iii) attachment to a host for feeding or phoresy, (iv) prey capture, (v) temporary attachment of two body parts, (vi) maintenance of contact during mating, (vii) manipulation of particles during grooming [95]. As you notice, the feather vane’s attachment does not fit any of these categories, so we add an eighth function: (viii) to allow for localized failure and prevent the catastrophic failure of the entire system. **Figure 2.21** shows examples of these types of adhesive functions in nature.

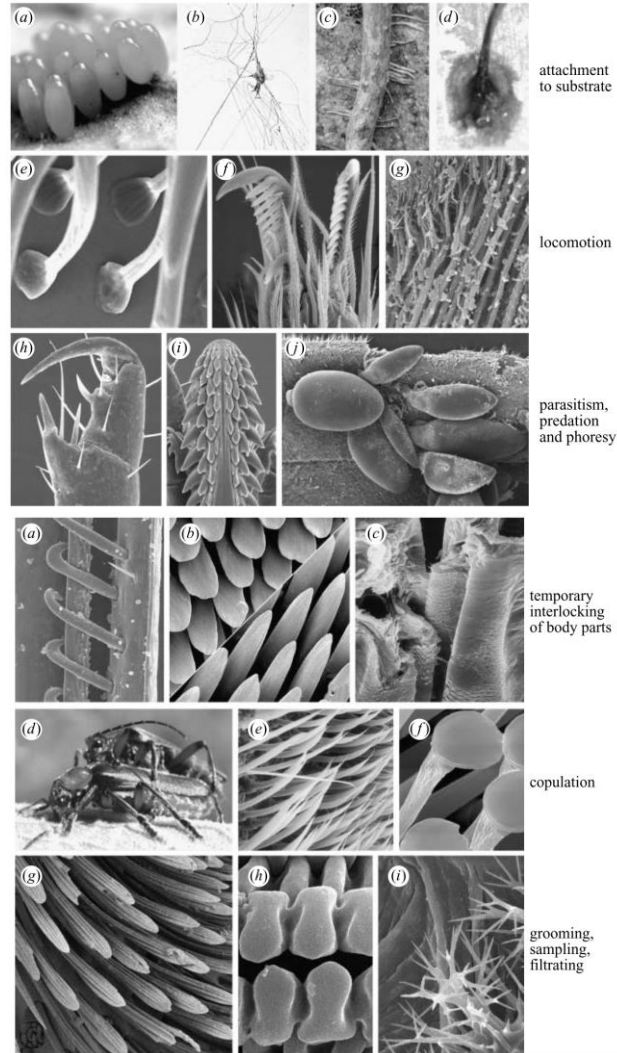


Figure 2.21 Functions of attachment [95]: Attachment to substrate (ex. eggs of butterfly, spider silk, ivy root, mussel thread; Locomotion (ex. fly leg hairs to adhere to glass, spider claws, grasshopper adhesive pad); Parasitism (ex. lice leg clamp, mouthpart of mite, aquatic mite); Temporary interlocking of body parts (ex. temporary locking between wings of sawfly, head arresting mechanism in damselfly, double tongue and groove between beetle wings); Copulation (ex. beetles, abdominal male fly appendage, setae of male beetle); Grooming, sampling, filtering (ex. foreleg of ant, labellum of the fly, filter system in spiracle of beetle).

Since the feather vane consists of hooks and grooves, we elaborate on the mechanical interlocking of hooks found in nature. The hook is mainly reported for long-term attachment; for example, hook-like structures are found in parasitic animals such as mites [96]. Additionally, the fore- and hind- wings of bees, wasps, butterflies, aphids and other insects can be interlocked with hooks to improve aerodynamic efficiency [11][12]. Hooks for short term attachment are found in

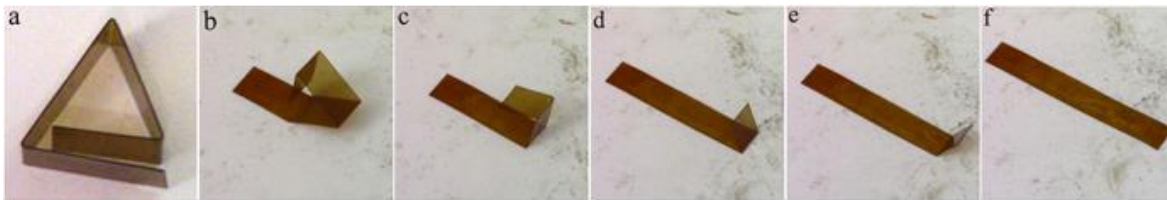


Figure 2.23 Shape memory polyamide returns to its original state after thermal annealing [101].

For the shape memory effect to occur, a stable polymer network and a reversible switching transition of the polymer are necessary [102]. The stable SMP network, which dictates the original shape, can be formed by molecule entanglement, crystalline phase, chemical cross-linking or an interpenetrated network [103–108] (**Figure 2.24**). Switching transitions in SMPs include: the crystallization/melting transition [109–111], vitrification/glass transition [112], liquid crystal anisotropic/isotropic transition [113–115], reversible molecule cross-linking, and supramolecular association/disassociation (**Figure 2.24**).

While the earliest shape memory polymers responded to thermo-sensitive stimuli, it was found that water could also serve as an actuator for recovery [116]. Water-driven shape recovery effects were found to have the glass transition as the reversible switch [102]. Below the glass transition temperature (T_g) the polymer is in the glassy state and is rigid, stiff and difficult to deform. Above T_g , the polymer is in the rubber state and is easy to deform [117]. Hydration can decrease the T_g to room temperature or below by weakening hydrogen bonding [117]. However, compared with thermal-induced recovery, the recovery stress in moisture recovery is lower due to a high sample-size dependency [117]. Water absorbs easily at the sample surface, but is difficult to penetrate inside of the material.

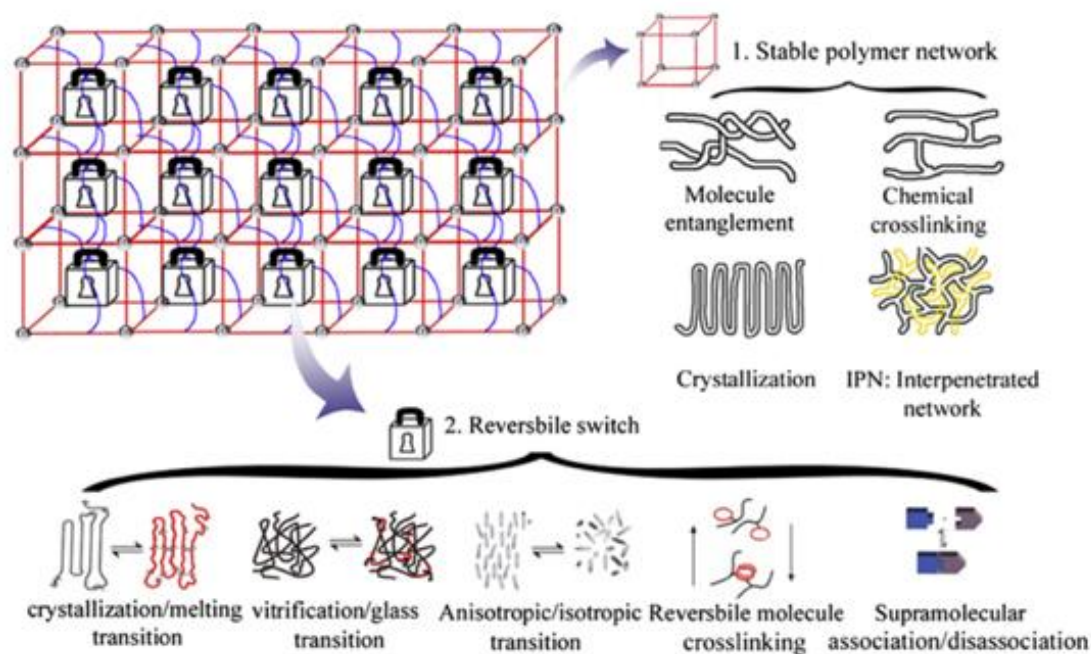


Figure 2.24 The various types of stable polymer networks and reversible switching transitions in shape memory polymers [102].

Shape memory polymers are often used in conjunction with other materials to alter material properties, yielding shape memory polymer composites (SMPCs). These composites can mechanically reinforce, enable or enhance stimuli effects, and allow for new functions of materials [102]. They have greatly expanded the possibilities for applications of shape memory polymers.

2.10. Conclusions

The features of avian wing and feather discussed in this chapter highlight characteristics that enable the bird wing's efficiency. The wing skeleton and flight feathers work together to form an airfoil that supports the bird's mass in flight and undergoes torsional and bending forces while maintaining a minimum weight. Both wing bones and feathers have a thin, dense exterior with reinforcing internal structures, efficiently tailored for the specific bird, and a composite microstructure. The coinciding design principles between these features reveal an apparent evolutionary trend toward structures that efficiently resist bending and torsion.

By examining structure-property relationships we reviewed the background of prominent features, from the nano- to the macroscale, which enable birds to fly. At the nanoscale fibrils β -keratin (in feathers) arrange to provide fiber bundles that exhibit a high degree of organization leading to superior unidirectional mechanical properties. At the mesoscale these fibrils organize themselves into fibers aligned to resist the specific loading requirements. At the macroscale emergent structural features have evolved to provide an exquisite selection of shape and form which, when combined synergistically with local mesoscale material arrangements, endow birds with ultra-lightweight structures possessing superior resistance to combined bending and torsional loading.

2.11. Acknowledgements

Chapters 2, in part, was published as a review article in *Materials Today*, authored by T. N. Sullivan, B. Wang, H.D. Espinosa, and M.A. Meyers. The dissertation author was the primary investigator and author on this publication. We thank Esther Cory and Dr. Robert Sah (UC San Diego) for assistance with μ -CT imaging. We acknowledge Dr. Katya Novitskaya for helpful discussions and Isabella Gomez and Israel Rea for image data gathering.

3. Scaling Relationships of Bird Wings and Feathers for Efficient Flight

Flight is not the exclusive domain of birds; mammals (bats), insects, and some fish have independently developed this ability by the process of convergent evolution. Birds, however, greatly outperform other flying animals in efficiency and duration. *Aves* are an incredibly diverse class of animal, ranging greatly in size and thriving in a wide variety of environments. As the most efficient natural fliers, they have evolved certain traits that scale across species despite their diversity. Here we explore the scaling trends of bird wings in connection with their flight performance. The tensile strength of avian bone is hypothesized to be a limiting factor in scaling the humerus with mass, which is corroborated by its experimentally found allometric scaling relations. Birds with high wing loading are found to have a greater percent of their wings composed of the humerus bone to compensate for smaller, narrower wings. Lastly, wing feather dimensions are found to generally scale isometrically with bird mass, with the exception of the spacing between barbules, which falls within the same range for birds of all masses. This is likely due to the transmissive properties of the barbule flaps that cover this space allowing for an optimized opening to let air through the vane while maintaining interlocking barbule connections. Our findings provide insight into the “design” of birds and may be translatable to more efficient designs of bird-inspired aircraft.

3.1. Introduction

Galileo Galilei was one of the first scientists to discuss scaling trends in nature, observing that a scaled-up “giant ten times taller than ordinary man” could not exist in the natural world unless his limbs were greatly altered to bear the extra mass[118]. Although he was unaware of it, Galileo was describing the concept of what is now called allometry. Allometry was originally coined in 1936 as a term to describe the discrepancy between the rate of growth of a part of the

body and the body as a whole, i.e. the deviation from self-similar scaling [119]. Researchers had discovered the greater relative growth rate of the male fiddler crab's large claw in relation to its body size and described this allometric trend as [119]:

$$y = bx^\alpha \tag{3.1}$$

where y is the part (in this case the fiddler crab's large claw), x is the whole body dimension, and b and α are constants. When $\alpha > 1$ allometry is positive, $\alpha < 1$ allometry is negative, and when $\alpha = 1$ the trend scales isometrically. Numerous allotropic relations have been discovered in nature since then, e.g. the adhesion pads of animals[120,121], metabolic rates of organisms[122–124], and limb bones of mammals[125–127].

Unlike allometry, isometry is the direct, self-similar scaling of body size with other features. A perfectly isometric organism would have a volume proportional to body mass, length proportional to mass to the power 1/3, and surface area proportional to mass to the power 2/3. **Figure 3.1** graphically shows the difference between the allometric and isometric growth rates of the human brain and heart [128–130].

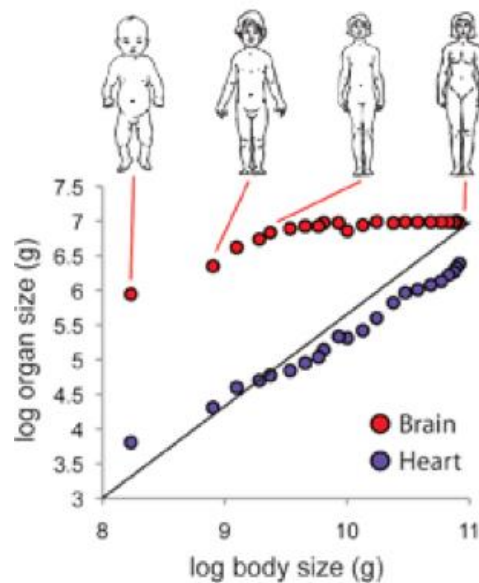


Figure 3.1 The human brain scales with positive allometry while the human heart scales isometrically [128–130].

Birds are a fascinating subject to study the effects of scaling due to their large variability in size and unparalleled natural flying ability. Because of the significance of the bird wing in flight, scaling trends of wing bones and feathers are of great interest to researchers. Previous work on the topic includes findings that the length of wing bones scale more steeply with mass than the length of hind limb bones[131]. This reflects the significance of creating longer airfoils (by increasing the length of wing bones) to support a heavier load. Pennycuik found that larger birds have higher aspect ratio wings despite wing area varying isometrically[24]. Additionally, the bending strength and flexural modulus of pneumatic bird bones (mostly wing bones) were found to negatively correlate with body mass, perhaps indicating a materials limit of bone. Lastly, primary feathers were determined to have relatively greater flexibility in more massive birds[132,133], one of the benefits of this being the potential for higher lift generation; more flexible wings have demonstrated greater lift production in flapping flight [134] as well as in the flight of insects [135].

To investigate wing scaling relationships relating to flight, H. Tennekes [136] simplified aerodynamic forces using Newton's laws of motion. A wing produces an amount of lift equal to the downward impulse of the surrounding air where the wing carrying capacity is dependent on wing size, airspeed, air density and the angle of attack [136]. To remain airborne in cruising flight, lift (L) must equal weight (W), and has the relation[136]:

$$L = W \propto c\rho v^2 A \quad (3.2)$$

where c is related to the angle of attack and is set to 0.3 (following Tennekes[136] work), ρ is air density, v is cruising air speed, and A is the projected area of the wing. The quantity W/A is generally referred to as wing loading. According to this equation, an increase in weight must be compensated by an increase in velocity and/or area of the wing. This is demonstrated in Tennekes'

“Great Flight Diagram” [136] shown in **Figure 3.2**, which describes scaling trends of weight, wing loading and flight speed from flying insects to airplanes. Note that the range in weight, from the lightest insect to the heaviest aircraft, is 12 orders of magnitude; cruising speed varies only by two orders of magnitude. Isometric scaling can now be applied to Equation 3.2. As a result, a bird’s cruising flight speed is predicted to be proportional to body mass to the power $1/6$ and wing loading to the power $1/3$. The solid diagonal line represents predicted values based on isometric scaling. Alerstam et al., however, experimentally determined that scaling relationships between these factors were weaker than predicted, meaning that birds which fly slower than predicted have low wing loading and birds that fly faster than predicted have high wing loading [137]. Here, we seek to further advance the understanding of scaling trends among birds by including their bone anatomy in order to better grasp the efficiency of bird wings and feathers. Through investigating these trends we can possibly create more efficient aircraft structures inspired by the bird.

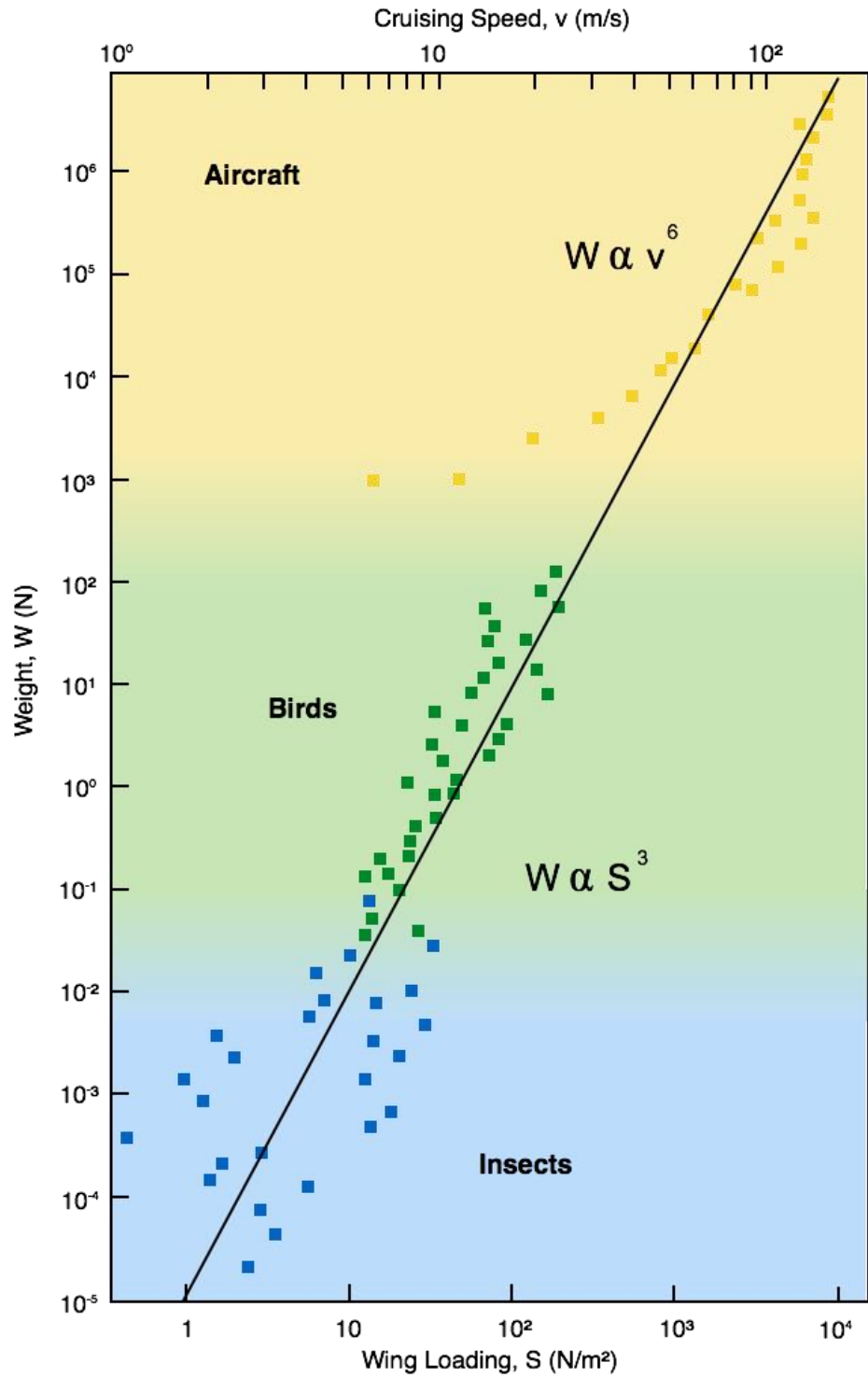


Figure 3.2 A replot of Tennekes’ “Great Flight Diagram” including the weight (W), cruising speed (v) and wing loading (S) of various flying insects, birds, and aircraft[136]. Here, the solid line describes predicted values based on isometric scaling of the wing span and weight.

3.2. Materials and Methods

3.2.1. Avian Bone Specimens

The San Diego Natural History museum's extensive collection of avian wing bones was utilized in this study. Access to this collection enabled the accumulation of data on a wide range of bird sizes. An example of some of the bones measured is shown in **Figure 3.3**.



Figure 3.3 Examples of humerus bones measured (top to bottom): Turkey vulture (*cathartes aura*), red-tailed hawk (*buteo jamaicensis*), Barn owl (*tyto alba*), American coot (*fulica americana*). The respective weights of these birds are 15.5 N, 10.9 N, 2.8 N and 4.35 N.

3.2.2. Avian Bone Characterization

For each humerus bone the length and diameter was measured using calipers, except for occasional instances where calipers did not have large enough resolution, in which case rulers were used. Length was taken as the maximum length of the humerus, or the distance between the most

proximal point of the head of the humerus to the most distal point of the trochlea of the humerus. Diameter was measured at the center of this length. The mass and wing span of many of the birds in the collection had been recorded by the museum, and these values were used in plots.

3.2.3. Feather Specimens

All feather samples were wing flight feathers (*remiges*) obtained postmortem and stored in ambient conditions. The San Diego Natural History Museum provided American White Pelican (*Pelecanus erythrorhynchos*) feathers, the Los Angeles Zoo provided Cape Vulture (*Gyps coprotheres*) feathers, and the San Diego Zoo provided all other feathers. Feathers were obtained under our research group's Federal Fish and Wildlife permit.

3.2.4. Feather Characterization

Larger feather features such as feather shaft length, rachis width and barb length were measured with calipers, optical micrographs, or rulers. For measuring the barbule spacing, which is at the micrometer scale, scanning electron microscopy was utilized. Both the Zeiss Sigma 500 scanning electron microscope (SEM) and the FEI SFEG UHR SEM from the Nano3 laboratory in Calit2 at UCSD were used. Samples placed in the FEI SEM were coated with a thin Iridium layer using an Emitech K575X Sputter Coater. Accelerating voltages of 3-5kV were used to image feather samples, which were secured to SEM stubs with conductive carbon tape. Dimensions of samples in SEM images were measured using the software ImageJ (National Institutes of Health, Bethesda, MD).

3.2.5. Data from Literature

Various data from literature were used to complete plots. Additional data on bone dimensions were obtained from Gilbert et al. [138]. Data on velocity, weight, wing area and wing span (except for cases in which data was provided by the San Diego Natural History museum) are from Pennycuik [139][140] and Greenewalt [141].

3.3. Results and Discussion

3.3.1. Allometric Scaling of Avian Wing Bone Due to Materials Limit

The humerus is arguably the most important wing bone as it connects the rest of the wing to the bird's body. It has to resist lift forces imposed on the wing against the weight of the bird. A simple isometric relationship would dictate that the length, L_H , of the humerus is proportional to mass^{1/3}, because mass is proportional to volume. However, the loading constraints, coupled with a constant strength of the bone, leads to a different result. The analysis below assumes isometric changes (length/diameter and diameter/thickness ratios are constant). For simplicity, the humerus is considered a hollow structure with diameter $2c$ and thickness t , as shown in **Figure 3.4**. The lift force on one wing is equal to half the weight of the bird. It is assumed to be evenly distributed along the humerus as well as point loaded at the distal end of the humerus, to represent loads transferred from the feathers and distal bones of the wing. The portion of the wing corresponding to the humerus exerts a force per unit length w on the humerus, while the remainder of the wing exerts a force F_2 at the distal end of the humerus. We assume the distributed force w is simplified to a point load at the center of the humerus so that $w(L_H)=F_1$. The moment (M) then corresponds to the sum of these two moments:

$$M = F_1 \frac{L_H}{2} + F_2 L_H \quad (3.3)$$

The maximum tensile stress in the top fibers is:

$$\sigma_T = \frac{Mc}{I} \quad (3.4)$$

and the moment of inertia, I , for a hollow cylinder (thickness \ll diameter) is[142]:

$$I = \pi c^3 t \quad (3.5)$$

substituting Equations 3.3 and 3.5 into 3.4, and rearranging, we obtain the following failure criterion:

$$\frac{F_1}{2} + F_2 = \frac{\sigma_T(\pi c^2 t)}{L_H} \quad (3.6)$$

The maximum tensile stress, σ_T , must lie below the strength and is assumed constant (for avian bone) and independent of mass. Both c and t scale with L_H ($c \propto L_H$, $t \propto L_H$) therefore we can substitute L_H into the equation:

$$\frac{F_1}{2} + F_2 \propto \pi \sigma_T L_H^2 \quad (3.7)$$

or

$$L_H \propto \left(\frac{F_1 + F_2}{\pi \sigma_T} \right)^{0.5} \quad (3.8).$$

Based on this analysis, humerus length is not expected to scale isometrically with mass as the mechanical strength of bone σ_T acts as a limiting factor. Here it is important to note that density of bone, ρ , is estimated as a constant for avian humerus bone. **Figure 3.5** shows experimental data demonstrating a dependency of $L_H \propto F^{0.45}$ which is close, but not equal, to the predicted value.

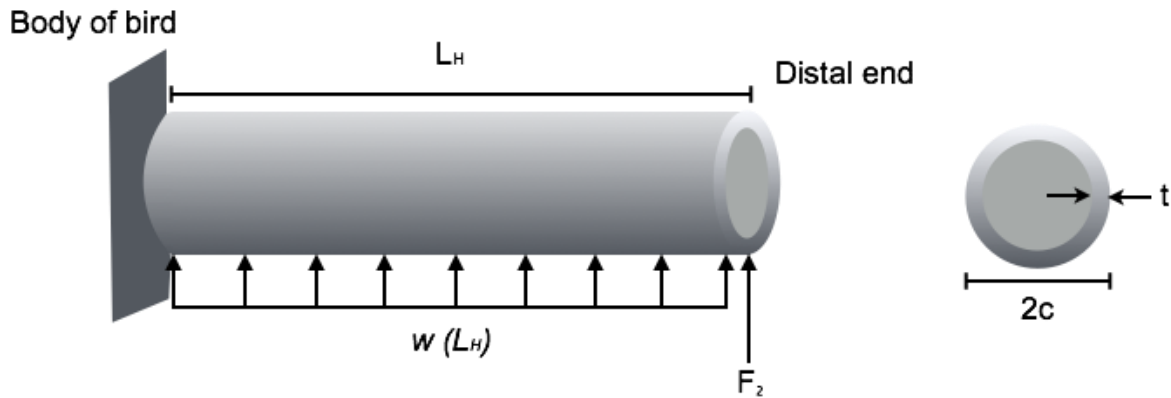


Figure 3.4 The humerus is considered to be a hollow cylinder with length L_H , diameter $2c$ and thickness t . The sum of the distributed force, $w(L_H)$, and the point load (F_2), which represents loading on the distal part of the wing, is equal to the weight of the bird (W) divided by 2.

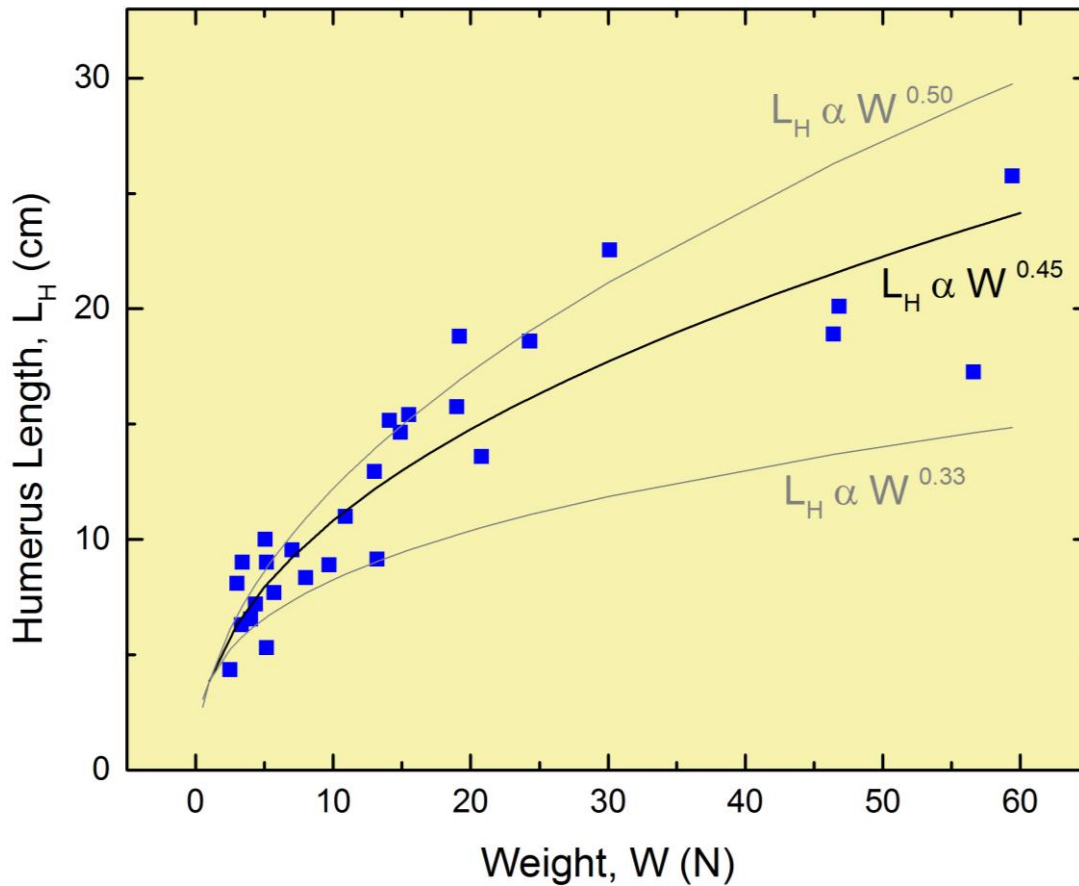


Figure 3.5 Experimental data demonstrates that the humerus length L_H scales allometrically with the weight W of the bird. The upper curve designates allometry from Equation 3.8. Isometric scaling would require $L_H \propto W^{0.33}$ (lower curve).

3.3.2. Allometric Scaling of Wing Bone to Accommodate Flight Style

When bird mass increases, the greater lift required can be generated by an increase in cruising speed or in wing area or both (see Equation 2). To closely examine scaling effects related to bird flight, various dimensions of bird wings, bone, weight and velocity are next investigated. In **Figure 3.6** the cruising speed is plotted against wing area of flying birds, with the color map reflecting the weight of the bird. Diagonal lines with slope $-(1/2)$, drawn in grey, show the predicted lift force F , calculated based on Equation 3.2. Note the good agreement between

predicted lift and bird weight, supporting Tennekes' assumption to set lift and weight equal to one another at cruising speed.

From Equation 3.2 we obtain the following:

$$v \propto \left(\frac{W}{A}\right)^{1/2} \quad (3.9)$$

With isometric scaling, where $W \propto l^3$ and $A \propto l^2$, the equation becomes:

$$v \propto \left(\frac{l^3}{l^2}\right)^{1/2} \quad (3.10)$$

It is further simplified so that the cruising speed (v) can be related to the projected area (A):

$$v \propto A^{1/4} \quad (3.11)$$

While most values in **Figure 3.6** do not fall on the predicted trend line, data fall within the range of $v \propto A^{1/2}$ ("upper bound") and $v \propto A^{1/8}$ ("lower bound"). Values above the isometric line correspond to a stronger contribution from cruising speed, and values below signify a predominant contribution from wing area in raising lift force.

Figure 3.6 shows clearly that the increasing lift requirement in larger birds is generally met by a combination of higher cruising speed and larger wing area. Only increasing the cruising speed (which corresponds to a vertical line pointing upward on the plot) would be an unsuitable strategy: heavy birds with insufficient wing area would have difficulty landing and taking off. It is not unreasonable that the upper bound corresponds to a cruising velocity that is proportional to linear size; it might be hypothesized that animals with longer legs can reach higher take-off velocities or tolerate higher landing speed. The lower bound is very likely related to a mechanical limit on wing area.

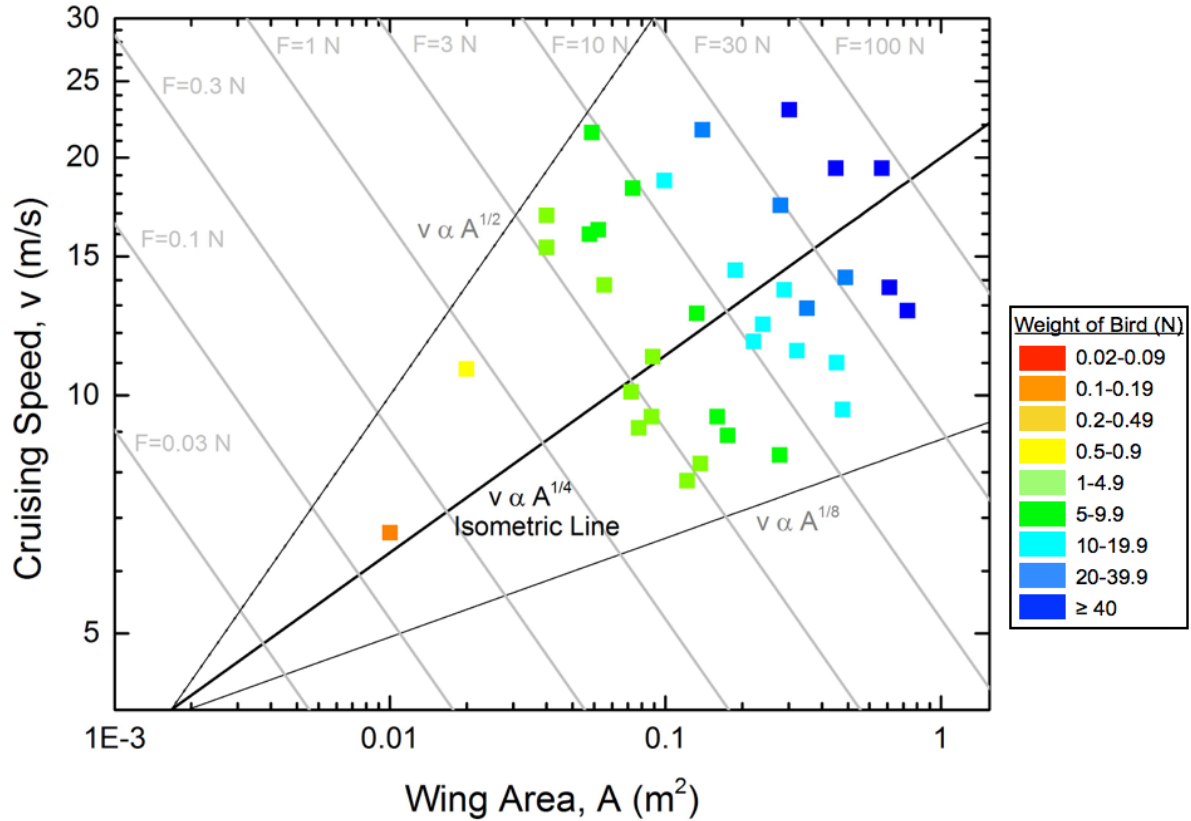


Figure 3.6 The cruising speed is plotted against wing area on a log - log scale for a variety of birds. The weight of the bird is indicated by the color coding. Diagonal grey lines represent calculated values of lift, which are nearly equal to the weight of the bird. Data plotted are from [139–141].

As a comparison, the same graph is plotted in **Figure 3.7**, with the color coding representing the percent of the wingspan composed of the humerus. This relative humerus length is generally greater above the isometric line, especially when comparing samples of similar weight. We argue that this is due to the relatively high wing loading of these birds because of their comparatively high cruising speed and low wing area. To compensate for high loading a greater percentage of the wing span must be composed of the humerus. A schematic describing this hypothesis is shown in **Figure 3.8** where both birds have the same total weight and humerus length, yet one has a smaller wing area.

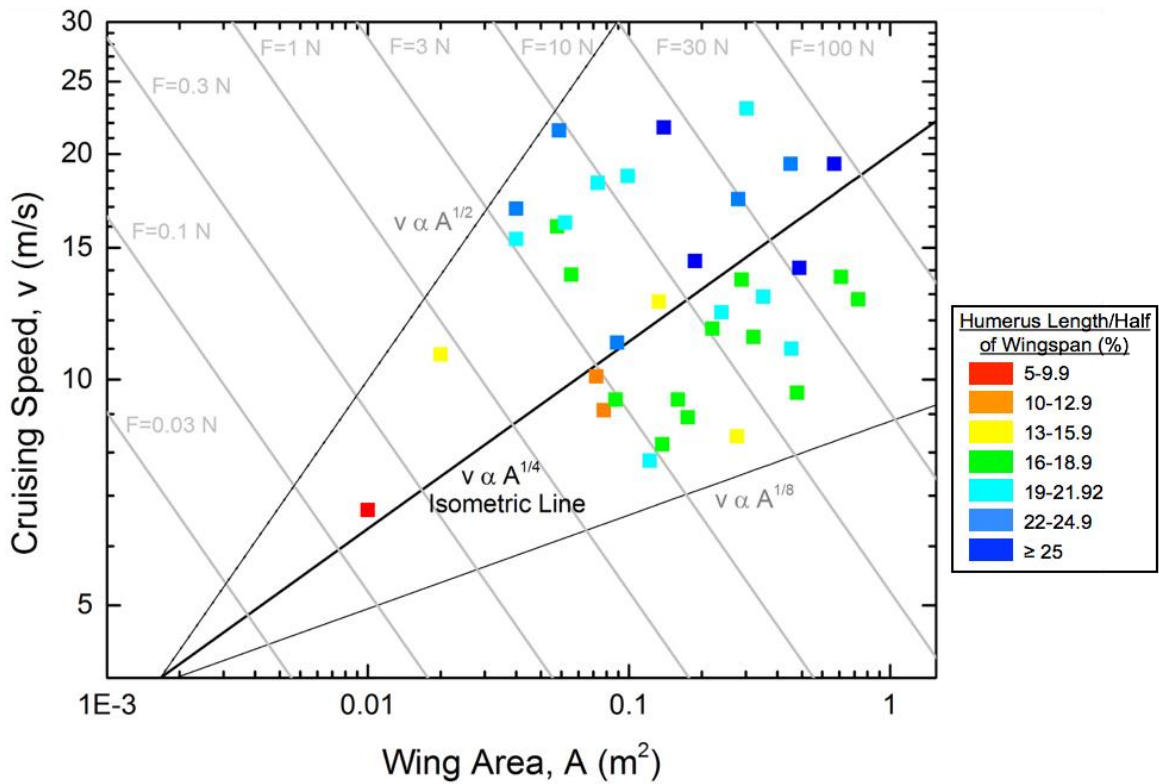


Figure 3.7 The cruising speed and wing area are plotted against one another. The percent wingspan composed of humerus (humerus length/half of wingspan) is plotted with color. Data plotted are from [139–141].

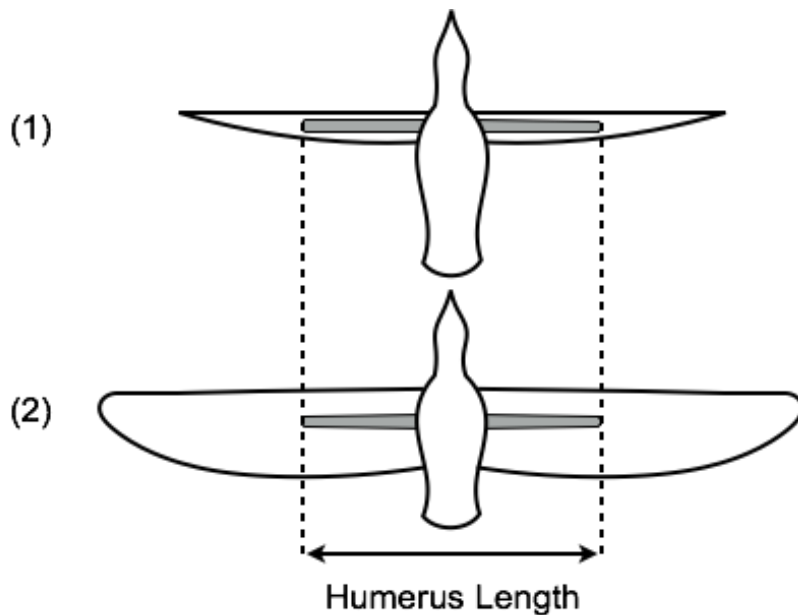


Figure 3.8 Birds (1) and (2) have the same mass and humerus length. Bird 1 however, has a much smaller wing area and therefore has higher wing loading. To compensate for this, a larger percent of bird 1’s wingspan is composed of humerus bone.

To more closely examine the relationship between percent of the wing composed of the humerus and wing loading, these values are plotted in **Figure 3.9** with the velocity color mapped. This chart shows the trend of increased relative humerus length with increased wing loading, generally following the trend of $L_H/L = 5.39\left(\frac{W}{A}\right)^{0.3}$, with a coefficient of determination of 0.46. This trend demonstrates that the humerus length serves as a variable that allows birds to possess a wide variety of wing shapes. While high-aspect ratio wings, such as those of bird 1 in **Figure 3.8**, allow for reduced aerodynamic drag and are ideal for gliding, broader, low aspect ratio wings permit maneuverability in flight. By adjusting the percent humerus length within the wing, nature has provided a means for the bird wing to be optimized for many different conditions. The outlier of the trend is the Chimney swift (*chaetura pelagica*). Swifts have exceptionally long wing feathers and hand bones (carpometacarpus) and small arm bones (humerus, ulna, radius)[143].

This allows their wings to morph to a greater extent in flight than other birds and provides them with greater maneuverability.

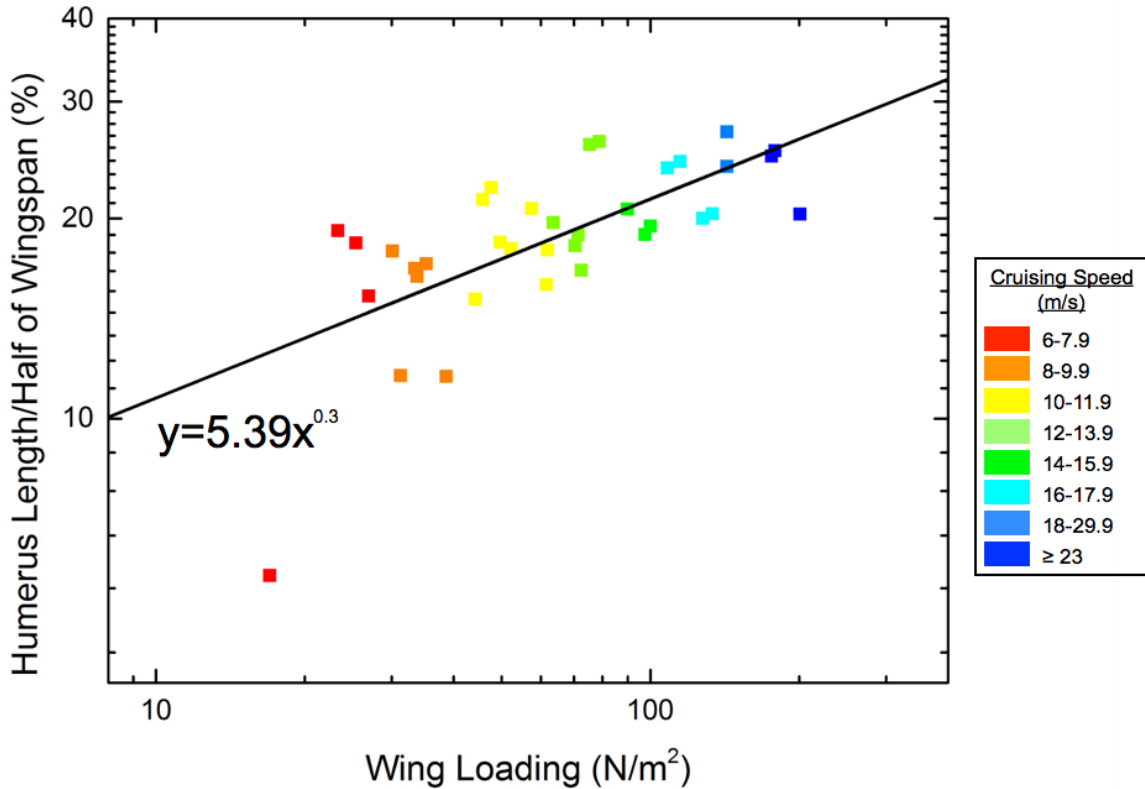


Figure 3.9 The percent of the wingspan L_H/L composed of the humerus plotted against wing loading W/A on a log-log scale. The cruising velocity is color mapped.

Plotting the humerus length and diameter against cruising speed (**Figure 3.10**) demonstrates that these humerus dimensions do not scale with speed. However the humerus length is shown to scale closely with the humerus diameter at a rate of $y = 0.32x^{0.8}$ ($R^2=0.87$). Perhaps birds have great variability, in their evolution, in cruising speed and wing area (as shown in **Figure 3.6**) while still maintaining the ability to fly due to the evolutionary capability of the humerus bone to scale based on the needs of the specific wing. In the next section we investigate scaling trends in the feather, an essential component of the bird wing for flight.

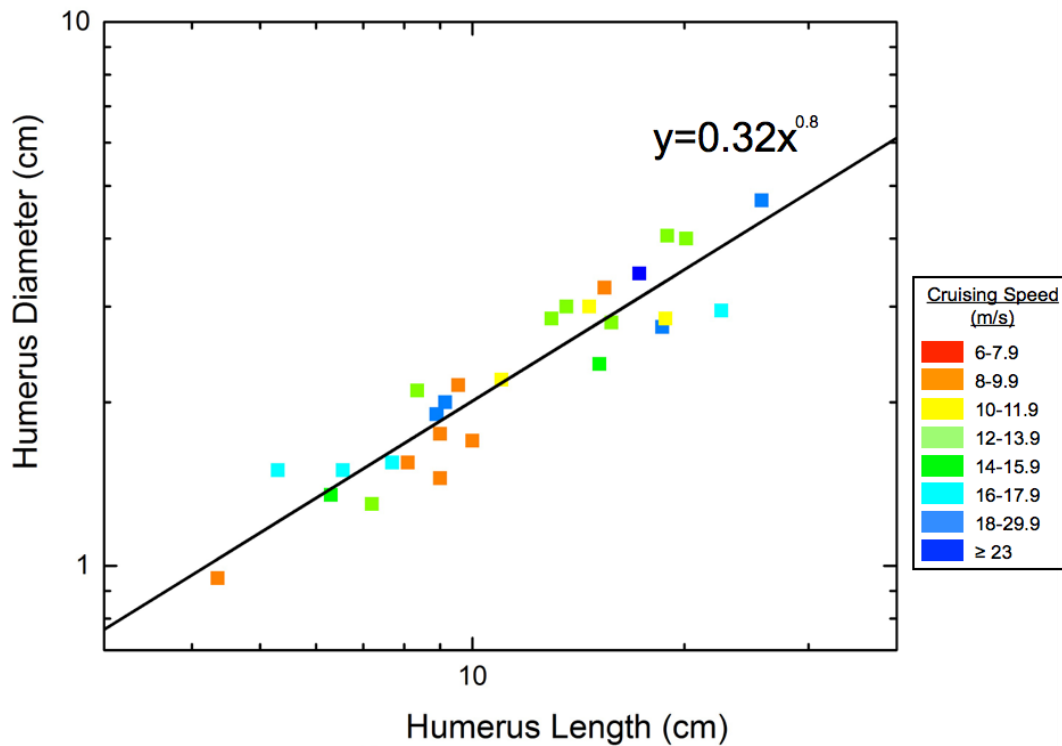


Figure 3.10 The humerus diameter and length are plotted as in Figure 4.6, with the cruising speed color-mapped. The cruising speed does not appear to correlate with the humerus dimensions.

3.3.3. Scaling Trends Observed in the Avian Feather

A large portion of the wing is composed of flight feathers, which are highly hierarchical β -keratinous integument structures . Due to their significance to bird flight[74], scaling relations between mass and feather dimension have been investigated. Within the flight feather, barbs branch from the main shaft and barbules branch from barbs. The increase in the size of feathers, L_F , with mass, m , can be expressed as a first approximation, assuming isometrical scaling $L_F \propto m^{1/3}$. **Figures 3.11-3.13** compare the experimental slope for feather length (0.30-0.34) [47,133] mid-shaft width (0.32-0.37) [47,132,133], and barb length on the trailing (0.27) and leading (0.25) [47] edge of the vane with the ideal 1/3 mass dependence. This trend demonstrates a quantifiable scaling relationship between the mass of birds and feather size. Interestingly, we found that the

spacing between hooked, trailing barbules remains within a range of 8-16 micrometers, with no apparent dependence on the mass of bird (**Figure 3.14**).

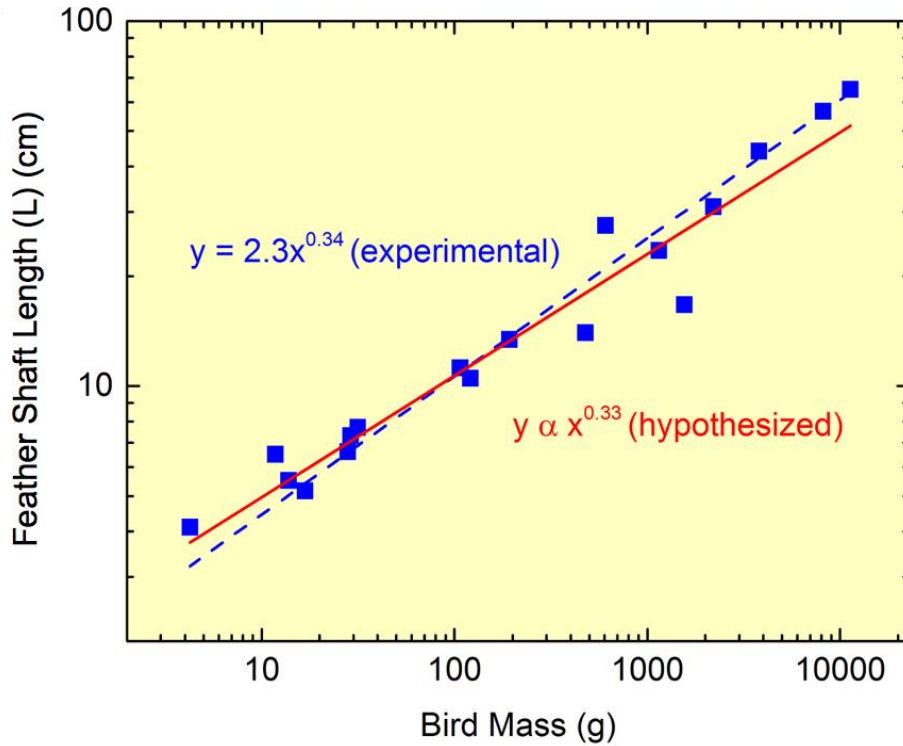


Figure 3.10 The total feather shaft length scales with bird mass following the trend $y=2.3x^{0.34}$ with an R^2 value of 0.95 (where measurement uncertainty is ± 0.05 cm). This trend is very close to the trend expected through isometric scaling with bird mass. Images taken from [47].

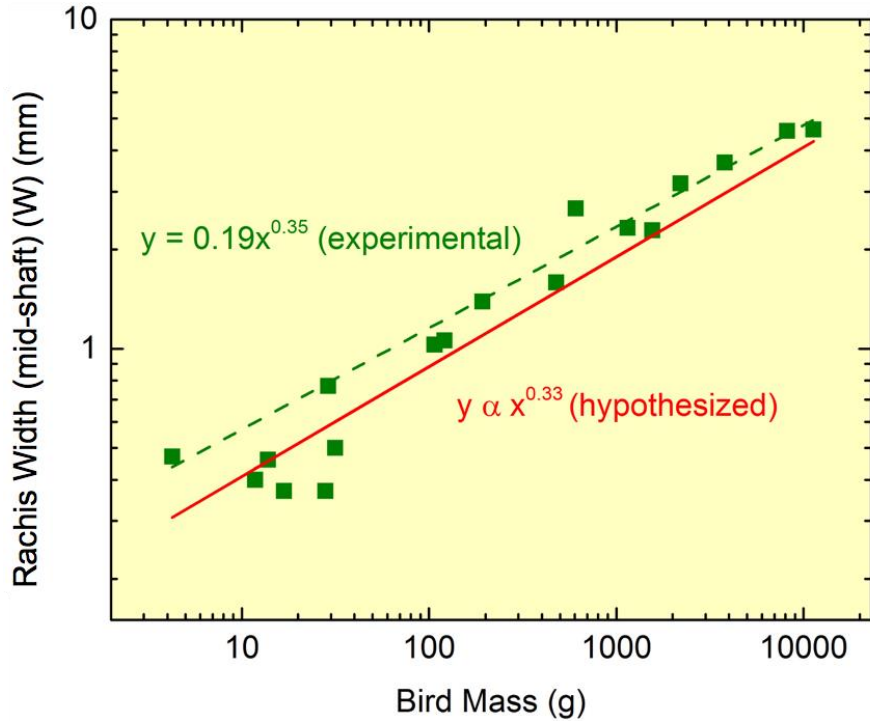


Figure 3.11 The width of the feather shaft at its midpoint scales with bird mass exponentially following the trend $y=0.19x^{0.35}$ with an R^2 value of 0.95 (measurement uncertainty is ± 0.02 mm)[47].

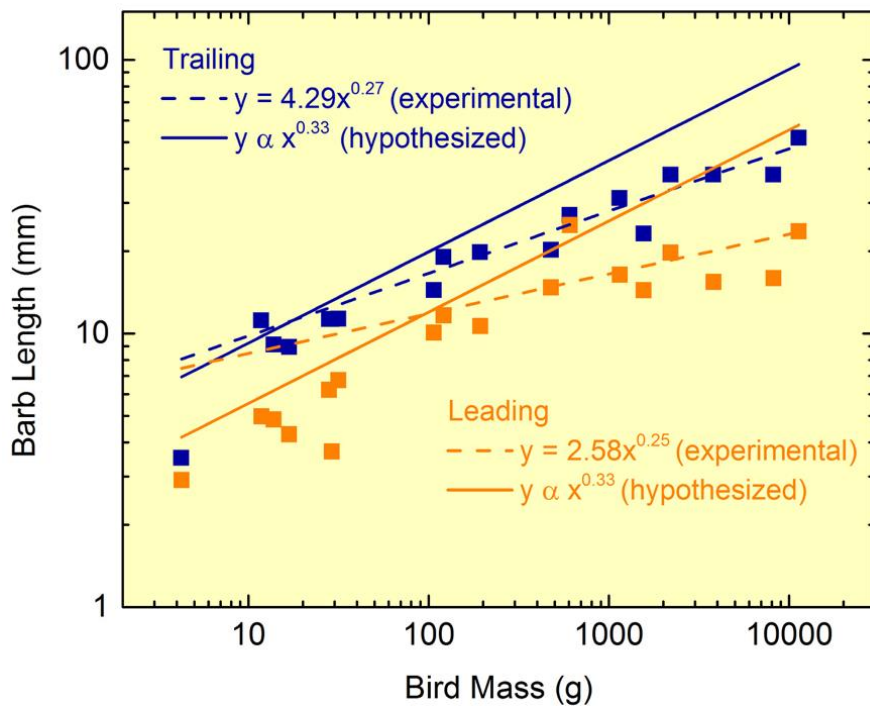


Figure 3.12 The barb length of the trailing and leading feather vane follow $y=4.29x^{0.27}$ ($R^2=0.91$), and $y=2.58x^{0.25}$ ($R^2=0.83$) respectively (standard deviations range from 0.02-0.2mm)[47].

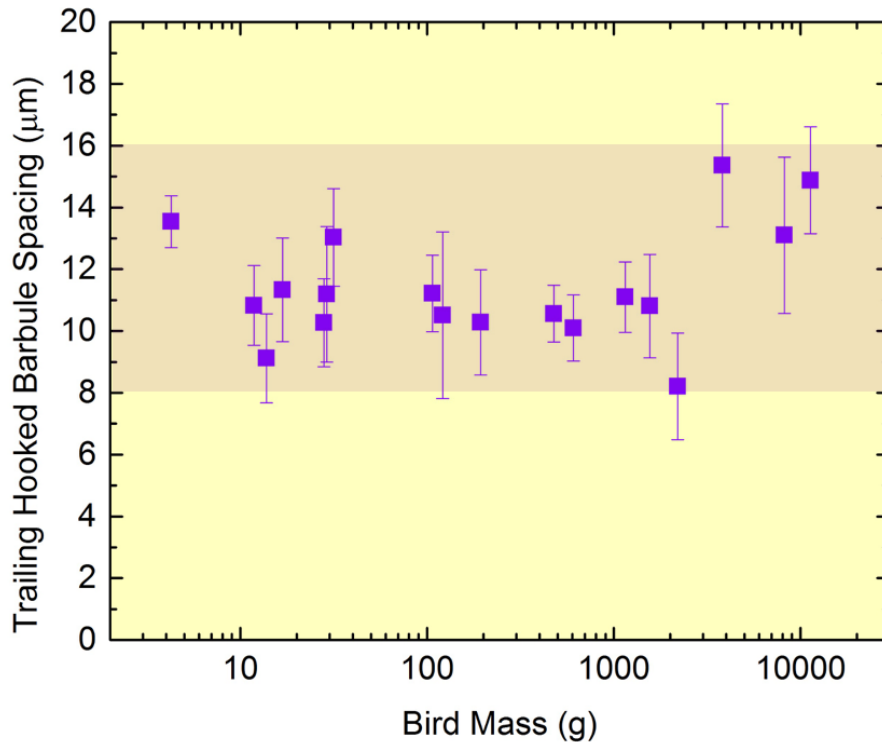


Figure 3.13 Surprisingly, the spacing between trailing hooked barbules does not follow this trend and ranges between 8-16 micrometers across all bird masses[47].

The gap between barbules (**Figure 3.15**) includes a thin membranous flap extending from each barbule to cover the space in between barbules so that the vane is able to capture more air. This is thought to allow the vane to act as an assembly of one-way valves [29]. During the upstroke (recovery stroke) the bird's primary feathers separate to allow air-flow through and prevent excessive downward forces on the wing [144]. We propose that these barbule flaps assist in preventing unwanted forces in the upstroke by allowing air to flow through the feather dorsally. In the downstroke (power stroke), however, the flaps do not allow air through and therefore maximize the capture of air by the feather. The simplified additively manufactured model of the flap structure within the feather vane is shown in **Figure 3.15 b-d** to demonstrate this. Thin, flexible flaps branch from hooked and grooved barbules to cover spaces between them. When air is blown at the bioinspired vane from the dorsal direction the flaps open (**Figure 3.15**) (where

circles denote the location of airflow); however, when air is blown ventrally the flaps remain closed (**Figure 3.15d**). **Figure 3.15e,f** shows the similarity of barbule spacing, yet remarkable difference in feather size between the Anna's Hummingbird (*Calypte anna*) and the Andean Condor (*Vultur gryphus*). The reason for the constancy in barbule spacing (8-16 μm) is proposed to be to retain low permeability of air through the feather independent of bird size. The feather must balance air flow with maintenance of its interlocking structure.

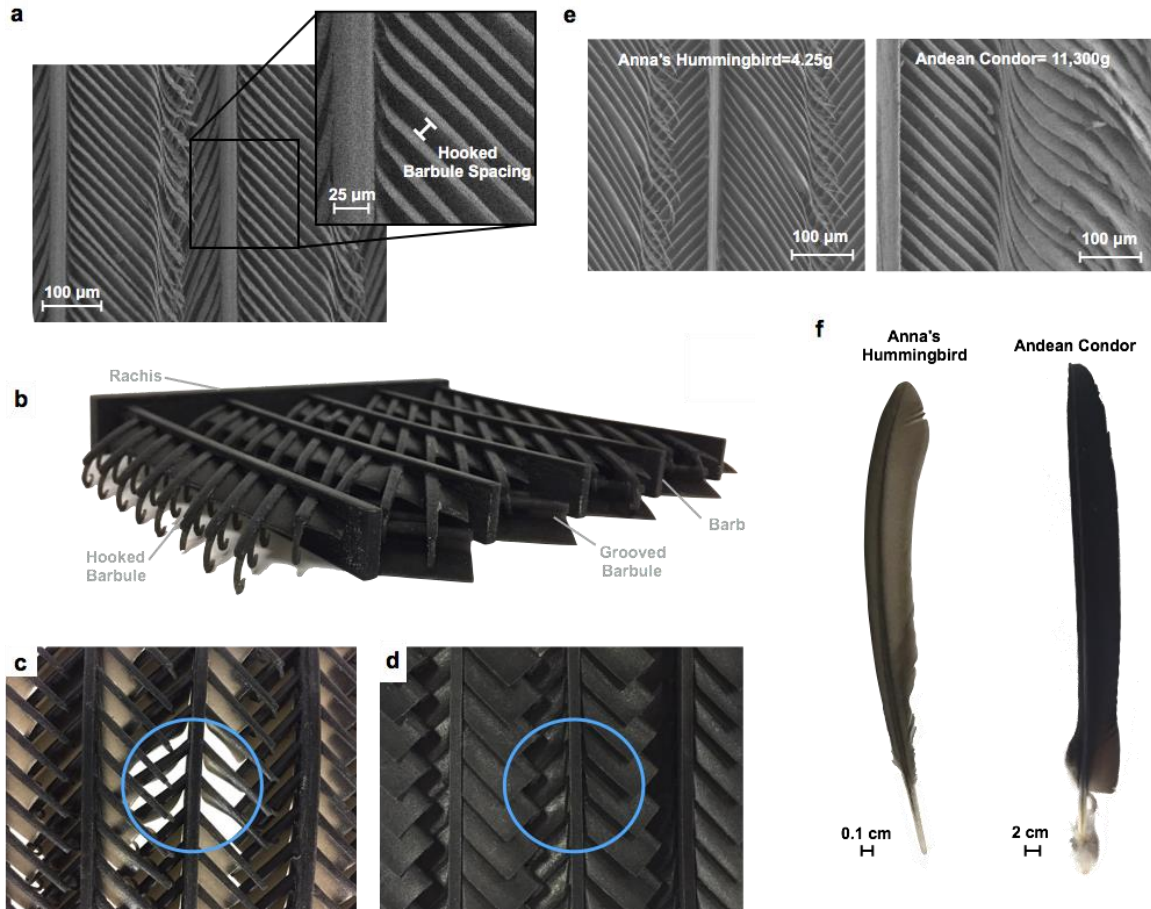


Figure 3.14 An example of the barbule spacing dimension is shown in (a). A bioinspired model created by additive manufacturing (b) was used to show the behavior of the barbule membrane flaps. This model is shown with air blown dorsally (c) and ventrally (d) at the vane, where circles represent the location of airflow. The similarities between the micro-scale barbules of the Anna’s Hummingbird (*Calypte anna*) (left) and the Andean Condor (*Vultur gryphus*) (right) are demonstrated in (e), while the macro-scale differences are shown in (f). Image taken from [47].

3.4. Conclusions

The complementary features between the avian bone and feather discussed here provide insight into nature’s approach at creating structures optimized for flight. The strength of avian bone is found to be a limiting factor in scaling the humerus for flexural loading, and is hypothesized to relate to the allometric scaling of the humerus with bird mass. We find that increased relative humerus length relates to increased wing loading, and hypothesize that this is an evolutionary

method utilized by nature to allow for greater variability in bird wings. This perhaps allows wings to be optimized for specific applications and flight styles.

Dimensions of the feather are found to scale isometrically with bird mass at nearly all hierarchical levels. An exception to this is the barbule spacing within the feather vane, which is revealed to consistently remain within the range 8-16 micrometers for birds of hugely different masses such as Anna's Hummingbird (*Calypte anna*) (4 g) and the Andean Condor (*Vultur gryphus*) (11,000 g). Constancy in barbule spacing is proposed to reflect the necessity to retain low permeability of air through the feather, independent of bird size. The feather must balance air-flow with maintenance of its interlocking structure.

Trends demonstrated in this chapter show that through the process of evolution, nature has optimized designs for flight. An understanding of how feathers and bird wings scale with mass can enable synthetic structures with maximized performance/weight for potential use in future transportation systems.

3.5. Acknowledgements

Chapter 3, in part, is published as a review article in *Materials Today*, authored by T. N. Sullivan, B. Wang, H.D. Espinosa, and M.A. Meyers. The dissertation author was the primary investigator and author on this publication.

Chapter 3 in part, is being prepared for submission by T.N. Sullivan, M.A. Meyers and E. Arzt. The dissertation author is the primary investigator and author on this publication.

We graciously acknowledge Phil Unitt (Curator of Birds and Mammals) from the San Diego Natural History Museum for allowing us access to the museum's avian bone collection and for providing the American White Pelican (*Pelecanus erythrorhynchos*) feathers. We also thank Mike Maxcy (Curator of Birds) and Dr. Cathleen Cox (Director of Research) from the Los Angeles

Zoo for the Cape Vulture (*Gyps coprotheres*) feathers and April Gorow (Research Coordinator) from the San Diego Zoo for all other feathers.

4. Resilience of Feather Barbs

The flying feathers of birds are keratinous appendages designed for maximum performance with a minimum weight penalty. Thus, their design contains ingenious combinations of components that optimize lift, stiffness, aerodynamics, and damage resistance. This design involves two main parts: a central shaft that prescribes stiffness and lateral vanes which allows for the capture of air. Within the feather vane, barbs branch from the shaft and barbules branch from barbs, forming a flat surface which ensures lift. Microhooks at the end of barbules hold barbs tightly together, providing the close-knit, unified structure of the feather vane and enabling a repair of the structure through the reattachment of un-hooked junctions. Both the shaft and barbs are lightweight biological structures constructed of keratin using the common motif of a solid shell and cellular interior. The cellular core increases the resistance to buckling with little added weight. Here we analyze the detailed structure of the feather barb and, for the first time, explain its flexural stiffness in terms of the mechanics of asymmetric foam-filled beams subjected to bending. The results are correlated and validated with finite element modeling. We compare the flexure of single barbs as well as arrays of barbs and find that the interlocking adherence of barbs to one another enables a more robust structure due to minimized barb rotation during deflection. Thus, the flexure behavior of the feather vane can be tailored by the adhesive hooking between barbs, creating a system that mitigates damage. The exceptional architecture of the feather vane will motivate the design of bioinspired structures with tailored and unique properties ranging from adhesives to aerospace materials.

4.1. Introduction

As described in section 2.7.2, the flight feather consists of a main shaft, and a feather vane composed, sequentially, of barbs that branch from the rachis and barbules that branch from barbs. Flight feathers must be lightweight and able to sustain aerodynamic loads without excessive

flexure or torsional damage. One of the ways feather components conform to these constraints is by having a sandwich structure, consisting of a solid shell and cellular core. Their dense exterior is composed of layers of ordered fibers in a matrix material which form a biological composite laminate. According to a study by Lingham-Soliar et al. [79], both the barb and rachis have fibers oriented in the axial direction along dorsal and ventral sides with thin crossed-fibers in the lateral walls.

Within the feather vane, barbs form a highly ordered lattice where they interlock with adjacent barbs via barbules to produce a tightly woven structure. On a given barb, proximal barbules have a grooved structure while distal barbules have four to five tiny microhooks (hooklets) along their length (**Figure 4.1**) [25,145]. Hooked barbules interlock with the neighboring barb's grooved barbules to form a "Velcro-like" connection that can be separated and re-zipped [146]. This enables repair of the damaged areas by re-hooking the hooks to grooves.

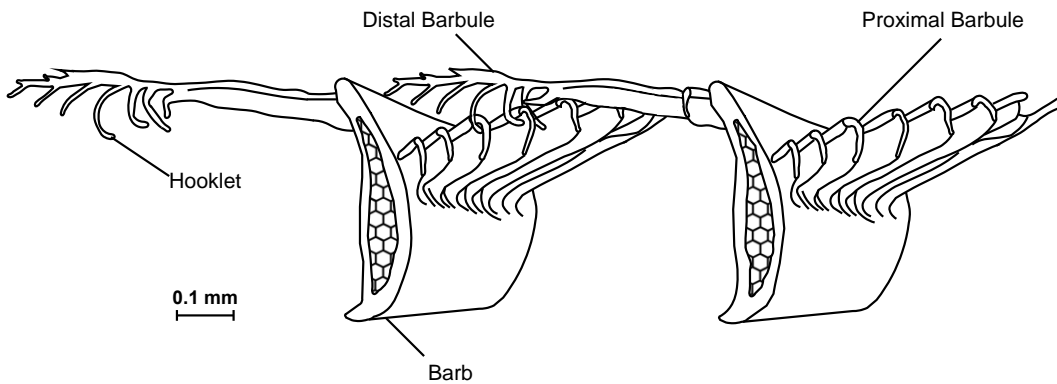


Figure 4.1 Barb and barbule structure: barbs are asymmetrically shaped and foam filled. On the distal side of the barb barbules have hooklets and on the proximal side barbules are grooved. Barbules from neighboring barbs interlock with each other. Redrawn[77] after Lucas and Stettenheim (1972) [145].

The evolutionary innovation of the interlocking feather vane is credited as the essential element which makes flight possible in birds [147,148] as it allows for a compact and cohesive

structure for aerodynamic efficiency [149]. The air transmissivity of the feather is a function of how tightly connected barbs are, and birds preen themselves daily to re-zip their feather vanes[6]. Similarities in the barb structure and interlocking mechanism across bird species are demonstrated in **Figure 4.2**, where feathers of the razor-billed curassow (*Mitu tuberosum*), house sparrow (*Passer domesticus*), and California seagull (*Larus californicus*) are shown. Since these structures are similar in nearly all flying birds [25], structural deformation concepts can be generalized to apply to most feathers.


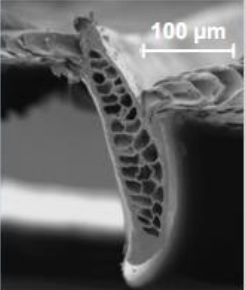
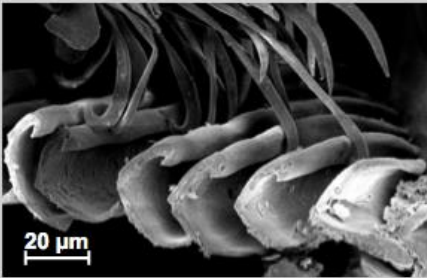


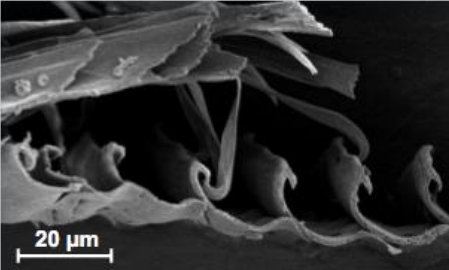


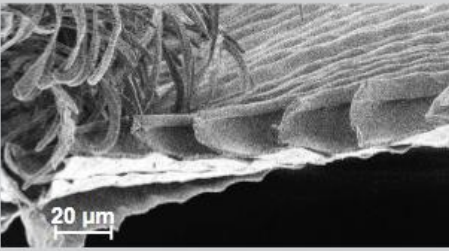
Species	Barb Cross Section	Barbule Connection
 <p data-bbox="305 569 516 615">Razor-billed curassow <i>Mitu tuberosum</i></p>	 <p data-bbox="764 338 829 359">100 µm</p>	 <p data-bbox="954 552 1019 573">20 µm</p>
 <p data-bbox="315 909 493 955">House Sparrow <i>Passer domesticus</i></p>	 <p data-bbox="773 663 837 684">50 µm</p>	 <p data-bbox="946 894 1011 915">20 µm</p>
 <p data-bbox="310 1272 483 1318">California Seagull <i>Larus californicus</i></p>	 <p data-bbox="776 1003 841 1024">50 µm</p>	 <p data-bbox="946 1230 1011 1251">20 µm</p>

Figure 4.2 Barbs and barbules from various bird species: in nearly all flying birds, barbs and barbules have a similar shape, as demonstrated in this comparison between the razor-billed curassow (*Mitu tuberosum*), house sparrow (*Passer domesticus*), and California seagull (*Larus californicus*) [77]. Razor-billed curassow photograph acknowledgement: <https://commons.wikimedia.org/wiki/File:MitutuberosaWhaldenerEndo.jpg>, Whaldener Endo (cropped image).

While barbules are an essential part of the feather vane, barbs make the greatest contribution to its stiffness as they are its most rigid component. For this reason we chose to study the flexural behavior of the barb. Qualitative observations have been made regarding this behavior, but there is a surprising lack of quantitative data and detailed analysis of their flexure behavior,

the mechanisms used by barbs to avoid being permanently deformed, and the reason for their evolution to an unusual asymmetrical shape.

4.2. Materials and Methods

4.2.1. Test Specimens

Feathers of an adult razor-billed curassow (*Mitu tuberosum*) were obtained postmortem and stored at ambient conditions. Feathers from the left wing within a total length range of 31-34 cm were used in experiments. To prepare the specimens for mechanical testing, barbs were cut from the trailing side of each feather, within the middle section of the rachis (between 45-80% of the total feather length). The ends of the barbs (on average approximately 25% of total barb length) were attached to a puck in groups of four. This number was chosen to provide a minimum amount of barbs that would allow for sufficient barbule interlocking. For the single barb tests, surrounding barbs were removed using a scalpel. Initial mounting of the barbs ensured that all had similar orientation, since barbules hold the barbs in place.

4.2.2. Mechanical Tests

A Bose Electroforce 3200 testing machine with a 50 gram Honeywell load cell (S/N: 1475925, Model: 31) was used for mechanical testing. A manufacturer-machined wedge was attached to the load cell screw and the scale was zeroed before measurements. Pucks were mounted onto a piece of aluminum that was clamped in suspension at the top of the machine. A schematic of the experimental setup is shown in **Figure 4.3**.

The samples were loaded and unloaded at a rate of 0.1 mm/sec and displaced ± 4 mm. The barb was loaded on its ventral side to simulate the direction of applied force on a barb as a bird is landing. Each sample completed four loading and unloading cycles and was stopped at a displacement of -4 mm in the fifth cycle. From these tests, force displacement curves were obtained.

A high-resolution digital camera was secured on a fixed tripod facing the set up. Images were taken prior to loading and used to determine the distance from the barb secured in the puck to the point of contact between the wedge and barb. This distance is called the effective barb length.

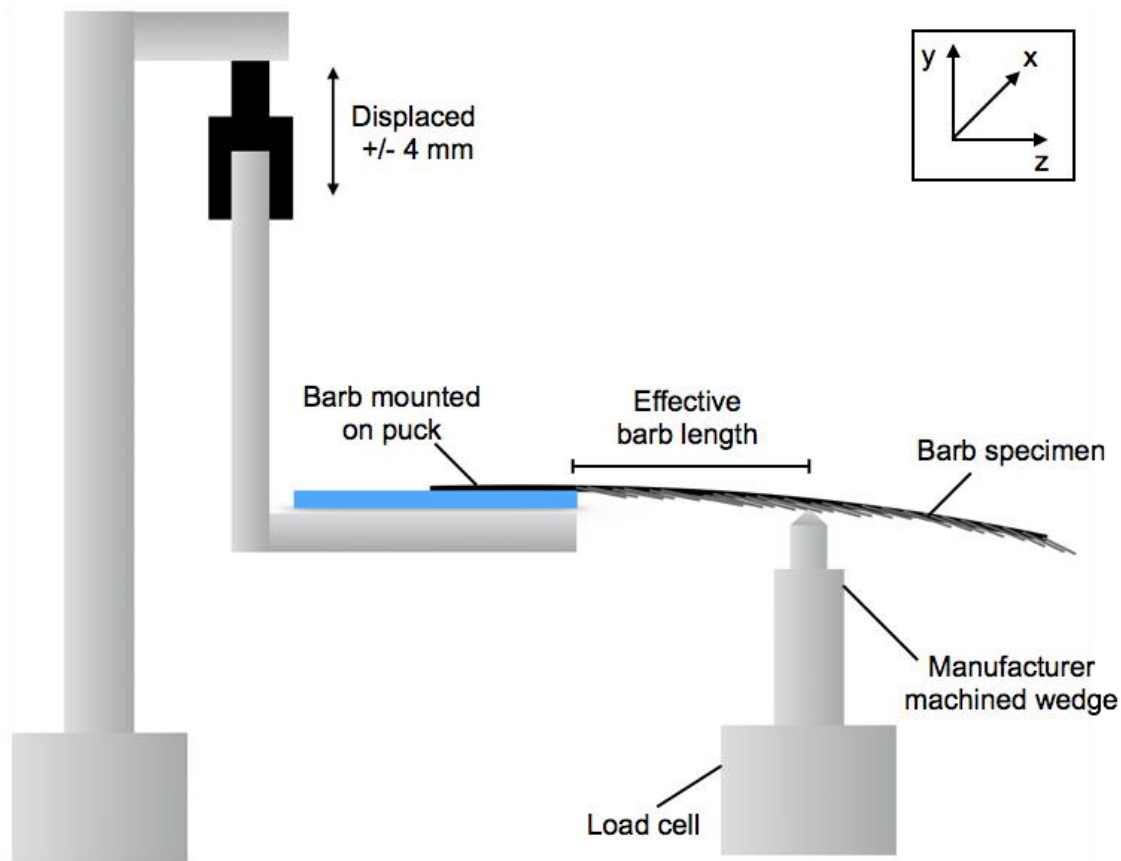


Figure 4.3 Experimental configuration: cantilever flexure tests on single barbs and four zipped barbs [77].

4.2.3. Scanning Electron Microscopy

After the tests, each barb was cut at the effective length as well as at its point of connection to the puck. The barbs were then mounted on a vertical Scanning Electron Microscope (SEM) stub, coated in iridium and imaged using a SEM. Some of the puck images were not used in analysis due to difficulty in obtaining clear images of cross sections after the experiment because of

remnants of the adhesive on samples. We followed a similar procedure to image cross sections of three untested barbs at 10% increments along their length.

4.2.4. Computer Aided-Design Measurements

Since barbs have an asymmetric and tapered structure, to accurately understand our data we characterized the shape change of barbs by measuring their respective area moments of inertia. We found these values for SEM images of barb cross-sections by tracing the barb's foam and cortex using SolidWorks (SolidWorks Corp., Waltham, MA, USA). Since the values given by SolidWorks were for the principal axes of the shape, they were transformed by applying a rotation so that the axes of all measurements were aligned with each other. The angle was calculated with the assumption that the hooked barbules remain horizontal along the length of the barb. While the area moments of inertia found using SolidWorks are with respect to the centroid of the foam or cortex, and not with respect to the total structure's neutral axis (which could not be found using SolidWorks), they are an accurate estimation.

4.2.5. Finite Element Modeling

The geometry of a sample's cross-section at its connection to the puck and at the end of its effective length was replicated from SEM images. In order to take into account the angular twisting of the barb, we assumed that the hooked barbules remain horizontal throughout the barb. We then executed a sweep between the two cross sections along the effective length to replicate the tapered structure of our experimental sample. Constituents of the cross section were considered isotropic and homogeneous, and included the cellular core $E_{\text{foam}} = 0.36 \text{ GPa}$, $\nu_{\text{foam}} = 0.33$ and the cortex $E_{\text{cortex}} = 5.50 \text{ GPa}$, $\nu_{\text{cortex}} = 0.40$, as explained in section 4.3.1.

4.2.6. Statistical Analysis

In order to minimize any localized noise spikes, raw data sets were smoothed with a median filter incorporating five surrounding points using the software Origin 9.0 (OriginLab Corp, Northampton, USA). This software was also used to find the standard error of the linear fit to the data's slope, which is included as error bars in **Figures 4.8** and **4.9**. This error was translated into a percent and used to obtain a displacement error, which is accounted for as error bars in **Figure 4.12**.

4.3. Theory and Calculations

4.3.1. Elastic Modulus of the Barb's Foam-filled Center

To create a theoretical model of the deflection behavior of a barb, one first has to determine the elastic modulus of its foam-filled core. This was calculated using the Gibson and Ashby [43] equations. The foam cells inside the barb were modeled as close-celled hexagonal prisms. From geometrical measurements of SEM images, the relative core/shell density ratio was found to be 0.152. This value, along with other geometrical parameters, was used to find the foam's relative elastic modulus:

$$\frac{E^*}{E_s} \approx \phi^2 \left(\frac{\rho^*}{\rho_s} \right)^2 + (1 - \phi) \frac{\rho^*}{\rho_s} \quad (4.1)$$

The gas pressure component of the equation was omitted because of the porous cell wall structure observed in SEM images. The variables are defined such that E^* is the elastic modulus of the foam, E_s is the elastic modulus of the solid cortex, ϕ is the volume fraction of the solid contained in the foam's cell edges, ρ^* is the density of the foam, and ρ_s is the density of the solid cortex [43]. The full calculations can be found in Appendix A.1.

By assuming that the elastic modulus of the barb cortex is equal to that of the rachis cortex, and using the accepted value of 5.50 GPa from literature for two-point bending [59], the elastic

modulus of the foam core was calculated to be 0.36 GPa. The Poisson's ratio $\nu_{\text{cortex}} = 0.40$ matched the value used by Bachmann et al. [59] for the rachis, where the value for a similar keratinous material is used because it has not been determined for feather keratin. Similarly, the Poisson's ratio of barb foam is unknown and therefore it was taken to be 0.33, which is the average value for closed cell foam according to Gibson and Ashby [43].

4.3.2. Simplified Block Model of Single Barb Deflection

A simplified model of the barb's complex geometry was created using rectangular blocks to form an asymmetrical cortex with a constant cross section and a foam-filled interior. The dimensions of the model were iterated until the x- and xy- area moments of inertia of the cortex and the x- area moment of inertia of the foam matched their respective counterparts found for the equivalent experimental barb (as discussed in section 4.4.4). These were deemed to be the most significant area moments of inertia to match our model due to their contributions in the cantilever flexure equation given in section 4.3.2.2. The length of the barb was set to equal 7.8 mm to match the length of the experimental barb.

4.3.2.1. Finding the Stress and Strain Expressions

Due to significant contributions in bending from the sidewalls, the barb structure could not be simplified using the volume fraction composite method. Additionally, because the barb is an asymmetric structure, the neutral axis does not pass through the centroid. The barb's neutral axis was calculated first.

The derivation begins with the assumption that plane cross-sections remain plane, so that strain is a linear function of x and y (Equation 4.2), and therefore by Hooke's law stress is as well (Equation 4.3) [150]. Definitions of variables are presented in Table 4.1.

$$\varepsilon_z^{(i)} = ax + by ; \quad \sigma_z^{(i)} = E_i(ax + by) \quad (4.2; 4.3)$$

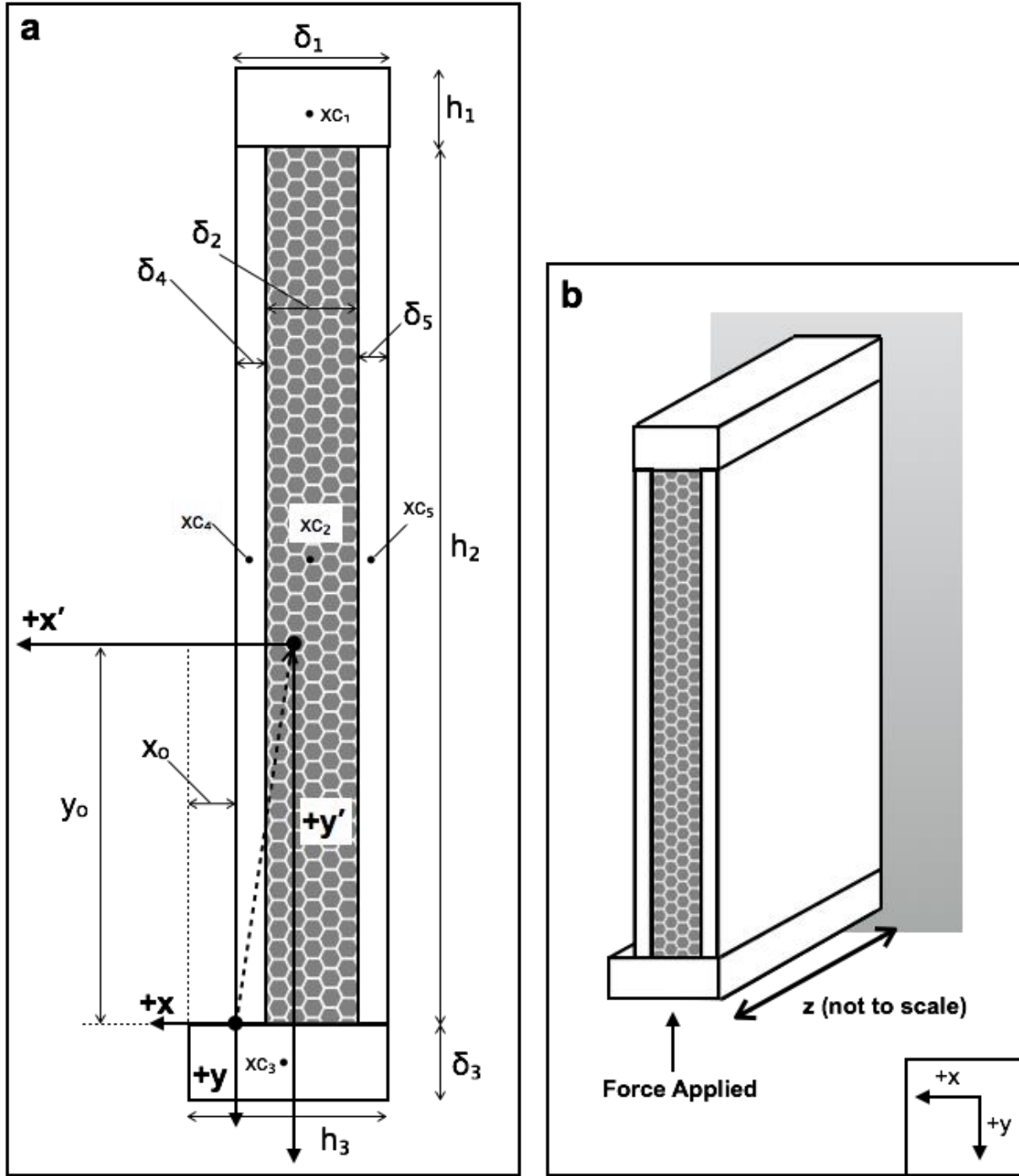


Figure 4.4 Simplified barb used in theoretical calculations: (a) the definitions of dimensions used, where $h_2=h_4=h_5$ (b) sketch of the orientation of the applied force.

Table 4.1 Definitions of variables used in Equations 4.2-4.18.

Symbol	Definition
a	Curvature of barb in the x-direction
b	Curvature of barb in the y-direction
$\epsilon_z^{(i)}$	Strain (z-axis) of each component i
$\sigma_z^{(i)}$	Stress (z-axis) of each component i
E_i	Elastic modulus of each component i
x_{ci}	Location of centroid of each component (along x)
y_{ci}	Location of centroid of each component (along y)
A_i	Area of each component
M_x	Moment in the x-direction
M_y	Moment in the y-direction
I_{xy}^i	The product of inertia of component i with respect to the x and y axes
I_x^i	The x-moment of inertia of component i
I_y^i	The y-moment of inertia of component i
θ	The angle between the location of the applied load and the y-axis

After these assumptions are made, the sum of the integrated stress of each component is set to equal zero to because the longitudinal force is equal to zero:

$$\sum_{i=1}^n \int_{A_i} \sigma_z^{(i)} dA = 0. \quad (4.4)$$

By substituting (4.3) into (4.4):

$$\sum_{i=1}^n E_i \int_{A_i} (ax + by) dA = 0. \quad (4.5)$$

The elastic modulus of each component is taken into account in contributing to the location of the neutral axis:

$$\int_{A_i} x dA = x_{ci} A_i, \quad \int_{A_i} y dA = y_{ci} A_i \quad (4.6)$$

$$\sum_{i=1}^n E_i [ax_{ci} A_i + by_{ci} A_i] = 0, \quad (4.7)$$

$$a \sum_{i=1}^n E_i A_i x_{ci} + b \sum_{i=1}^n E_i A_i y_{ci} = 0. \quad (4.8)$$

The location of the coordinate origin for which (x_0, y_0) is solved using:

$$\sum_{i=1}^n E_i A_i x_{ci} = 0, \quad \sum_{i=1}^n E_i A_i y_{ci} = 0 \quad (4.9, 4.10)$$

Equations (4.9), (4.10) will be satisfied provided that the coordinate origin is at the point:

$$x_0 = \frac{\sum E_i A_i x_{ci}}{\sum E_i A_i}, \quad y_0 = \frac{\sum E_i A_i y_{ci}}{\sum E_i A_i} \quad (4.11, 4.12)$$

Therefore,

$$\sum_{i=1}^n E_i A_i (x_{ci} - x_0) = 0, \quad \sum_{i=1}^n E_i A_i (y_{ci} - y_0) = 0. \quad (4.13, 4.14)$$

The solutions for the specific case of the barb are found in Appendix A.2.

4.3.2.2. Deriving the Inverse Curvature and Deflection of the Barb in Flexure

The curvature is derived in order to solve for the barb's deflection. The relationship between the moment M_x and the stress in each component (Equation 4.15) was used to find the relationship between the curvatures a and b :

$$M_x = \sum_{i=1}^n \int_{A_i} y \sigma_z^{(i)} dA. \quad (4.15)$$

Since the moments are known, the equations can be solved for numerical values. A similar process for M_y is applied and shown in Appendix A.3. The linear stress condition was applied to yield (Equation 4.16), and then these values were integrated (Equation 4.17).

$$M_x = \sum_{i=1}^n \int_{A_i} y E_i (ax + by) dA \quad (4.16)$$

$$M_x = \sum_{i=1}^n E_i \left[a \int_{A_i} xy dA + b \int_{A_i} y^2 dA \right] \quad (4.17)$$

These equations are further simplified to include area moments of inertia:

The following variables were then introduced to simplify the calculations of solving for a and b :

$$E = \frac{\sum_i E_i A_i}{A}, \quad I_x = \frac{\sum_i E_i I_x^i}{E}, \quad I_y = \frac{\sum_i E_i I_y^i}{E}, \quad I_{xy} = \frac{\sum_i E_i I_{xy}^i}{E}.$$

Using these variables, the moment equations are rewritten as:

$$M_x = a E I_{xy} + b E I_x ; \quad (4.18)$$

$$-M_y = a EI_y + b EI_{xy}. \quad (4.19)$$

Upon solving Equations (4.18) and (4.19) for a and b , we obtain Equations (4.20) and (4.21), which also specify the relationship between the curvatures a and b and deflections u and v [39].

$$a = \frac{I_{xy}M_x + I_xM_y}{E(I_{xy}^2 - I_xI_y)} = -\frac{\partial^2 u}{\partial z^2} \quad (4.20)$$

$$b = -\frac{I_yM_x + I_{xy}M_y}{E(I_{xy}^2 - I_xI_y)} = -\frac{\partial^2 v}{\partial z^2} \quad (4.21)$$

The differential Equations (4.20) and (4.21) are solved to produce Equations (4.22) and (4.23) which describe deflections in the x (u) and y (v) directions.

$$u = \frac{I_{xy}F_y z^3}{3E(I_{xy}^2 - I_xI_y)} \quad (4.22)$$

$$v = -\frac{I_yF_y z^3}{3E(I_{xy}^2 - I_xI_y)} \quad (4.23)$$

A sketch of the simplified barb used in calculations is shown in Figure A.1 of the Appendix along with the definitions of variables used for length are given. Dimensions used are listed in Table A.2 of the Appendix A.2.

4.3.3. Analytical Model of Single Barb Deflection

To more accurately represent the cross sectional changes that occur throughout the barb's effective length, we created a more complex analytical model. We begin with an equation similar to the one described in the previous section:

$$b = -\frac{\partial^2 v}{\partial z^2} = -\frac{M_x I_y(z)}{E_s(I_x(z)I_y(z) - I_{xy}(z))} = \frac{F(L-z)I_y(z)}{E_s(I_x(z)I_y(z) - I_{xy}(z))} \quad (4.24)$$

Note that the expression of b differs from Equation (4.21): E_s is the cortex's elastic modulus, the load is only considered in the y-direction, L refers to the effective length, and $I_x(z)$, $I_y(z)$ and $I_{xy}(z)$ are equivalent inertias of the geometry. These inertias follow a z-dependent trend that takes into account the cross-sectional changes. As stated in sections 4.2.3 and 4.2.4, we

characterized this trend by measuring the I_x , I_y , and I_{xy} of three different barbs at every 10% along their length. Moreover, we defined I_x , I_y , I_{xy} such that: $I_x = I_{xcortex} + \alpha I_{xfoam}$, $I_y = I_{ycortex} + \alpha I_{yfoam}$, $I_{xy} = I_{xycortex} + \alpha I_{xyfoam}$ where α is a weighing factor that takes into account the fact that the foam has differing elastic properties ($\alpha = \frac{E^*}{E_s}$, see Equation (4.1) and Appendix A.1 for details).

From Equation (4.24) we integrate twice to find the deflection v at the end of the cantilever, with the imposed boundary conditions $v = 0$ and $dv/dz = 0$ at $z = 0$:

$$\frac{\partial v}{\partial z} = \frac{F}{E_s} \int_0^z \frac{I_y(z)(L-z)}{I_x(z)I_y(z) - I_{xy}^2(z)} dz , \quad (4.25)$$

$$v(L) = \frac{F}{E_s} \int_0^L dz \int_0^z \frac{I_y(\zeta)(L-\zeta)}{I_x(\zeta)I_y(\zeta) - I_{xy}^2(\zeta)} d\zeta . \quad (4.26)$$

4.3.4. Finite Element Model of a Single Barb in Flexure

The finite element model (FEM) was created in Abaqus and mimicked the conditions of the aforementioned experiment. A barb was clamped on one end and lowered a prescribed displacement of 0.45mm in the y-direction (see **Figure 4.11**). The other end of the barb remained free, contacting an analytically rigid cylindrical wedge. A hard contact interaction was defined between the two solids, and the reaction force was measured at the wedge. The barb was drawn as a 7.8mm long, tapered structure with an asymmetrical cross section to closely match the dimensions of one of the experimental barbs and foam was embedded in the cortex. At the barb's fixed end its height was 635 μ m, while at the end contacting the wedge its height was 464 μ m. The finite element mesh was created out of 54,787 tetrahedral quadratic elements (105,583 nodes). More details on the FEM are discussed in section 4.2.5

4.4. Results and Discussion

4.4.1. Materials Characterization

The cross sections of untested feather barbs show that closer to the rachis the barb is highly asymmetric; it becomes smaller and more symmetrical towards the tip (**Figure 4.4 a**), as previously observed by Proctor et al. [25]. Foam core cells were found to be most homogeneous in size at the tip and most diverse in size between the rachis and the center of the barb (**Figure 4.4 b-d**). Perhaps a larger total area of foam allows nature to create cells of varying size, with larger cells at the interior of the barb to reduce the amount of material and decrease density while maintaining bending resistance. Indeed, this has been observed in the porcupine quills, which consist of a keratinous foam-filled shell [151,152].

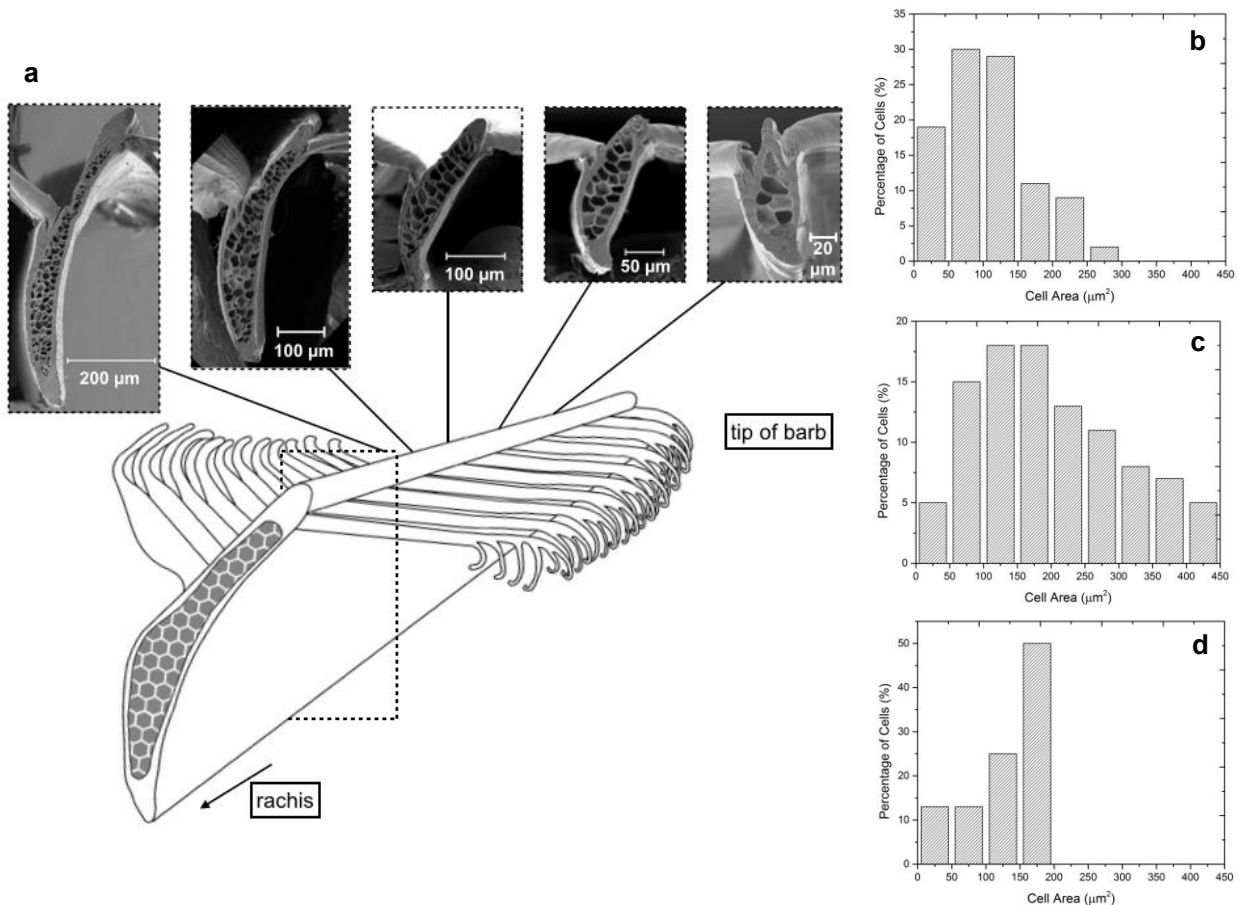


Figure 4.5 (a) Barb cross sectional shape and size: the barb becomes smaller and more symmetrical towards the tip. Characterizing the foam of the barb: The cell size distribution of the foam shows that at (b) 5% and especially (c) 30% from the rachis the cell size is more diverse than at (d) 90% of the barb length from the rachis.

Along the barb the cortex area to foam core area ratio ranges from 0.7 to 2.3. The ratio slightly decreases from 10 to 20 percent of the barb's length, and then increases from 40 to 70 percent. Towards the end of the tip the relative amount of cortex increases to compensate for the smaller cross sectional area. It is plausible that this range of ratios is optimized for the stiffness, weight and type of loading the barb experiences in flight.

Throughout its length, the barb's dorsal-ventral stiffness is reinforced by dorsal-ventral cortex walls which are thicker than the lateral cortex walls. This is for two reasons: (1) higher loading in flight is applied to the barb in the dorsal-ventral direction, and (2) the barb is able to twist along its lateral walls when loading becomes critically large. The x-, y- and xy- area moments of inertia of the barb's cortex and foam were found to follow an exponential decay trend, as shown in **Figure 4.5**.

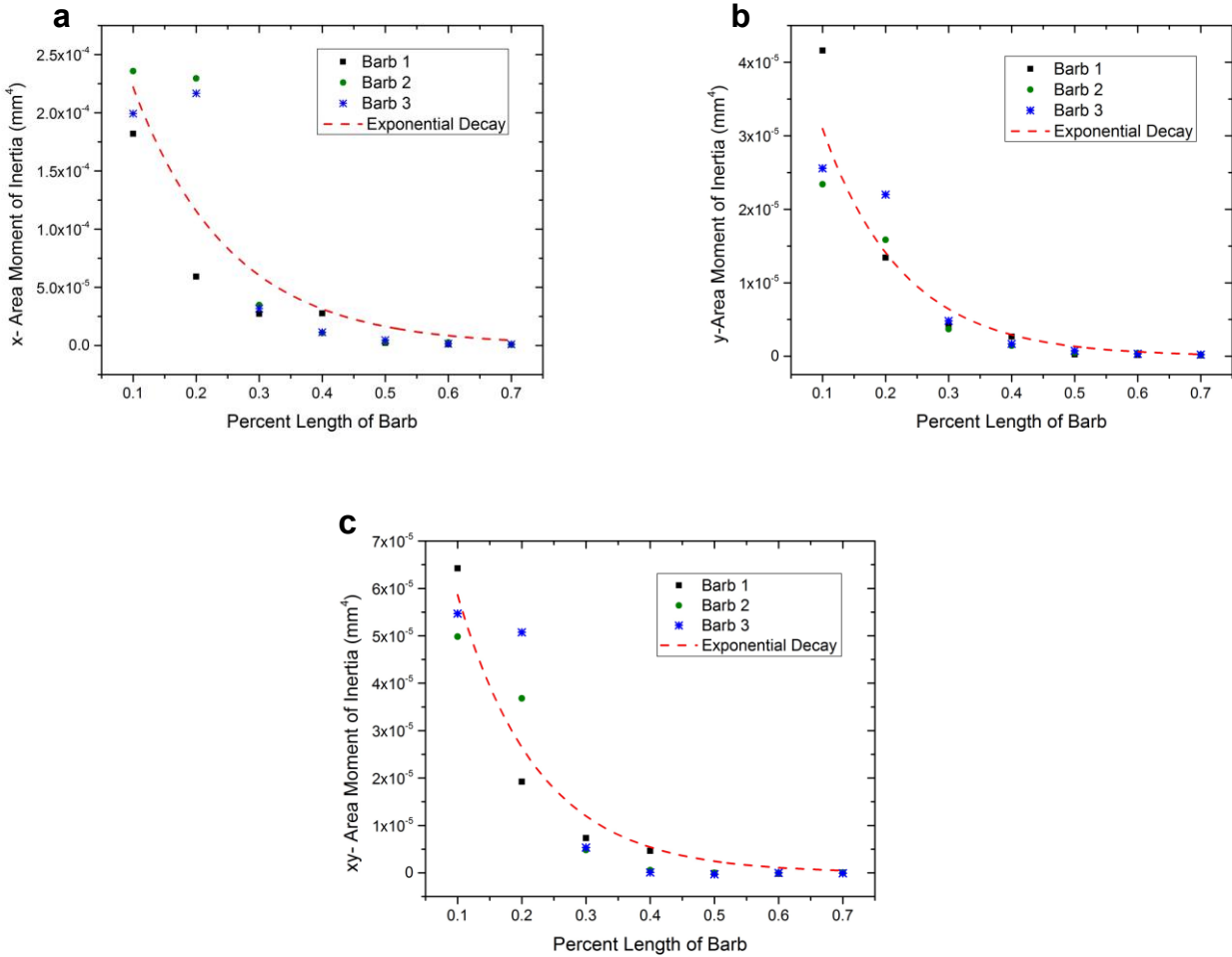


Figure 4.6 The (a) x-, (b) y- and (c) xy- area moments of inertia of the barb's cortex and foam were found to follow an exponential decay trend. The foam and cortex were combined as explained in section 4.3.3.

4.4.2. Cyclic Testing of Single Barbs

A representative experimental plot of displacement and force versus time displayed in **Figure 4.6** shows that the resistance force initially rises linearly with an increase in displacement, and then slightly decreases as the barb twists. Twisting along the z-axis causes the stiffness to decrease with respect to the y-axis because its height is now its width. Since this twisting occurs before the maximum displacement, the maximum resistive force appears just before the barb twists, not at the point of maximum displacement. The insets (a) and (b) of **Figure 4.6** explain this process of barb flexure. When the barb is unloaded, the resistive force sharply drops and then

rises as a reaction to the untwisting of the barb. This trend is apparent for each of the four cycles of all tests. Through this flexure stratagem, the barb can undergo large displacements without catastrophic failure. These results are similar to visual observations by Butler et al. [153], who stated that the asymmetry, thinner lateral walls of the cortex, and slenderness of the barb result in its twisting when dangerously large loads are applied. It is important for the barbs to deform without mechanically failing because they are essential to bird flight and are only replaced during molting, which usually occurs annually [26]. This twisting action also ensures that loads are distributed more effectively to neighboring barbs.

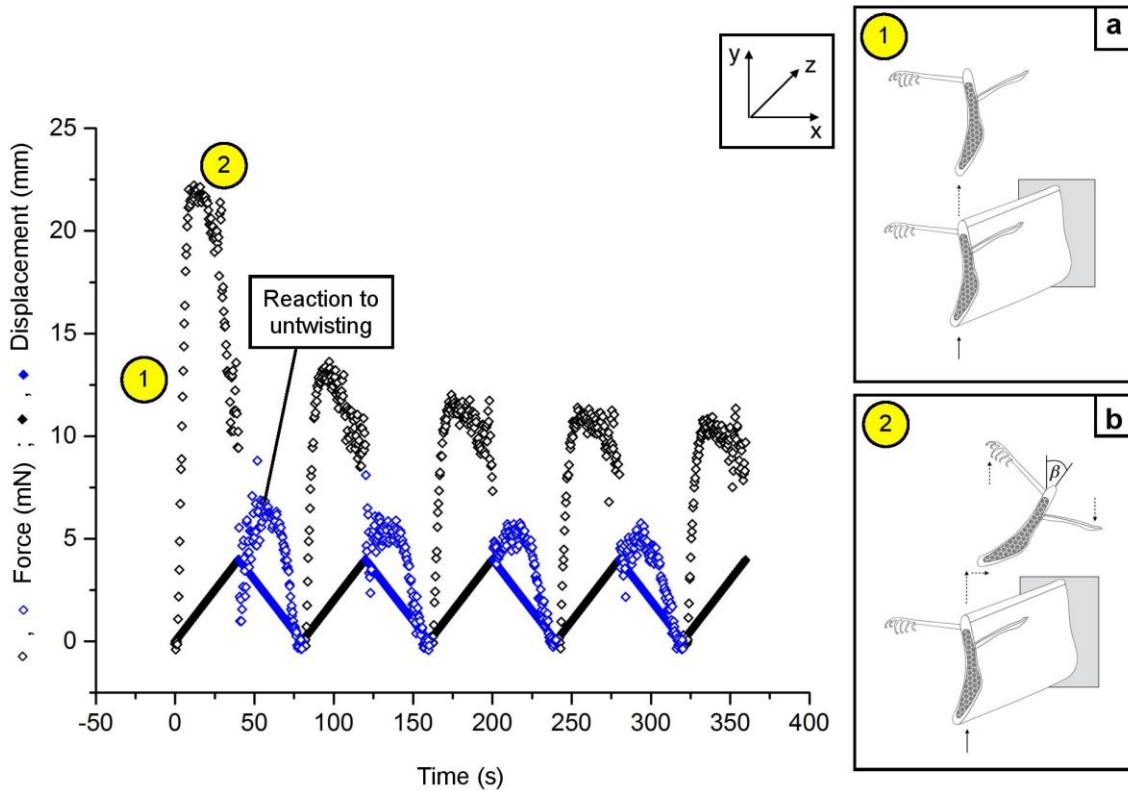


Figure 4.7 The deflection of a barb: a typical experimental plot of displacement and force as a function of time. Black indicates loading and blue indicates unloading. The barb first (a) deflects in the y-direction, then (b) twists, resulting in a decrease in stiffness with respect to the y-axis.

To understand the repeatability of the flexure tests, the maximum force of the first and second cycle were compared. The difference between these forces, measured in percentage (which we define as percent damage), is plotted versus the maximum force and effective barb length (**Figure 4.7**). Shorter barbs require higher forces for damage and have a larger percent damage that likely corresponds to yielding, including linear and permanent deformation of the cortex. Longer barbs have lower maximum forces and a smaller percent damage which conceivably corresponds to elastic instability (buckling). Examples of experimental force versus deflection plots for two test cycles are shown in the inset of **Figure 4.7**, one with (a) 40% and another with (b) 7% damage. Although some of the tests show significant amounts of damage, the barbs continue to offer some level of resistance and it has been reported (Liu et al. [154]) that this damage can be reversed by hydration.

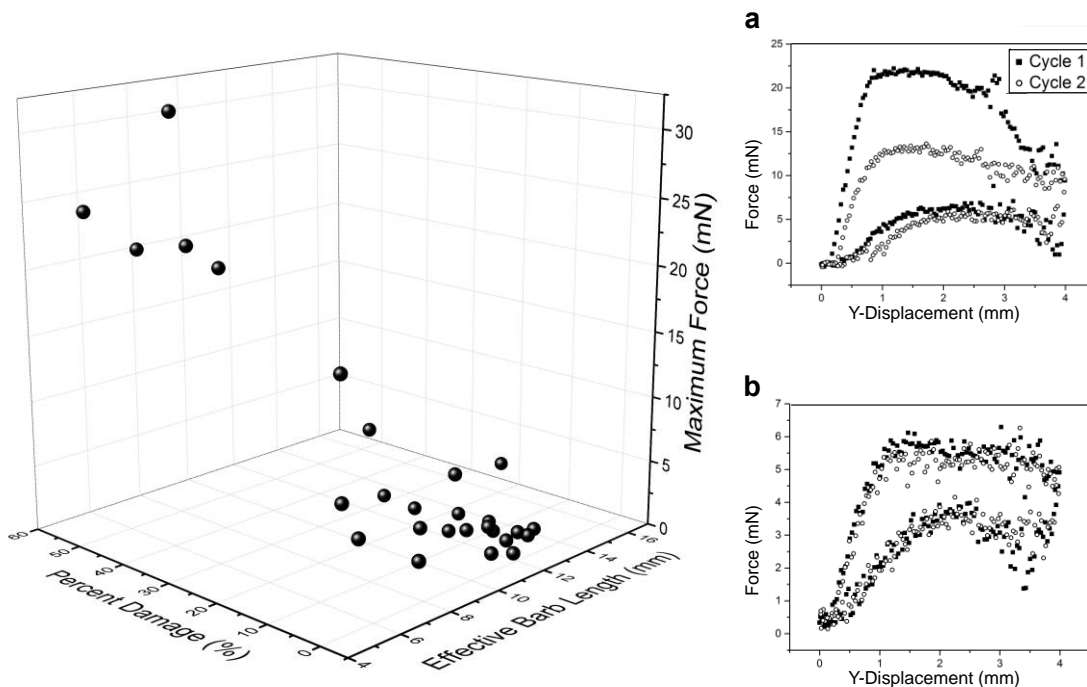


Figure 4.8 The repeatability of flexure tests: the maximum force and effective barb length are plotted against the percent damage between the first and second cycles. With shorter barbs there are higher resistive forces and stresses, therefore the percent damage increases. The insets show examples of force displacement curves for two cycles of loading and unloading of single barbs with (a) 40% (b) 7% damage.

4.4.3. Linear Deflection of Single Barbs

The slope of the linear portion of the first cycle of force versus deflection curves for experimental trials was plotted against the effective length of the samples in **Figure 4.8**. As expected by the classic cantilever equation, $Force/Deflection=(3*EI)/Length^3$, the force/deflection increases with a reduction in effective length. The average of the moments of inertia for the SEM images of the barb at the point of connection to the puck were taken and assumed to be a constant cross section for comparison to experimental data. Since the barbs are a tapered cross section with some variation in size, there is slight deviation from this trend.

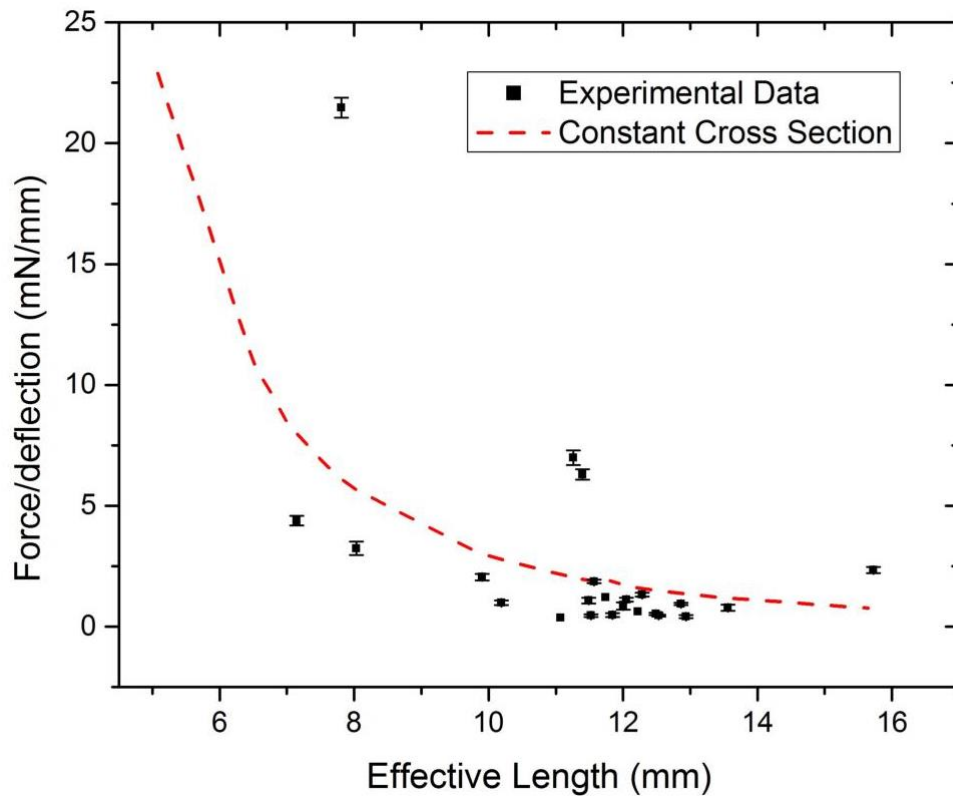


Figure 4.9 Experimental slope of force versus deflection: the slope of the linear portion of the first cycle of experimental trials versus the effective length of each sample. The slope of a barb with a constant cross section throughout its length is shown for comparison.

4.4.4. Comparison between the Experimental Results and Models

Since we observed a rapid decay for the values of area moments of inertia along the length of the barb, we were able to predict equivalent moments of inertia for all samples for which we had clear puck and effective length end images. We assumed an exponential decay correlation between the area moments of inertia of these two sections and integrated between the percentages of barb length to find an equivalent area moment of inertia representing the tapered structure. By injecting these values of moments of inertia into Equation (4.22), we were able to calculate an analytical force/deflection for experimental data. This is plotted with the experimental data as a histogram in **Figure 4.10**.

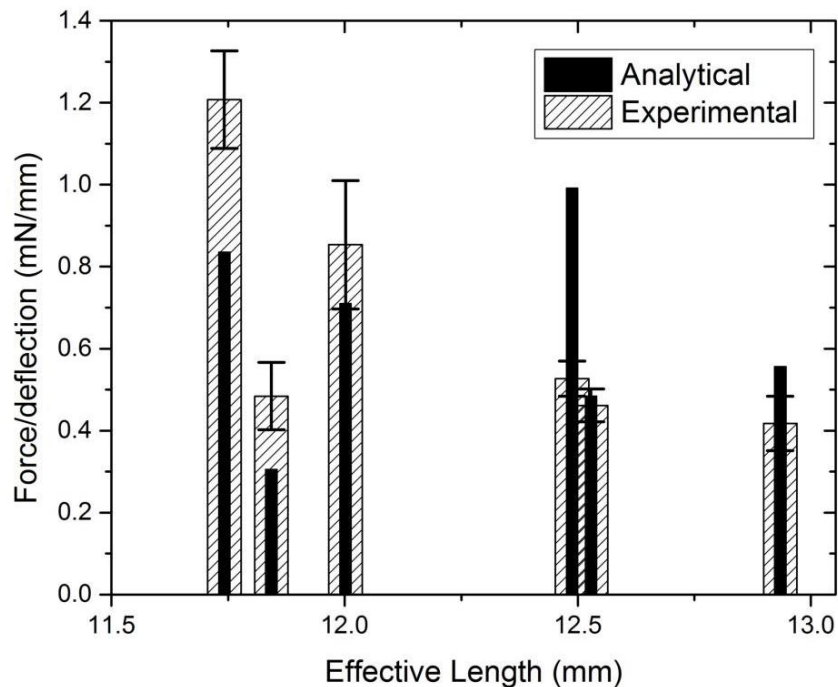


Figure 4.10 Comparison between the analytical and experimental force/deflection for the linear region of single barbs. Analytical calculations are based on the method described in section 4.3.3.

Images of the FEM simulation with the von Mises stresses plotted are shown in **Figure 4.11** at a prescribed displacement of 0.045mm. Near the side of the barb held in place, stresses are highest on the dorsal and ventral sides. Perhaps this further explains why cortex walls are thicker

on those sides. At the point at which the barb contacts the wedge, stresses are highest on the dorsal side at the foam-cortex interface due to compression.

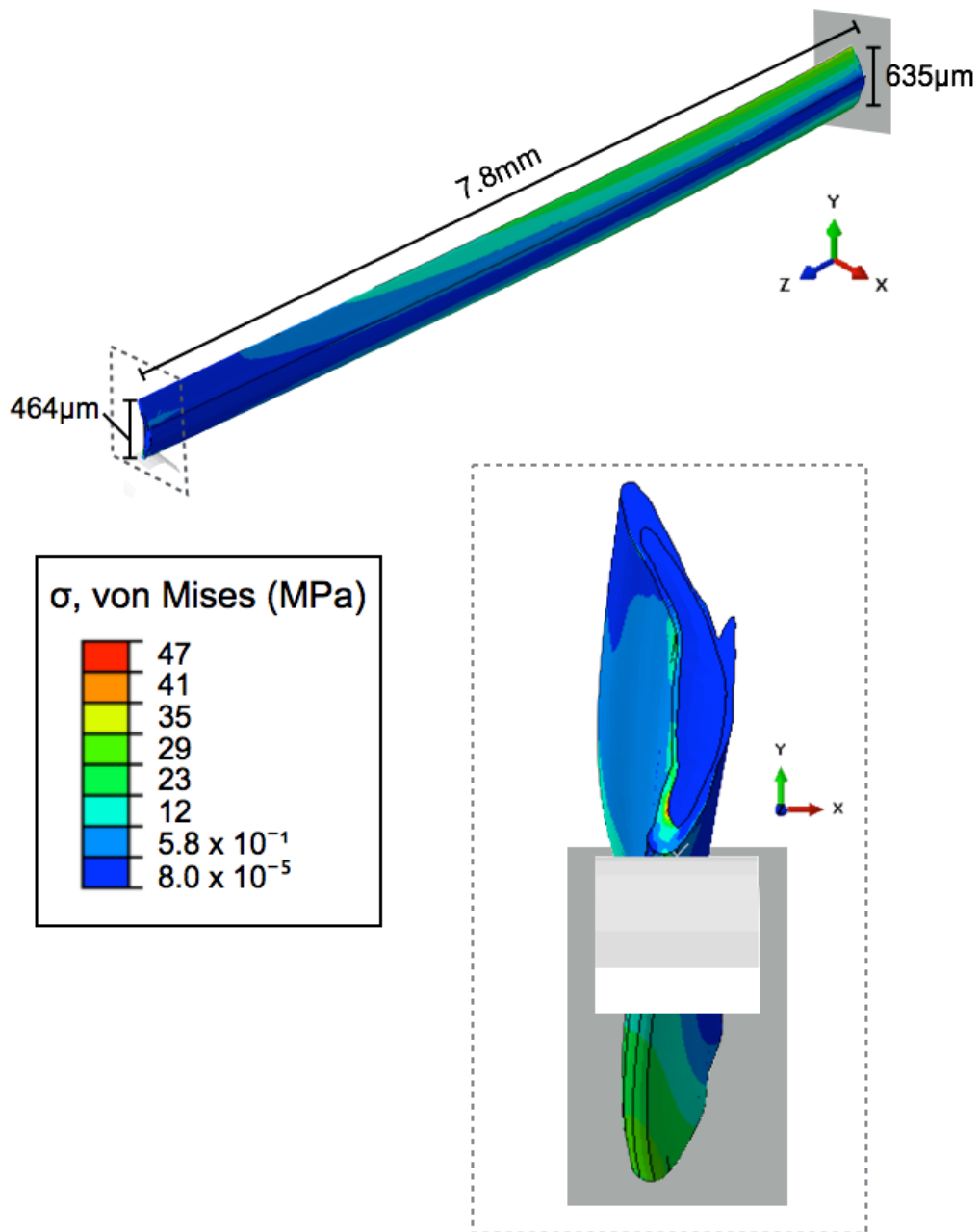


Figure 4.11 Finite element model of the deflected barb with the von Mises stress (MPa) plotted. Higher stresses appear on the dorsal and ventral sides of the end held in place and at the foam-cortex interface of the end contacting the wedge. This stress plotted corresponds to a prescribed displacement of 0.045mm. For better visualization the image is scaled by 100.

The simplified block model, analytical model, and FEM are compared with a sample's experimental data in **Figure 4.12**. As demonstrated in this figure, all models are in reasonable agreement with the data. The FEM simulations provide a method of justifying the experimental results by accounting for the complicated geometry and simulating experimental conditions to great detail. The analytical model allows us to compare our theory with multiple experimental data points with relative ease. Lastly, the simplified block model enables an improved understanding of the deflection and explains the structural response of barb deformation so that it might be applied to engineered synthetic structures.

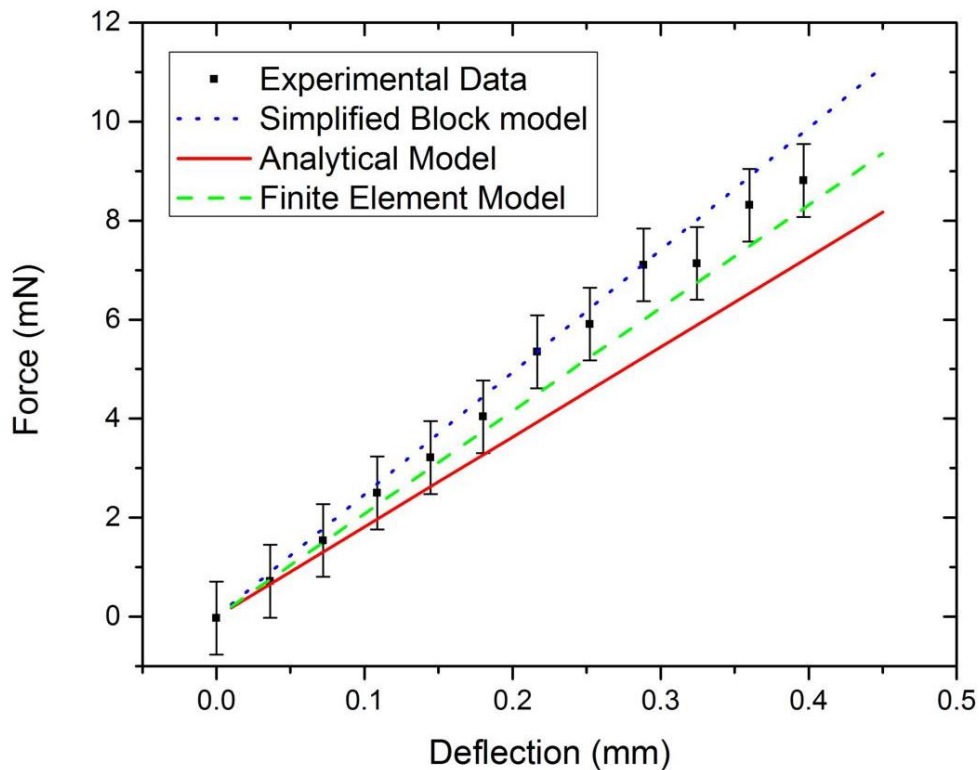


Figure 4.12 Comparison of the force versus deflection of an experimental run, a representative simplified block model, analytical model based on analysis presented in section 4.3.3, and finite element model described in section 4.3.4.

4.4.5. Deflection of Multiple Barbs

The linear region of the force-deflection curve describes flexure before the yielding of the structure. Experiments reveal that this region extends to a larger displacement for groups of four zipped barbs compared to single barb samples. The highlighted region of **Figure 4.13a,b** is the linear portion of four zipped barbs and single barb flexure test cycles, respectively. The arrowed line in each plot represents the y-displacement corresponding to the linear region, which we define as r . This value of r is plotted in **Figure 4.13c** against the effective barb length for four zipped barbs and single barb tests.

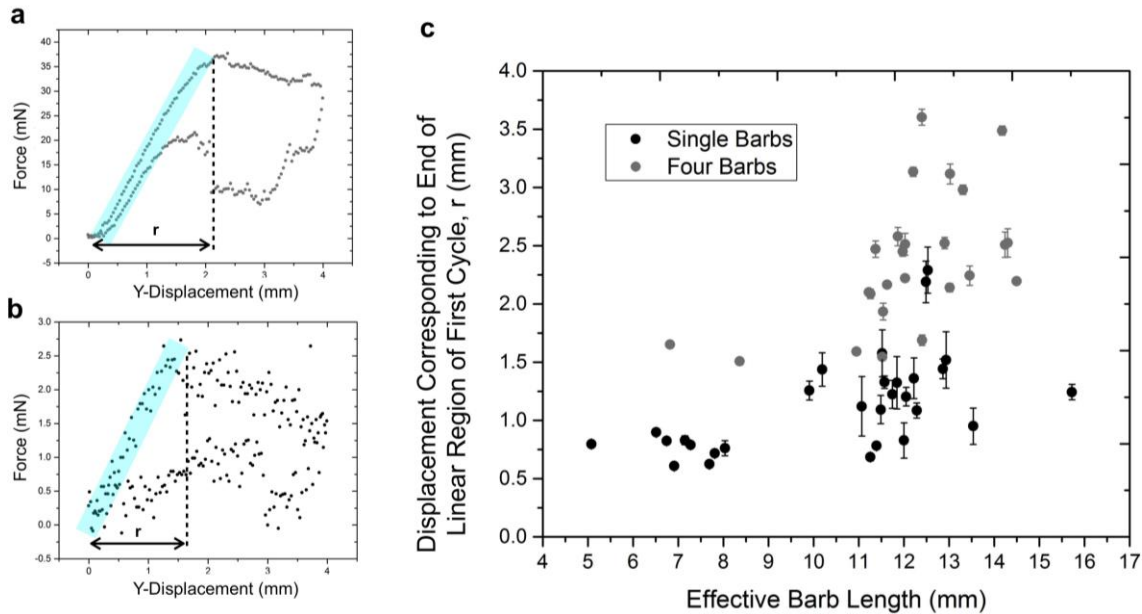


Figure 4.13 Yielding point of four-zipped barbs and single barbs: an example of the first cycle of flexure tests for (a) four-zipped barbs and (b) single barbs. The linear portion of the cycle to the point of yielding is highlighted. The arrowed line “ r ” shows the y-displacement corresponding to the end of the linear region. This displacement “ r ” is plotted against the effective barb length in (c) and indicates that four-zipped barbs are able to deflect to larger amount without yielding than single barbs.

Four zipped barbs are made more robust by the adhesion of the barbules to one another. This adhesion postpones the onset of barb twisting, thereby preventing the reduction in stiffness with respect to the y-axis, which results in yielding of the structure. This is consistent with visual

observations by Butler et al. [153], who stated that there is an increase in lateral stability when groups of barbs are attached to each other. The flexure behavior of the feather vane can therefore be tailored by the adhesive mechanism between barbs, allowing for a system that mitigates damage. For example, if a part of the feather vane is severely damaged, the total vane will not be compromised because the damaged portion will become detached as critically large loads are applied.

4.4.6. Strengthening Mechanisms of the Feather Vane

The adhesion mechanism that accounts for progressive deformation of the feather consists of the outward sliding of the barbules in the grooves of the juxtaposed barbs. As stated in the introduction, this mechanism is similar to a “Velcro” connection that allows neighboring barbules to hold (hook) barbs together. Hooklets on the distal barbules slide along the grooved proximal barbules, allowing barbs to move closer and further from each other. **Figure 4.14a** is a micrograph of the hooklet interlocking with a grooved proximal barbule, and **Figure 4.14b** shows a series of zipped barbule connections. Ideas from the feather vane mechanism can inspire new types of single-direction adhesives or lightweight, damage tolerant aerospace materials.

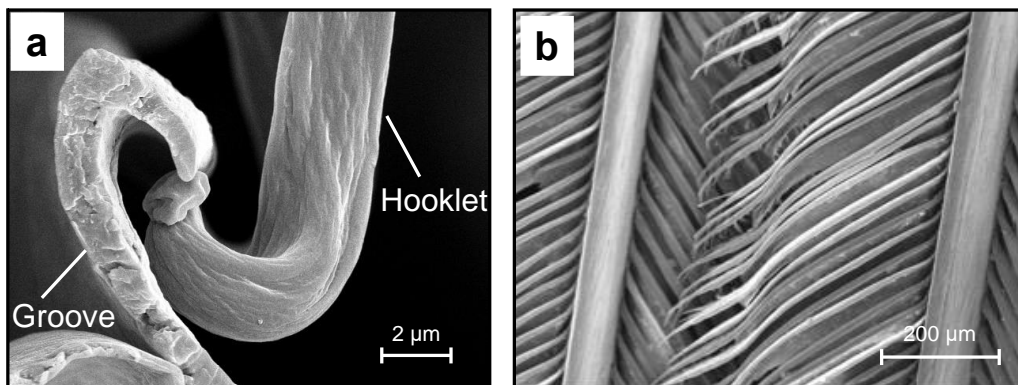


Figure 4.14 The interlocking structure of the barbules: micrographs of the House sparrow (*Passer domesticus*) show (a) the hooklet sliding into the grooved proximal barbule, (b) overlapping barbules within a feather.

4.5. Conclusions

The morphology of the feather vane was investigated and the flexural behavior of un-zipped and zipped barbs was quantitatively measured for the first time. The following significant enhancements of our understanding were accomplished:

- When loaded in cantilever orientation, un-zipped barbs deflect in the y-direction and then twist due to their asymmetry. By twisting the barb becomes less stiff with respect to its y-axis and therefore its maximum resistive force occurs before the maximum displacement of the barb.
- A finite element simulation, analytical model and a simplified block model were found to be in close agreement with experimental data.
- It was established experimentally that compared to un-zipped barbs, zipped barbs displace to a greater distance before yielding due to barbules which prevent barb rotation.
- A barbule-inspired interlocking mechanism is proposed and created through additive manufacturing.
- The insights obtained from this experimental study, along with the theoretical models and FEM, will be useful for creating a variety of bioinspired structures ranging from materials with a tailored stiffness to new adhesives.

4.6. Acknowledgements

Chapter 4, in full is published in *Acta Biomaterialia* and is authored by T.N. Sullivan, A. Pissarenko, S.A. Herrera, D. Kisailus, V.A. Lubarda and M.A. Meyers. The dissertation author was the primary investigator and author on this publication.

We would like to thank Andy Kietwong and Kyle Adriany for helpful discussion and Paulina Villegas and David Moncivais for image data gathering.

5. Feather Barbules

Barbules provide adhesion within the vane through an interlocking hook and groove mechanism to allow for the effective capture of air. This functional adhesive can reattach if structures unfasten from one another, preventing catastrophic damage of the vane. Here, using pelican primary feathers as a model material, we investigate the in-plane adhesion and stiffness of barbules. With guineafowl, pelican and dove feathers we determine the effect of barbules on the feather vane's ability to capture air. The vane is found to have directional permeability, and the effect of detaching barbules on the feather's competency is determined to be a function of barb dimensions. Barbules are underexplored structures imperative to the adeptness of the feather in flight with potential to provide bioinspired solutions to aerospace materials.

5.1. Introduction

Flight feathers have an architecture consisting of a main shaft (*rachis* and *calamus*), and a vane in which *barbs* branch from the rachis and *barbules* branch from barbs [26,75] (**Figure 5.1a**). Rigid barbs serve as the vane's backbone while barbules interlock, resulting in cohesion of the vane [149] (**Figure 5.3c**). On a given barb, proximal barbules are grooved while distal barbules have microhooks (hooklets) at their ends, adhering adjacent barbs [25,145] (**Figure 5.1b-e, 5.2**).

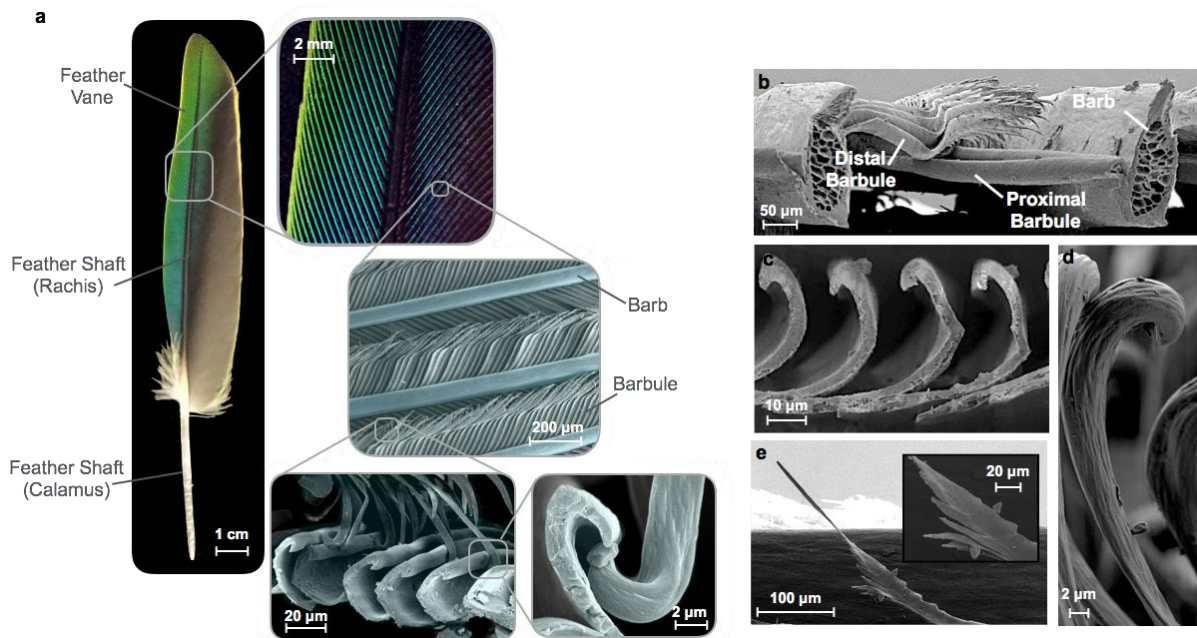


Figure 5.1 (a) Flight feathers are composed of a main shaft (rachis and calamus), barbs that branch from the rachis and barbules that stem from barbs. (b) Hooked, distal barbules branch from the left barb to interlock with the neighboring barb's grooved, proximal barbules. This allows neighboring barbs to adhere to one another and form a tightly woven material that traps air. (c) Grooved barbules are sliced to reveal their cross sections. (d) Micro-hooks (hooklets), such as the one pictured here, occur at the end of hooked barbules. In most bird species there are ridges at the ends of grooved barbules (e), possibly to increase friction. Figure 1a taken from [47], other figures taken from [155].

The sophisticated architecture of barbule adhesion evolved during the Late Jurassic period with the advancement of aerial locomotion [13]. These structures are capable of detaching (unzipping) and reattaching, thus preventing irreversible damage to the entire vane [146] (**Figure 5.3b**). The barbule is considered a fundamental element for bird flight because it allows the feather vane to capture air effectively, mitigates irremediable damage by permitting localized failure, and enables the repair of damaged areas through preening [6,147,148]. For these reasons, feathers are an advantageous material for the bird wing as opposed to a continuous structure, such as the bat's skin flaps (*patagium*) (**Figure 5.3a**).

Despite the importance of barbules to bird flight, they have been largely neglected from research, possibly due to their micro-scale dimensions. Kovalev et al. [146] investigated the

separation force of hooklets in swan (*Cygnus olor*) feathers and found they typically collectively separate at $\sim 0.27\text{mN}$. Additionally, despite a lack of experimental inquiry, many researchers assume that flight feathers are impervious to air [30,145] due the membranous flaps of barbules (**Figure 5.1c**) that overlap. A few published experiments report vaguely that there is a difference in feather transmissivity of 10-1000% [29,156] between the dorsal and ventral direction, due to barbules that act as one-way valves (V. Loughheed is cited by [156]). While these works are fundamental to understanding barbule adhesion and vane permeability, there is ample room for investigation.

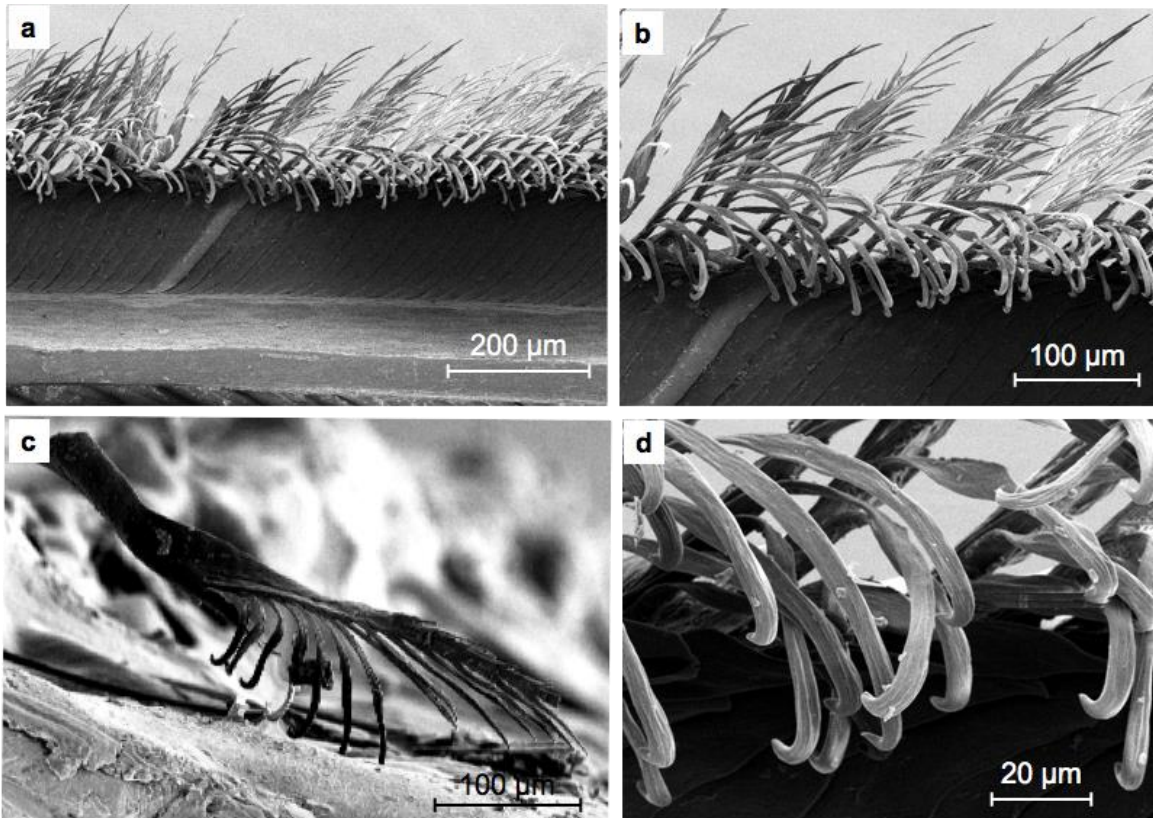


Figure 5.2 Hooked Barbule SEM images of the American white pelican (*Pelecanus erythrorhynchos*) demonstrate their abundance on each distal barbule.

Here we examine three aspects of the barbule, essential to the vane's function: 1) its adhesive properties, 2) stiffness, and 3) ability to capture air. We demonstrate that these three facets of barbules allow the feather vane to be a versatile material capable of maintaining lift while remaining flexible, and provide insight into specific features of barbules that are of high relevance to the feather's efficiency. Research in this area has the potential to lead to the fabrication of bioinspired control surfaces for enhanced performance of aerospace materials.

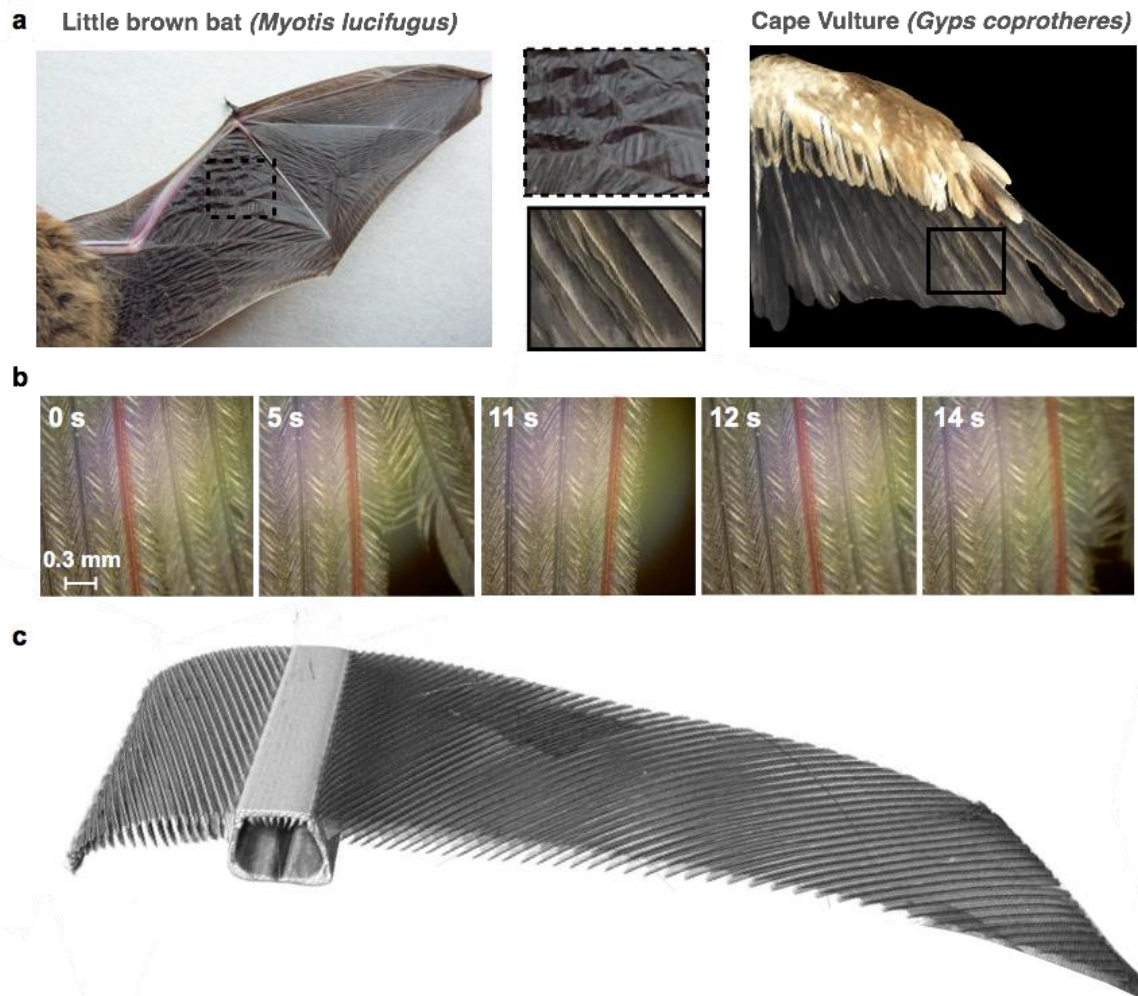


Figure 5.3 (a) Bat's wings are composed of continuous skin flaps (*patagium*) while the complex feathers of birds allow for localized failure. (b) One of the advantages of the feather vane is that it can be separated and reattached; images of the feather vane taken at various moments during unzipping and re-zipping. The vane begins in tact (0s), then begins to unzip (5s), becomes completely detached (11s), is released and returns back to its original position (12s), and is unzipped again (14s). A barb is highlighted in red to mark its position throughout the various frames. (c) A micro-computerized tomography (μ -CT) generated image of an Andean Condor (*Vultur gryphus*) feather shows the cohesion of the vane. Figure 5.3a left from Salix, Wikimedia commons (2011); Figure 5.3a right and 5.3b from [155], Figure 5.3c taken from [47].

5.2. Materials and Methods

5.2.1. Feather Samples

All feather samples used in experiments were wing flight feathers (*remiges*) obtained postmortem and stored in ambient conditions. The San Diego Natural History Museum provided American White Pelican (*Pelecanus erythrorhynchos*) feathers. San Diego Zoo provided the Bartlett's Bleeding Heart Dove (*Gallicolumba crinigera*) and Crested Guineafowl (*Guttera pucherani*) feathers. Feathers were obtained under our research group's Federal Fish and Wildlife permit.

5.2.2. Feather Vane Adhesion

The trailing vane of American White Pelican remiges were cut into rectangular pieces at ~50% of the shaft's length and secured to a stainless steel shim using epoxy. Each of the five samples tested had a width of 4-6 mm and length of 10-20 mm. The shim was clamped in a mechanical testing device and cut in its center just prior to testing (**Figure 5.4**). Tests were carried out in tension, with displacements applied perpendicular to the length of barbs at a strain rate of $3 \times 10^{-3} \text{ s}^{-1}$. Force was measured with a 250 g load cell, and displacement determined using a linear variable differential transformer. Experiments were done *in situ* with an optical microscope (objective of 2.5x) and images were analyzed using MATLAB (The Mathworks, Natick, MA, USA) software's image processing functions to track two rows of points at predetermined y-positions.

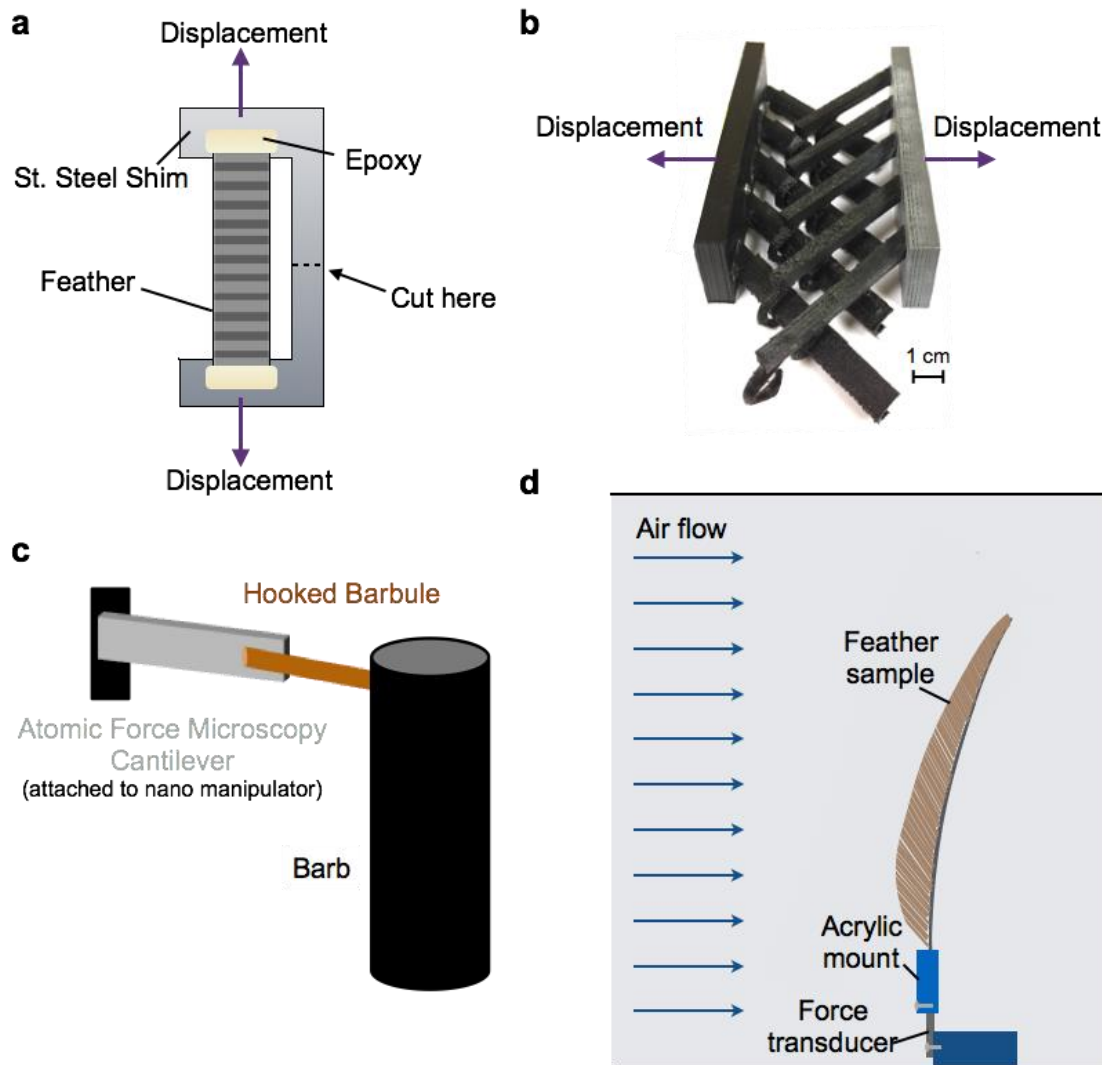


Figure 5.4 Schematics of various experiments: (a) experimental setup of feather vane tension tests; the darker lines within the feather represent barbs and lighter lines barbules. (b) Bioinspired interlocking barbules, with arrows showing directions of displacement in tension tests. (c) Atomic force microscopy (AFM) cantilever attached to the nano-manipulator, used to displace a single hooked barbule during *in situ* SEM flexure tests. (d) Wind tunnel experimental setup; the feather is subjected to ventral airflow. Figure taken from [155].

5.2.3. Barbule Flexure Tests

The American White Pelican distal barbule's out-of-plane stiffness was measured by *in situ* SEM. First, barbs from the trailing edge of remiges were cut off of the rachis at 20-50% of the feather shaft length (from the base). A single barb was then isolated and secured to a SEM stub

using conductive tape with the distal portion of the barb facing upwards. Following this, a nanomanipulator applied a prescribed displacement via an AFM cantilever to a single hooked barbule of the barb secured on the SEM stub (**Figure 5.4c**). These experiments were inspired by works of Naraghi et al. [157] and Roenbeck et al.[158], who did similar tests on inorganic materials.

A digital image correlation program in MATLAB was used to determine the displacement of the hooked barbule, and the barbule stiffness was calculated as follows. The bending of the AFM cantilever and barbule are analogous to springs in series:

$$\delta_{total} = \delta_{barbule} + \delta_{cantilever} \quad (5.1)$$

The total deflection (δ_{total}) was applied to the system through the nanomanipulator. The cantilever deflection ($\delta_{cantilever}$) was obtained directly from digital image correlation and therefore the barbule deflection ($\delta_{barbule}$) was determined. We use a force balance between the barbule and cantilever (Equation 5.2) to obtain an equation for the flexural stiffness of the barbule (Equation 5.3). The stiffness of the AFM cantilever (~0.58 N/m) can be estimated from geometry and materials properties (**Table 5.1**), so we are able to solve for the stiffness of the barbule.

$$F_{barbule} = F_{cantilever} \quad (5.2)$$

$$k_{barbule} = k_{cantilever} \times \delta_{cantilever} / \delta_{barbule} \quad (5.3)$$

However, as shown in the images from the test, the cantilever contacts the barbule at an angle (**Figure 5.5a**). Based on the angle theta (θ) the force component perpendicular to the barbule is computed and used to calculate the flexural stiffness of the barbule (0.061 N/m).

Table 5.1 Cantilever Stiffness Summary

Parameter	Value	Units
Elastic Modulus	169	GPa
Length	457.16	μm
Top Surface Width	49.09	μm
Bottom Surface Width	61.22	μm
Thickness	2.88	μm
Normal Stiffness	0.58	N/m

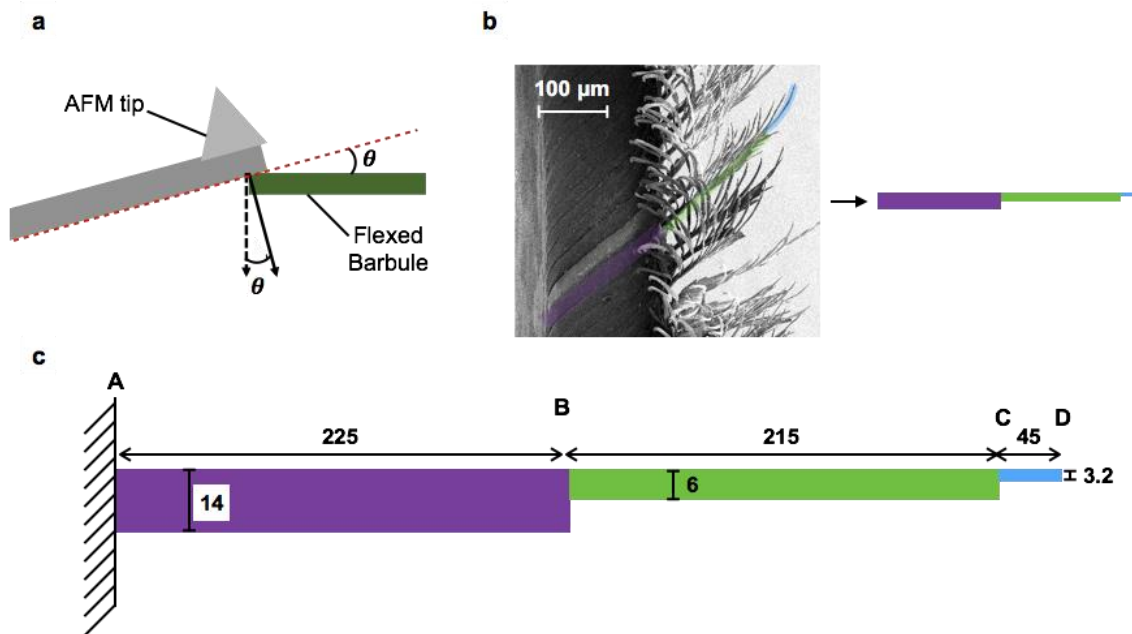


Figure 5.5 (a) The AFM cantilever contacts the barbule at angle θ to the normal; the dotted black line is the corrected force component. (b) The barbule structure is simplified into three sections (purple, green and blue). (c) The dimensions of the simplified barbule were found by averaging corresponding dimensions measured in SEM images. All dimensions are in microns. Figure from [155].

5.2.4. Wind Tunnel Test Specimens and Setup

Wind tunnel tests were conducted on remiges from Bartlett’s Bleeding Heart Dove, the American White Pelican, and the Crested Guineafowl. These three birds represent a wide variety of flying birds of various sizes, lifestyles and flight styles. Nearly all feathers were used in their entirety during tests, the exceptions being some Pelican feathers that were sliced from the base in order to properly fit in the wind tunnel.

A square wind tunnel with a height of 36 cm and a length of ~9 m was used in experiments. The wind tunnel was calibrated to determine the airspeed for each of its programmed power settings by inputting pitot tube measurements and the atmospheric air density into Bernoulli's equation. Following this, a force transducer (using load cell RB-Phi-203, $100 \text{ g} \pm 0.05 \text{ g}$) was fabricated, calibrated and mounted inside of the wind tunnel. Feather samples were secured in an acrylic mount attached firmly to the force transducer. For each test, the center of the feather shaft was marked and aligned with the center of the acrylic mount to ensure consistent directionality during tests.

Force measurements were made at airspeeds of 0, 6.91, 10.20, 13.50, 16.80 and 20.09 m/s. This range of airspeeds covered the approximate range of speeds that the feathers encounter in actual flight. The force of the acrylic mount with no feather sample was measured at each airspeed to normalize force readings of the sample data. Images of samples were taken during the tests using a camera mounted on the exterior of the wind tunnel. **Figure 5.4d** is a schematic of the placement of the force transducer and feather samples in the wind tunnel.

5.2.5. Wind Tunnel: Barbule Adhesion and Air Capture

For experiments testing the effect of unzipping in the wind tunnel, feather samples were placed unaltered into the acrylic mount with their ventral side facing the airflow; the force was measured at each airspeed. Following this, feathers were taken out of the mount, unzipped using a fine-tooth comb and tweezers, placed back in the wind tunnel, and re-tested. This was repeated once more with a more vigorous unzipping process. Three feathers from each species were tested. Images were taken before and after each unzipping process.

5.2.6. Wind Tunnel: Directional Permeability of the Vane

In experiments investigating the effect of the extended membranous "flaps" of barbules on the ability of the vane to capture air, the force of unaltered feather samples was measured first in

the ventral, then in the dorsal direction at each airspeed. Following this, each feather was lightly coated in SCIGRIP 66 Fast Set Flexible Vinyl Cement (SCIGRIP, Durham, NC, USA) which allowed the vane to remain flexible, yet sealed the flaps closed and prevented the vane from unzipping. After drying for at least 60 minutes, coated feathers were tested in the wind tunnel facing the airflow dorsally and then ventrally. The mass of feather samples was measured before and after the coating. Three feathers of each species were tested.

5.2.7. Barbule Characterization

Barbules of remiges from the American White Pelican (*Pelecanus erythrorhynchos*), Bartlett's Bleeding Heart Dove (*Gallicolumba crinigera*) and Crested Guineafowl (*Guttera pucherani*) were imaged using SEM. Sections of the vane were sliced with a razor blade at 50-60% of the total shaft length, and then sonicated in ethanol for a few minutes. Following this, they were air dried, mounted to an SEM stub and imaged. The dimensions of sections of the barbules were measured using the software ImageJ (National Institutes of Health, Bethesda, MD). All feather specimens were obtained from adult birds postmortem and stored at ambient conditions.

5.2.8. Statistical Analysis

A General Linear Model and Tukey's comparison test (95% confidence intervals) were used to compare results of unzipping experiments between bird species as well as the results of directional permeability tests. All statistical analyses were carried out using Minitab version 17.

5.3. Results and Discussion

5.3.1. Adhesion Within the Feather Vane

Adhesion within the pelican feather vane is investigated by applying in-plane tension to “unzip” a rectangular section of the vane separated from the shaft. As barbs rotate, hooks of distal barbules slide along the grooves of proximal barbules and then rapidly unhook and detach in

brittle-like separation (**Figure 5.6a**). Prior to failure, barbules maintain adhesion as barbs rotate uniformly in the proximal direction (**Figure 5.6b**).

Figure 5.7a schematically represents how samples were cut from the vane. These samples were then mounted as demonstrated in **Figure 5.4a** and the vane was pulled apart in tension, with the distributed force (w) applied perpendicular to barbs along the barb length (L) (**Figure 5.7b**). The corresponding force applied to a hooked or grooved barbule is $F = wd$ where d is the spacing between barbules (as shown in **Figure 5.7c**). A free body diagram containing one pair of barbules is shown in **Figure 5.7d**. In this diagram, the forces are in equilibrium:

$$\sum F = 0 \quad (5.4)$$

Next, we establish the summation of moments using point O as a basis, where counter clockwise rotation is assumed positive:

$$\sum M_O = F(L_h \cos \beta - L_g \cos \alpha) \quad (5.5)$$

where $\alpha = 17.9 \pm 2.0^\circ$, $\beta = 41.8 \pm 2.3^\circ$, $L_g = 603.2 \pm 8.6 \mu\text{m}$, and $L_h = 409.1 \pm 20.8 \mu\text{m}$.

Inserting these values into equation 5.5, we have:

$$\sum M_O = (-2.69 \times 10^{-4})F \quad Nm \quad (5.6)$$

Thus, there is a clockwise rotation (in the proximal direction) until total equilibrium is reached.

When connected to the shaft, however, the vane prefers to rotate distally due to the angle at which barbs branch from the rachis [159]. This difference in rotational preference between the hierarchical levels of the feather is thought to help maintain the area of the vane; if both barbs and barbules favored distal rotation, the vane would easily collapse. Similar geometric differences between hooked and grooved barbules are evident in many other flying birds such as the

guineafowl and the dove, indicating that the attachment behavior witnessed here is not specific to the pelican feather.

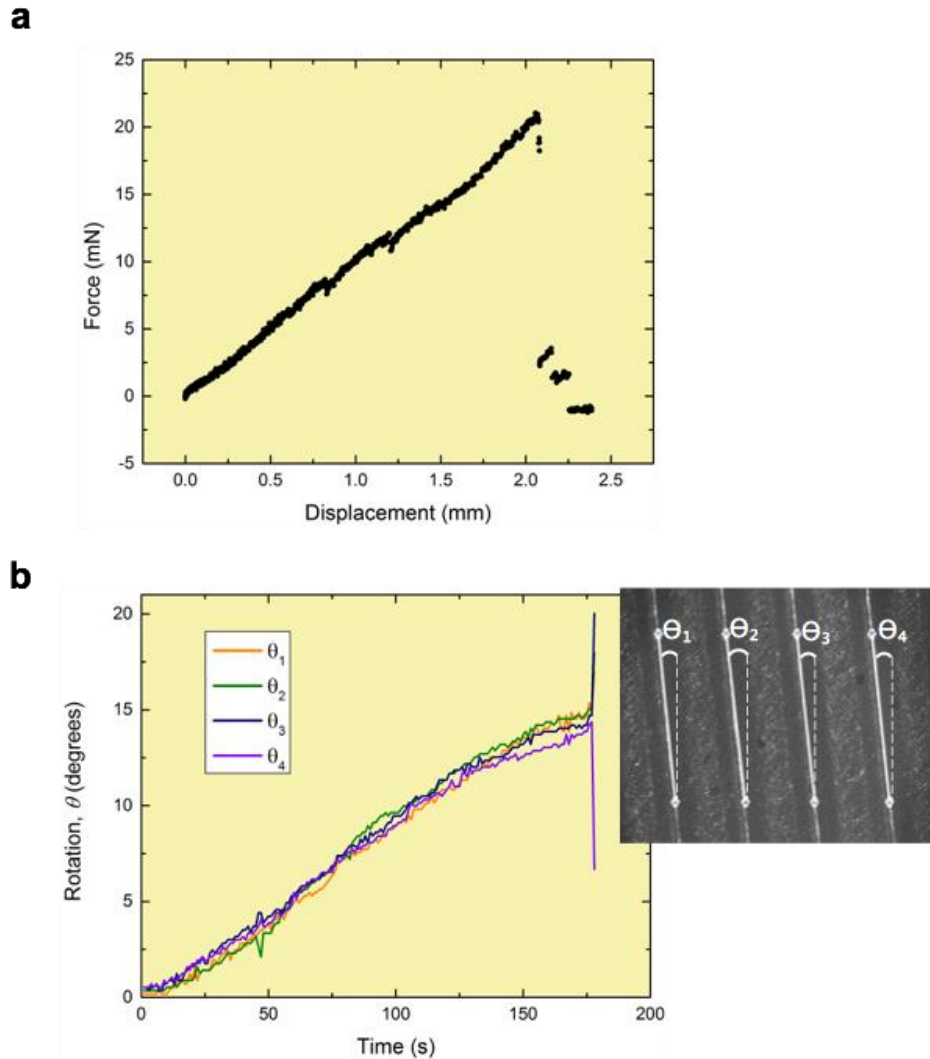


Figure 5.6 In-plane tension tests of the pelican feather vane: (a) An example plot of the measured force vs. displacement reveals that on the macro-scale pelican feathers exhibit brittle-like failure when unzipped. (b) Before failure, barbules maintain attachment as barbs rotate proximally at angle θ throughout the test. This angle is shown in the optical microscope image (b, right) where dashed lines mark the original position of the barbs, and the solid white lines trace the ending position of barbs. Figure taken from [155].

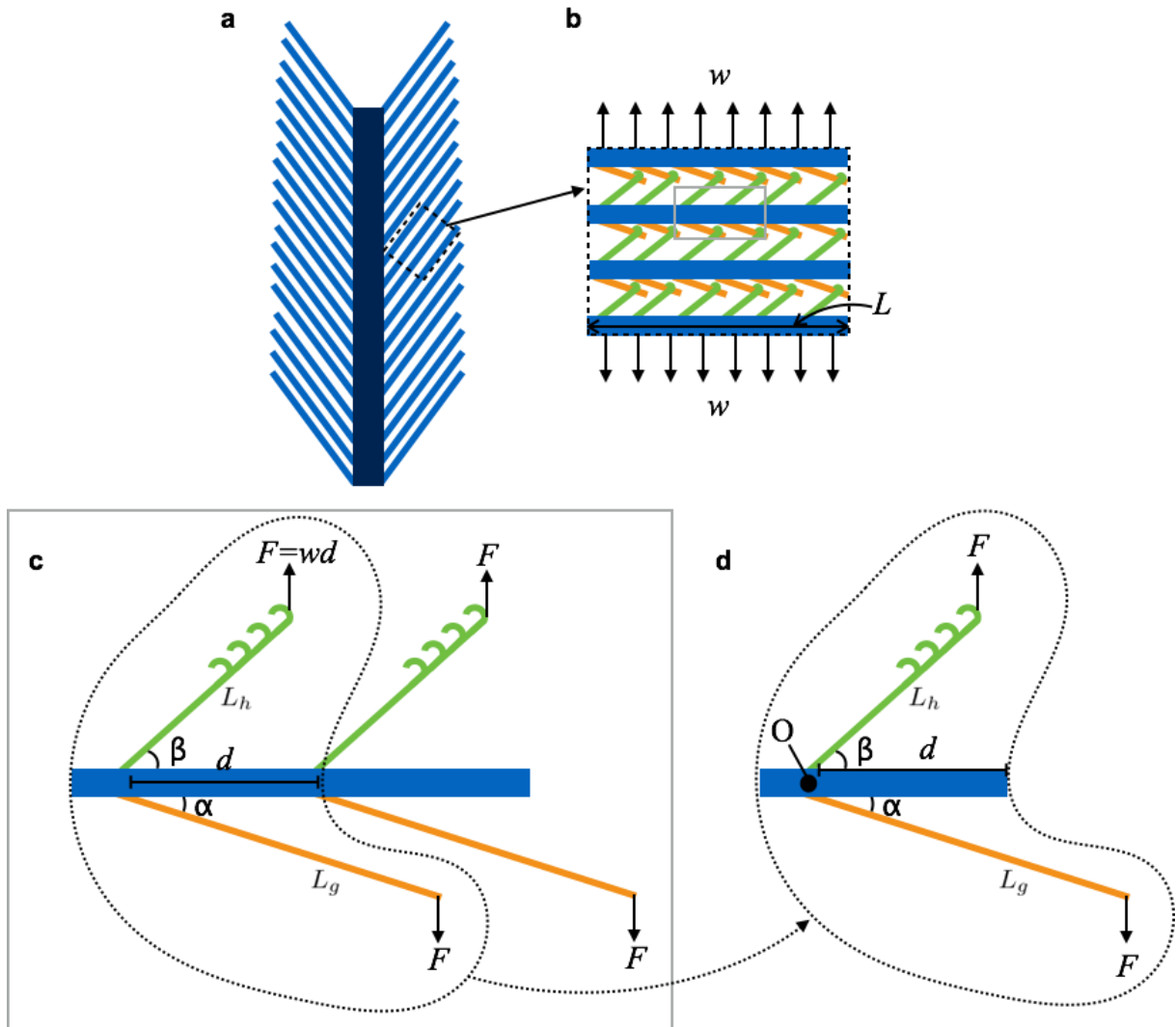


Figure 5.7 Schematic of the lengths and angles of the hooked barbule (L_h , β) and grooved barbule (L_g , α) from in-plane adhesion experiments: (a) A rectangular section of the feather vane is sliced. This rectangular section is mounted as shown in Figure 5.4a and pulled apart in tension with barbs secured perpendicular to the direction of the applied force, where L is the length of barbs (b). (c) A closer view of a single barb and two pairs of hooked and grooved barbules, demonstrating the force applied to a single hook or groove is F which is equal to the distributed load w multiplied by the distance d between hooks and grooves. (d) A free body diagram is drawn describing the force applied to a single hook or groove. While the sum of forces is equal to zero, the sum of moments is not equal to zero (see Equations 5.4-5.6).

Modelling the detachment of a single hooklet is a very complex problem, and an accurate solution may require the use of finite elements. As depicted in **Figure 5.8**, a load (P) is applied to the end of the hook (segment 2), which causes both it and the longer beam (segment 1) to undergo large deflections (**Figure 5.8b**). The large deflection of both segments 1 and 2 results in the detachment of the hooklet from the groove.

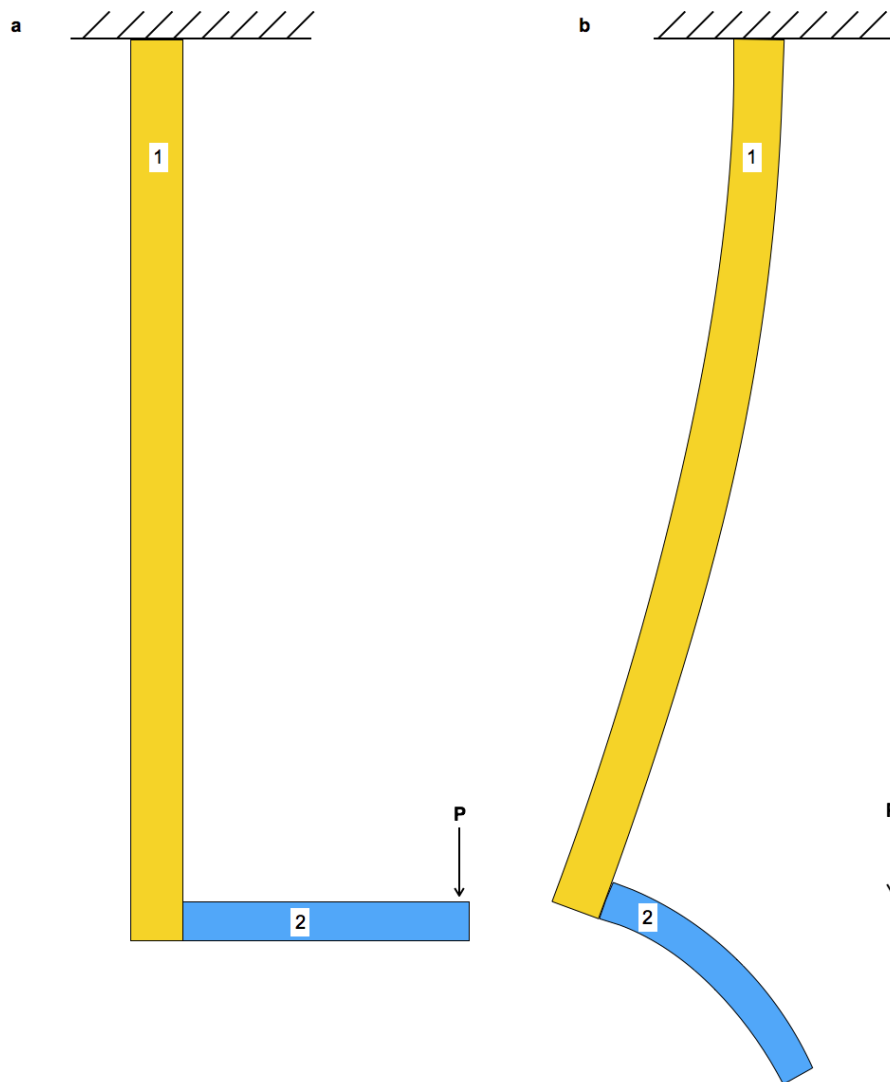


Figure 5.8 (a) The simplified hooklet is shown with an applied load P at the end of segment 2. (b) Both the long and short segments (1 and 2) of the hooklet are expected to undergo large deflections with the application of load P . An accurate solution to this problem would likely require the use of finite elements.

For large deflections, such as the deflections demonstrated in both segments 1 and 2 in **Figure 5.8b**, the exact differential equation of the deflection curve must be used, which assumes the beam material remains linearly elastic[160]:

$$\kappa = \frac{d\theta}{ds} = -\frac{M}{EI} \quad (5.7)$$

where $d\theta/ds$ is the curvature of the beam, or the rate of change of the angle of rotation of the deflection curve (θ) with respect to the distance measured along the curve (s). In the case of large deflections, simplifications cannot be applied to this equation, and therefore Equation 5.7 must be solved for using the exact expression for curvature[160]:

$$\frac{\frac{d^2v}{dx^2}}{\left[1+\left(\frac{dv}{dx}\right)^2\right]^{3/2}} = -\frac{M}{EI} \quad (5.8)$$

Experimentally the detachment of barbules involves large deflections (segments 1 and 2). For simplification purposes and a first approximation, we assume segment 1 to be rigid. We create a simplified model (**Figure 5.9**) to approximate the detachment of a single hooklet from a groove. Therefore, we can represent segment 2 as a cantilever beam which undergoes large deflections with the applied load (P) (**Figure 5.9b**). The dimensions used in calculations were approximately based on scanning electron microscope images and are listed in Table 5.2, where segment 2 is assumed to be a cylindrical beam with diameter t_2 .

The cantilever beam AB representing segment 2 (**Figure 5.9b**) is subject to a load P at its end which results in the displacement of point B to B'. The angle of rotation of the end of the beam is represented by θ_b , and the horizontal and vertical displacements are δ_h and δ_v . The length of beam AB' is assumed to be equal to the initial length L_2 , following the assumptions of Gere and Timoshenko [160] that axial changes due to direct tension are disregarded. The solution

to determine the angle θ_b for large deflections of a cantilever beam is presented by Gere and Timoshenko [160] as:

$$F(k) - F(k, \phi) = \sqrt{\frac{PL_2^2}{EI}} \quad (5.9)$$

where terms in Equation 5.9 are defined as [160]:

$$k = \sqrt{\frac{1 + \sin \theta_b}{2}} \quad (5.10)$$

$$\phi = \arcsin \frac{1}{k\sqrt{2}} \quad (5.11)$$

$F(k)$ is a complete integral of the first kind:

$$F(k) = \int_0^{\pi/2} \frac{dt}{\sqrt{1 - k^2 \sin^2 t}} \quad (5.12)$$

$F(k, \phi)$ is an incomplete integral of the first kind:

$$F(k, \phi) = \int_0^{\phi} \frac{dt}{\sqrt{1 - k^2 \sin^2 t}} \quad (5.13)$$

These equations are solved numerically, assuming that θ_b falls within 0° and 90° . One subsequently finds k from Equation 5.10, $F(k)$ from Equation 5.12, calculating ϕ from Equation 5.11, and using k and ϕ to find $F(k, \phi)$ from Equation 5.13, which is then used to calculate load P from Equation 5.9.

If we assume that the angle θ_b for the deflection of beam AB (segment 2) is 45° , we can use the table of values presented in [160] which are adapted from [161]. This table shows that for an angle of 45° :

$$\frac{PL_2^2}{EI_2} \approx 2 \quad (5.14)$$

Therefore, we can solve for P by inserting values for L_2 , E and I_2 presented in Table 5.2, where the area moment of inertia I_2 is calculated assuming a circular shape with a radius equal to $t_2/2$. This results in a calculated force (P) for the separation of a hook equal to 0.049 mN.

Table 5.2 Values used to determine the force necessary for a deflection of θ_b of 45°. Values are used in Equations 5.7-5.23.

Variable	Definition	Value
L_1	Length of first segment of hook	100 μm
L_2	Length of second segment of hook	30 μm
t_1	Thickness of first segment of hook	4 μm
t_2	Thickness of second segment of hook	3 μm
E	Elastic modulus of hook, value from Bachmann, et al. [71]	5.5 GPa
I_1	Moment of inertia of segment 1	$1.25 \times 10^{-23} \text{ m}^4$
I_2	Moment of inertia of segment 2	$3.98 \times 10^{-24} \text{ m}^4$
E_{modulus}	Elastic modulus of hook, value from Bachmann, et al. [71]	5.5 GPa
M_1	Moment of beam L_1	$F^*(28 \times 10^{-6}) \text{ Nm}$
M_2	Moment of beam L_2	$F(28 \times 10^{-6}) \text{ Nm}$
E_{hook}	Calculated energy required to detach a single hook	$5.2 \times 10^{-10} \text{ Nm}$
ΔW	Total amount of work in the experiment	$2.0 \times 10^{-5} \text{ Nm}$
$n_{\text{hooked interface}}$	Total number of hooked connections per barb interface	792
$W_{\text{barb interface}}$	Work per barb interface	$1.25 \times 10^{-6} \text{ Nm}$
W_{hook}	Work of a single hooked connection	$1.58 \times 10^{-9} \text{ Nm}$

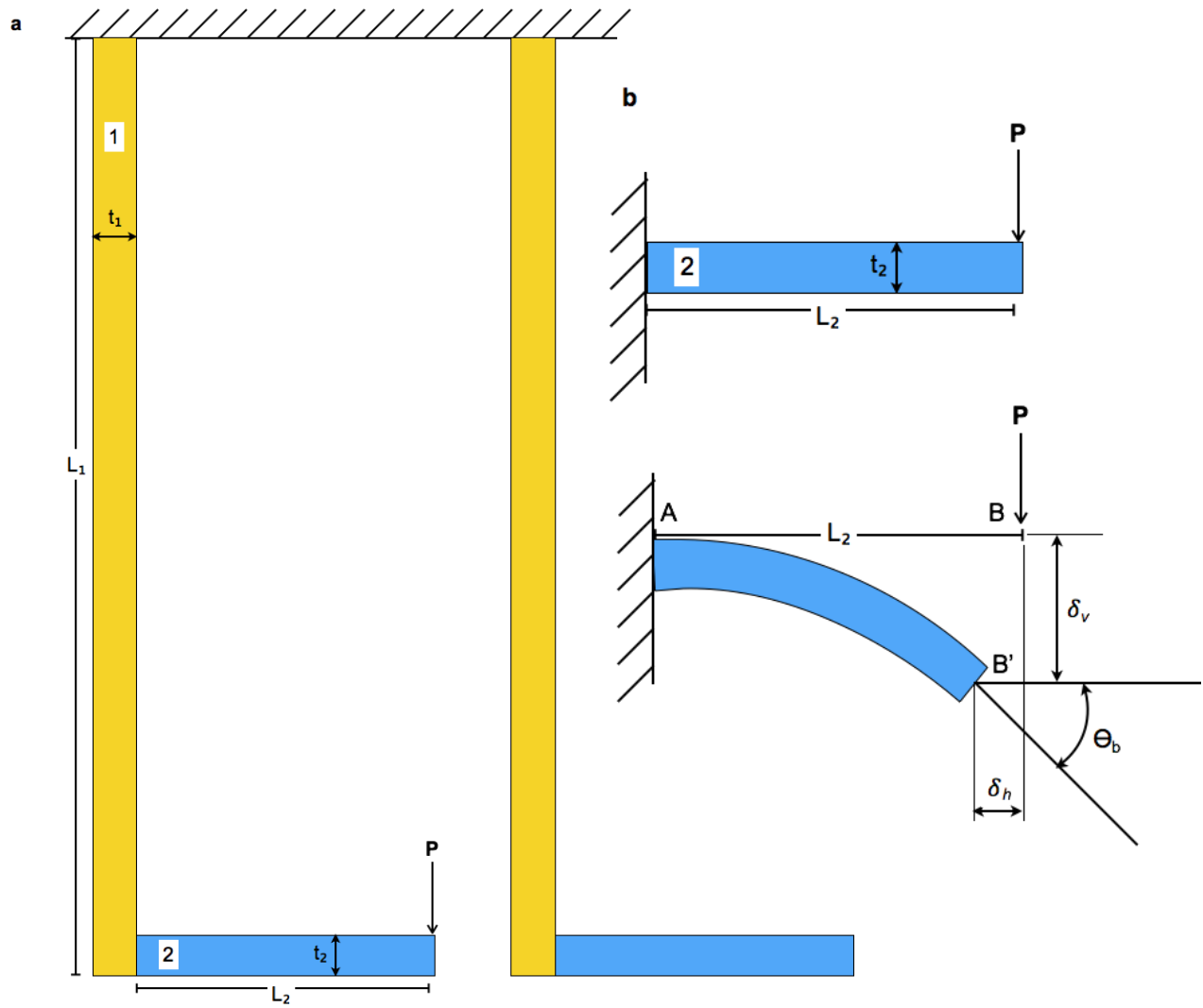


Figure 5.9 (a) Schematic of the idealized microhook used in calculations, where dimensions are listed in Table 5.2. (b) Because segment 1 is assumed to be rigid, segment 2 is configured as a cantilever beam that undergoes large deflections. Terms are defined in section 5.3.1.

To compare the above results (which account for the large deflection of the smaller beam segment) with solutions following simplifications used in expressions for small deflections, we present another model based on Meyers and Chen, 2014 [1], which was originally used to calculate the separation force of VELCRO hooks. First, barbule microhooks are simplified and idealized as

shown previously in **Figure 5.9a**. We assume that the hook will detach by slipping-off of the groove when segments 1 and 2 deflect a total of 90°:

$$\theta = \theta_1 + \theta_2 = \frac{\pi}{2} \quad (5.15)$$

where angles θ_1 and θ_2 are given in **Figure 10**. The beams L_1 and L_2 are subjected to bending moments due to a force F . Moment (M_1) for beam L_1 is given by:

$$M_1 = F \left[L_2 - \left(\frac{t_1}{2} \right) \right]. \quad (5.16)$$

Similarly, the moment (M_2) for beam L_2 is:

$$M_2 = F \left[L_2 - \left(\frac{t_1}{2} \right) \right]. \quad (5.17)$$

The beam deflections v are related to the angle θ by:

$$\theta = \frac{dv}{dx} = \frac{M}{EI} x \quad (5.18)$$

Substituting equations 5.15, 5.16 and 5.17 into equation 5.18, we have:

$$\theta_1 + \theta_2 = \frac{M_1}{EI_1} L_1 + \frac{2M_2}{EI_2} L_2 = \frac{\pi}{2} \quad (5.19)$$

where the cross sections of the hook are assumed to be circular with the radius being half of the hook's thickness. The resulting moments of inertia are listed in **Table 5.2**. The calculated force of separation per hook is found to be 0.013 mN. It is important to note that while this model takes into account the flexure of both segments of the hook, the simplification of this problem to use the small deflection equation is incorrect.

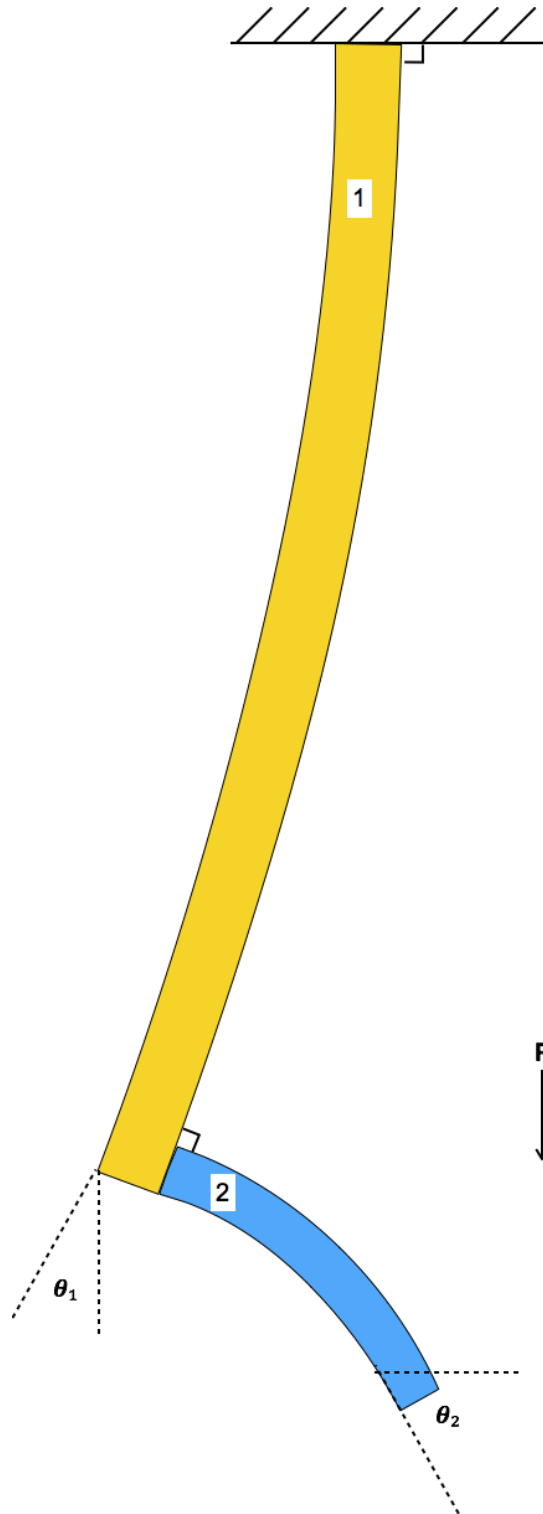


Figure 5.10 (a) Schematic of the idealized microhook used in calculations. (b) The definition of θ_1 and θ_2 are obtained when both segments 1 and 2 undergo large deflections.

Following this, the energy required for the separation of a single hooked connection (E_{hook}) is estimated. We use our model describing the large deflection of segment 2 of the hook, and assume the maximum deflection is $\theta_b = 45^\circ$ at pull-off. Considering the material to be linear elastic with a straight force-deflection curve we have:

$$E_{hook} = \frac{1}{2}FL_2\sin(\pi/4) \quad (5.20)$$

Using the data plotted in **Figure 5.6a**, we obtain the work (ΔW) of deformation for the entire specimen by integrating under the curve. Since there are a total of 16 barb interfaces in the sample, and only one interface where failure occurs, we determine the work per barb interface ($W_{barb\ interface}$):

$$W_{barb\ interface} = \frac{\Delta W}{16} \quad (5.21)$$

Through measuring scanning electron micrographs, we estimate that there are an average of 6 barbules per 100 μm of barb length. Because each barb within the sample is 4.4 mm in length, there are an estimated 264 hooked barbules along each barb interface. Each hooked barbule however, is estimated to have three microhooks that engage and interlock with grooves. Therefore, there are an approximated 792 successful hooked connections ($n_{hooked\ interface}$) per interface. To determine the amount of work per hooked connection (W_{hook}), the work for a single barb interface ($W_{barb\ interface}$) is divided by the number of hooked connections per interface ($n_{hooked\ interface}$) to obtain:

$$W_{hook} = \frac{W_{barb\ interface}}{n_{hooked\ interface}} \quad (5.22)$$

Finally, the first law of thermodynamics is used to relate the work and energy of a single hooked connection, where we neglect the heat term:

$$W_{hook} = E_{hook} \quad (5.23)$$

We find that W_{hook} (1.58×10^{-9} Nm) is an order of magnitude different from E_{hook} (5.2×10^{-10} Nm). The difference in these values is likely due to the assumption segment 1 is rigid, the simplification of the hook shape and dimensions, and not considering other factors such as sliding of hooks in grooves, stored elastic energy due to flexure of barbules, or angular differences between forces. However, this first attempt in solving for the force required to detach barbules demonstrates an initial approach in simplifying this complex problem into an intelligible process. We highly recommend future work be done to more accurately describe the force required to detach a single hooklet, possibly through finite element simulations.

5.3.2. Barbule Flexure

Since barbules are the least rigid component of the feather vane, their stiffness is an integral part of the vane's critical "unzipping" mechanism. A method for measuring the stiffness of barbules is developed through *in-situ* scanning electron microscopy (SEM) experiments in which an atomic force microscopy (AFM) tip connected to a nano-manipulator displaces a single barbule (**Figure 5.4c**). Critical snapshots from *in-situ* SEM experiments are shown in **Figure 5.11a**. The flexural stiffness of a single hooked Pelican barbule was experimentally measured to be 0.061 N/m.

To confirm that the entire length of the barbule was deflected in experiments, we calculate a simplified theoretical flexural stiffness of the barbule using dimensions from SEM characterization. The hooked barbule is modeled as three connected cylindrical sections with different diameters and lengths (**Figure 5.5b**). Using the dimensions in **Figure 5.5c**, the stiffness of the simplified cantilever is calculated by finding the area moments of inertia of the cylinders and converting them to be a function of the area moment of inertia of section C through D. These are then inserted into Equation 5.24 along with the accepted value of the Elastic modulus for

flexure of the rachis cortex (5.5 GPa)[71]. This value is used because the Elastic modulus of the barbule is unknown.

$$\delta = \int_0^{Length} \frac{M}{EI_{total}} dx = \int_C^D \frac{M(x)}{EI_{CD}} dx + \int_B^C \frac{M(x)}{12.4 EI_{CD}} dx + \int_A^B \frac{M(x)}{367 EI_{CD}} dx \quad (5.24)$$

Through this method, we find that the stiffness of the barbule is 0.048 N/m. Since this highly simplified estimate is within 20% of the experimental value (0.061 N/m), the viability of this method is confirmed. Although the stiffness measured in this experiment is specific to a hooked pelican barbule (since barbule length[47] and cross section vary among birds) the results can be used to determine an order of magnitude of barbule stiffness for these structures, as this is the first time barbule stiffness has been measured.

In flight, forces due to airflow cause barbules to first deflect and then slide along one another until they rapidly detach. It is hypothesized, therefore, that a stiffer barbule will allow the vane to handle larger out-of-plane forces before unzipping. This in turn would increase the vane's capacity for loading before local failure, and thus impact the maximum force the vane could sustain in flight. Barbule stiffness can be used in conjunction with future work to relate the in-plane adhesive properties to the out-of-plane forces of flight.

5.3.3. Barbule Adhesion and the Feather's Ability to Capture Air

The significance of barbule adhesion to the feather's ability to capture air is measured in wind tunnel experiments. In these tests, the drag force is compared between intact feathers and unzipped feathers, where barbules are disengaged. Experiments reveal that the drag force of the feather decreases as the percentage of unzipped barbs within the vane increases. This effect is magnified at higher airspeeds (**Figure 5.11b,c**). The drag force [162],

$$F_{drag} = \frac{1}{2} \rho u^2 c_D A, \quad (5.25)$$

is comprised of several factors: ρ is air density, u is the speed of the feather relative to the air, C_D is the drag coefficient of the feather, and A is the orthographic projected area of the vane onto a plane perpendicular to the flow. Due to its flexible nature, as air velocity increases the force on the feather vane causes barbs to deflect away from airflow. When deflected to an extreme the projected area of the vane (A) becomes smaller than its original size, subsequently decreasing the drag force (F_{drag}). Since unzipped barbs are less restricted in movement [77], this deflection occurs at a lower velocity for unzipped barbs than zipped barbs. In these experiments, a larger drag force corresponds to a vane that is able to capture air more effectively.

While feathers from all three birds studied here (dove, pelican, and guineafowl) demonstrate a decrease in drag force with an increase in percent of unzipped barbs, each exhibits this at a different magnitude. **Figure 5.11c** displays the absolute value of the slope of force versus the percent of vane unzipped. The guineafowl feather consistently has the highest slope value, meaning that it is most dramatically effected by unzipping, while the dove feather has the lowest slope value, being the least effected by unzipping. This is again related to the drag equation: the guineafowl has long, narrow barbs (**Figure 5.11d**) that deflect relatively easier, reducing the vane's drag force to a greater extent than the other species' feathers (as demonstrated through Tukey's comparison test). The dove feather however, has thicker, stiffer barbs (**Figure 5.11d**) making deflection difficult and therefore maintaining a similar projected area whether or not the vane is unzipped. Perhaps this is an evolutionary reflection of the flight style of each bird; both the dove and pelican rely on flight as their primary mode of locomotion, whereas guineafowl mainly run with only occasional flight. Consequentially, a reduction in ability to capture air would arguably be more detrimental to the dove and pelican's survival than the guineafowl.

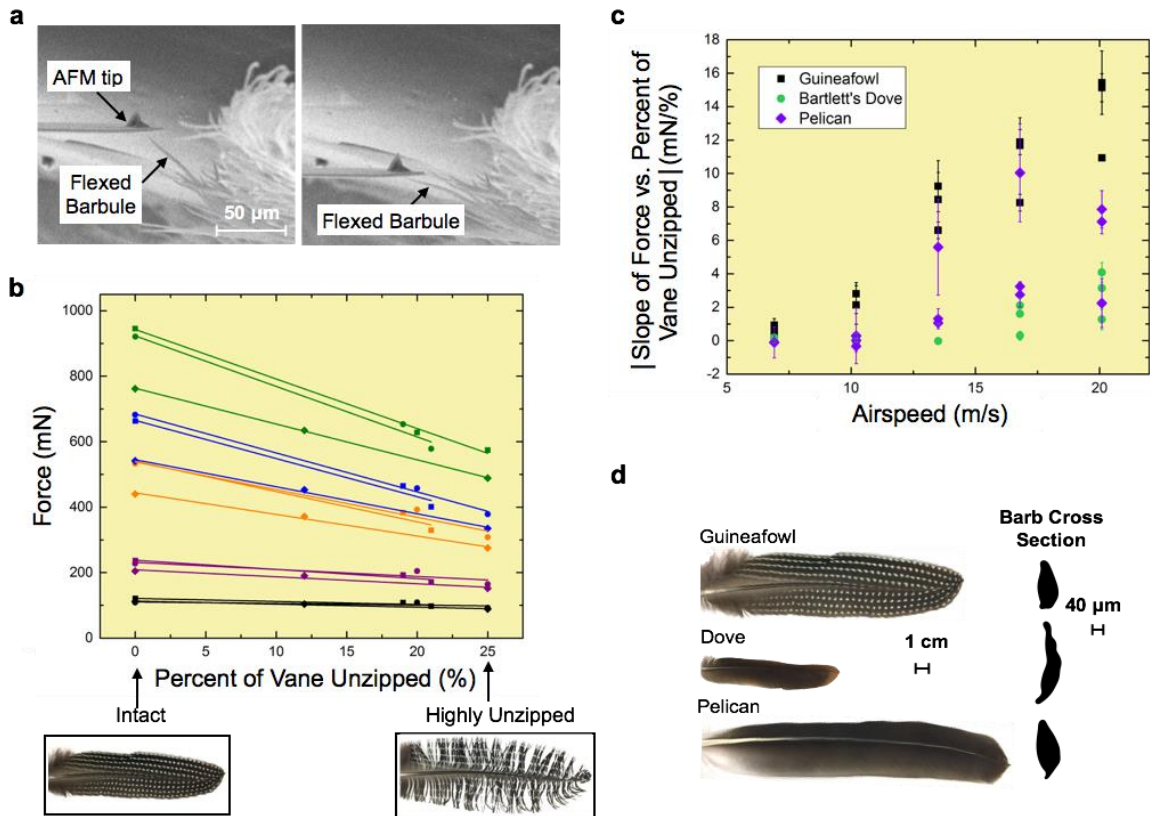


Figure 5.11 (a) Critical snapshots of the barbule during *in situ* SEM flexure experiments: (left) at the initial position immediately before contact, (right) at the maximum load, just before separation. (b) Force versus percent of the vane unzipped for the guineafowl feather. Colors correspond to the airspeed feathers were tested at: black is 6.91m/s, purple is 10.20m/s, orange is 13.50 m/s, blue is 16.80 m/s, and green is 20.09m/s. Images are examples of the guineafowl feather intact and highly unzipped. (c) The absolute value of the slope of force versus percent of vane unzipped is plotted against airspeed. The guineafowl consistently has the highest slope, meaning that it is most effected by unzipping. (d) Dimensions of each species' feather barbs relate to the effect of unzipping. Figure from [155].

5.3.4. Directional Permeability of the Feather Vane

Not only do barbules provide adhesion to allow barbs to trap air effectively, they are hypothesized to capture air via thin, overlapping, membranous side flaps. These flaps (**Figure 5.12a**) appear as one-way valves, impermeable to air flow in the ventral direction but not in the dorsal direction. An additively manufactured model conceptually demonstrates this in **Figure 5.12b,c**: with dorsal airflow the flaps open and with ventral airflow flaps remain closed.

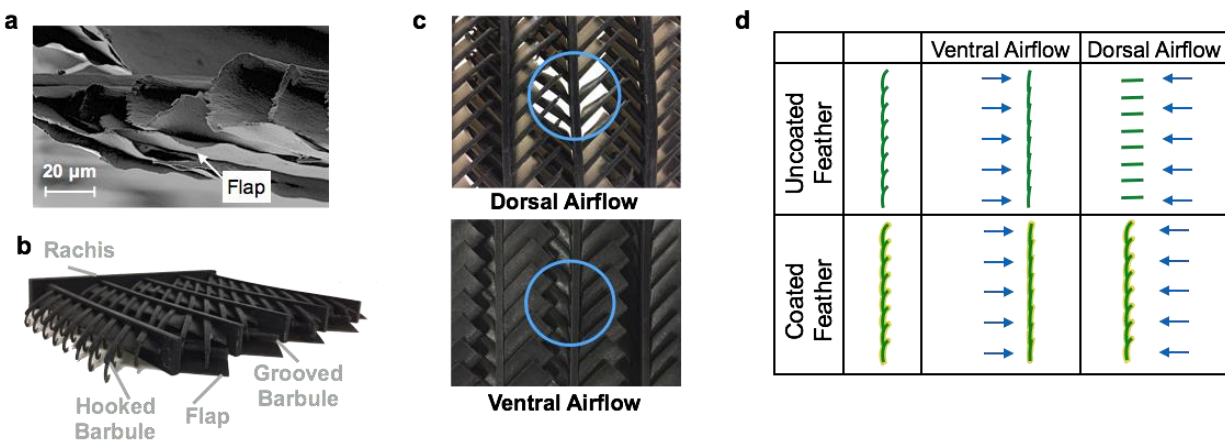


Figure 5.12 (a) An arrow points to an example of a barbule membrane. (b) A simplified, 3D-printed model of the feather vane, and (c) the hypothesized reaction of membrane flaps as air is blown dorsally (top) and ventrally (bottom), where circles represent the location of airflow. (d) Schematic of the expected differences in the vane with and without a coating for dorsal and ventral airflow. Figures 5.9a,d from [155], figures 5.9b,c from [47].

The difference in permeability of the feather with ventral and dorsal airflow is measured by sealing barbule membrane flaps shut with a coating, and comparing the uncoated and coated drag force of the feather. The schematic in **Figure 5.12d** demonstrates the experiment's hypothesis. Although a very thin coating of flexible vinyl cement is used to seal feathers, there are inherent differences in stiffness between coated and uncoated feathers. These are accounted for in a normalization whereby the ratio between coated and uncoated samples due to the added stiffness of the coating is assumed to be the same for ventral and dorsal airflow. Thus one has:

$$f = \frac{Force_{dorsal,coated}}{Force_{dorsal,uncoated}} / \frac{Force_{ventral,coated}}{Force_{ventral,uncoated}} \quad (5.26)$$

The factor f represents a normalized (accounting for the difference in stiffness introduced by coating) ratio between the dorsal and ventral drag force exerted by the feather. If $f=1$ there is no effect of sealing barbule flaps closed, but if $f > 1$ the opening of flaps reduces the drag force. **Figure 5.13a** demonstrates that this value (f) increases with airspeed, which corroborates its meaning as a measure of the effect of the barbule membranes. With higher airspeeds, membranes are bent back more intensely, resulting in an augmented difference between coated and uncoated samples reflected in the rising value of f . Additionally, a General Linear Model determined that for all species the $Force_{ventral,coated} / Force_{ventral,uncoated}$ is significantly different ($P=0.00$) from the $Force_{dorsal,coated} / Force_{dorsal,uncoated}$, further highlighting the effect of the membrane flaps on the directional permeability of the feather.

It is proposed that flaps are designed with unidirectional permeability dependent on airflow direction because birds require more power in flight on the down/power stroke (corresponding to ventral airflow) than on the up/recovery stroke (dorsal airflow). Interestingly, at the macro-scale, during the upstroke the bird's primary feathers spread apart and separate from one another to allow air-flow between them and prevent excessive downward forces on the wing [144]. Our findings suggest that the microstructural barbule flaps of wing flight feathers assists with this efficient measure.

Since the effect of membrane flaps (f) is similar for all species tested (dove, pelican, guineafowl), the spacing between barbules that is covered by these flaps is measured to determine how this scales between birds (**Figure 5.13b**). As discussed in chapter 3, despite other dimensions of the feather scaling proportionally to $\text{mass}^{1/3}$ [47,132,133], barbule spacing is found to narrowly vary between 8-16 μm for all birds measured, ranging from Anna's Hummingbird (*Calypte anna*) (4 g) to the Andean Condor (*Vultur gryphus*) (11,000 g) [47] (**Figure 3.12**). Constancy in barbule spacing is proposed to be to retain low permeability of air through the feather, independent of bird size. The feather must balance air flow with maintenance of its interlocking structure.

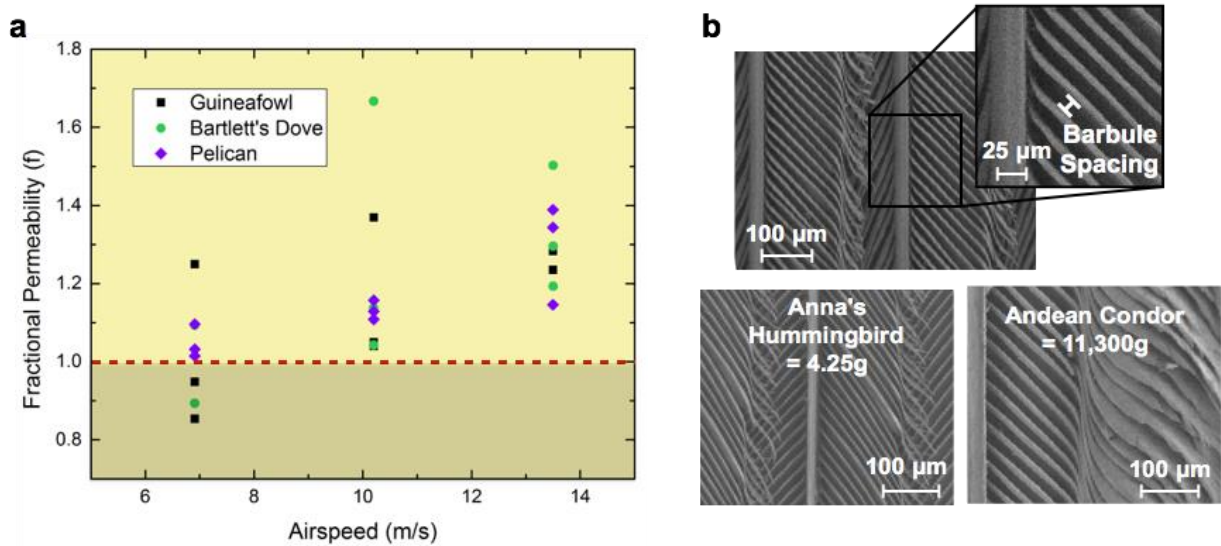


Figure 5.13 (a) Experimental results plotting f , a quantitative measurement of the effect of barbule membranes on air capture, vs. airspeed for the three species tested. An example of the barbule spacing dimension is shown in (b) along with SEM images that exhibit the similarities between the micro-scale barbules of Anna's Hummingbird (*Calypte anna*) (left) and the Andean Condor (*Vultur gryphus*) (right). Figure 5.10a from [155], figure 5.10b from [47].

5.4. Conclusions

The intricate design of the feather contributes to the unparalleled efficiency of bird flight. Here we investigate aspects of the barbule, the smallest structure in the feather, essential to the vane's function. Tests involving barbule adhesion demonstrate that the feather vane maintains in-plane tautness through contrasting directions of rotational preference at each hierarchical level. Experiments on bioinspired hook and groove barbules reveal that hooks must balance conflicting requirements for adhesion and effective re-adhesion, two important properties of the vane. A method for testing barbule stiffness is developed by *in-situ* SEM experiments; this stiffness is crucial in understanding the critical failure of barbule connections. When barbules are unzipped, feathers are found to less effectively capture air; the magnitude of this effect is correlated to the barb's dimensions. Lastly, the feather vane is found to have unidirectional permeability due to membranous barbule flaps that act as one-way valves and are similar in size among birds.

Barbule features examined in this dissertation are highly interrelated and work cooperatively with barbs to create a feather vane system that is exceptionally efficient and effective. For example, barbule stiffness and hook and groove shape influence feather vane attachment, which, along with vane permeability and barb stiffness, impacts the ability of the vane to sustain loading in flight. Barbules are exquisitely developed structures that enable impressive failure aversion combined with air capture. These multi-functional structures provide inspiration for new, more efficient aerospace materials with features such as tailored permeability and localized failure. Prototypes of designs incorporating these features are discussed in the next chapter.

5.5. Acknowledgements

Chapter 5, in full, is published in *Advanced Functional Materials*, authored by T.N. Sullivan, M. Chon, R. Ramachandramoorthy, M.R. Roenbeck, T.-T. Hung, H.D. Espinosa, and M.A. Meyers. The dissertation author was the primary investigator and author on this publication.

We graciously thank Dr. Steve Roberts (UC San Diego) for assistance with the wind tunnel. We also thank the San Diego Zoo (April Gorow, Research Coordinator) for providing feather samples to us. Assistance with additive manufacturing by Frances Su, Profs. Joanna McKittrick and Michael Tolley is gratefully acknowledged. We appreciate the assistance provided by Esther Cory and Prof. Robert Sah (UC San Diego) for μ -CT scans.

6. Hydration Induced Shape and Strength Recovery of the Feather

As a necessary appendage to the bird wing for flight, feathers have been optimized to fit the requirements of aerial locomotion. One of the recently discovered, fascinating aspects of this is the feather's ability to recover its shape with hydration. This feature significantly enhances the maintenance of flying capability. Thus, feathers damaged by predators or other external forces have a natural ability to recover their shape and strength. We analyze this evolutionary capability and, for the first time, demonstrate that the feather shaft can recover its strength after being bent to failure when subject to a hydration step. The matrix of the nano-composite structure within the feather shaft is thought to swell when hydrated, reorienting the stiffer fibers back to their original position. While these straightened fibers allow for shape recovery, they also permit the restoration of feather strength. Experiments were done to test this theory. Smart, self-healing composites based on approaches learned from the feather shaft have the potential to allow for the creation of a new class of resilient materials.

6.1. Introduction

Imperative for bird flight, feathers are an evolutionary marvel designed to be lightweight yet able to endure the intense loads of flight [24]. Flying feathers of birds consist of a main shaft (*rachis* and *calamus*) and a vane that branches from the *rachis*. The *rachis* is foam-filled and rectangular (**Figure 6.1a**), while the *calamus* is hollow and elliptical, embedded under the skin (**Figure 6.1b**). Although the vane captures the majority of air in flight, it transfers loading to the shaft, which possesses higher rigidity and strength. Maintenance of the shaft is therefore pertinent to a bird's survival, especially since feathers are usually only replaced once a year [26].

Feathers are composed entirely of β -keratin, a "dead tissue" formed by keratinous cells [78]. This biopolymer can be considered a hierarchical fiber-reinforced composite (**Figure 6.1c,d**): at the sub-nanoscale crystalline β -keratin filaments (~ 3 nm in diameter) are embedded

within amorphous matrix proteins. This filament-matrix composite forms macrofibrils (~200nm in diameter) which are surrounded by amorphous inter-macrofibrillar material. Macrofibrils then bundle to form fibers (3-5 μm in diameter) and these in turn form ordered lamellae within the dense exterior of the feather shaft [63,78,79,81,163]. The fiber direction within these lamellae varies depending on the side and location along the feather shaft [63] as well as the species of bird [87].

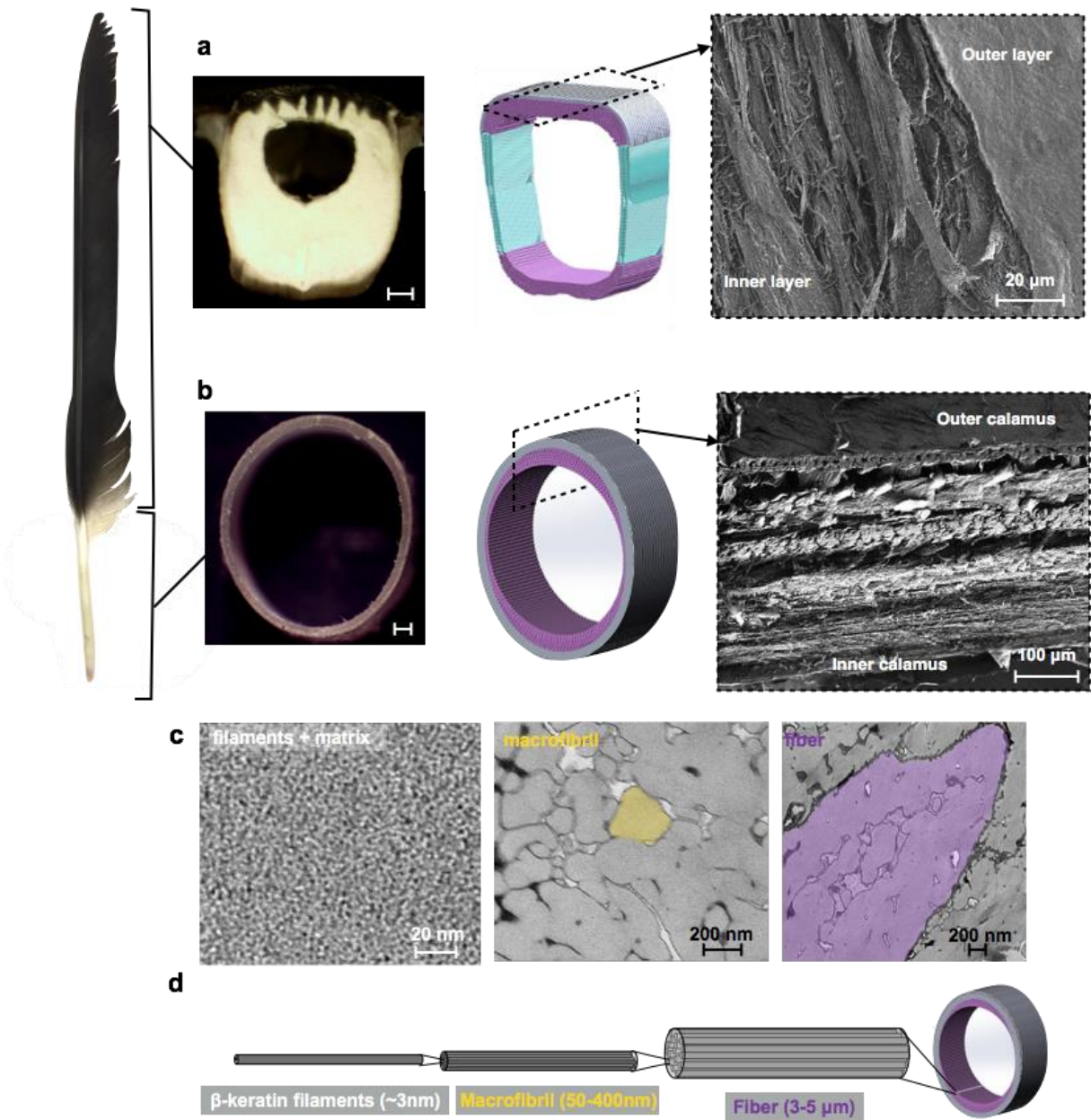


Figure 6.1 The hierarchical structure of the feather: The flight feather of the Cape Vulture (*Gyps coprotheres*) is divided into the (a) rachis and (b) calamus. Optical microscope images of both sections are shown in the leftmost images (scale bar is 0.5mm). Fiber models of the feather sections illustrate that fibers run longitudinally along the shaft (purple), and circumferentially (gray) within the calamus and dorsal side of the rachis, while fibers alternate at $\pm 45^\circ$ angles (green) in the lateral walls of the rachis. On the right, SEM images of the dorsal rachis and calamus confirm the orientations of fibers in the corresponding sections of fiber models. (c) TEM images reveal a filament and matrix structure that forms macrofibrils which in turn form fibers, (d) a schematic of this is drawn to clarify this structure. Fiber model images in (a,b,d) adapted from B. Wang, et al. (2017)[164].

Studies on α -keratin reveal that matrix proteins are water-sensitive while intermediate filaments are crystalline and not mechanically affected [81,165,166]. Although the structure of β -keratin differs from α -keratin, both possess similar structure consisting of an amorphous matrix and crystalline filaments, and therefore the matrix of β -keratin is generally agreed upon as behaving similarly to that of α -keratin [78,154,166,167]. Additionally, the mechanical properties of both keratins demonstrate similar sensitivity to water content: as the humidity increases, breaking strain increases while the stiffness and strength decrease [70,168].

Along with other keratinous materials, the feather has demonstrated the ability to recover its shape from a deformed state when hydrated [169]. The amorphous matrix material in the feather can be likened to a shape memory polymer (SMP). In SMPs, as described in section 2.9, the shape memory effect is often related to changes in the macromolecular structure due to factors such as glass transition, reversible cross-linking and melting transition [102]. For example, SMPs can be rigid and stiff below the glass transition temperature, but rubber-like and deformable above this temperature, allowing the polymer to recover its shape [117]. For the β -keratin matrix, hydration is hypothesized to serve as the actuator which raises the material above the glass transition point.

Here, we examine the shape memory effect of the feather shaft due to hydration and reveal its relation to its strength recovery after failure. A model for feather recovery by hydration is hypothesized and its recovery is described. Research in this area has the potential to lead to the expansion of the capabilities of shape memory polymer composites by incorporating concepts developed by nature over millions of years.

6.2. Materials and Methods

6.2.1. Test Specimens

Flight feathers of the Cape Vulture (*Gyps coprotheres*) were obtained postmortem and stored in ambient conditions. Sections of the calamus and rachis were sliced with a razor and measured using calipers to ensure similar dimensions between samples. The ends of each feather shaft section were then fixed in the center of a 5 mm square aluminum tube using epoxy to prepare samples for bending tests. Each completed sample had 18 mm of exposed rachis between the blocks, with a block length of 22 mm in length at each end. Cortex samples used in swelling and tension tests were sliced into rectangular pieces from each corresponding section of the rachis or calamus. The Los Angeles Zoo provided the Cape Vulture (*Gyps coprotheres*) feathers, which were obtained under our research group's Federal Fish and Wildlife permit.

6.2.2. Flexure Tests on the Feather Shaft

Calamus and rachis samples were tested in four-point bending to mitigate the effects of the naturally curved feather shaft and prevent local crushing stresses. Bending tests were initially done directly on feather sections, but due to the non-uniform cross section of the shaft, samples rotated and twisted in loading, preventing measurement of pure bending. To address this issue, we adapted the method developed by Corning and Biewener[64] in which tests are conducted on the feather sample with its ends embedded (as described in 6.2.1).

Feather samples were tested with their dorsal side facing upwards, to mimic the main loading orientation on the feather shaft when the bird is in flight. As shown in (**Figure 6.2**), steel rollers of the top and bottom fixtures were placed at the inner and outer most location of the blocks. A rate of displacement of 0.01 mm/s was applied using an Instron Universal Testing Machine model 3347 (Instron Corporation, Norwood, MA, USA).

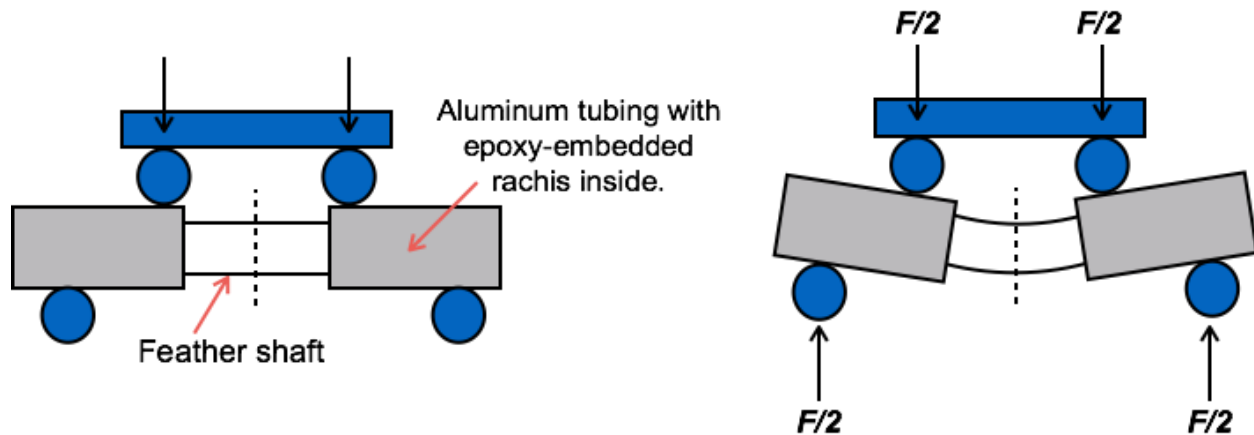


Figure 6.2 Four Point Bending: Flexure tests were conducted on feather samples embedded in aluminum tubing. Steel rollers contacted the inner and outer parts of the top and bottom of the aluminum tubing.

6.2.3. Cyclical Flexure Tests on the Feather Shaft

All twenty calamus and rachis samples were tested to failure for five cycles. Five of the calamus and rachis samples were hydrated for 24 hours between stress cycles, while the other half were not. Samples were given the same amount of recovery time in total, with hydrated samples allowed to dry for 72 hours in ambient conditions, and dry samples placed in ambient conditions for 96 hours. Before and after tests, samples were imaged using optical microscopy. Additionally, each sample was weighed before testing. This ensured that hydrated samples had returned to their original state.

6.2.4. Water Retention and Swelling Experiments

The rachis and calamus were sliced into sections as well as rectangular cortex strips. Optical micrographs and the initial mass of each sample were recorded before and after 24 hours of hydration. Dimensions were measured using ImageJ software (National Institutes of Health, Bethesda, MD).

6.2.5. Tensile Tests on Cortex

Rectangular strips of the cortex from each side (dorsal, ventral, and lateral) ~8-10 mm in length and along the transverse direction about ~1-2.5 mm in width were cut along the longitudinal direction using a razor blade. Where applicable, the foam was removed mechanically without damaging the cortex by using a wooden scraper. The sample extremities were secured in sand paper using a cyanoacrylate adhesive. The samples were extended in tension using an Instron model 3347 testing apparatus at a strain rate of 10^{-3} /s. Four samples were tested for each side and section.

6.2.6. Transmission Electron Microscopy

Transmission electron microscopy was used to view the filament and matrix structure within β -keratin. To do so, feather sections were stained using an osmium tetroxide staining method with lead post-staining [170]. Small blocks of feather samples were soaked in a 0.15M Cacodylate buffer for 6 hours. Samples were removed from the buffer solution and soaked overnight in a 2% Glutaraldehyde-buffer solution. Following this, samples were taken out from the solution and rinsed with the Cacodylate buffer solution. Samples were then placed in a potassium ferrocyanide, Cacodylate buffer, and osmium tetroxide solution at a chilled temperature overnight. Then feather specimens were rinsed with chilled distilled water and placed in a chilled 2% Uranyl acetate solution and soaked overnight. Following this, they were washed with distilled water and gradually dehydrated to 100% ethanol and then 100% acetone. After this step, samples were then infiltrated with Spurr's low viscosity epoxy resin through a series of gradient solutions of epoxy and acetone. Finally specimens were set to harden in the resin. A Leica Ultracut UCT ultramicrotome with a diamond knife was used to prepare thin electron transparent slices. These were placed on 300 mesh TEM grids and were post-stained with lead.

Lastly, these feather samples were imaged using an FEI Technai 12 Spirit transmission electron microscope.

6.3. Results and Discussion

6.3.1. Shape and Strength Recovery of the Feather

Time-lapse images of severely deformed cortex and rachis sections submerged in water (**Figure 6.3 a,b**) demonstrate that the feather has the ability to recover its shape when subjected to hydration. While this is quite interesting in itself, evolutionarily it is essential to a bird's survival for the feather to also recover its strength with hydration. An understanding of the nano-composite structure of the feather, with the amorphous matrix behaving as a SMP with hydration, suggests that the feather shaft strength does recover with hydration. To evaluate this hypothesis, we cyclically test sections of the calamus and rachis to failure in four-point bending. Half of the samples tested are hydrated for 24 hours after failure and dried for 72 hours before re-testing; the other half of samples are left in ambient conditions for 96 hours.

The results corroborate this hypothesis. The effect of shape recovery on strength is demonstrated in plots of the five cycles for a non-hydrated calamus sample (**Figure 6.4a**) and a calamus sample with a hydration step (**Figure 6.4b**). It is clear from these plots that the sample with a hydration step is able to recover its ultimate strength to a much greater extent than the sample without hydration. The rachis exhibited similar results.

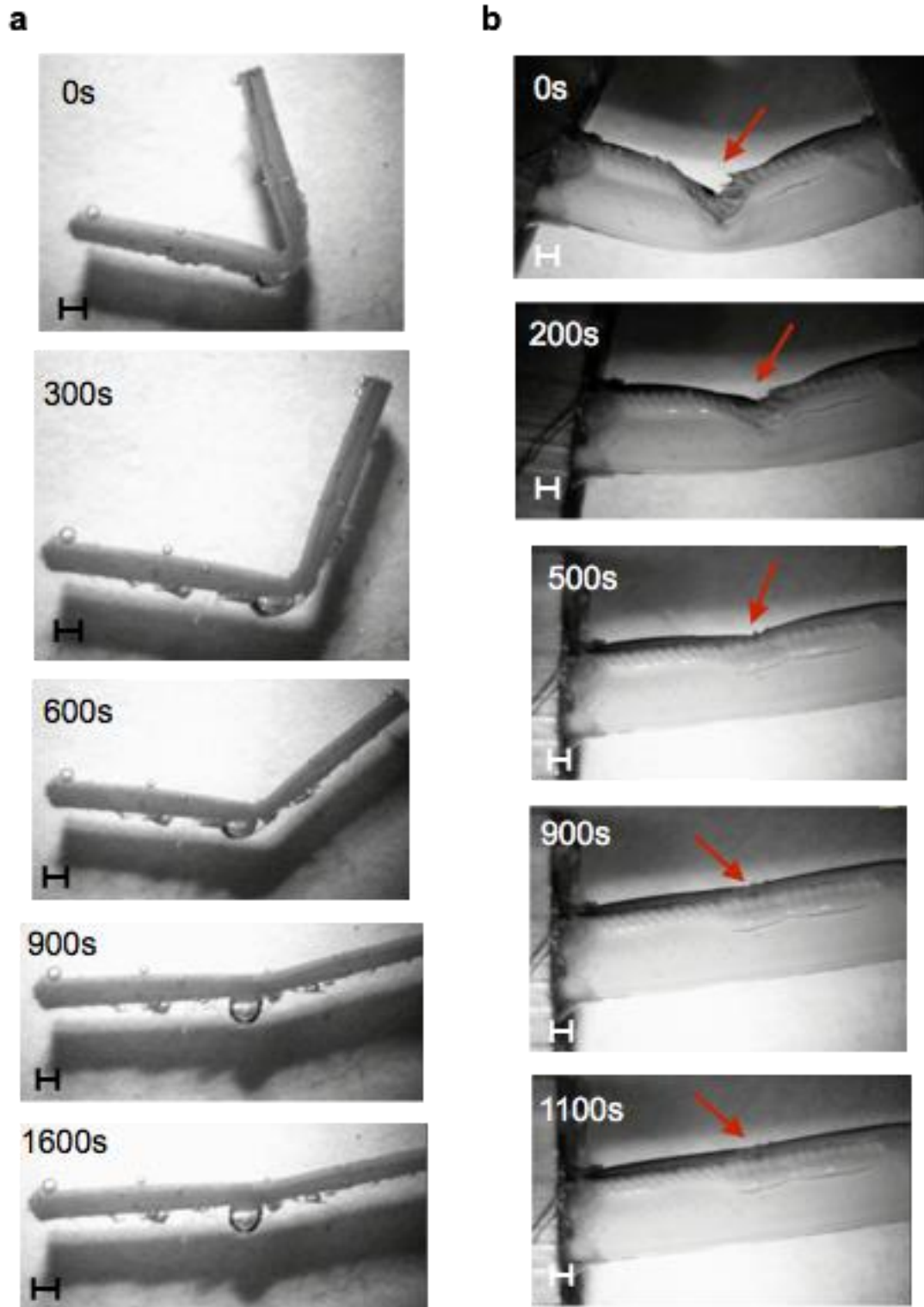


Figure 6.3 Recovery of the feather shaft in water: (a) A strip of the feather shaft cortex is severely deformed and recovers in water. (b) A rachis section with the vane removed is bent and recovers in water, red arrows highlight the location of the deformation. All scale bars are 1mm.

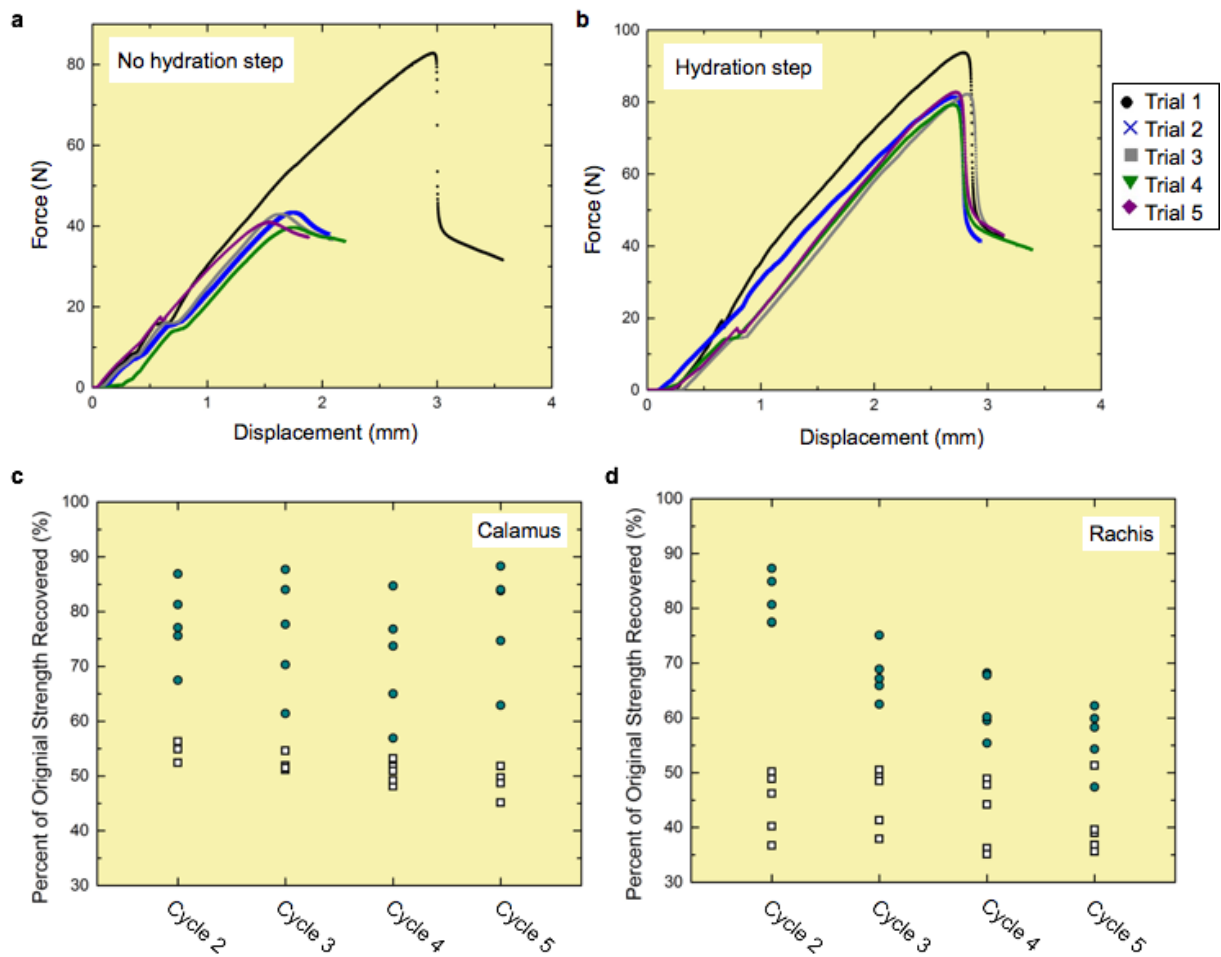


Figure 6.4 Strength recovery of the feather shaft through hydration: Flexural test data of a calamus sample with no hydration step (a) and with a hydration step between test trials (b). The strength recovery of samples, as compared with the maximum strength of cycle one, without a hydration step (white squares) and with a hydration step (cyan circles) for calamus (c) and rachis (d) samples.

To verify the differences between hydrated and non-hydrated recovery, optical micrographs of calamus samples are shown after failure (**Figure 6.5 a,b left**) and after recovery (**Figure 6.5 a,b right**), where a is not hydrated and b is subjected to a hydration step. In images of the failed samples (left), buckling is visible perpendicular to the longitudinal axes, highlighted by black arrows. After recovery (right), the hydrated sample (**Figure 6.5b**) appears to no longer have visible buckling while the non-hydrated sample (**Figure 6.5a**) remains largely unchanged.

These images represent the typical response of samples tested. Thus, not only is the shape recovered upon hydration, but also the strength. After five cycles, the strength of the hydrated sample is ~80% of the original strength, while that of the dry feather is only ~55%. This strength recovery is important to the flying ability of the bird, after feathers are broken by predator attack, fight, or catastrophic events.

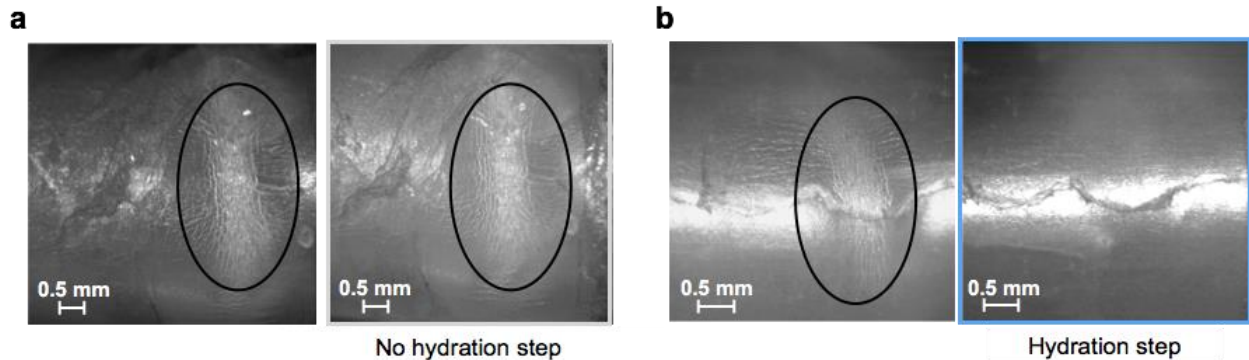


Figure 6.5 (a) Optical microscope images of calamus samples tested until failure (left a,b) and recovered with no hydration step (a, right) and with a hydration step (b, right). Scale bars are 0.5 mm.

In order to establish the structural changes induced by bending the shaft up to failure (irreversible buckling), sections were made after deformation. A schematic of the shaft cortex with the “squarish” section and cellular foam core is shown in **Figure 6.6 a**. The segment was cut longitudinally as indicated by the dashed line. The representation shown in **Figure 6.6 a** identifies the observation plane. Rachis samples in **Figure 6.6b-d** are cross sections sliced along the longitudinal axis of the shaft as shown in **Figure 6.6 a**. Samples in **Figure 6.6 c,d** are tested until failure, while the sample in **Figure 6.6 b** is not tested. The sample in **Figure 6.6 d** is hydrated after failure while the others are not hydrated. Severe local buckling on the dorsal side of the rachis is apparent in the deformed, non-hydrated sample (**Figure 6.6 c**). Corresponding scanning electron micrographs show the details of failure within this sample: fiber splitting at the cortex-foam interface and within regions of local buckling. Scanning electron micrographs reveal

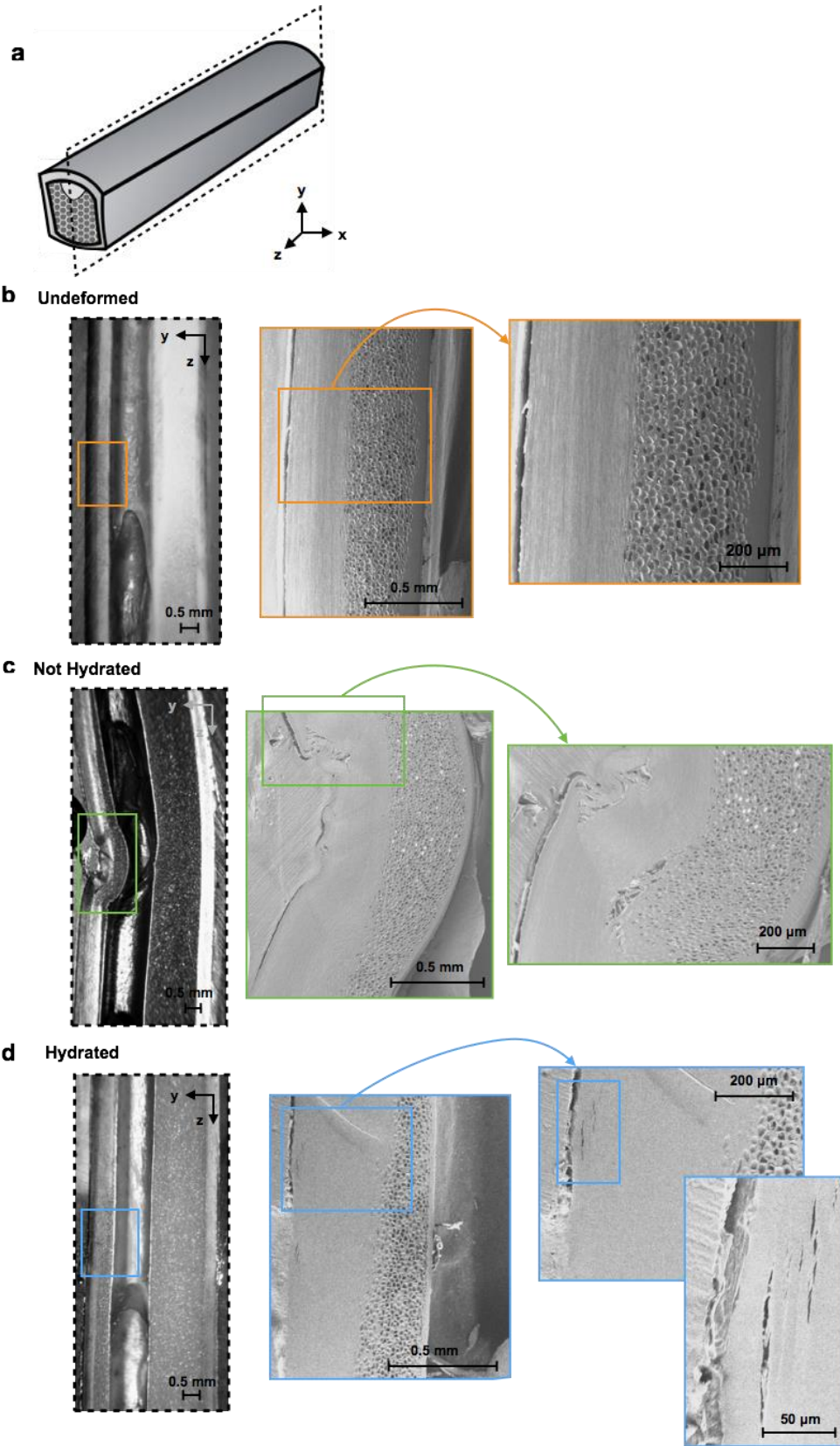
minimal damage in the hydrated sample with micro-cracks forming between lamellae within the dorsal cortex. At the macro-scale there appears to be no difference between the untested and hydrated rachis samples (**Figure 6.6 b,d** respectively). The untested sample, which serves as a reference, does not show any damage, indicating that the cracks viewed in **Figure 6.6 c,d** are due to flexure tests.

To compare all data of hydrated and non-hydrated samples, the percent difference between the ultimate strength of each cycle and the sample's original cycle (cycle 1) was determined. This value was found for each sample and is called the percent of original strength recovered. These percentage values are plotted against the cycle number for both the calamus (**Figure 6.4 c**) and the rachis (**Figure 6.4 d**), where samples not subjected to hydration are represented by white squares and samples with a hydration step are cyan circles. A general linear model determined that for both the calamus and rachis, samples with a hydration step have a significantly different percent of strength recovered than the dry samples ($P=0.00$).

While rachis and calamus samples with a hydration step recover to a comparable degree during the second cycle ($81.6 \pm 4.4 \%$, $77.7 \pm 7.2 \%$ respectively), calamus samples are able to maintain a similar level of recovery throughout the five cycles while rachis samples decrease in recovery to an average of $56.4 \pm 5.8 \%$ by cycle 5. A general linear model confirms this, with significantly different results for recovery between cycle 2 and cycles 3-5 for the rachis ($P=0.00$) and no significant difference between trials for the calamus ($P>0.05$). Discrepancies in recovery behavior between the rachis and calamus after the second cycle could be due differences in cross-sectional shape, the presence of foam in the rachis sections and the distinct lamellar structure within the cortex of each. As a simpler structure, the calamus perhaps recovers to a greater extent in later trials because failure solely occurs on the dorsal side. The rachis must recover not only in

its dorsal cortex, but also in the lateral walls, which collapse in failure. Additionally, the rachis' foam undergoes failure with each trial, and since it is composed of many very thin fibers, it undergoes unrecoverable damage such as fiber breaking after the second trial. Differences in recovery due to lamellar structure will be discussed in detail in the following section.

Figure 6.6 Recovery of the feather shaft: Feather shafts were sliced open along the dotted line shown in (a) to view the y-z cross section. Samples shown in (c,d) were tested to failure in bending, while sample (b) was not tested. The sample shown in (c) was not hydrated after testing and buckling is clearly visible in the optical microscope and SEM images. The sample shown in (d) was hydrated after buckling and clearly shows less damage, with small cracks visible at high magnification. The untested sample (b) does not have damage.



6.3.2. Mechanism for Shape Memory Recovery

A mechanism for the shape memory and strength recovery effect in feather keratin is proposed in **Figure 6.7**. A β -keratin strip is shown in its initial configuration as a layered nanocomposite. Since the tensile strength of fibers is much higher than their compressive strength, when the feather is bent buckling occurs with accommodation by the amorphous matrix. This Euler buckling is shown in **Figure 6.7**, and is labeled “Deformation in bending”. As mentioned previously, the matrix is more affected by hydration than the stiffer crystalline fibers [154,166–168]. Therefore, upon wetting, water molecules penetrate preferentially into the amorphous matrix, causing it to swell and plasticize. The flow stress of the hydrated matrix is assumed to be considerably lower than the fibers. **Figure 6.8** shows the hypothetical response of the cortex in dry and hydrated conditions, separating the responses of the fibers and matrix. Fibers show minimal hydration effect, while the amorphous matrix softens considerably. This is indicated by an increase in spacing between fibers from d_0 to d_1 in **Figure 6.7**, “Initial Hydration”. This, in combination with the elastic energy stored in the fibers due to buckling, cause the fibers to straighten, since they are elastically loaded in compression. As a result, the radius of curvature increases from R_1 to R_2 . The matrix swells further in **Figure 6.7**, “Final Hydration” to have a larger spacing d_2 so that fibers completely reorient to their original position. The last stage, dehydration, corresponds to the removal of water molecules from the amorphous matrix, which shrinks back to a spacing d_0 (**Figure 6.7**, “Drying”). Thus, the initial configuration is recreated and the shape memory effect cycle is completed.

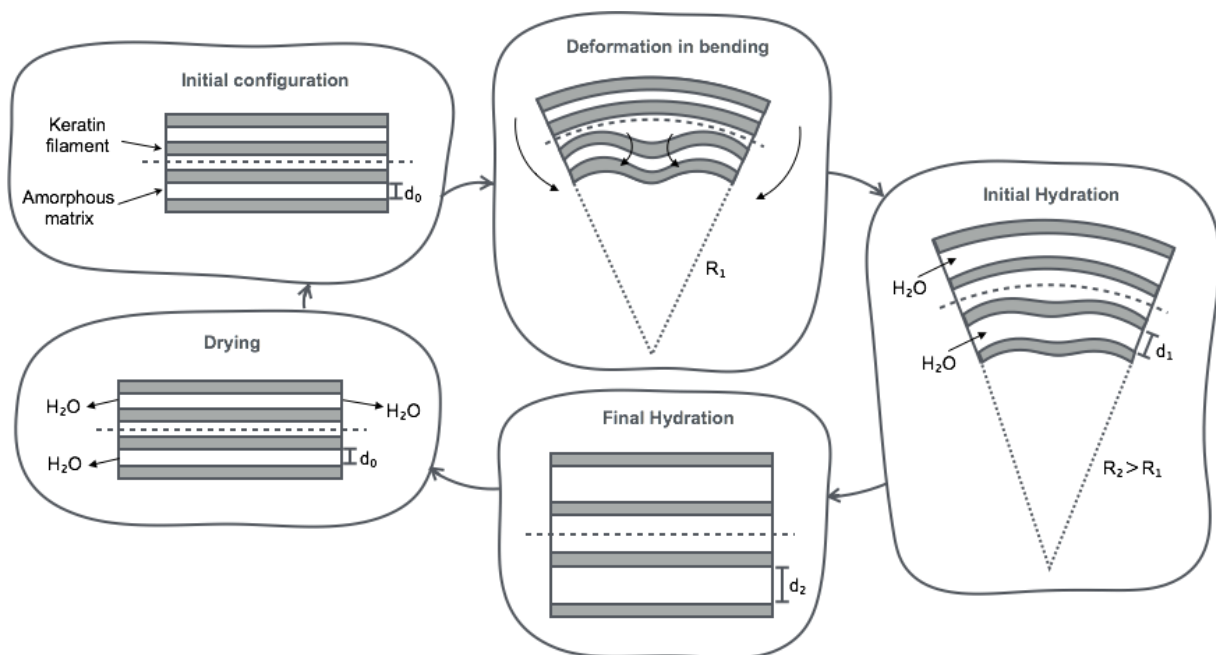


Figure 6.7. The proposed mechanism for shape and strength recovery of the feather shaft. The cycle begins in the “initial configuration” showing the composite structure of β -keratin filaments in an amorphous matrix. The fibers undergo “deformation in bending” and buckle in compression. It is unclear if fibers buckle in plastic or elastic deformation, and this is the subject of future research. When hydrated, water molecules penetrate preferentially into amorphous matrix causing swelling (indicated by $d_1 > d_0$) and therefore straightening of fibrils and the radius of curvature increases from R_1 to R_2 . The matrix then fully swells as spacing grows to d_2 and completely straightens fibers. Lastly, the sample dries and water molecules diffuse out of amorphous material, which loses its plasticizing effect.

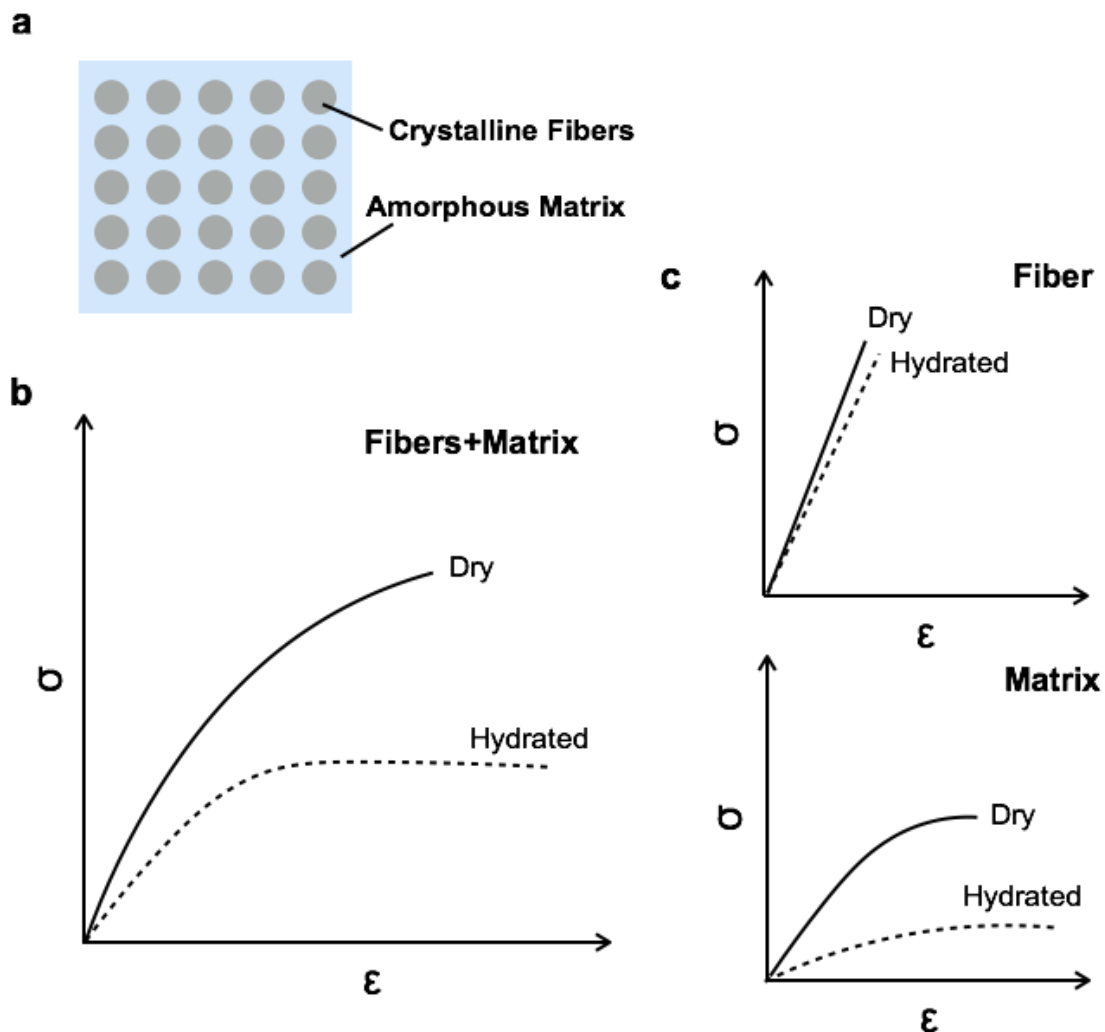


Figure 6.8 Schematic representation of different mechanical responses of fiber and matrix in the feather shaft. (a) Cross-section showing crystalline fibers and amorphous matrix; (b) overall response of feather in dry and hydrated conditions; (c) matrix and fiber responses.

To determine if this theory is accurate, various dimensions of shaft sections and cortex strips were measured and compared before and after hydration. Significant swelling occurred within samples; **Figure 6.9 b** shows an optical micrograph of a feather cross section before hydration, with a tracing of the outer surface of the same feather after hydration. **Figure 6.9 a** plots the percent difference in dimensions of the calamus and rachis with 24 hours of hydration, where measured dimensions of circumference and length are demonstrated in **Figure 6.9 c**. The

rachis circumference is found to greatly increase in dimension while its length is not. The calamus has a less extreme difference in swelling between the length and circumference, with on average less circumferential and more length swelling than the rachis.

Figure 6.9 d shows the change in length, thickness and width of strips of the dorsal side of the rachis and calamus (as shown in **Figure 6.9 e,f** respectively). The dorsal rachis is chosen because it is the side of the rachis that undergoes the most damage in flexure and, unlike the calamus, each side of the rachis has a different fiber orientation. Dorsal rachis strips exhibited very low or even negative swelling in the length dimension, with the greatest amount of swelling occurring in the thickness. Calamus samples, on average, demonstrated less swelling in both thickness and width when compared to the rachis, but more swelling in length.

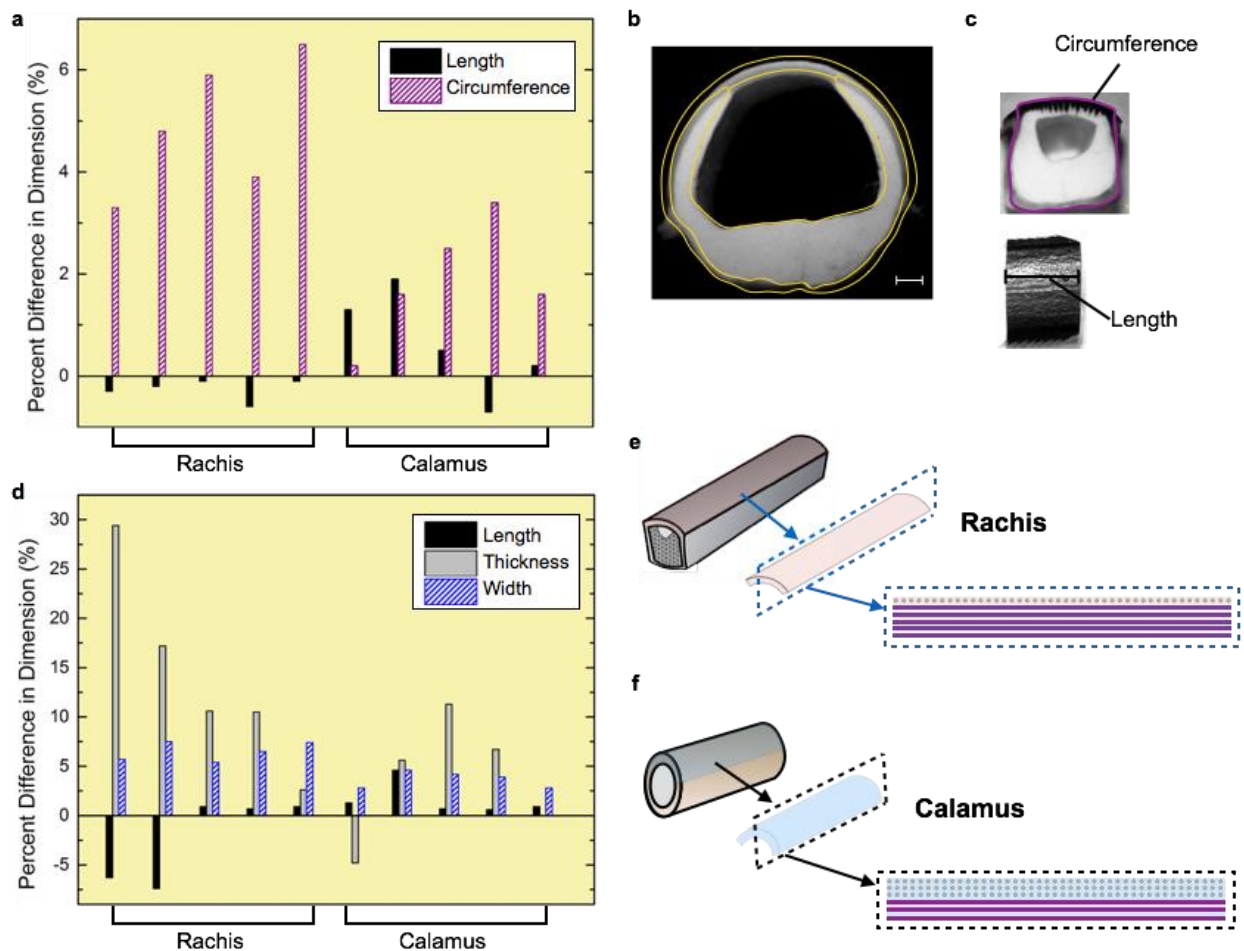


Figure 6.9 Experiments were conducted to determine if the feather swells upon hydration: (a) the length, circumference and area of cross sections (as shown in c) of the rachis and calamus were compared before and after hydration. (b) The images show the initial cross section, while the yellow outline shows the cross-sectional profile of the sample after hydration (scale bar is 1 mm). (d) The length, thickness and width of cortex strips from the dorsal rachis (e) and calamus (f) were measured before and after hydration.

The proposed mechanism described in **Figure 6.7** should theoretically result in hydration-induced swelling in the dimensions perpendicular to the fibers, and no swelling in the direction of the fibers. While both the dorsal rachis and the calamus have an inner layer in which fibers run along the length of the shaft and an outer layer in which fibers run perpendicularly to the shaft, the calamus has a much thicker outer layer than the rachis. This is demonstrated in the scanning

electron micrographs in **Figure 6.1a,b**. As a result, the calamus has more fibers running perpendicularly to the shaft than the dorsal rachis. This is shown in the schematics in **Figure 6.9 e,f** where dots indicate fibers running out of the page. Based on these differences in fiber alignment, the rachis should swell more extremely in thickness and width and less in length than the calamus. This hypothesis is supported by the results of the swelling tests, which on average demonstrate this trend. Interestingly, the data indicate that on average the thickness dimension swells most in the rachis. Overall, data show that the feather swells more in the direction perpendicular to the fibers, and less in the direction of the fibers.

6.4. Conclusions

Synergistically, the design and material properties of the feather shaft allow for its shape recovery through a hydration step. Here we quantitatively prove, for the first time, the feather's ability to recover strength with hydration, and explain this phenomenon through experimentally supported models involving the swelling of the feather's matrix material with hydration.

The shape was completely recovered after hydration, when deformed beyond the buckling limit. Both the calamus and rachis were found to recover their strength to a considerably greater degree with a hydration step than without one. The calamus flexure strength consistently recovered to a larger extent over multiple cycles (to ~80%), than the rachis' (to ~55%) with the number of test cycles. This is likely due to the macro-structural differences between the rachis and calamus, especially the foam within the rachis, which likely becomes permanently damaged as cycles progress. Sections of the rachis and calamus were found to swell when hydrated, with the rachis swelling more extremely in circumference than the calamus, and the calamus swelling more in the length. These results support the hypothesized behavior of the matrix material swelling perpendicularly to the fiber direction, due to differences in the fiber direction in the rachis and

calamus. Lastly, failure in local buckling and recovery of the feather shaft was simulated, providing insight into the location of stresses as the shaft fails in flexure and recovers.

Perhaps the shape memory recovery of the feather contributes to an explanation for why birds of most species take baths. In a behavioral biology study it was found that birds with access to bathing water flew more accurately than those without bathing water.[171] Our research here could serve as a possible reason for why bathing is highly important to the bird. Additionally, understanding the phenomenon witnessed with strength recovery in the feather shaft can be applied to further the capabilities of shape memory composites, resulting in new smart, self-healing materials. Although multiple deformation cycles to the onset of buckling were applied, it is highly unlikely that a feather will be subjected to this extreme damage during its lifetime, and one deformation cycle is a good measure.

6.5. Acknowledgements

Chapter 6, in full, will be revised and submitted for publication to *Advanced Materials*, authored by T.N. Sullivan, Y. Zhang, Z. Liu, P. Zavattieri and M.A. Meyers. The dissertation author is the primary investigator and author on this manuscript.

We graciously thank Mason Mackey at the National Center for Microscopy and Imaging Research, Dr. Shiteng Zhao and Haocheng Quan for assistance with TEM. We also thank the Los Angeles Zoo (Mike Maxcy, Curator of Birds and Dr. Cathleen Cox, Director of Resarch) for providing feather samples to us.

7. Bioinspired Designs of the Avian Feather

Bioinspiration is the appreciation of knowledge learned from nature to create novel, insightful designs. Although it is not a new concept, the field has experienced recent growth and popularity due to new experimental techniques. Bioinspiration requires the distillation of only a few relevant aspects of the natural design from a highly complex biological organism or system. Due to this simplification process, bioinspiration is also used to develop a deeper understanding of biological materials; this process is called bioexploration. **Figure 7.1** shows the cycle of investigating a biological specimen, in this case the mandible of a sea urchin, studying it through the lens of materials science and engineering, creating bioinspired designs based on what is learned (bioinspiration), and in turn learning more about nature through bioexploration[172].

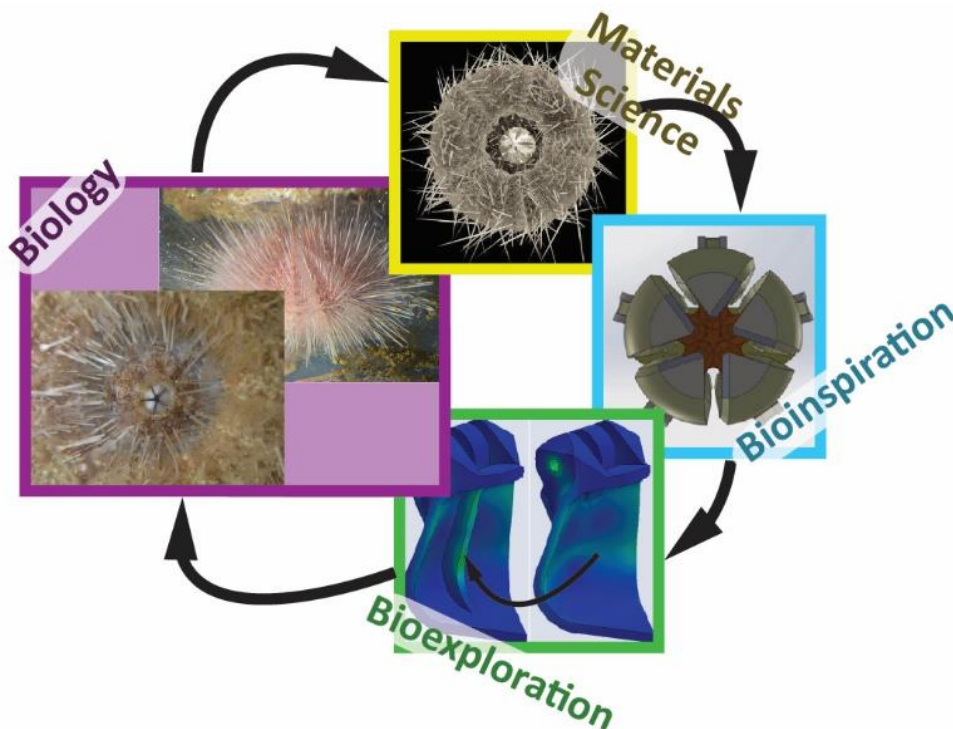


Figure 7.1 The study of nature allows for the creation of refined bioinspired designs which ultimately allows for a better understanding of the natural system through bioexploration [172]. This is shown here for the sea urchin. Its mandible mechanism is studied using materials science methods, and inspires a synthetic prehensile mechanism, which, in turn, improves our understanding of the animal through bioexploration.

In this chapter we briefly cover a background of bioinspired and analogous designs based on the bird wing and its components, discuss our recent advances in bioinspired feather designs, and introduce ideas for additional bioinspired designs based on the feather.

7.1. Introduction and Background: Bird Wing Bioinspiration and Analogous Designs

Advancements in engineering and design have resulted in solutions similar to those utilized by the bird wing and its components. While some of these solutions are bioinspired, others arose independent to the study of natural systems. Despite recent advances, there is still much room for development of bioinspired materials, structures, and designs using insights from the study of birds.

7.1.1. Avian Wing Shape Design

There have been many advances in commercial wing shape; two significant improvements with striking resemblance to the bird wing are winglets and the flexible wing. Winglets are small, roughly vertical surfaces usually located at the wing tips of an aircraft. They are used on aircraft because they can lessen wingtip vortices, reduce drag by about 20%, and allow wings to provide the same amount of lift with a smaller wingspan [173]. Likewise, in many large flying birds, feathers curl upward in flight at wing tips (**Figure 7.2a**) to serve as winglets. A more recent improvement, the composite wing of the Boeing 787 allows it to flex to be more efficient and dampen turbulence [174,175]. The wing's flexibility is especially apparent in take-off and landing. Similarities between the in-flight wingspan shape of the Andean condor and the Boeing 787 are depicted in **Figure 7.2a and b**, respectively.

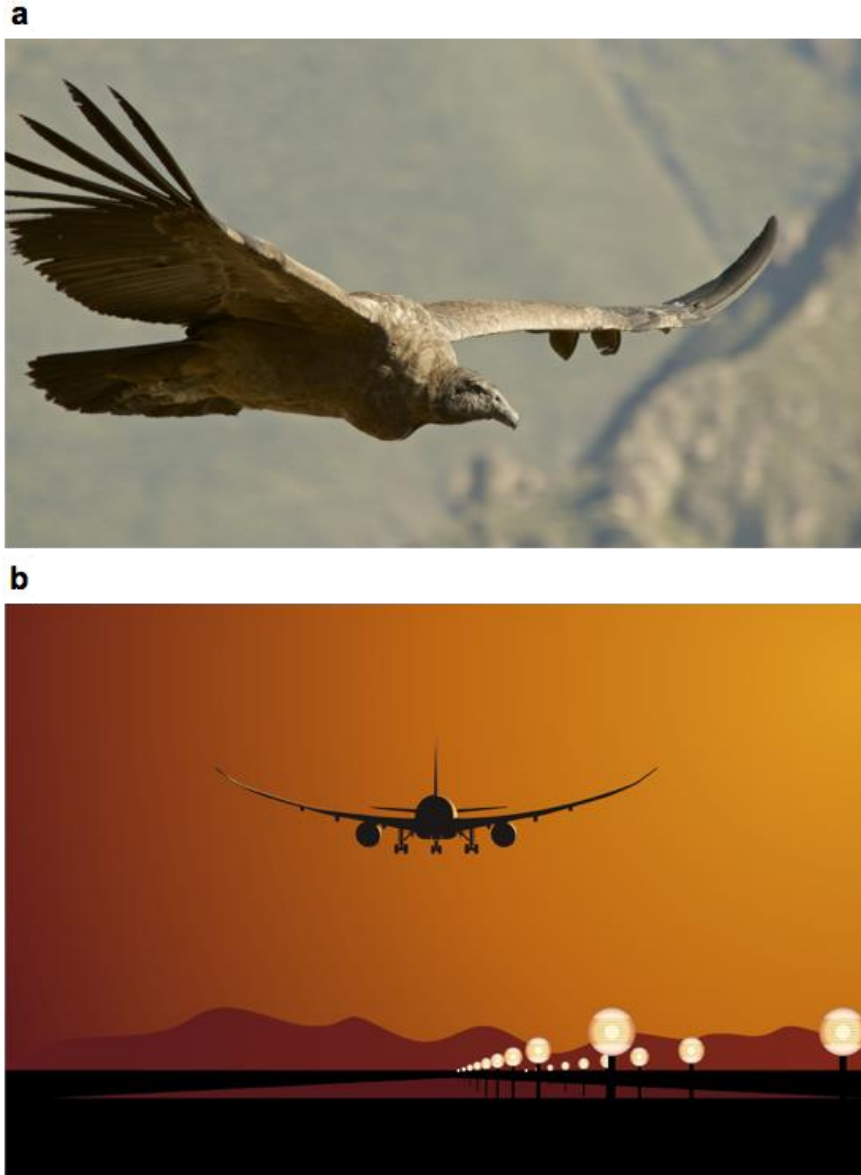


Figure 7.2 Many analogous solutions have been developed through evolution and engineering: (a) The Andean condor’s feathers curl upward at its wing tips for more efficient flight. (b) A similar curvature is observed in the flexible wings of a Boeing 787.

7.1.2. Avian Wing Bone Design

Reinforcing struts identified in pneumatic avian bone inspired the fabrication of a nickel metallic foam with crisscrossing “struts” (**Figure 7.3a**) [176]. As in avian bone, these struts provide a lightweight method of maintaining structural integrity. Research has suggested that a structure with a core of angled micro-struts (**Figure 7.3b**) is theoretically at least 7 times stiffer

than the best open cell foam [177–179]. Although not bioinspired, inclined struts are commonly used to reinforce the ribs of airplane wings (**Figure 7.3c**) [180–182]. These ribs transmit loads from the skin of the wing and stringers to the spars.

Bird bones suggest lightweight solutions for torsion resistant structures. Through the process of convergence engineers have developed similar solutions for increasing the torsional stiffness in large container ships, which have significant torsional moments generated by unsymmetrical wave or cargo loading [183–185]. Torsion boxes, or stiffened skins of materials with a lightweight core, are installed in the upper hulls of ships to increase the strength of the ship's exterior in high-risk areas, while maximizing space for cargo and minimizing weight [185]. Torsion boxes in ships are analogous to the dense exterior found in torsionally resistant bird bones.

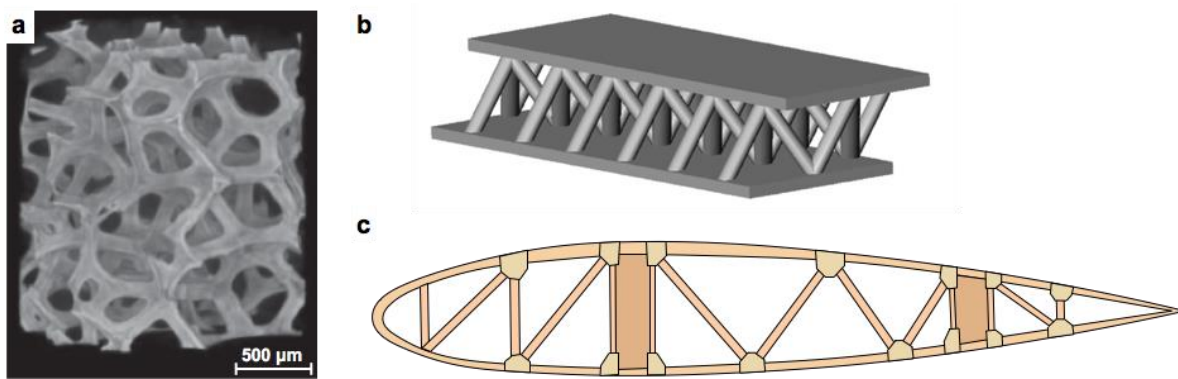


Figure 7.3 Engineering has led to similar designs as those found in the avian feather and bone: (a) Nickel metallic foam inspired by the struts in avian bone (taken from X. Jin et al. (2014) [176]), (b) a computer aided design model of diagonal struts in a multifunctional cellular material (taken from A.G. Evans et al. (2001) [177]). The supporting structures in airplane wing ribs (c) have an analogous design and purpose to the struts in avian bone.

7.1.3. Feather Design

Similar to the foam-filled feather, recreational snow skis are designed primarily for a tailored longitudinal stiffness. These skis are composites with faces generally made of aluminum or fiber-reinforced polymer separated by a foam-filled core [43,186–188]. For additional longitudinal reinforcement some skis have reinforcing ridges along their length, similar to the stiffening dorsal ridges of the feather rachis [43,189] shown in **Figure 7.4a**.

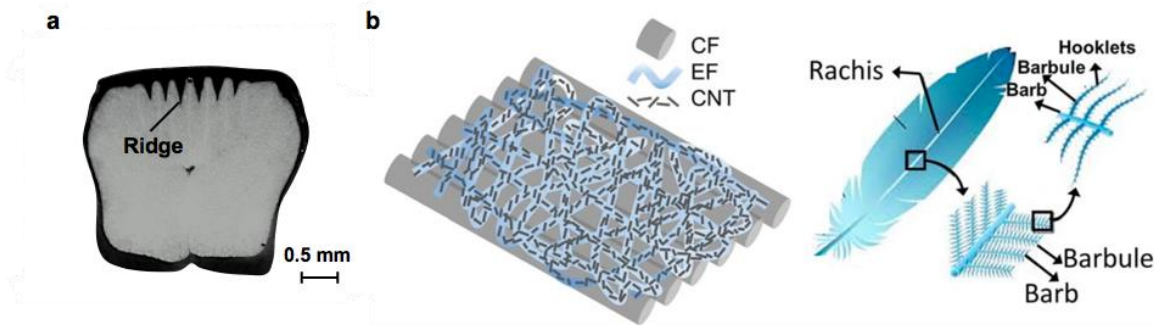


Figure 7.4 (a) A cross section of a primary feather from the American White Pelican (*Cathartes aura*) demonstrates the reinforcing ridges on the dorsal side of the feather [47]. The hierarchical synthetic composite (b) is inspired by the degrees of hierarchy in the feather (taken from V. Drakonakis et al. (2014) [190]).

As demonstrated in the avian feather, hierarchical composites can greatly increase the efficiency and mechanical properties of a structure. Although it is extremely difficult to manufacture materials with the same level of hierarchy as nature, several techniques have been used to fabricate micro- and nano-structured materials including self-assembly, freeze casting and electrospinning [190–203]. The latter method was used to create a feather-inspired composite structure with nanofibrous fractal interlayers [190]. In this design, a polymer-carbon nanotube suspension was electrospun onto a carbon fiber bed as an interlayer between lamina. Carbon nanotubes represent the micro- and nano-scale barbules, the electrospun fiber the micro-scale barbs, and the carbon fiber serves as the rachis (**Figure 7.4b**). This composite was shown to have significantly higher mechanical properties than the carbon fiber laminate with no interlayer [190].

7.2. Materials and Methods

7.2.1. Fabrication of Barbule Inspired Structures by Additive Manufacturing

Bioinspired feather vanes were drawn in the Computer Aided Design program SolidWorks (SolidWorks Corp., Waltham, MA, USA) and fabricated via additive manufacturing (3D printing). Our first model was created using ABS plastics to illustrate the concept of interlocking barbule attachment. Following this, flexible barbule hooks and grooves were printed using thermoplastic polyurethane NinjaFlex filament (<http://ninjatek.com/products/ninjaflex-filaments>) with a Makerbot 3D printer. The remaining barbule-inspired designs were 3D-printed using a Stratasys Objet260 Connex3 printer (Stratasys, MN, USA). TangoBlack and VeroClear (Stratasys, MN, USA) filament as well as combinations of the two were used to print the structures.

7.2.2. Fabrication of Bioinspired Feather Laminate

Since synthetic materials with β -keratin-like properties are not easily accessible, and because we are observing differences in fiber orientations, we used regularly available composite materials. The center of the composite, which resembles the medullary foam of the shaft is composed of a polyethylene foam cylinder with a density of 0.035 g/cm^2 and a compressive modulus of 0.139 MPa. The foam cylinders were 1½” in diameter and 14” long, purchased from the foam factory (www.thefoamfactory.com). The cortex of the synthetic feather shaft was fabricated using unidirectional S-glass fiberglass (www.acpsales.com) with an elastic modulus of 86 GPa, fracture strength of 4.5 GPa and tensile strength of 4.7 GPa. Epoxy resin system 2000 epoxy resin and hardener 2020-A (www.fibreglast.com) was used with the fiberglass to create each lamina. The epoxy and hardener had a tensile modulus of 2.89 GPa, flexural strength of 0.12 GPa, and tensile strength of 0.07 GPa.

Four types of samples were fabricated with a total of four layers of fiberglass in each sample. Sample type A had all fibers oriented longitudinally, B had all fiber oriented circumferentially, C had fibers oriented at a 45° angle, and D had the first two layers oriented longitudinally and the outer two layers oriented circumferentially. Each of these types of samples either reflected the orientation of fibers in a part of the feather shaft or served as a means of comparison.

7.2.3. Adhesion Tests of Flexible Bioinspired Hooks and Grooves

Hooks and grooves inspired by the barbules of the feather vane were drawn in SolidWorks (SolidWorks Corp., Waltham, MA, USA) and 3D printed using a MakerBot 2 Replicator (MakerBot, New York, NY, USA). In order to explore the differences in adhesion due to hook shape, five different hook shapes were created and with the same groove shape.

In the adhesion experiments, hooks and grooves were manually interlocked before testing and “barbs” were secured in testing grips. Tension was applied to the sample by displacing barbs apart from one another at a strain rate of $1.6 \times 10^{-3} \text{ s}^{-1}$ using an Instron 3342 mechanical testing machine (Instron Corp.) with a load cell of $500 \text{ N} \pm 0.5 \text{ N}$. Each set of hooks was tested three times with the same set of grooves.

Hooks and grooves were then tested for their ability to re-adhere without external assistance (as witnessed in the feather vane). This was done by bringing hooks and grooves back to their original gauge length, and then displacing barbs apart from one another (without manually interlocking hooks and grooves) at a strain rate of $1.6 \times 10^{-3} \text{ s}^{-1}$. This test was repeated three times.

7.3. Results and Discussion: Barbule Inspired Structures

Results from previous chapters provide new insight about the feather, leading to the creation of bioinspired designs. While these bioinspiration efforts provide innovative solutions, they also allow us to simplify the feather’s complex structure so that we may more easily

understand nature's design. Arguably the most important aspect of barbule adhesion is the interlocking hook-and-groove mechanism. Despite their importance in flight, they are understudied and the author of this dissertation does not know of any attempt to create a barbule inspired structure. Here we develop several barbule-inspired designs based on results obtained in studies discussed in previous chapters.

7.3.1. Barbule Structure Simplification

Using scanning electron micrographs, the general interlocking structure of the barbule's hook and groove mechanism was explored with the goal of capturing the principal elements of the mechanism. Multiple hooks were observed to branch from a single distal barbule and fit into juxtaposed grooved proximal barbules. Both sets of barbules branch from barbs at an angle and are thought to slide along one another initial detachment occurs. From these initial observations, the first bioinspired model of the barbule structure was fabricated through 3D printing (**Figure 7.5**).

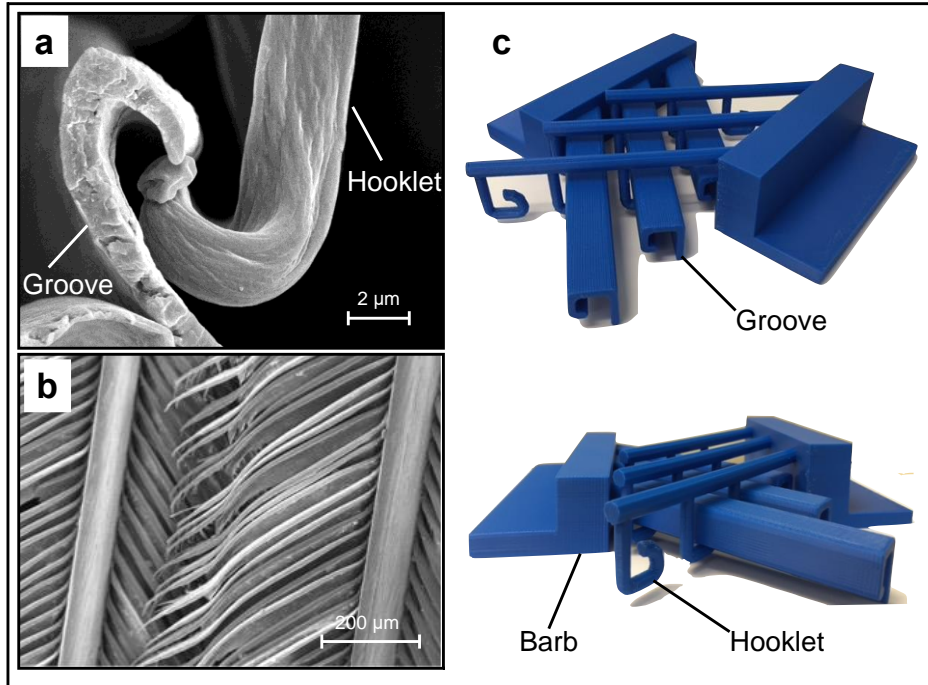


Figure 7.5 The interlocking structure of the barbules: micrographs of the House sparrow (*Passer domesticus*) show (a) the hooklet sliding into the grooved proximal barbule, (b) overlapping barbules within a feather. This interlocking mechanism was simplified and then constructed using additive manufacturing to create a three-dimensional model (c). Taken from [77].

7.3.2. Flexible Barbule Design

Observing the unzipping of the feather clearly reveals that barbules exhibit elastic deflection when pulled apart. This is not captured by the initial model, which is composed of rigid ABS plastics. In an attempt to copy the compliance of barbule connections, hook and grooved barbules were printed with a flexible filament material (NinjaFlex filament, Elastic Modulus=12 MPa) (**Figure 7.6**). However, the thick groove structure was too rigid to flex when barbules were unzipped, and therefore this model did not exhibit the elastic response desired.

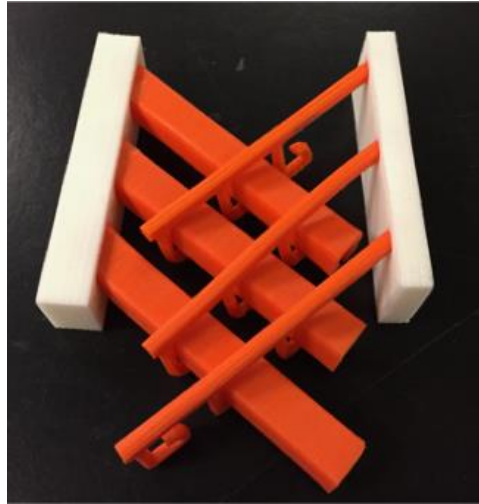


Figure 7.6 The second attempt at a barbule bioinspired model, using a flexible filament material for the barbule hooks and grooves.

Following this, hooks and grooves were altered to have a thinner, more flexible design. These were 3D-printed using the same flexible filament material and were found to exhibit a controllably elastic response (**Figure 7.7**). Different hook designs were printed and mechanically tested in adhesion to determine any differences in response based on shape.

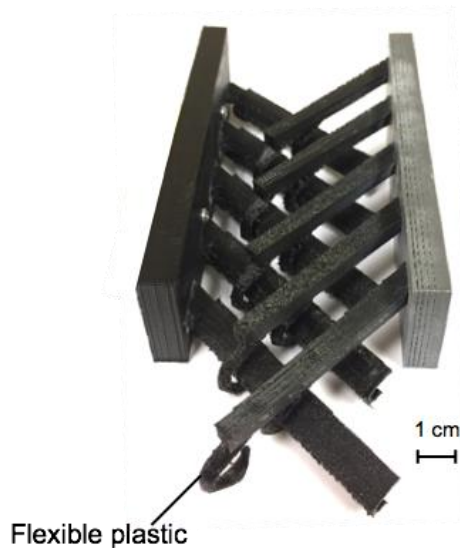


Figure 7.7 The third attempt at creating a bioinspired barbule model. Barbules were thinner and composed of a flexible filament material.

Adhesion experiments with 3D-printed grooves and various bioinspired hooks elucidate important features of hook design in the vane through simplification and scaling-up. Bioinspired barbules are composed of material with a considerably lower elastic modulus (NinjaFlex filament) than the feather to compensate for their significantly larger dimensions, providing a similar stiffness and comparable adhesion characteristics to the feather. The hook thickness, shape and wrap at its end were investigated as aspects influencing adhesion. Hooks A-C are thicker at the base of the hook (4mm) than hooks D and E (2.2mm); hooks A,C and D have a rectangular shape while hooks B and E have a circular shape. Lastly, hook C has a shorter tip and therefore wraps around grooves less effectively than the other shapes.

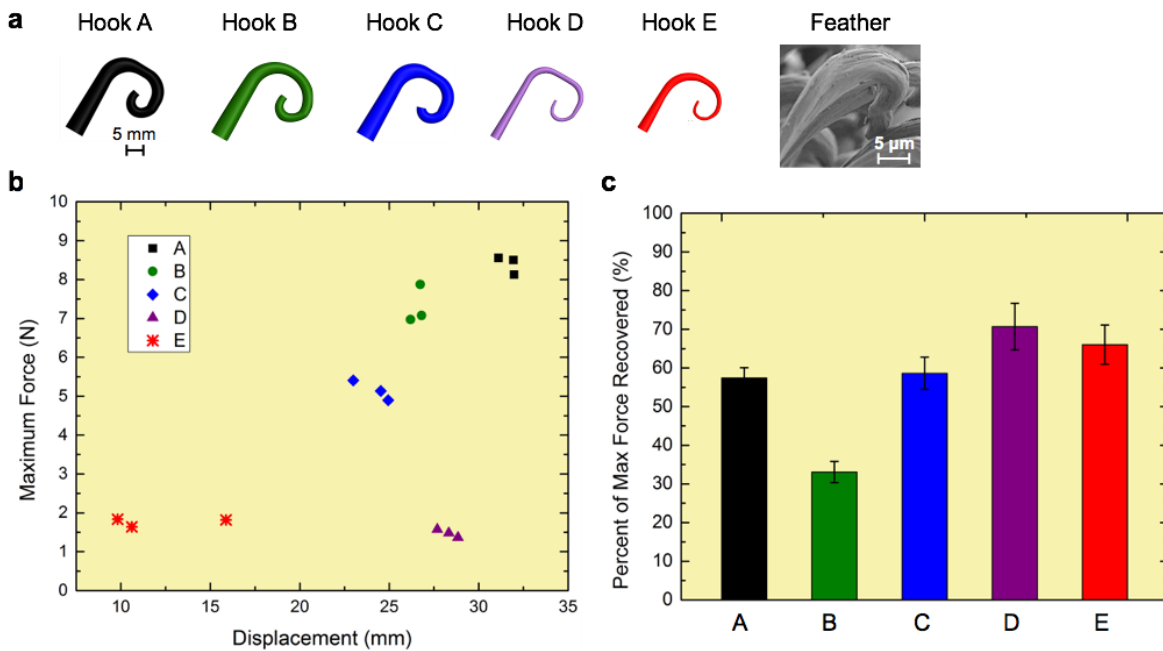


Figure 7.8 Adhesion of bioinspired hook and groove structures [155]: (a) Hooks A-E were created through 3D printing. (b) The maximum force vs. displacement for tension tests of the hook and groove structures reveal that hook A has the maximum force of adhesion. (c) Hooks D and E were found to have the highest percent of maximum force recovered in re-adhesion tests. The same set of grooves were used for all adhesion tests.

As one of the thicker hooks created, A, has the highest maximum adhesion force, effectively wrapping around the groove structure with a rectangular-shaped hook (**Figure 7.8 a,b**).

Re-adhesion experiments, measured by the percent of maximum force recovered in cyclical tests without manually interlocking hooks, reveal that hooks D and E perform best while hook B re-adheres worst (**Figure 7.8c**). The flexibility of hooks D and E (due to their small thickness) allow them to easily bend around grooves and re-attach when displaced back to their original position. Hook E, however, has less total hook length than hook D, resulting in a smaller displacement at its maximum force. The increased curvature of hook B serves as an obstacle for re-adhesion, though it provides a tight-fitting connection to the groove for interlocking adhesion. In these experiments it was found that a rectangular hook shape provides more strength for interlocking attachment than a circular hook shape [63]; thinner hooks allow for enhanced recovery of attachment, and a wrapped hook tip (as compared between A and C) increases the maximum force but does not significantly influence re-adhesion. Both experiments demonstrate the importance of the hook shape on two necessary functions of the vane: adhesion and the ability to re-adhere. Hooks evolved to strike an optimum balance between these two functions with seemingly contrasting requirements.

7.3.3. Barbule Inspired Designs With Membrane Flaps

Research on the directional permeability of the feather vane (as described in Section 5.2.6) shed light on the importance of the membrane flaps that extend from each barbule. These flaps act as one-way valves, allowing air to flow dorsally through the vane but not ventrally (**Figure 7.9a,b**). In this manner, the flaps act as one-way valves to capture air when the bird is executing a downstroke, but allow air through in the upstroke. A bioinspired model of barbules with these flaps was 3D printed out of flexible material (Stratasys FLX9095 filament) to describe this directional permeability (**Figure 7.9c,d**).

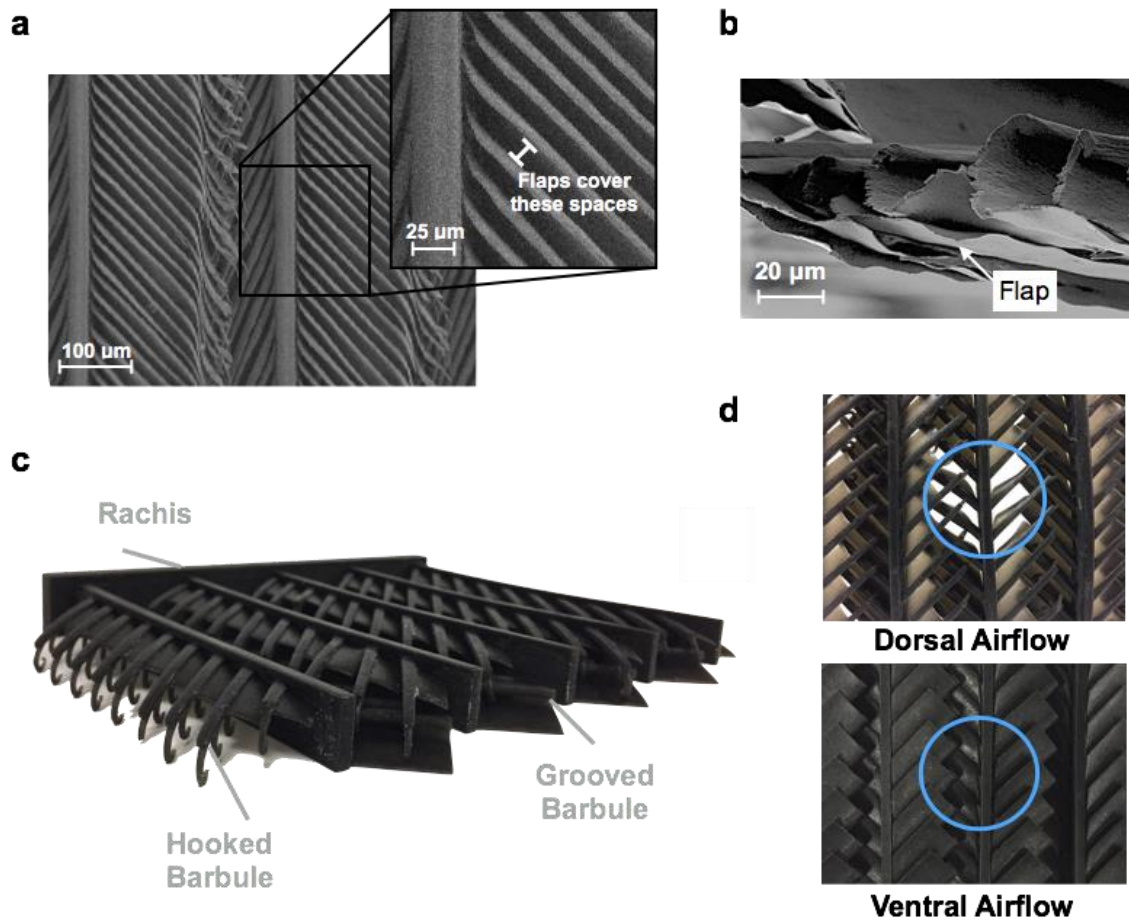


Figure 7.9 The directional permeability in the feather vane is due to membrane flaps that extend from barbules to act as one way valves covering the space between barbules. Scanning electron micrographs show these flaps (a,b). (c) A simplified 3D printed model of the feather vane, and (d) the reaction of membrane flaps as air is blown dorsally (top) and ventrally (bottom) where blue circles represent air flow. Images from [155].

With this information acquired, a complete feather structure was 3D printed (**Figure 7.10**). The membrane flaps were printed with a flexible material to allow them to flex open with dorsal airflow. Barbules, however, were composed of stiff material to permit hooks to slide along grooves with ease. Barbs were made out of flexible material so that they are able to bend apart from one another as barbules are unzipped.

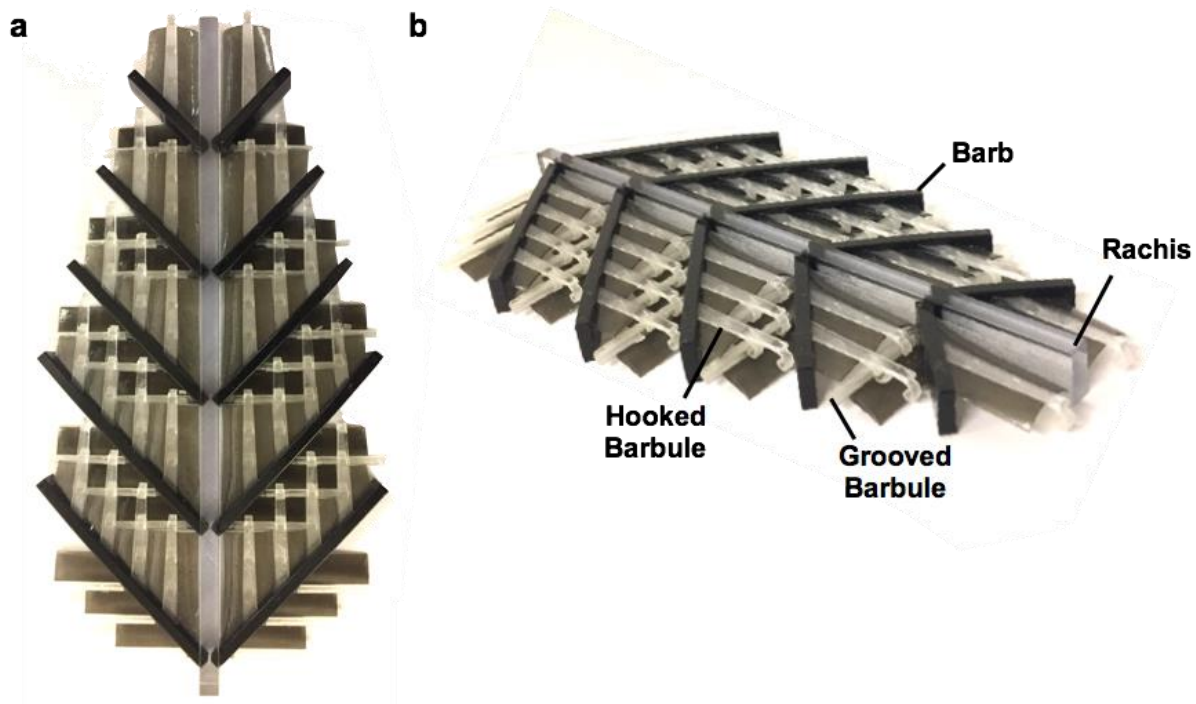


Figure 7.10 (a,b) Features of the feather vane were simplified and 3D printed into a bioinspired model of the entire feather.

7.3.4. Barbule-Inspired Designs to Allow for Tailored Air Permeability

By analyzing 3D printed models we realized that the feather vane may have two levels of control over air permeability. First, as previously discussed, membranes allow for air to flow through the spaces between barbules dorsally but not ventrally. Second, as hooks slide along grooves, expansion within the feather vane perhaps offers another level of tailored permeability. When hooks are slid close to the base of the groove, the vane is much tighter than when hooks are at the tip of the groove, nearly ready to detach. This concept was used to create a bioinspired design that mimics this behavior. **Figure 7.11** shows an assembly of barbules attached on either end with a flexible material. As this is stretched, barbules slide along one another leading to slight openings between each barb's set of barbules. **Figure 7.11 b** shows the opening within the vane by stretching, indicated by the four hands pulling it apart.

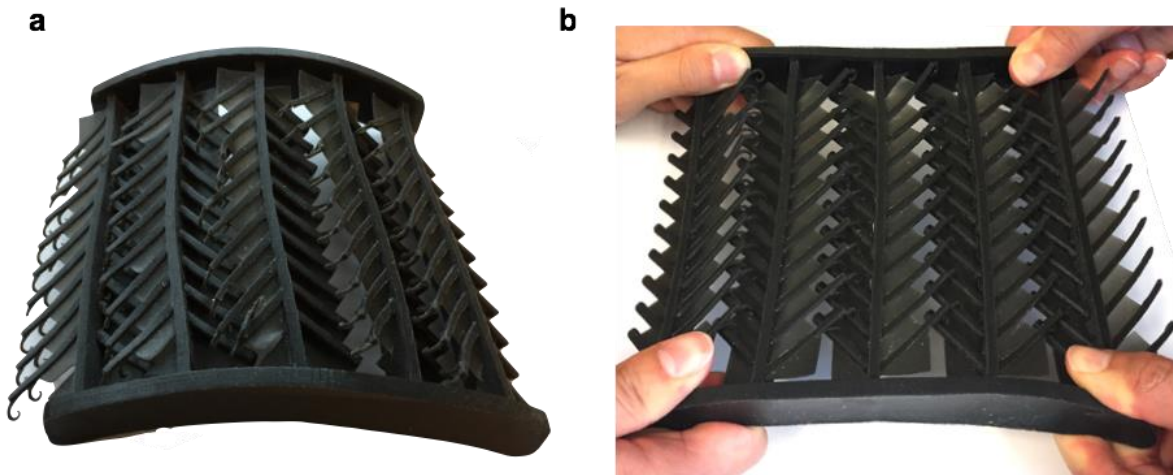


Figure 7.11 (a) Barbules are bounded on both ends with a flexible material, (b) when these ends are pulled apart, feather become more permeable as space between each barb's barbules opens.

Hooks were identified as a weak point of the design, because their thin structure has a tendency to break. To overcome this, another design was created with only grooves, where each groove slides into one another (**Figure 7.12**). These structures are not able to completely detach due to stoppers placed at the end of each groove. Adding this feature makes the design more amenable to real-world applications where tailored permeability is desired, but complete material failure is detrimental.

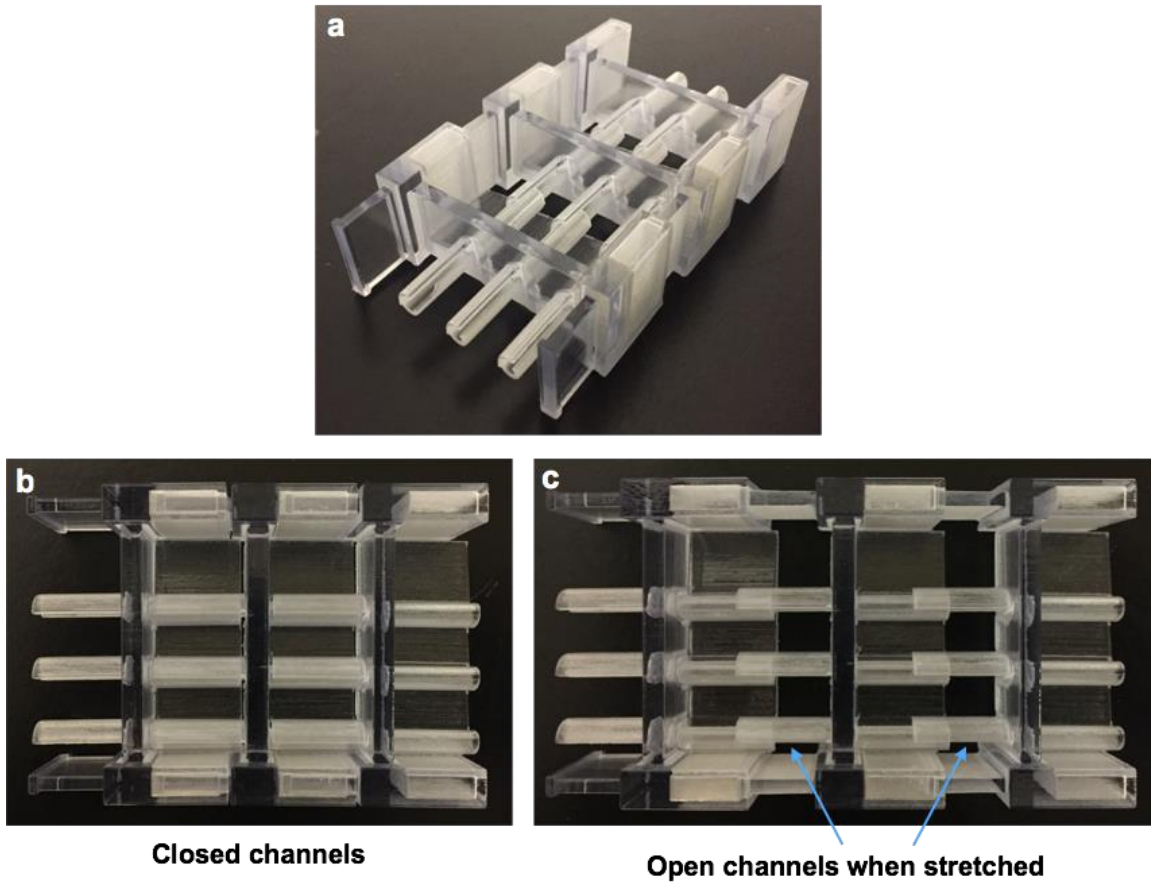


Figure 7.12 Grooved structures that slide along one another were created to allow for a design that has tailored permeability based on the distance edges are pulled apart from one another.

To display the same behavior, we realized the structure could be simplified even further to aid in ease of manufacturing. Therefore, a square tubing model was created that allows for increased permeability when pulled apart (**Figure 7.13a**). A square slides within a hollow tube until it is stopped at the end of the tubing, behaving similarly to a piston. This model was scaled down further to allow for more flexibility in the material (**Figure 7.13b,c**).

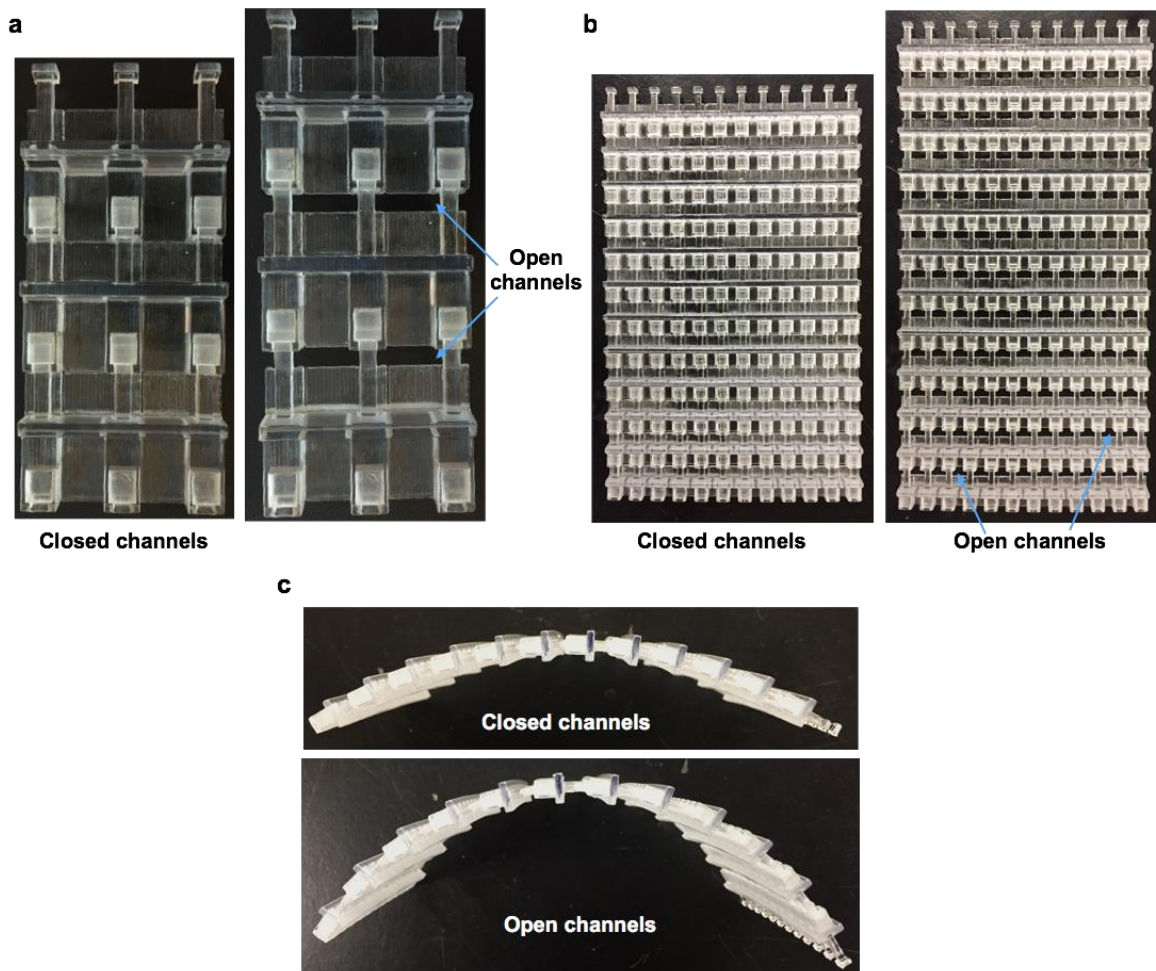


Figure 7.13 The square tubing model: (a) Squares slide through a tube and are stopped at the end. This allows the material to have tailored permeability. (b) As the material is scaled down smaller, it becomes more flexible as shown in (c).

One of the shortcomings identified with this design is that it maintains a rigid structure in the direction perpendicular to the sliding. To allow for more flexibility, the design was altered to have sliding in two dimensions (**Figure 7.14a-d**). This structure also becomes more flexible when stretched open (**Figure 7.14d**) due to the increase in spacing between sections.

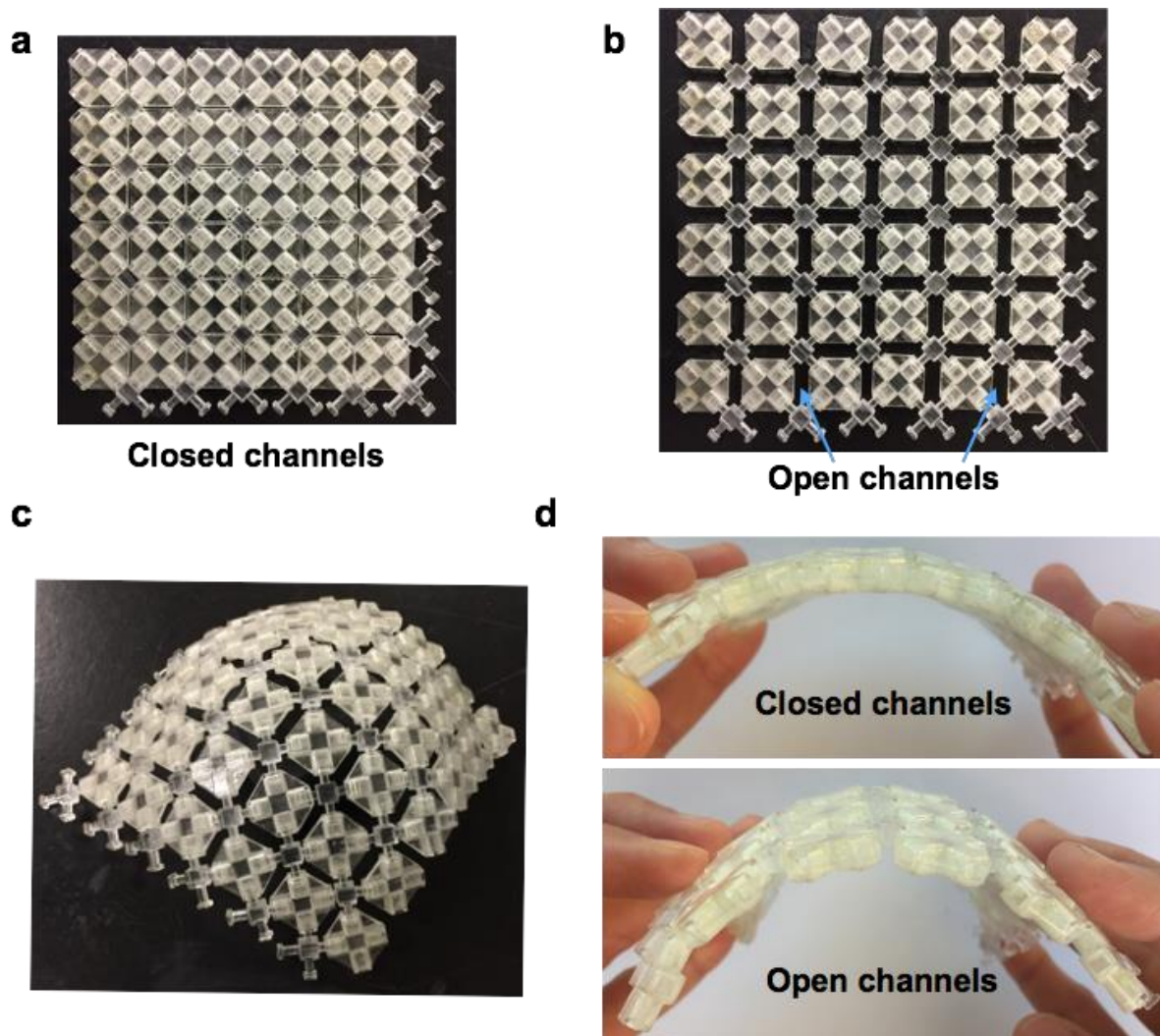


Figure 7.14 (a,b)The square tubing model was altered to stretch in two dimensions, allowing for increased flexibility in the material (c) which is reflected in images of the maximum radius of curvature of closed and opened samples (d).

In further departure from the original barbule mechanism, a tridimensional structure was created by using, now triple grooved elements (along three axes) that slide in three dimensions. The cube manufactured by this method is shown in **Figure 7.15** with its bottom right corner shown compressed and top left corner shown stretched in **Figure 7.15 b**.

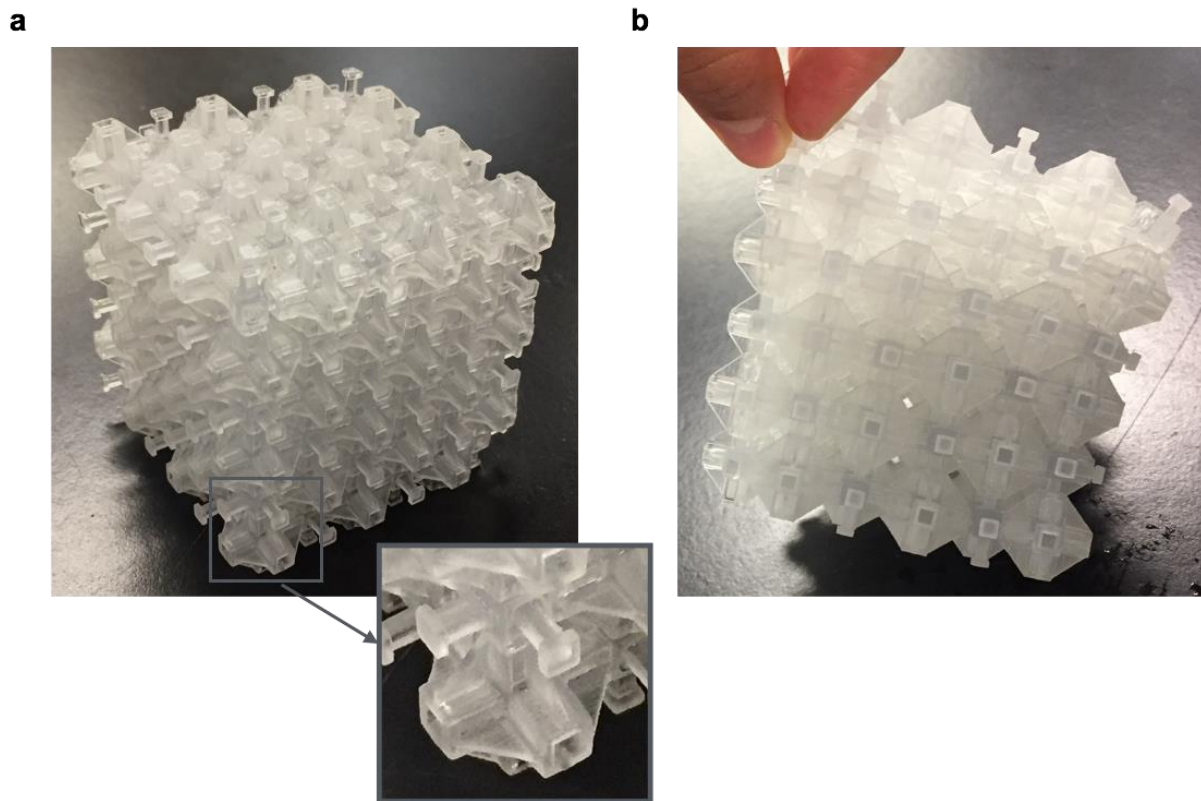


Figure 7.15 Tridimensional structure using the grooved design in which each element has six pegs aligned with three orthogonal axes.

7.3.1. Summary of Bioinspired Barbules

The complex nature of barbules provides fertile ground for insight into new, bioinspired designs. Here we pursue designs that relate to the most important aspects of our research discoveries. The timeline of our bioinspired designs shown in **Figure 7.16** demonstrates the evolution and incorporation of various features into designs.

Figure 7.16 Timeline of the evolution of bioinspired barbule designs: from the feather to tridimensional structures.

**Interlocking Hooks
and Grooves**



**Incorporating the
Flexible Membrane**



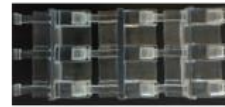
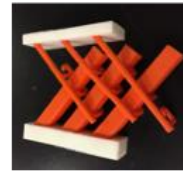
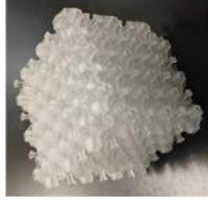
**Stretching to achieve
tailored permeability**



**Two-dimensional
sliding for increased
flexibility**



**Three-dimensional
sliding**



Time

7.4. Designs Inspired by the Feather Shaft

7.4.1. Bioinspired Medullary Foam Design

The study of the avian feather shaft provides unique opportunities for the development of novel bioinspired structures and materials. The extreme requirements of lightweight, structural stiffness and strength are highly desirable features in synthetic structures, especially in transportation systems. For example, the structure of the feather's foam can be mimicked through 3D-printing and/or electrospinning to create a new type of hierarchical foam composed of fibrous closed cells. This "foam within a foam" concept is shown **Figure 7.17**. This hierarchical foam would result in a novel design that maintains stiffness while decreasing overall weight.

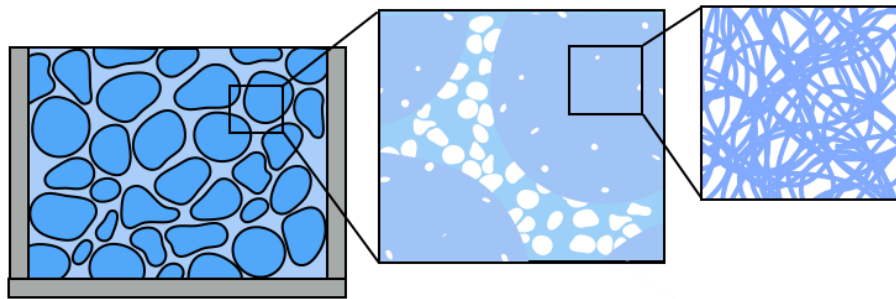


Figure 7.17 A foam structure inspired by the fibrous closed-cell structure of the feather's medullary foam would have novel properties.

7.4.2. Bioinspired Feather Laminate Design

By simulating the fiber directionality within the distal rachis, where fibers run longitudinally on the top and bottom and at $\pm 45^\circ$ angles on the sides, a new type of composite I-beam can be created with increased torsional stiffness [204]. Its bending stiffness would be maintained while the $\pm 45^\circ$ fibers would provide additional torsion resistance to expand the functionality of the common I-beam structure. While we did not attempt to fabricate an I-beam structure, foam-filled fiberglass composites were created following fiber directions utilized in the feather shaft (**Figure 7.18**). Four configurations for the reinforcing fibers are shown. This is akin

to the design of conventional composites, but the presence of a cellular core adds an additional, and important component to the cylindrical beam.

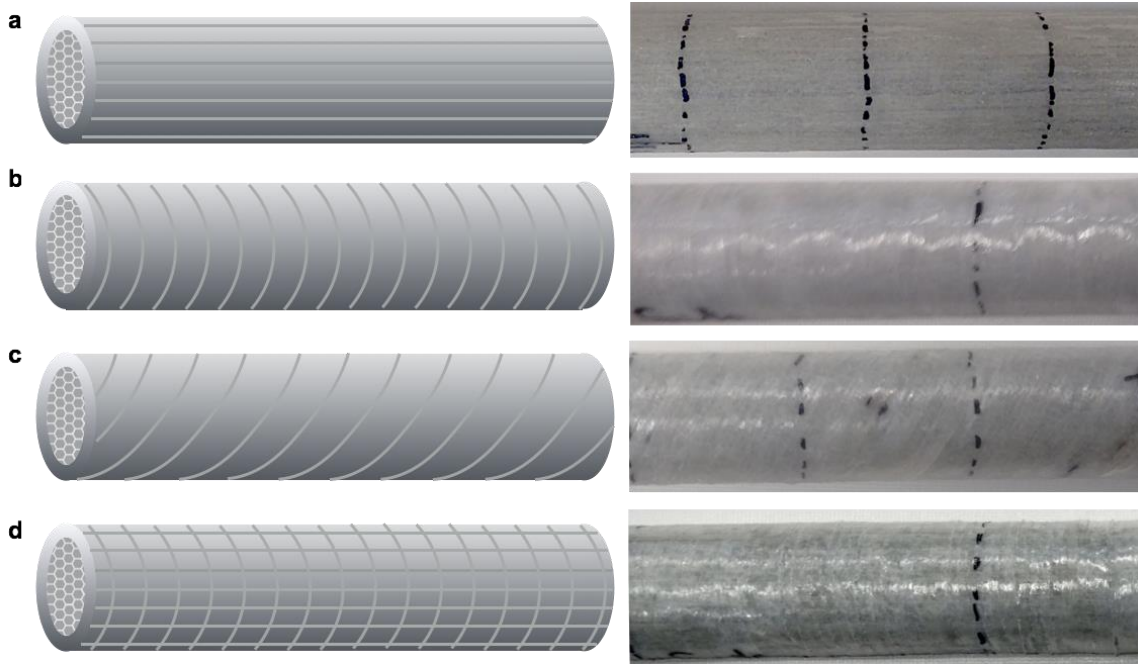


Figure 7.18 Four types of cylindrical feather shaft-inspired samples were created. (a) Has fibers running longitudinally along the shaft, (b) Has fibers running circumferentially around the shaft, (c) has fibers running at a 45 degree angle along the shaft, (d.) Has two inner layers running along the axis of the shaft and a two outer layers running circumferentially around the foam.

7.4.3. Shape Memory Recovery Inspired Design Concept

The mechanisms discovered in shape memory recovery of the feather shaft can be employed to create more effective shape memory composites. We have created a simplified bioinspired model that employs the swelling concept witnessed in β -keratin (**Figure 7.19**). In this model, the cellulose sponge (light color) swells when hydrated, reorienting the stiffer “fibers” (dark color) back into position. This same concept could be used to create new bioinspired shape memory composites for applications ranging from biomedical devices to self-healing materials.

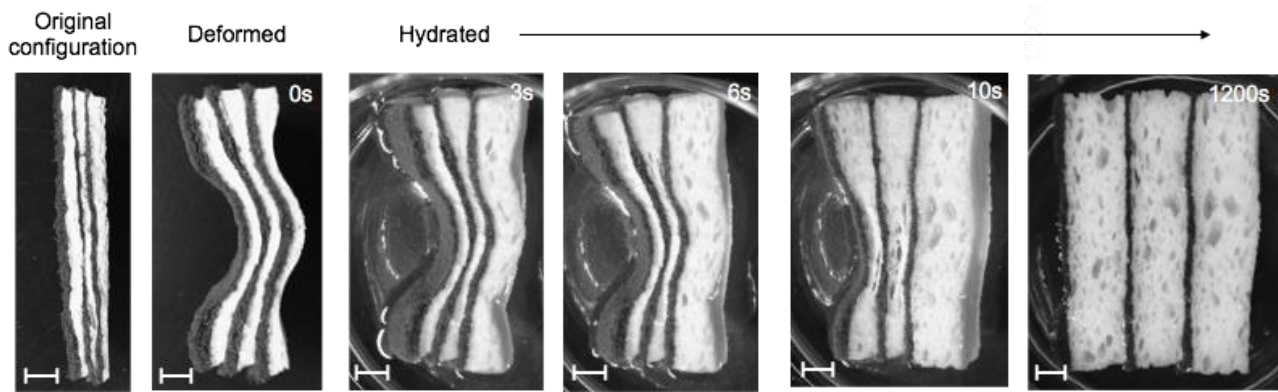


Figure 7.19 Shape Memory Bioinspired Composite Structure.

7.4.4. Shape Change Inspired Design

Lastly, a column inspired by the changing shape of the rachis from circular to rectangular provides a structure that is optimized for torsion in one area (circular portion) and for bending stiffness in the other (rectangular portion). A possible use for these structures would be as support columns to create more earthquake-resistant buildings where both torsional or bending stiffness can be tailored along the length of the column [205].

7.5. Conclusions

There is great potential for the creation of novel, bioinspired designs based on the feather. Through the evolution of over 3 billion years of life on Earth, nature has developed unique structures and materials. Bird flight has evolved starting over 50 million years ago, providing the intricate designs witnessed today. In this chapter, the barbule structure is simplified to create bioinspired designs for the first time. Experiments on synthetic hook and groove barbules reveal that hooks must balance conflicting requirements for adhesion and effective re-adhesion, two

important properties of the vane. New designs based on the tailored permeability of the feather vane are created. Bioinspired feather shaft designs are discussed, and the laminate structure within the feather vane is fabricated using fiberglass and epoxy. Research on the feather vane is just beginning, and we believe it is still rich in potential for novel bioinspired designs.

7.6. Acknowledgements

Chapter 7, in part, is published as a review article in *Materials Today*, authored by T. N. Sullivan, B. Wang, H.D. Espinosa, and M.A. Meyers. The dissertation author was the primary investigator and author on this publication.

Chapter 7, in part, is published in *Acta Biomaterialia* and is authored by T.N. Sullivan, A. Pissarenko, S.A. Herrera, D. Kisailus, V.A. Lubarda and M.A. Meyers. The dissertation author was the primary investigator and author on this publication.

Chapter 7, in part, is published in *Advanced Functional Materials*, authored by T.N. Sullivan, M. Chon, R. Ramachandramoorthy, M.R. Roenbeck, T.-T. Hung, H.D. Espinosa, and M.A. Meyers. The dissertation author was the primary investigator and author on this publication.

Chapter 7, in part, will be revised and submitted for publication to *Advanced Materials*, authored by T.N. Sullivan, Y. Zhang, Z. Liu, P. Zavattieri and M.A. Meyers. The dissertation author is the primary investigator and author on this manuscript.

Chapter 7, in part, is being prepared for submission for publication, authored by T.N. Sullivan, T.-T. Hung and M.A. Meyers. The dissertation author is the primary investigator and author on this manuscript.

We would like to acknowledge undergraduate students Estelle Jouret and Keenan Finney for assistance with feather shaft laminate fabrication.

8. Summary and Future Outlook

For thousands of years mankind has marveled at the bird's ability to fly; in Greek mythology, Icarus gained this ability using bird feathers and wax but approached the sun and fell to his death as the feathers loosened. Leonardo da Vinci, Otto von Lilienthal, and the medieval monk Eilmer of Malmesbury developed glider designs based on birds and bats. The crowning step was to attach a motor and propeller to it, which was done by the Wright brothers and Alberto Santos-Dumont.

While advances in science and technology have provided us the ability to fly using airplanes and spaceships, the efficiency of a bird in flight continues to be elusive. Over fifty million years of evolution and natural selection have allowed for birds with a multitude of designs, with the most efficient, effective, and better adapted structures being what we witness today. These structures and materials are a source of inspiration to engineers. In this dissertation, elements of the flight feather are explored to uncover novel concepts transferable to the design of manufactured aerospace materials and structures. A particular emphasis is placed on the feather's resilient and lightweight properties as these are highly desirable traits to mimic in commercial applications.

8.1. Summary

To better understand the efficiency of bird wings in flight, we investigate scaling relationships of the bird wing and its components. The strength of avian bone is hypothesized to be a limiting factor in the scaling of the humerus with mass. This is supported by its experimentally determined allometric scaling relationship. We also find that the relative humerus length relates to increased wing loading and speculate that this allows for greater variability in specific applications and flight styles. By studying scaling effects in feathers, we have uncovered a fascinating fact: while feather shaft length, rachis width and barb length all scale isometrically with bird mass, barbule spacing is approximately the same, 8-16 μm , independent of the size of

the bird. We suggest that this spacing is an optimal dimension evolved over millions of years to provide a specific level of permeability through the vane for enhanced flying efficiency.

In this dissertation, each component of the feather vane is investigated. Due to its asymmetrical shape, the rotation or twisting of barbs allows it to become less stiff with respect to its y-axis. Several models were created to describe the barb's linear flexure behavior. Zipped and un-zipped barbs demonstrate different flexure behaviors, with zipped barbule connections preventing the rotation of barbs and allowing for a more robust vane. An interest in the significance of barbule connections led us to further investigate these structures.

Barbule adhesion experiments indicate that the feather vane maintains in-plane tautness through contrasting directions of rotational preference at each hierarchical level. The stiffness of a single barbule, which is crucial in understanding the critical failure of barbule connections, is found by *in-situ* SEM experiments. When barbules are unzipped feathers are found to less effectively capture air, where the magnitude of this is correlated to barb dimensions. Finally, the feather vane is experimentally determined to have unidirectional permeability due to membranous barbule flaps that act as one-way valves. Barbules are exquisitely developed structures that enable impressive failure aversion combined with air capture.

The resilience of the nanoscale composite β -keratin is revealed through experiments on the feather shaft. The feather's ability to recover strength with hydration is demonstrated, and explained through experimentally supported models. The swelling and softening of the feather's matrix material with hydration is thought to allow for the reorientation of crystalline fibers, enabling the recovery of the shaft's strength.

Finally, bioinspired structures reflecting the most significant parts of our research on barbules and feather shaft were created. An invention disclosure was submitted on the design of

the interlocking mechanism. This mechanism has many interesting potential applications such as directionally-controlled adhesive or a novel aerospace material.

8.2. Future Outlook

In closing, this dissertation points to the possibility of framing avian flight feather design as a combined material and structural optimization problem subject to aerodynamic constraints. Feathers provide a complex synergy that enables the efficiency of birds through material-structure specialization for flight. These multi-functional β -keratinous structures provide inspiration for new, more efficient aerospace materials with features such as tailored permeability and localized failure. While modern research has resulted in some instances of analogous solutions to increase torsional and bending stiffness, there are very few efforts of deliberate bioinspiration of the feather. We feel that this is an area rich with opportunity for creating advanced materials and structures. Therefore, we anticipate that with improvements in mathematical and computational tools for multi-material multi-scale optimization and design, and experimental tools based on additive manufacturing, bioinspiration based on studies contained in this dissertation will be applied to further man-made structures to exhibit the same degree of sophistication and complexity as observed in bird's wings.

9. Appendix

9.1. Foam Calculations

The closed-cell foam inside of the barb was simplified to a hexagonal prism shape. The relative density was calculated where A_r is the aspect ratio [43] :

$$\frac{\rho^*}{\rho_s} = \frac{2}{\sqrt{3}} \frac{t}{l} \left\{ 1 + \frac{\sqrt{3}}{2A_r} \right\}.$$

Table 9.1 below shows the definitions and values measured for each variable.

Table 9.1 Values for Foam Calculations

Variable	Definition	Value
ρ^*/ρ_s	Density of Foam / Density of solid	0.152 ± 0.08
$t = t_f$	Thickness of foam cell-wall	$0.875 \pm 0.37 \mu m$
l	Foam cell edge length	$9.78 \pm 2.37 \mu m$
A_r	Aspect ratio h/l_f	1.83 ± 0.67
h	Height of foam cell	$17.92 \pm 4.97 \mu m$
t_e	Thickness of foam cell edge (corner)	$3.39 \pm 2.08 \mu m$
ϕ	Volume fraction of cell located in the cell edges	0.627 ± 0.83
Z_f	Number of faces that meet at an edge on a single cell	3.6 [10]
\bar{n}	Average number of cells per single cell	4.5 [10]
$\frac{E^*}{E_s}$	Foam elastic modulus / Solid material elastic modulus	0.066

Next, the volume fraction was calculated [43]:

$$\phi = \frac{t_e^2}{t_e^2 + \frac{Z_f}{\bar{n}} t_f l}.$$

This is the volume of solid material contained in cell edges. The remaining volume fraction of the cell $(1 - \phi)$ is in cell faces.

Lastly, to find the relative elastic modulus we used [43]:

$$\frac{E^*}{E_s} \approx \phi^2 \left(\frac{\rho^*}{\rho_s} \right)^2 + (1 - \phi) \frac{\rho^*}{\rho_s},$$

where the influence from internal gas pressure is ignored because of the porosity observed in SEM images of the cells.

9.2. Determining the Location of the Neutral Axis

The solutions for the specific case of the barb are found in section 9.2.

Using the dimensions given in **Figure 9.1**, the location of the neutral axis for each rectangular piece is solved for in terms of an arbitrarily set location of the overall neutral axis (x_o, y_o) , which incorporates the elastic modulus of each piece:

The location of the centroid of each rectangular piece (x_{ci}) is determined along the x-axis:

$$x_1 = -h_3 + x_o + \frac{\delta_1}{2}$$

$$x_2 = -h_3 + x_o + \delta_5 + \frac{\delta_2}{2}$$

$$x_3 = \frac{h_3}{2} - x_o$$

$$x_4 = x_o - h_3 + \delta_2 + \delta_5 + \frac{\delta_4}{2}$$

$$x_5 = -h_3 + x_o + \frac{\delta_5}{2}$$

The location of the centroid of each rectangular piece (y_{ci}) is determined along the y-axis:

$$y_1 = -h_2 + y_o - \frac{h_1}{2}$$

$$y_2 = -\frac{h_2}{2} + y_o$$

$$y_3 = y_o + \frac{\delta_3}{2}$$

$$y_4 = -\frac{h_4}{2} + y_o$$

$$y_5 = -\frac{h_5}{2} + y_o$$

These equations are used in the Equations (4.8) and (4.9) to find the actual location of the neutral

axis x_0, y_0 .

$$x_0 = h_3 - \frac{E_1[\delta_1 A_1 + h_3 A_3 + A_4(2\delta_2 + \delta_4 + 2\delta_5) - \delta_5 A_5] + E_2(\delta_2 A_2 + 2\delta_5 A_2)}{2[E_1(A_1 + A_3 + A_4 + A_5) + E_2 A_2]},$$

$$y_0 = \frac{E_1(2h_2 A_1 + h_1 A_1 - \delta_3 A_3 + h_4 A_4 + h_5 A_5) + E_2(h_2 A_2)}{2[E_1(A_1 + A_3 + A_4 + A_5) + E_2 A_2]}.$$

The specific values used in calculations can be found in Table 9.2.

Table 9.2 Simplified barb dimensions. Units are in micrometers unless otherwise labeled.

Dimension	
δ_1	79
δ_2	48
δ_3	39
δ_4	16.5
δ_5	16.5
h_1	40
h_2	454
h_3	103
h_4	454
h_5	454
z	7809
$I_{xcortex}$	$6.93 \times 10^8 \mu m^4$
I_{xfoam}	$3.76 \times 10^8 \mu m^4$
$I_{ycortex}$	$1.14 \times 10^7 \mu m^4$

9.3. Deriving the Inverse Curvature of M_y

The derivation of the relationship between the moment M_y and the inverse curvature is listed below. This was used to obtain Equations (4.17) and (4.18) of the main text.

We begin with the moment-stress relationship:

$$M_y = \sum_{i=1}^n \int_{A_i} x \sigma_z^{(i)} dA.$$

By substituting expressions of $\sigma_z^{(i)}$, we obtain:

$$M_y = \sum_{i=1}^n \int_{A_i} x E_i (ax + by) dA$$

i.e.,

$$M_y = \sum_{i=1}^n E_i \left[a \int_{A_i} x^2 dA + b \int_{A_i} xy dA \right].$$

Therefore:

$$-M_y = a \sum_{i=1}^n E_i I_y^i + b \sum_{i=1}^n E_i I_{xy}^i,$$

where

$$I_y^i = \int_{A_i} x^2 dA \text{ and } I_{xy}^i = \int_{A_i} xy dA.$$

9.4. Acknowledgments

Chapter 9, in full is published in *Acta Biomaterialia* and is authored by T.N. Sullivan, A. Pissarenko, S.A. Herrera, D. Kisailus, V.A. Lubarda and M.A. Meyers. The dissertation author was the primary investigator and author on this publication.

10. References

- [1] M.A. Meyers, P.-Y. Chen, *Biological Materials Science: Biological Materials, Bioinspired Materials, and Biomaterials*, Cambridge University Press, Cambridge, UK, 2014.
- [2] S. St.Clair, Burdock Burrs-Nature's Velcro, *All Nat.* (2011).
<http://allofnature.blogspot.com/2011/11/burdock-burrs-natures-velcro.html>.
- [3] Barcroft media, Microcosmos: scanning electron microscope images of insects, household items and human body parts, *Telegr.* (2017).
- [4] C. Suddath, A Brief History of: Velcro, *Time.* (2010).
- [5] N.P. Group, *Bioinspired Materials*, (2016). nature.com (accessed May 31, 2016).
- [6] J.J. Videler, Avian Flight, in: T.R. Birkhead (Ed.), *Oxford Ornithol. Ser.*, Oxford University Press, Oxford, UK, 2005: pp. 2–7.
- [7] Smithsonian National Air and Space Museum, Leonardo da Vinci's Codex on the Flight of Birds, *Smithson. Natl. Air Sp. Museum.* (2013).
<https://airandspace.si.edu/exhibitions/codex/>.
- [8] Ask Nature, High speed train silently slices through air, *Ask Nat.* (2016).
<https://asknature.org/idea/shinkansen-train/#.WePhWRNSx24> (accessed January 1, 2017).
- [9] A. McFadyen, Kingfisher, *Flickr.* (2015).
<https://www.flickr.com/photos/46443141@N07/albums> (accessed January 1, 2017).
- [10] S. Doshi, 500 Series Shinkansen, *Flickr.* (2006).
<https://www.flickr.com/photos/samdoshi/331876289/in/photostream/> (accessed January 1, 2017).
- [11] T. Lingham-Soliar, N. Murugan, A new helical crossed-fibre structure of β -keratin in flight feathers and its biomechanical implications., *PLoS One.* 8 (2013) e65849.
doi:10.1371/journal.pone.0065849.
- [12] R.L. Nudds, G.W. Kaiser, G.J. Dyke, Scaling of avian primary feather length., *PLoS One.* 6 (2011) e15665. doi:10.1371/journal.pone.0015665.
- [13] J. Clarke, Feathers before flight, *Science.* 340 (2013) 690–692.
- [14] A. Louchart, L. Viriot, From snout to beak: The loss of teeth in birds, *Trends Ecol. Evol.* 26 (2011) 663–673. doi:10.1016/j.tree.2011.09.004.
- [15] Y. Seki, M. Mackey, M.A. Meyers, Structure and micro-computed tomography-based finite element modeling of Toucan beak, *J. Mech. Behav. Biomed. Mater.* 9 (2012) 1–8. doi:10.1016/j.jmbbm.2011.08.003.

- [16] F.T. Muijres, L.C. Johansson, M.S. Bowlin, Y. Winter, A. Hedenström, Comparing aerodynamic efficiency in birds and bats suggests better flight performance in birds, *PLoS One*. 7 (2012). doi:10.1371/journal.pone.0037335.
- [17] A. Wolfson, *A Recent Study in Avian Biology*, University of Illinois Press, Urbana, 1955.
- [18] X. Xu, K. Wang, K. Zhang, Q. Ma, L. Xing, C. Sullivan, D. Hu, S. Cheng, S. Wang, A gigantic feathered dinosaur from the Lower Cretaceous of China, *Nature*. 484 (2012) 92–95.
- [19] P. Chen, Z. Dong, S. Zhen, An exceptionally well-preserved theropod dinosaur from the Yixian Formation of China, *Nature*. 391 (1998) 147–152.
- [20] R.C. Mckellar, B.D.E. Chatterton, A.P. Wolfe, P.J. Currie, A Diverse Assemblage of Late Cretaceous Dinosaur and Bird Feathers from Canadian Amber, *Science* (80-.). 333 (2011) 1619–1622. doi:10.1126/science.1203344.
- [21] Z. Chuang, X. Lida, *Bird-Like Dinosaur Sported Bizarre Tail Feathers*, 2008. <https://www.livescience.com/2987-bird-dinosaur-sported-bizarre-tail-feathers.html>.
- [22] Z. Chuang, X. Lida, *Gigantoraptor*, *Sci. Am.* (2007). <https://www.scientificamerican.com/article/gigantoraptor-is-a-bird-is-a-dinosaur-is-a-mystery/>.
- [23] E.N. Kurochkin, I.A. Bogdanovich, On the origin of avian flight: Compromise and system approaches, *Biol. Bull.* 35 (2008) 5–17.
- [24] C.J. Pennycuick, *Modelling the Flying Bird*, 1st ed., Elsevier, Burlington, USA, 2008.
- [25] N.S. Proctor, P.J. Lynch, *Manual of Ornithology: Avian Structure & Function*, first ed., Yale UP, New Haven, USA, 1993.
- [26] F.B. Gill, *Ornithology*, second ed., W.H. Freeman, New York, USA, 1995.
- [27] P.M. O’Connor, L.P.A.M. Claessens, Basic avian pulmonary design and flow-through ventilation in non-avian theropod dinosaurs., *Nature*. 436 (2005) 253–256.
- [28] L. Xing, R.C. Mckellar, X. Xu, K. Tseng, H. Ran, P.J. Currie, M.J. Benton, J. Zhang, A.P. Wolfe, Q. Yi, A Feathered Dinosaur Tail with Primitive Plumage Trapped in Mid-Cretaceous Amber, *Curr. Biol.* 26 (2016) 1–9. doi:10.1016/j.cub.2016.10.008.
- [29] W. Muller, G. Patone, Air transmissivity of feathers, *J. Exp. Biol.* 201 (1998) 2591–2599. <http://www.ncbi.nlm.nih.gov/pubmed/9716511>.
- [30] J. Dyck, The Evolution of Feathers*, *Zool. Scr.* 14 (1985) 137–154. doi:10.1111/j.1463-6409.1985.tb00184.x.
- [31] K.E.J. Campbell, E.P. Tonni, *Size and Locomotion in Teratorns (Aves : Teratornithidae)*,

- Auk. 100 (1983) 390–403.
- [32] B. Bruderer, D. Peter, A. Boldt, F. Liechti, Wing-beat characteristics of birds recorded with tracking radar and cine camera, *Ibis* (Lond. 1859). 152 (2010) 272–291. doi:10.1111/j.1474-919X.2010.01014.x.
- [33] E. Novitskaya, M.S. Ribero Vairo, J. Kiang, M.A. Meyers, J. McKittrick, Reinforcing Structures in Avian Wing Bones, *Adv. Bioceram. Biotechnol. II.* (2014) 47–56.
- [34] J.M. V. Rayner, *Form and function in avian flight*, Plenum Press, New York, 1988.
- [35] C. Pennycuik, The strength of the pigeon's wing bones in relation to their function, *J. Exp. Biol.* 46 (1967) 219–233. <http://jeb.biologists.org/content/46/2/219.short>.
- [36] I.H. Abbott, A.E. von Doenhoff, *Theory of Wing Sections*, Dover Publications, New York, 1959.
- [37] S.M. Swartz, M.B. Bennett, D.R. Carrier, Wing bone stresses in free flying bats and the evolution of skeletal design for flight, *Nature.* 356 (1992) 133–135.
- [38] F.P. Beer, E.R. Johnston Jr., J.T. Dewolf, D.F. Mazurek, *Mechanics of Materials*, Fifth, McGraw-Hill, New York, 2009.
- [39] E.P. Popov, *Engineering Mechanics of Solids*, second ed., Prentice Hall, Upper Saddle River, 1998.
- [40] E. Novitsakaya, M.S. Ribero Vairo, M.M. Porter, V.A. Lubarda, M.A. Meyers, J. Mckittrick, Analysis of Reinforcing Struts in Avian Wing Bones, *J. Mech. Behav. Biomed. Mater. Under Rev.* (2016).
- [41] R. Ennos, *Solid Biomechanics*, Princeton University Press, Princeton, 2012.
- [42] E.R. Dumont, Bone density and the lightweight skeletons of birds., *Proc. Biol. Sci.* 277 (2010) 2193–2198. doi:10.1098/rspb.2010.0117.
- [43] L.J. Gibson, M.F. Ashby, *Cellular Solids: Structure & Properties*, second ed., Cambridge University Press, Cambridge, 1997.
- [44] J. Cubo, A. Casinos, Incidence and mechanical significance of pneumatization in the long bones of birds, *Zool. J. Linn. Soc.* 130 (2000) 499–510. doi:10.1006/zjls.
- [45] J.D. Currey, R. McN.Alexander, The thickness of the walls of tubular bones, *J. Zool. London.* 206 (1985) 453–468. doi:10.1111/j.1469-7998.1985.tb03551.x.
- [46] M.A. Meyers, P.-Y. Chen, A.Y.-M. Lin, Y. Seki, Biological materials: Structure and mechanical properties, *Prog. Mater. Sci.* 53 (2008) 1–206. doi:10.1016/j.pmatsci.2007.05.002.
- [47] T.N. Sullivan, B. Wang, H.D. Espinosa, M.A. Meyers, Extreme lightweight structures:

- avian feathers and bones, *Mater. Today*. (2017).
- [48] H.D. Espinosa, J.E. Rim, F. Barthelat, M.J. Buehler, Merger of structure and material in nacre and bone - Perspectives on de novo biomimetic materials, *Prog. Mater. Sci.* 54 (2009) 1059–1100. doi:10.1016/j.pmatsci.2009.05.001.
- [49] J.Y. Rho, L. Kuhn-Spearing, P. Zioupos, Mechanical properties and the hierarchical structure of bone, *Med. Eng. Phys.* 20 (1998) 92–102. doi:10.1016/S1350-4533(98)00007-1.
- [50] N. Reznikov, R. Shahar, S. Weiner, Bone hierarchical structure in three dimensions, *Acta Biomater.* 10 (2014) 3815–3826. doi:10.1016/j.actbio.2014.05.024.
- [51] S. Weiner, W. Traub, Bone Structure : From Angstroms To Microns, *FASEB J.* 6 (1992) 879–885.
- [52] H.D. Barth, E.A. Zimmermann, E. Schaible, S.Y. Tang, T. Alliston, R.O. Ritchie, Characterization of the effects of x-ray irradiation on the hierarchical structure and mechanical properties of human cortical bone, *Biomaterials.* 32 (2011) 8892–8904. doi:10.1016/j.biomaterials.2011.08.013.
- [53] P. Fratzl, H.S. Gupta, E.P. Paschalis, P. Roschger, Structure and mechanical quality of the collagen-mineral nano-composite in bone, *J. Mater. Chem.* 14 (2004) 2115–2123. doi:10.1039/b402005g.
- [54] K.J. Bundy, *Composite material models for bone*, CRC Press, Boca Raton, FC, 1989.
- [55] R.H. Bonser, Longitudinal variation in mechanical competence of bone along the avian humerus., *J. Exp. Biol.* 198 (1995) 209–212.
- [56] E. De Margerie, S. Sanchez, J. Cubo, J. Castanet, Torsional resistance as a principal component of the structural design of long bones: Comparative multivariate evidence in birds, *Anat. Rec. - Part A Discov. Mol. Cell. Evol. Biol.* 282 (2005) 49–66. doi:10.1002/ar.a.20141.
- [57] R.H.C. Bonser, P.P. Purslow, The Young's Modulus of Feather Keratin, *J. Exp. Biol.* 198 (1995) 1029–1033.
- [58] I.M. Weiss, H.O.K. Kirchner, The peacock's train (*Pavo cristatus* and *Pavo cristatus mut. alba*) I. structure, mechanics, and chemistry of the tail feather coverts., *J. Exp. Zool. A. Ecol. Genet. Physiol.* 313 (2010) 690–703. doi:10.1002/jez.641.
- [59] T. Bachmann, J. Emmerlich, W. Baumgartner, J.M. Schneider, H. Wagner, Flexural stiffness of feather shafts: geometry rules over material properties, *J. Exp. Biol.* 215 (2012) 405–415.
- [60] D.G. Crenshaw, Design and materials of feather shafts: very light, rigid structures, *Symp. Soc. Exp. Biol.* 43 (1980) 485–486.

- [61] R.H.C. Bonser, The mechanical properties of feather keratin, *J. Zool.* 239 (1996) 477–484. doi:10.1111/j.1469-7998.1996.tb05937.x.
- [62] P.P. Purslow, J.F.V. Vincent, Mechanical Properties of Primary Feathers from the Pigeon, *J. Exp. Biol.* 72 (1978) 251–260.
- [63] B. Wang, M.A. Meyers, Light like a feather : a fibrous natural composite with a shape changing from round to square, *Adv. Sci.* 4 (2016).
- [64] W. Corning, A. Biewener, In vivo strains in pigeon flight feather shafts: implications for structural design, *J. Exp. Biol.* 201 (Pt 22 (1998) 3057–65. <http://www.ncbi.nlm.nih.gov/pubmed/9787125>.
- [65] W.R. Corning, A.A. Biewener, In vivo strains in pigeon flight feather shafts: implications for structural design, *J. Exp. Biol.* 201 (1998) 3057–3065.
- [66] R. Lockwood, J.P. Swaddle, J.M. V Rayner, Avian Wingtip Shape Reconsidered: Wingtip Shape Indices and Morphological Adaptations to Migration, 1998.
- [67] J. Kiang, Avian Wing Bones, M.Sc. Thesis, University of California, San Diego, 2013.
- [68] J. Cubo, L. Menten, A. Casinos, Sagittal long bone curvature in birds, *Ann. Des Sci. Nat. - Zool. Biol. Anim.* 20 (1999) 153–159. doi:10.1016/S0003-4339(00)88883-8.
- [69] K.P. Dial, Avian Forelimb Muscles and Nonsteady Flight : Can Birds Fly without Using the Muscles in Their Wings ?, *Auk.* 109 (1992) 874–885.
- [70] Z.Q. Liu, D. Jiao, M.A. Meyers, Z.F. Zhang, Structure and mechanical properties of naturally occurring lightweight foam-filled cylinder – The peacock’s tail coverts shaft and its components, *Acta Biomater.* 17 (2015) 137–151. doi:10.1016/j.actbio.2015.01.035.
- [71] T. Bachmann, J. Emmerlich, W. Baumgartner, J.M. Schneider, H. Wagner, Flexural stiffness of feather shafts: geometry rules over material properties., *J. Exp. Biol.* 215 (2012) 405–15. doi:10.1242/jeb.059451.
- [72] C.J. Pennycuick, Gliding Flight of the Dog-Faced Bat *Rousettus Aegyptiacus* Observed in a Wind Tunnel, *J. Exp. Biol.* 55 (1971) 833–845. <http://jeb.biologists.org/content/55/3/833%5Cnhttp://jeb.biologists.org/content/55/3/833.full.pdf%5Cnhttp://jeb.biologists.org/content/55/3/833.short>.
- [73] O. Lilenthal, *Der Vogelflug als Grundlage der Fliegekunst*, Third, Oldernbourg, R., Munchen and Berlin, 1889.
- [74] R.E. Brown, A.C. Cogley, Contributions of the propatagium to avian flight, *J. Exp. Zool.* 276 (1996) 112–124. doi:10.1002/(SICI)1097-010X(19961001)276:2<112::AID-JEZ4>3.0.CO;2-R.
- [75] P.R. Stettenheim, The Integumentary Morphology of Modern Birds—An Overview, *Am.*

Zool. 40 (2000) 461–477.

- [76] C. Kazilek, S. Deviche, Feather Biology, Ask A Biol. Arizona State Univ. (2016). <https://askabiologist.asu.edu/explore/feather-biology> (accessed April 11, 2017).
- [77] T.N. Sullivan, A. Pissarenko, S.A. Herrera, D. Kisailus, V.A. Lubarda, M.A. Meyers, A lightweight, biological structure with tailored stiffness: the feather vane, *Acta Biomater.* 41 (2016) 27–39. doi:10.1016/j.actbio.2016.05.022.
- [78] B. Wang, W. Yang, J. McKittrick, M.A. Meyers, Keratin: Structure, mechanical properties, occurrence in biological organisms, and efforts at bioinspiration, *Prog. Mater. Sci.* 76 (2016) 229–318. doi:10.1016/j.pmatsci.2015.06.001.
- [79] T. Lingham-Soliar, R.H.C. Bonser, J. Wesley-Smith, Selective biodegradation of keratin matrix in feather rachis reveals classic bioengineering, *Proc. R. Soc. Biol. Sci.* 277 (2010) 1161–1168.
- [80] J. McMurry, R. Fay, *Chemistry: Biochemistry*, Pearson Prentice Hall, 2003.
- [81] R.D.B. Fraser, T.P. MacRae, G.E. Rogers, *Keratins: their composition, structure and biosynthesis*, 1972.
- [82] R.D.B. Fraser, D.A.D. Parry, The structural basis of the two-dimensional net pattern observed in the X-ray diffraction pattern of avian keratin, *J. Struct. Biol.* 176 (2011) 340–349. doi:10.1016/j.jsb.2011.08.010.
- [83] J. McKittrick, P.Y. Chen, S.G. Bodde, W. Yang, E.E. Novitskaya, M.A. Meyers, The structure, functions, and mechanical properties of keratin, *JOM.* 64 (2012) 449–468. doi:10.1007/s11837-012-0302-8.
- [84] T. Lingham-Soliar, N. Murugan, A New Helical Crossed-Fibre Structure of B -Keratin in Flight Feathers and Its Biomechanical Implications, *PLoS One.* 8 (2013).
- [85] C.M. Laurent, C. Palmer, R.P. Boardman, G. Dyke, R.B. Cook, Nanomechanical properties of bird feather rachises : exploring naturally occurring fibre reinforced laminar composites, *J. R. Soc. Interface.* (2014).
- [86] B. Busson, P. Engström, J. Doucet, Existence of various structural zones in keratinous tissues revealed by X-ray microdiffraction, *J. Synchrotron Radiat.* 6 (1999) 1021–1030. doi:10.1107/S0909049599004537.
- [87] C.M. Laurent, C. Palmer, R.P. Boardman, G. Dyke, R.B. Cook, Nanomechanical properties of bird feather rachises: exploring naturally occurring fibre reinforced laminar composites., *J. R. Soc. Interface.* 11 (2014) 20140961. doi:10.1098/rsif.2014.0961.
- [88] S.E. Naleway, M.M. Porter, J. McKittrick, M.A. Meyers, Structural design elements in biological materials: Application to bioinspiration, *Adv. Mater.* 27 (2015) 5455–5476.

- [89] B. Wang, M.A. Meyers, Nanoindentation on Feathers Rachises, (2016).
- [90] G.J. Cameron, T.J. Wess, R.H.C. Bonser, Young's modulus varies with differential orientation of keratin in feathers, *J. Struct. Biol.* 143 (2003) 118–123. doi:10.1016/S1047-8477(03)00142-4.
- [91] T. Bachmann, S. Klän, W. Baumgartner, M. Klaas, W. Schröder, H. Wagner, Morphometric characterisation of wing feathers of the barn owl *Tyto alba pratincola* and the pigeon *Columba livia*, *Front. Zool.* 4 (2007) 23. doi:10.1186/1742-9994-4-23.
- [92] G.D. Macleod, Mechanical Properties of Contour Feathers, *J. Exp. Biol.* 87 (1980) 65–71.
- [93] T. Lingham-Soliar, Feather structure, biomechanics and biomimetics: the incredible lightness of being, *J. Ornithol.* 155 (2013) 323–336. doi:10.1007/s10336-013-1038-0.
- [94] S.G. Bodde, M.A. Meyers, J. McKittrick, Correlation of the mechanical and structural properties of cortical rachis keratin of rectrices of the Toco Toucan (*Ramphastos toco*), *J. Mech. Behav. Biomed. Mater.* 4 (2011) 723–732.
- [95] S.N. Gorb, Biological attachment devices: exploring nature's diversity for biomimetics., *Philos. Trans. A. Math. Phys. Eng. Sci.* 366 (2008) 1557–1574. doi:10.1098/rsta.2007.2172.
- [96] P.E. Hunter, R.M.T. Rosario, Associations of mesostigma t a with other arthropods, (1988) 393–417.
- [97] E.S. Nielsen, I.F.B. Common, *The insects of Australia: Lepidoptera*, Cornell University Press, New York, 1991.
- [98] S.N. Gorb, P.J. Perez Goodwyn, Wing-locking mechanisms in aquatic Heteroptera, *J. Morphol.* 257 (2003) 127–146. doi:10.1002/jmor.10070.
- [99] Q. Meng, J. Hu, A review of shape memory polymer composites and blends, *Compos. Part A Appl. Sci. Manuf.* 40 (2009) 1661–1672. doi:10.1016/j.compositesa.2009.08.011.
- [100] M. Cabanlit, D. Maitland, T. Wilson, S. Simon, T. Wun, M.E. Gershwin, J. Van De Water, Polyurethane shape-memory polymers demonstrate functional biocompatibility in vitro, *Macromol. Biosci.* 7 (2007) 48–55. doi:10.1002/mabi.200600177.
- [101] X. Xiao, D. Kong, X. Qiu, W. Zhang, Y. Liu, S. Zhang, F. Zhang, Y. Hu, J. Leng, Shape memory polymers with high and low temperature resistant properties, *Sci. Rep.* 5 (2015) 14137. doi:10.1038/srep14137.
- [102] H. Meng, G. Li, A review of stimuli-responsive shape memory polymer composites, *Polymer (Guildf)*. 54 (2013) 2199–2221. doi:10.1016/j.polymer.2013.02.023.
- [103] J.L. Hu, S. Mondal, Structural characterization and mass transfer properties of segmented polyurethane: Influence of block length of hydrophilic segments, *Polym. Int.* 54 (2005)

- 764–771. doi:10.1002/pi.1753.
- [104] J. Hu, Z. Yang, L. Yeung, F. Ji, Y. Liu, Crosslinked polyurethanes with shape memory properties, *Polym. Int.* 54 (2005) 854–859. doi:10.1002/pi.1785.
- [105] C. Liu, H. Qin, P.T. Mather, Review of progress in shape-memory polymers, *J. Mater. Chem.* 17 (2007) 1543. doi:10.1039/b615954k.
- [106] A.B. Victor, V.N. Varyukhin, V.V. Yurii, The shape memory effect in polymers, *Russ. Chem. Rev.* 74 (2005) 265. doi:10.1070/RC2005v074n03ABEH000876.
- [107] W. Voit, T. Ware, R.R. Dasari, P. Smith, L. Danz, D. Simon, S. Barlow, S.R. Marder, K. Gall, High-strain shape-memory polymers, *Adv. Funct. Mater.* 20 (2010) 162–171. doi:10.1002/adfm.200901409.
- [108] S. Zhang, Z. Yu, T. Govender, H. Luo, B. Li, A novel supramolecular shape memory material based on partial β -CD-PEG inclusion complex, *Polymer (Guildf)*. 49 (2008) 3205–3210. doi:10.1016/j.polymer.2008.05.030.
- [109] F.L. Ji, J.L. Hu, T.C. Li, Y.W. Wong, Morphology and shape memory effect of segmented polyurethanes. Part I {cyrillic, ukrainian}: With crystalline reversible phase, *Polymer (Guildf)*. 48 (2007) 5133–5145. doi:10.1016/j.polymer.2007.06.032.
- [110] Y. Zhu, J.L. Hu, K.W. Yeung, Y.Q. Liu, H.M. Liem, Influence of ionic groups on the crystallization and melting behavior of segmented polyurethane ionomers, *J. Appl. Polym. Sci.* 100 (2006) 4603–4613. doi:10.1002/app.23009.
- [111] F. Ji, Y. Zhu, J. Hu, Y. Liu, L.-Y. Yeung, G. Ye, Smart Polymer Fibers with Shape Memory Effect, *Smart Mater. Struct.* 15 (2006) 1547–1554. doi:10.1088/0964-1726/15/6/006.
- [112] I. a. Rousseau, T. Xie, Shape memory epoxy: Composition, structure, properties and shape memory performances, *J. Mater. Chem.* 20 (2010) 3431. doi:10.1039/b923394f.
- [113] I.A. Rousseau, P.T. Mather, Shape Memory Effect Exhibited by Smectic-C Liquid Crystalline Elastomers, *J. Am. Chem. Soc.* 125 (2003) 15300–15301. doi:10.1021/ja039001s.
- [114] I.A. Rousseau, H. Qin, P.T. Mather, Tailored phase transitions via mixed-mesogen liquid crystalline polymers with silicon-based spacers, *Macromolecules*. 38 (2005) 4103–4113. doi:10.1021/ma048327y.
- [115] S. Ahn, P. Deshmukh, R.M. Kasi, Shape Memory Behavior of Side-Chain Liquid Crystalline Polymer Networks Triggered by Dual Transition Temperatures, *Macromolecules*. 43 (2010) 7330–7340. doi:10.1021/ma101145r.
- [116] W.M. Huang, B. Yang, L. An, C. Li, Y.S. Chan, Water-driven programmable polyurethane shape memory polymer: Demonstration and mechanism, *Appl. Phys. Lett.*

- 86 (2005) 1–3. doi:10.1063/1.1880448.
- [117] W.M. Huang, B. Yang, Y. Zhao, Z. Ding, Thermo-moisture responsive polyurethane shape-memory polymer and composites: a review, *J. Mater. Chem.* 20 (2010) 3367–3381. doi:10.1039/b922943d.
- [118] G. Galilei, *Dialogues Concerning Two New Sciences*, Dover Publications, New York, 1914.
- [119] J.S. Huxley, G. Tesissier, Terminology of Relative Growth, *Nature*. 137 (1936) 780–781. doi:10.1038/148225a0.
- [120] E. Arzt, S. Gorb, R. Spolenak, From micro to nano contacts in biological attachment devices, *Proc. Natl. Acad. Sci.* 100 (2003) 10603–10606. doi:10.1073/pnas.1534701100.
- [121] D. Labonte, C.J. Clemente, A. Dittrich, C.-Y. Kuo, A.J. Crosby, D.J. Irschick, W. Federle, Extreme positive allometry of animal adhesive pads and the size limits of adhesion-based climbing, *Proc. Natl. Acad. Sci.* 113 (2016) 1297–1302. doi:10.1073/pnas.1519459113.
- [122] G.B. West, J.H. Brown, B.J. Enquist, A General Model for the Origin of Allometric Scaling Laws in Biology, *Science* (80-.). 276 (1997) 122–126. doi:10.1126/science.276.5309.122.
- [123] O. Dreyer, R. Puzio, Allometric scaling in animals and plants, *J. Math. Biol.* 43 (2001) 144–156. doi:10.1187/cbe.10-08-0099.
- [124] T. McMahon, *Size and Shape in Biology*, 179 (1973) 1201–1204.
- [125] J. Bou, A. Casinos, J. Ocaña, Allometry of the limb long bones of insectivores and rodents, *J. Morphol.* 192 (1987) 113–123. doi:10.1002/jmor.1051920204.
- [126] R.M.N. Alexander, A.S. Jayes, G.M.O. Maloiy, E.M. Wathuta, Allometry of the limb bones of mammals from shrews (*Sorex*) to elephant (*Loxodonta*), *J. Zool.* 189 (1979) 305–314. doi:10.1111/j.1469-7998.1979.tb03964.x.
- [127] H. Lin, Fundamentals of zoological scaling, *Am. J. Phys.* 50 (1982) 72. doi:10.1119/1.12990.
- [128] K.L. Moore, T.V.N. Persaud, M.G. Torchia, *The Developing Human*, Elsevier, Philadelphia, PA, 2013.
- [129] D.W. Thompson, *On Growth and Form*, Cambridge University Press, Cambridge, UK, 1917.
- [130] A. Shingleton, Allometry: The study of biological scaling, *Nat. Educ.* 3 (2010) 2.
- [131] M. Olmos, A. Casinos, J. Cubo, Limb allometry in birds, *Ann. Nat. Sci. Zool. Anim. Biol.* 17 (1996) 39–49.

- [132] X. Wang, R.L. Nudds, C. Palmer, G.J. Dyke, Size scaling and stiffness of avian primary feathers: Implications for the flight of Mesozoic birds, *J. Evol. Biol.* 25 (2012) 547–555. doi:10.1111/j.1420-9101.2011.02449.x.
- [133] S.E. Worcester, The scaling of the size and stiffness of primary flight feathers, *J. Zool.* 239 (1996) 609–624. doi:10.1111/j.1469-7998.1996.tb05947.x.
- [134] P. Gopalakrishnan, D.K. Tafti, Effect of Wing Flexibility on Lift and Thrust Production in Flapping Flight, *AIAA J.* 48 (2010) 865–877. doi:10.2514/1.39957.
- [135] A.M. Mountcastle, S.A. Combes, Wing flexibility enhances load-lifting capacity in bumblebees., *Proc. Biol. Sci.* 280 (2013) 20130531. doi:10.1098/rspb.2013.0531.
- [136] H. Tennekes, *The Simple Science of Flight: From Insects to Jumbo Jets*, 4th ed., MIT Press, Cambridge, Massachusetts, 2000.
- [137] T. Alerstam, M. Rosen, J. Backman, P.G.P. Ericson, O. Hellgren, Flight speeds among bird species : Allometric and phylogenetic effects, *PLoS Biol.* 5 (2007).
- [138] B.M. Gilbert, L.D. Martin, H.G. Savage, *Avian Osteology*, B. Miles Gilbert, Laramie, Wyoming, 1981.
- [139] C.J. Pennycuick, Flight of auks (Alcidae) and other northern seabirds compared with southern procellariiformes: ornithodolite observations, *J. Exp. Biol.* 128 (1987) 335–347. doi:10.1016/0198-0254(87)90303-7.
- [140] C.J. Pennycuick, Predicting wingbeat frequency and wavelength of birds, *J. Exp. Biol.* 150 (1990) 171–185.
- [141] C.H. Greenewalt, *The Flight of Birds: The Significant Dimensions, Their Departure from the Requirements for Dimensional Similarity, and the Effect on Flight Aerodynamics of That Departure*, American Philosophical Society, Philadelphia, 1975. doi:10.1080/14786443908649806.
- [142] M.F. Ashby, *Materials Selection in Mechanical Design*, 3rd Editio, Pergamon Press, Burlington, USA, 2005.
- [143] U.K. Muller, D. Lentink, Turning on a Dime, *Science* (80-.). 306 (2004) 1899–1900. doi:10.1126/science.1107070.
- [144] A. Azuma, *The Biokinetics of Flying and Swimming*, Second, American Institute of Aeronautics and Astronautics, Inc., Reston, USA, 2006.
- [145] A.M. Lucas, P.R. Stettenheim, Structure of Feathers, in: *Avian Anat. Integument*, US Department of Agriculture, Washington, D.C., USA, 1972: pp. 341–419.
- [146] A. Kovalev, A.E. Filippov, S.N. Gorb, Unzipping bird feathers, *J. R. Soc. Interface.* 11 (2014) 20130988.

- [147] J. Barlee, Flight, in: A. Landsborough Thomson (Ed.), *A New Dict. Birds*, Nelson, London, UK, 1964.
- [148] R.H.J. Brown, Flight, in: A.J. Marshall (Ed.), *Biol. Comp. Physiol. Anim.*, Academic Press, New York, USA, 1961.
- [149] L. Alibardi, Cell organization of barb ridges in regenerating feathers of the quail: Implications of the elongation of barb ridges for the evolution and diversification of feathers, *Acta Zool.* 88 (2007) 101–117.
- [150] R.D. Cook, W.C. Young, *Advanced Mechanics of Materials*, first ed., Macmillan, New York, 1985.
- [151] W. Yang, J. McKittrick, Separating the influence of the cortex and foam on the mechanical properties of porcupine quills, *Acta Biomater.* 9 (2013) 9065–9074.
- [152] W. Yang, C. Chao, J. McKittrick, Axial compression of a hollow cylinder filled with foam: A study of porcupine quills, *Acta Biomater.* 9 (2013) 5297–5304.
- [153] M. Butler, A.S. Johnson, Are melanized feather barbs stronger ?, *J. Exp. Biol.* 207 (2004) 285–293.
- [154] Z.Q. Liu, D. Jiao, Z.F. Zhang, Remarkable shape memory effect of a natural biopolymer in aqueous environment, *Biomaterials.* 65 (2015) 13–21.
- [155] T.N. Sullivan, M. Chon, R. Ramachandramoorthy, M.R. Roenbeck, T.-T. Hung, H.D. Espinosa, M.A. Meyers, Reversible Attachment with Tailored Permeability: The Feather Vane and Bioinspired Designs, *Adv. Funct. Mater.* 1702954 (2017) 1702954. doi:10.1002/adfm.201702954.
- [156] A. Raspet, Biophysics of Bird Flight, *Science.* 132 (1960) 191–200.
- [157] M. Naraghi, G.H. Bratzel, T. Filleter, Z. An, X. Wei, S.T. Nguyen, M.J. Buehler, H.D. Espinosa, Atomistic investigation of load transfer between DWNT bundles “crosslinked” by PMMA oligomers, *Adv. Funct. Mater.* 23 (2013) 1883–1892. doi:10.1002/adfm.201201358.
- [158] M.R. Roenbeck, A. Furmanchuk, Z. An, J.T. Paci, X. Wei, S.T. Nguyen, G.C. Schatz, H.D. Espinosa, Molecular-Level Engineering of Adhesion in Carbon Nanomaterial Interfaces, *Nano Lett.* 15 (2015) 4504–4516. doi:10.1021/acs.nanolett.5b01011.
- [159] A.R. Ennos, J.R.E. Hickson, A. Roberts, Functional morphology of the vanes of the flight feathers of the pigeon *Columba livia*, *J. Exp. Biol.* 198 (1995) 1219–1228.
- [160] J.M. Gere, S.P. Timoshenko, *Mechanics of Materials*, 3rd ed., PWS-Kent Publishing Company, Boston, 1991.
- [161] C. Rojahn, *Large deflections of elastic beams*, Stanford University, 1968.

- [162] G.K. Batchelor, *An Introduction to Fluid Dynamics*, Cambridge University Press, Cambridge, UK, 1967.
- [163] J. McKittrick, P.Y. Chen, S.G. Bodde, W. Yang, E.E. Novitskaya, M.A. Meyers, The structure, functions, and mechanical properties of keratin, *JOM*. 64 (2012). doi:10.1007/s11837-012-0302-8.
- [164] B. Wang, M.A. Meyers, Seagull feather shaft: Correlation between structure and mechanical response, *Acta Biomater.* 48 (2017) 270–288. doi:10.1016/j.actbio.2016.11.006.
- [165] M. Feughelman, *Mechanical properties and structure of alpha-keratin fibers: wool, human hair and related fibers*, University of New South Wales Press, 1997.
- [166] R.D.B. Fraser, T.P. MacRae, *The mechanical properties of biological materials (proceedings of the symposia of the society for experimental biology)*, in: J.F.V. Vincent, J.D. Currey (Eds.), *Mol. Struct. Mech. Prop. Keratins.*, Cambridge University Press, Cambridge, UK, 1980: pp. 211–246.
- [167] M. Feughelman, M.S. Robinson, *The Relationship Between Some Mechanical Properties of Single Wool Fibers and Relative Humidity*, *Text. Res. J.* 37 (1967). doi:10.1177/058310248001200917.
- [168] B. Wang, W. Yang, J. McKittrick, M.A. Meyers, *Keratin: Structure, Mechanical Properties, Occurrence in Biological Organisms, and Efforts at Bioinspiration*, *Prog. Mater. Sci.* 76 (2015) 229–318. doi:10.1016/j.pmatsci.2015.06.001.
- [169] Z.Q. Liu, D. Jiao, Z.F. Zhang, Remarkable shape memory effect of a natural biopolymer in aqueous environment, *Biomaterials.* 65 (2015) 13–21. <http://linkinghub.elsevier.com/retrieve/pii/S0142961215005463>.
- [170] B.K. Filshie, G.E. Rogers, *An electron microscope study of the fine structure of feather keratin.*, *J. Cell Biol.* 13 (1962) 1–12. <http://www.pubmedcentral.nih.gov/articlerender.fcgi?artid=2106060&tool=pmcentrez&rendertype=abstract>.
- [171] B.O. Brilot, L. Asher, M. Bateson, Water bathing alters the speed-accuracy trade-off of escape flights in European starlings, *Anim. Behav.* 78 (2009) 801–807. doi:10.1016/j.anbehav.2009.07.022.
- [172] M.B. Frank, S.E. Naleway, T.S. Wirth, J.-Y. Jung, C.L. Cheung, F.B. Loera, S. Medina, K.N. Sato, J.R.A. Taylor, J. McKittrick, *A Protocol for Bioinspired Design: A Ground Sampler Based on Sea Urchin Jaws*, *J. Vis. Exp.* (2016) 1–8. doi:10.3791/53554.
- [173] R.T. Whitcomb, *A design approach and selected wind- tunnel results at high subsonic speeds for wing-tip mounted winglets*, 1976. <http://ntrs.nasa.gov/archive/nasa/casi.ntrs.nasa.gov/19760019075.pdf>.

- [174] Boeing, 787 Dreamliner by design, (2017). http://www.boeing.com/commercial/787/by-design?cm_re=42552-_-Hero+rotator-_-787+Dreamliner+By+Design#/superior-tech (accessed January 1, 2017).
- [175] J. Paur, Boeing 787 passes incredible wing flex test, *Wired*. (2010). <https://www.wired.com/2010/03/boeing-787-passes-incredible-wing-flex-test/> (accessed January 1, 2017).
- [176] X. Jin, B. Shi, L. Zheng, X. Pei, X. Zhang, Z. Sun, Y. Du, J.H. Kim, X. Wang, S. Dou, K. Liu, L. Jiang, Bio-inspired multifunctional metallic foams through the fusion of different biological solutions, *Adv. Funct. Mater.* 24 (2014) 2721–2726. doi:10.1002/adfm.201304184.
- [177] A.G. Evans, J.W. Hutchinson, N.A. Fleck, M.F. Ashby, H.N.G. Wadley, The topological design of multifunctional cellular metals, *Prog. Mater. Sci.* 46 (2001) 309–327. doi:10.1016/S0079-6425(00)00016-5.
- [178] M.F. Ashby, A. Evans, N.A. Fleck, L.J. Gibson, J.W. Hutchinson, H.N.G. Wadley, *Metal Foams A Design Guide*, Elsevier, 2000.
- [179] B. Budiansky, On the minimum weights of compression structures, *Int. J. Solids Struct.* 36 (1999) 3677–3708. doi:10.1016/S0020-7683(98)00169-3.
- [180] Federal Aviation Administration, *Aircraft Structures- Federal Aviation Administration*, in: *Aviat. Maint. Tech. Handb. - Airframe*, 2012: p. 48.
- [181] L. Krog, A. Tucker, M. Kemp, R. Boyd, Topology Optimisation of Aircraft Wing Box Ribs, in: *10th AIAA/ISSMO Multidiscip. Anal. Optim. Conf.*, American Institute of Aeronautics and Astronautics, Albany, NY, 2004: pp. 1–16. doi:10.2514/6.2004-4481.
- [182] G.D. Swanson, Z. Gurdal, J.H. Starnes, Structural efficiency study of graphite-epoxy aircraft rib structures, *J. Aircr.* 27 (1990) 1011–1020. doi:10.2514/3.45975.
- [183] J.K. Paik, A.K. Thayamballi, P.T. Pedersen, Y. Il Park, Ultimate strength of ship hulls under torsion, 2001. doi:10.1016/S0029-8018(01)00015-4.
- [184] K. Iijima, T. Shigemi, R. Miyake, A. Kumano, A practical method for torsional strength assessment of container ship structures, *Mar. Struct.* 17 (2004) 355–384. doi:10.1016/j.marstruc.2004.08.011.
- [185] E. Alfred Mohammed, S.D. Benson, S.E. Hirdaris, R.S. Dow, Design safety margin of a 10,000 TEU container ship through ultimate hull girder load combination analysis, *Mar. Struct.* 46 (2016) 78–101. doi:10.1016/j.marstruc.2015.12.003.
- [186] K.D. Schmidt, M.A. Robinson, *Fiber Glass Ski With Channel Construction*, 3503621, 1970.
- [187] J.G. Howe, *Ski Construction*, 5820154, 1998.

- [188] H.M. Anderson, Laminated Ski Having a Foan Filled Honeycomb Core, 3276784, 1966.
- [189] W.H. Vinton, Ski, 2277281, 1942.
- [190] V.M. Drakonakis, C.N. Velisaris, J.C. Seferis, C.C. Doumanidis, Feather-inspired carbon fiber reinforced polymers with nanofibrous fractal interlayer, *Polym. Compos.* (2014). doi:10.1002/pc.23168.
- [191] C. Sanchez, H. Arribart, M.M.G. Guille, Biomimetism and bioinspiration as tools for the design of innovative materials and systems., *Nat. Mater.* 4 (2005) 277–288. doi:10.1038/nmat1339.
- [192] M. Li, H. Schnablegger, S. Mann, Coupled synthesis and self-assembly of nanoparticles to give structures with controlled organization, *Nature.* 402 (1999) 393–395. doi:10.1038/46509.
- [193] C.M. Niemeyer, B. Ceyhan, M. Noyong, U. Simon, Bifunctional DNA-gold nanoparticle conjugates as building blocks for the self-assembly of cross-linked particle layers, *Biochem. Biophys. Res. Commun.* 311 (2003) 995–999. doi:10.1016/j.bbrc.2003.10.103.
- [194] D. Iacopino, A. Ongaro, L. Nagle, R. Eritja, D. Fitzmaurice, Imaging the DNA and nanoparticle components of a self-assembled nanoscale architecture, *Nanotechnology.* 14 (2003) 447–452. doi:10.1088/0957-4484/14/4/308.
- [195] B.W. Shenton, S.A. Davis, S. Mann, Directed Self-Assembly of Nanoparticles into Macroscopic Materials Using Antibody - Antigen Recognition **, *Adv. Mater.* 11 (1999) 449–452.
- [196] S. Deville, E. Saiz, R.K. Nalla, A.P. Tomsia, Freezing as a path to build complex composites., *Science.* 311 (2006) 515–518. doi:10.1126/science.1120937.
- [197] S. Sadeghpour, A. Amirjani, M. Hafezi, A. Zamanian, Fabrication of a novel nanostructured calcium zirconium silicate scaffolds prepared by a freeze-casting method for bone tissue engineering, *Ceram. Int.* 40 (2014) 16107–16114. doi:10.1016/j.ceramint.2014.07.039.
- [198] M. Hafezi, N. Nezafati, A. Nadernezhad, M. Yasaei, A. Zamanian, S. Mobini, Effect of sintering temperature and cooling rate on the morphology, mechanical behavior and apatite-forming ability of a novel nanostructured magnesium calcium silicate scaffold prepared by a freeze casting method, *J. Mater. Sci.* 49 (2014) 1297–1305. doi:10.1007/s10853-013-7813-8.
- [199] L. Jing, K. Zuo, Z. Fuqiang, X. Chun, F. Yuanfei, D. Jiang, Y.P. Zeng, The controllable microstructure of porous Al₂O₃ ceramics prepared via a novel freeze casting route, *Ceram. Int.* 36 (2010) 2499–2503. doi:10.1016/j.ceramint.2010.07.005.
- [200] M. Bognitzki, W. Czado, T. Frese, A. Schaper, M. Hellwig, M. Steinhart, A. Greiner, J.H. Wendorff, Nanostructured fibers via electrospinning, *Adv. Mater.* 13 (2001) 70–72.

doi:10.1002/1521-4095(200101)13:1<70::AID-ADMA70>3.0.CO;2-H.

- [201] R. Ramaseshan, S. Sundarrajan, R. Jose, S. Ramakrishna, Nanostructured ceramics by electrospinning, *J. Appl. Phys.* 102 (2007). doi:10.1063/1.2815499.
- [202] M.P. Prabhakaran, J. Venugopal, S. Ramakrishna, Electrospun nanostructured scaffolds for bone tissue engineering, *Acta Biomater.* 5 (2009) 2884–2893. doi:10.1016/j.actbio.2009.05.007.
- [203] R. Ostermann, D. Li, Y. Yin, J.T. McCann, Y. Xia, V 2O 5 nanorods on TiO 2 nanofibers: A new class of hierarchical nanostructures enabled by electrospinning and calcination, *Nano Lett.* 6 (2006) 1297–1302. doi:10.1021/nl060928a.
- [204] A. Ghobarah, M.N. Ghorbel, S.E. Chidiac, Upgrading Torsional Resistance of Reinforced Concrete Beams Using Fiber-Reinforced Polymer, *J. Compos. Constr.* 6 (2002) 257–263. doi:10.1061/(ASCE)1090-0268(2002)6:4(257).
- [205] C. Arnold, Earthquake Effects on Buildings, in: *Des. Earthquakes, A Man. Archit.*, Federal Emergency Management Agency, 2006.